Multi-Layer-Graphene-Nanoclay-Epoxy Nanocomposites – Theory and Experimentation

A RASHEED

PhD

2016

Multi-Layer-Graphene-Nanoclay-Epoxy Nanocomposites – Theory and Experimentation

AATIF RASHEED

A thesis submitted in partial fulfilment of the requirements of the University of Northumbria at Newcastle for the degree of Doctor of Philosophy

Research undertaken in the Faculty of Engineering Sciences

November 2016

Abstract

The influence of Multi-Layer Graphene (MLG) and nanoclay on the performance of epoxy based nanocomposites has been studied. First, the theoretical aspects of nano-fillers and their impact on mechanical, thermal, and electrical properties of nanocomposites have been discussed. Then, nanocomposites were produced with varying weight fraction of nano-fillers (0.05, 0.1, 0.3, 0.5, and 1.0 wt%). It was observed that organic solvent, if not completely removed, causes porosity which acts as stress raiser and deteriorates the mechanical properties. The influence of reinforcement morphology on the mechanical properties of epoxy nanocomposites was studied using two nano-fillers: MLG and nanostructured graphite (NSG). It was observed that mechanical properties of nanocomposites were higher when the filler had corrugated and fluted topography. Modeling and simulation of epoxy nanocomposites were carried out using finite element method. It was observed that graphene based nano-fillers are efficient in scattering and dissipation of heat flux thereby increasing the thermal stability of epoxy nanocomposites. The macro-topography of bulk samples of monolithic epoxy and nanocomposites was modified by treating the samples with the abrasive papers. It was observed that surface notches, when exceed certain depth, cause degradation in mechanical properties. It was further observed that tensile properties are more sensitive to topography than flexural properties.

Key words: Multi-Layer Graphene (MLG); Nanostructured graphite (NSG); Macro-topography; Epoxy; Nanoclay; Modeling; Simulation; Mechanical properties.

Table of contents

Chapter-1

Mechanical, Thermal, and Electrical Properties of Graphene-Epoxy Nanocomposites – A Review

Chapter-2

Influence of Macro-Topography on Damage Tolerance and Fracture Toughness of MLG-Nanoclay-Epoxy Nanocomposites

---

Chapter-3

Fractography Analysis with Surface Roughness Features of MLG-Nanoclay-Epoxy Nanocomposites

Chapter-4

Conclusions and future work

Acknowledgements

All extols to the Almighty, who by His eternal benevolence gave me ability and potency to complete my thesis within predetermined time. It is a great honor and gratification for me that Dr. Fawad Inam supervised me in my research work. First of all, I would like to pay my regards to him as his worthwhile guidance, immaculate suggestions, fathomless support and encouragement played a key role in completion of my research work.

I am deeply grateful to my co-supervisor Dr. Islam Shyha for his proofreading and valuable feedback of the research articles. The experimental part could not be completed without the assistance of lab technicians and assistants. First of all, I would like to acknowledge the efforts of Dr. Pietro Maiello who trained me on SEM, EDS and XRD. I am also deeply thankful to Mr. Phil Donelley, Mr. Simon Neville, and Mr. Sam Hutchinston for training me on tensile testing machine, hardness tester, impact tester, and Alicona optical microscope.

During this research work, many people supported and helped me at various stages. I would like to thank all of them for their upright and procedural assistance. I would like to express gratitude to Jiacheng Wei, Mohd Shahneel Sahurdin, and Chichi Okolo for their useful suggestions.

I am most beholden to Northumbria University Newcastle, for providing me scholarship and material support to fulfill financial requirements. I believe it won`t be justified not to concede the great endurance of my loving mother, kind father, siblings, and all my family members for their sincere and generous affection and prayers which enabled me to complete my research work.

Declaration

I declare that the work contained in this thesis has not been submitted for any other award and that it is all my own work. I also confirm that this work fully acknowledges opinions, ideas and contributions from the work of others.

Any ethical clearance for the research presented in this thesis has been approved. Approval has been sought and granted by the Faculty Ethics Committee/University Ethics Committee/external committee on January 2015.

I declare that the word count of this thesis is 48,487 (including references).

Name: Aatif Rasheed

Signature:

Date:

1 List of abbreviations

3RM: Three roll milling,

A: Aramid fibers,

APTS-GO: Amino-functionalized graphene oxide (GO),

ATGO: 3-Aminopropyltriethoxysilane functionalized silica nanoparticles attached GO,

ATP: Attapulgite,

ATS: 3-amino functionalized silica nanoparticles,

CM: Centrifugal mixing,

CNF: Carbon nanofiber,

CNTs: Carbon nanotubes,

DGEBA-f-GO: Diglycidyl ether of bisphenol-A functionalized GO,

DRA: Discontinuously reinforced aluminum,

DRTi: Discontinously reinforced titanium,

EGNPs: Amine functionalized expanded graphene nanoplatelets,

EMCs: Epoxy matrix composites,

fGnPs: Polybenzimidazole functionalized graphene platelets (GnPs),

GF: Graphene foam,

G-NH_2: Amino-functionalized GNPs,

GNs: Amine functionalized graphene sheets,

GNSs: Graphene nanosheets,

GO: Graphene oxide,

GP: Graphite particles,

GPTS-GO: Epoxy functionalized GO,

G-Si: Silane modified GNPs,

HPH+3RM: High pressure homogenizer + three roll milling,

HSM: High speed mixing,

m-nanoclay: Surface modified nanoclay,

m-CNFs: Triazole functionalized carbon nanofibers,

MERGO: Microwave exfoliated reduced graphene oxide,

m-GnP: Surface modified GnP,

m-GP: Surface modified graphene platelets,

MS: Mechanical stirring,

MS + USn: Mechanical stirring + Ultrasonication,

MWCNTs: Multi-walled carbon nanotubes,

MWNTs: Multi-walled carbon nanotubes,

ND: Nanodiamond,

P: Polyacrylonitrile (PAN) fibers,

p-CNFs: Pristine carbon nanofibers,

PEA: Polyetheramine,

phr: Per hundred parts of resin,

PMCs: Polymer matrix composites,

Q/I: Quasi-isotropic,

RGO: Thermally reduced graphene oxide,

SATPGO: 3-Aminopropyltriethoxysilane modified silica nanoparticles attached graphene oxide,

SCFs: Short carbon fibers,

ShM: Shear mixing,

Silane-f-GO: Silane functionalized GO,

SM: Speed mixing,

Sn: Sonication,

Sn+BM: Sonication + Ball milling,

Sn+MgSr: Sonication + Magnetic stirring,

Sn+MS: Sonication + Mechanical stirring,

SWNTs: Single-walled carbon nanotubes,

TEM: Transmission electron microscopy,

TPE: Two phase extraction,

UG: Unmodified graphene nanoplatelets,

U-GnP: Unmodified graphene platelets,

USn: Ultrasonication.

2 Introduction

The Polymer Matrix Composites (PMCs) are the first manufactured composite materials during World War II [1]. The PMCs applications started on larger scale during 1950s while during 1960s, the applications in consumer sporting equipment extensively increased their market. During the energy crises in 1970s, the demand for PMCs further increased due to their relatively low cost. During this period, the properties of PMCs, the design methodologies and manufacturing capabilities were further modified. With the improvement in other properties, the maximum service temperature for PMCs also increased. The PMCs have replaced aerospace structural alloys such as aluminum alloys as they are prone to corrosion and fatigue failure. The high-performance PMCs are increasingly finding demand in the infrastructure commodity market. The matrices used in PMCs can broadly be divided into two types: (1) thermosetting polymers, and (2) thermoplastic polymers.

Among thermosetting resins, epoxy is the most commonly used matrix of choice for composites and has found applications in numerous fields. The stiff and fragile structure of monolithic epoxy accomplices the innate cracks to cause fracture and therefore the applications of monolithic epoxy are not ubiquitous. Because of its stiff and fragile structure, crack generation and fracture is a major concern in the monolithic epoxy. The ability of a material containing crack to resist fracture, known as fracture toughness, is a simple yet trustworthy indicator of the material's damage tolerance and hindrance against fracture, and is considered as one of the most important mechanical properties of the engineering materials. The fracture toughness depends upon how the pre-existing and newly formed cracks propagate within a material. Monolithic epoxy, because of its stiffness, cannot prevent crack propagation and is vulnerable to fracture. However, it is

well established that when reinforced especially by nano-fillers, such as metallic oxides [2–4], nanoclays [5–7], carbon nanotubes (CNTs) [8–10], and other carbonaceous materials [11–13], its ability to withstand crack propagation is propitiously improved. Among various nano-fillers, graphene has recently been employed as reinforcement in epoxy to enhance the fracture related properties of the produced epoxy-graphene nanocomposites.

There is an exponential rise in the use of graphene in the last decade. Novoselov et al. [14] experimentally produced Single Layer Graphene (SLG) using scotch-tape method and a low cost method to synthesize graphene on large scale was presented by Stankovich et al. [15] allowing the extension of the applications of graphene to industrial scale. In 2014, 2009 research papers were published on graphene in which about 830 papers were on graphene-epoxy nanocomposites produced using solution casting technique. It shows that epoxy and solution casting technique are still preferred choices as polymer matrix and production method, respectively. It can also be deduced that the academics are at the moment not interested in introducing some new polymer matrix or to invent some new production method to produce Graphene Based Polymer Nanocomposites (GBPNCs). Instead, research has been carried out to explore the role of graphene in influencing the polymer properties both theoretically and experimentally. To the best of our knowledge, no article is yet published in which SLG was used in polymer matrices to produce nanocomposites. One reason could be that the SLG is not yet at everyone's disposal. However, the trends indicate that the graphene would surpass other reinforcements no sooner it becomes easily available. Therefore, extensive theoretical research has been carried out in the last decade to justify the use of graphene as reinforcement in polymers.

2.1 Problem statement

There is no detailed information available studying the influence of surface roughness of nano-fillers and of nanocomposites on the performance of epoxy nanocomposites. The surface roughness significantly affects the most important aspects of nanocomposites. For example, the topography of nano-fillers may significantly influence the interfacial interactions by mechanical interlocking and chemical interactions by increasing the surface area and surface energy. Similarly, the topography of nanocomposites bulk samples significantly dictates the performance of nanocomposites. For example, the surface notches generate a triaxial state of stress. The triaxial state of stress may not be severe in ductile materials such as non-ferrous metals. However, it becomes quite severe in case of brittle materials such as epoxy. Therefore, extensive study is required to ace the influence of nano-fillers, macro-topograpy, and dispersion state on the performance of nanocomposites.

2.2 Objective

The thesis is divided into four chapters of literature and experimental work. The main objectives of the thesis are listed below.

1. To investigate the influence of surface roughness on mechanical properties of monolithic epoxy and MLG-nanoclay-epoxy samples. The surface roughness values studied include waviness (W_a), roughness average (R_a), root mean square value (R_q), and maximum roughness height (R_{max} or R_z).
2. To analyze the fracture patterns of monolithic epoxy and MLG-nanoclay-epoxy as-cast samples and with tailored topography.

Chapter-1

Mechanical, Thermal, and Electrical Properties of Graphene-Epoxy Nanocomposites – A Review

---

3 Abstract

Among thermosetting resins, epoxy is the most commonly used matrix of choice for composites and has found applications in numerous fields. The stiff and fragile structure of monolithic epoxy accomplices the innate cracks to cause fracture and therefore the applications of monolithic epoxy are not ubiquitous. The ability of a material containing a crack to resist fracture, known as fracture toughness, is a simple yet trustworthy indicator of the material's damage tolerance and hindrance against fracture, and is considered as one of the most important mechanical properties. The fracture toughness depends upon how the pre-existing and newly formed cracks propagate. Monolithic epoxy, because of its brittleness, cannot prevent crack propagation and is vulnerable to fracture. However, it is well established that when reinforced especially by nano-fillers, such as metallic oxides, nanoclays, carbon nanotubes, and other carbonaceous materials, its ability to withstand crack propagation is propitiously improved. Among various nano-fillers, graphene has recently been employed as reinforcement in epoxy to enhance the fracture related properties of the produced epoxy-graphene nanocomposites. In this review, mechanical, thermal, and electrical properties of graphene reinforced epoxy nanocomposites will be correlated with the surface roughness features, morphology, weight fraction, dispersion state, and surface functionalization of graphene.

4 Introduction

The Polymer Matrix Composites (PMCs) have found extensive applications in aerospace, automotive, and construction owing to ease of processing and high strength to weight ratio which is an important property required for aerospace applications [16]. Among different polymers, epoxy is the most commonly used thermosetting polymer matrix in PMCs [1]. The damage tolerance and fracture toughness of epoxy can be enhanced with the incorporation of (nano-) reinforcement such as metallic oxides [2–4], nanoclays [5–7], carbon nanotubes (CNTs) [8–10], and other carbonaceous materials [11–13]. After the groundbreaking experiments on the two dimensional material graphene by Nobel Laureates, Sir Andre Geim and Konstantin Novoselov [14] from the University of Manchester, graphene came into the limelight in the research community mainly because of its excellent electrical [17], thermal [18], and mechanical properties [19]. Graphene found widespread applications in electronics [20], bio-electric sensors [21], energy technology [22], lithium batteries [23], aerospace [24], bio-engineering [25], and various other fields of nanotechnology [26]. There is an exponential rise in the use of graphene in different research areas mainly because of the properties inherited in, and transferred by, graphene to the processed graphene based materials.

To summarize the research trends related to graphene based nanocomposites, multiple review articles were recently published in which various aspects of graphene based nanocomposites were discussed [27–33]. There are numerous ways to produce and characterize graphene based materials [27]. The graphene based materials were studied for different properties such as thermal properties [28], mechanical properties [29], electrical properties [30], rheological properties [31], microwave adsorption [32,33], environment and toxicological impacts [34], and gas barrier properties [35]. These materials have found

biological applications especially related to toxicity [36] and in other applications like electrically conductive adhesives [37] and selective photoredox reactions [38]. Because of their hierarchical pore structures, these materials were found suitable for gas sorption, storage and separation [39]. Various factors influence the mechanical properties of graphene based materials, e.g. γ-ray irradiation was found to have strong influence on structure-property relationship [40]. Various theoretical models were developed to predict the mechanical properties of epoxy-graphene nanocompsites and correlated with interphases and interfacial interactions [41]. It was presented that continuum mechanics can be used to predict the minimum graphene sheet dimensions and optimum number of layers for good reinforcement [42]. Graphene was compared with other reinforcements, such as nanoclays [43] and CNTs [44], and was shown to have properties superior to the other nano-fillers. To improve interfacial interactions, various surface modifications were employed and their influence on performance of polymer nanocomposites was studied [45].

To date, eclectic reviews [27–33] on graphene composites are covering a broad range of graphene related issues, it can however be observed that there is an obvious gap in review articles discussing mechanical, thermal, and electrical properties of epoxy-graphene nanocomposites. Therefore, this review article discusses the correlation between graphene structure, morphology, weight fraction, dispersion, surface modifications, and the corresponding mechanical, thermal, and electrical properties of epoxy-graphene nanocomposites.

5 Epoxy as matrix

There are various types of epoxy which have wide range of applications because of their superior attributes such as handling characteristics, improvement in composite mechanical properties, acceptable cost, and processing flexibility [1]. The epoxies have found some 'high-end' applications including aerospace, marine, automotive, high-performance sports equipment (such as tennis rackets), electronics, and industrial applications [46]. Due to their superior properties, such as high strength and stiffness, carbonaceous materials are most widely used at present as reinforcement in advanced Epoxy Matrix Composites (EMCs) [47–50].

Epoxy resins are of particular interest to structural engineers because these resins provide a unique balance of chemical and mechanical properties combined with extreme processing versatility. When a composite is produced from epoxy-graphite using hand lay-up process, a great flexibility in aligning the fraction of fibers in a particular direction is available which is dependent upon the in-service load on the composite structural member. In-plane isotropy could also be achieved by stacking the resin impregnated fiber layers at equal numbers of 0°, +45°, -45°, and 90°. There are other stacking sequences as well to achieve in-plane isotropy. The specific stiffness of quasi-isotropic epoxy-graphite laminated composite is higher than many structural metals. The highest specific strength achieved in epoxy-graphite is higher than common structural metals with the exception of ultrahigh-strength steels and some β- titanium alloys. For example, the epoxy-carbon crutch is 50% lighter still stronger than aluminium crutch [1].

6 Graphene as reinforcement

Graphene, a densely packed honey-comb crystal lattice made of carbon atoms having the thickness equal to the atomic size of one carbon atom, has revolutionized the scientific parlance due to its exceptional physical, electrical, and chemical properties. The graphene now found in various applications was previously considered only a research material and a theoretical model to describe the properties of other carbonaceous materials such as fullerenes, graphite, Single-Walled Carbon Nanotubes (SWNTs), and Multi-Walled Carbon Nanotubes (MWNTs). It was believed that the real existence of stand-alone single layer graphene would not be possible because of thermal fluctuations as the stability of long-range crystalline order found in graphene was considered impossible at finite (room) temperatures. This perception was turned into belief by experiments when stability of thin films was found to have direct relation with the film thickness i.e. stability of film decreases with decrease in film thickness [51]. However, graphene can be currently found on a silicon substrate or suspended in a liquid and ready for processing. Although its industrial applications are not ubiquitous, it is widely used for research purposes, e.g. as reinforcement in PMCs and has shown significant improvement in different (mechanical, thermal, electrical etc.) properties of produced nanocomposites [51–55].

The ability of a material to resist propagation of an advancing crack is vital to prevent failure/fracture [56]. The graphene can significantly improve fracture toughness of epoxy at very low volume fraction by deflecting the advancing crack in the matrix. The details of the influence of various kinds of graphene/graphite nanoplatelets (GNPs) on fracture toughness of epoxy nanocomposites are listed in Table 1. In all the composite systems mentioned in Table 1, epoxy was used as matrix and the nanocomposites were produced using solution casting technique except [57] where resin infiltration method was

Table 1: A brief record of epoxy based nanocomposites studied for improvement in fracture toughness values.

Sr.	Authors	Year	Reinforcement/(wt%)	Dispersion method	% increase in K_{1C} (MPa.m$^{1/2}$)	Remarks	Ref.
1	Wan et al.	2014	GO (0.25 wt%)	Sn + BM	25.6	K_{1C} drops after 0.25 wt% of reinforcement	[58]
			DGEBA-f-GO (0.25 wt%)		40.7		
2	Sharmila *et al.*	2014	MERGO (0.25 wt%)	MS + USn	63	K_{1C} drops after 0.25 wt% of reinforcement	[59]
3	Zhang *et al.*	2014	GnPs (0.5 wt%)	Sn	27.6	Trend still increasing	[60]
			fGnPs (0.3 wt%)		50.5	K_{1C} drops after 0.3 wt% of reinforcement	
4	Moghadam *et al.*	2014	UG (0.5 wt%)	3RM	55	K_{1C} drops after 0.5 wt% of reinforcement	[61]
			GO (0.5 wt%)		57		
			G-NH_2 (0.5 wt%)		86		
			G-Si (0.5 wt%)		86		
5	Ma et al.	2014	m-GnP (1 wt%)	MS + Sn	131	K_{1C} drops after 1 wt% of reinforcement of m-GnP	[62]
6	Chandrasekaran *et al.*	2014	TRGO (0.5 wt%)	3RM	44.5	Trend still increasing	[63]
			GNP (1 wt%)		49	K_{1C} drops after 1 wt%	
			MWCNTs (0.5 wt%)		12.7	Trend still increasing	
7	Wan et al.	2014	GO (0.1 wt%)	Sn + BM	24	K_{1C} improves with silane functionalization	[64]
			Silane-f-GO (0.1 wt%)		39		
8	Zaman *et al.*	2014	m-nanoclay (2.5 wt%)	MS	38	K_{1C} drops after 2.5 wt% m-nanoclay	[65]
			m-GP (4 wt%)		103	Trend still increasing	
9	Jiang *et al.*	2014	SATPGO (0.5 wt%)	USn	92.8	K_{1C} drops after 0.5 wt% of reinforcement	[66]
10	Shokrieh *et al.*	2014	GPLs (0.5 wt%)	Sn	39	K_{1C} drops after 0.5 wt% of reinforcement	[67]
			GNSs (0.5 wt%)		16		
11	Jia et al.	2014	GF (0.1 wt%) (resin infiltration)	None	70	K_{1C} did not change much between 0.1 wt% to 0.5 wt%	[57]
12	Tang et al.	2013	Poorly dispersed RGO (0.2 wt%)	Sn	24	Trend still increasing	[68]
			Highly dispersed RGO (0.2 wt%)	Sn + BM	52		
13	Wang et al.	2013	GO 10.79 µm (0.5wt%)	USn	12	K_{1C} drops after 0.5 wt% of reinforcement	[56]
			1.72 µm (0.5 wt%)		61		
			0.70 µm (0.1 wt%)		75		
14	Chandrasekaran *et al.*	2013	GNPs* (0.5 wt%)	3RM	43	Dispersion and K_{1C} improved with three roll milling	[69]
15	Li et al.	2013	APTS-GO (0.5 wt%)	USn	25	Trend still increasing	[70]
			GPTS-GO (0.2 wt%)		43	K_{1C} drops after 0.2 wt% of reinforcement	

16	Shadlou *et al.*	2013	ND (0.5 wt%)	USn	No effect	Fracture toughness improvement is higher by CNF and GO (high aspect ratio) compared with that by spherical ND	[71]
			CNF (0.5 wt%)		4.3		
			GO (0.5 wt%)		39.1		
17	Jiang *et al.*	2013	GO (0.1 wt%)	Sn	31	Trend remains same after 1 wt% of reinforcement	[72]
			ATS (1 wt%)		58.6	K_{1C} drops after 0.1 wt% of reinforcement	
			ATGO (1 wt%)		86.2		
18	Liu et al.	2013	p-CNFs (0.4 wt%)	Sn	41	Trend still increasing	[73]
			m-CNFs (0.4 wt%)		80		
19	Wang et al.	2013	ATP (1 wt%)	Sn	14	K_{1C} drops after 0.1 wt%	[74]
			GO (0.2 wt%)		19	Trend still increasing after 0.2 wt%	
			ATP (1 wt%) + GO (0.2 wt%)		27	K_{1C} drops with the further increase in ATP of reinforcement	
20	Alishahi *et al.*	2013	ND (0.5 wt%)	Sn	-26.9	Trend still increasing	[75]
			CNF (0.5 wt%)		19		
			GO (0.5 wt%)		23		
			CNT (0.5 wt%)		23.8		
21	Ma et al.	2013	U-GnP (0.5 wt%)	MgSr + USn	49	Trend still increasing	[76]
			m-GnP (0.5 wt%)		109		
22	Feng et al.	2013	Graphene (0.5 wt%)	Sn	76	K_{1C} decreases after 0.5 wt% of reinforcement	[77]
23	Chatterjee *et al.*	2012	GnPs (5 µm, 2 wt%)	3RM	60	Trend still increasing	[78]
			GnPs (25 µm, 2 wt%)		80		
			CNTs (2 wt%)		80		
			CNT:GnP = (9:1) (2 wt%)		76		
24	Chatterjee *et al.*	2012	EGNPs (0.1 wt%)	HPH + 3RM	66	K_{1C} drops after 0.1 wt% of reinforcement	[79]
25	Zaman *et al.*	2011	GP (2.5 wt%)	Sn + MS	57	The surface modification significantly improved the K_{1C}	[80]
			m-GP (4 wt%)		90		
26	Rana et al.	2011	CNFs	Sn + MS	40	K_{1C} is dependent upon mixing time	[81]
27	Bortz *et al.*	2011	GO (0.5 wt%)	3RM	60	K_{1C} drops after 0.5 wt% of reinforcement	[82]
28	Zhang *et al.*	2010	CNFs (0.5 wt%)	3RM	19.4	Trend still increasing	[83]
			SCFs (15 wt%)		125.8		
			SCF (10 wt%)/CNF (0.75 wt%)		210		
29	Fang et al.	2010	GNs	MS + Sn	93.8	Better results with combination of MS and Sn	[84]
30	Jana et al.	2009	GP with "puffed" structure (5 wt%)	Sn	28	Trend still increasing	[85]
31	Rafiee *et al.*	2009	SWNT (0.1 wt%)	Sn + MS	17	Graphene platelets have more influence on K_{1C} than CNTs	[86]
			MWNT (0.1 wt%)		20		

employed. The incorporation of graphene in epoxy can increase its fracture toughness as high as 131% [62]. It can also be observed that graphene size, weight fraction, surface modification, and dispersion mode have strong influence on the improvement in fracture toughness values of the produced epoxy-graphene nanocomposites. Monolithic epoxy shows brittle fracture and crack propagates beeline that results in straight fracture surfaces. The schematic of interaction of advancing crack in epoxy with the graphene sheets is shown in Figure 1. Initially the crack propagates through the epoxy matrix as there are no significant intrinsic mechanisms available in monolithic epoxy to restrict crack propagation. However, no sooner the crack faces strong graphene sheets ahead, it surrenders and subdues. Nevertheless, the extent of strengthening the matrix and crack bridging by graphene strongly depends upon its dispersion state and interfacial interactions with the epoxy matrix [87].

7 Fracture toughness

The successful employment of epoxy based nanocomposites relies on the ability of the composite system to meet design and service requirements. The epoxy based

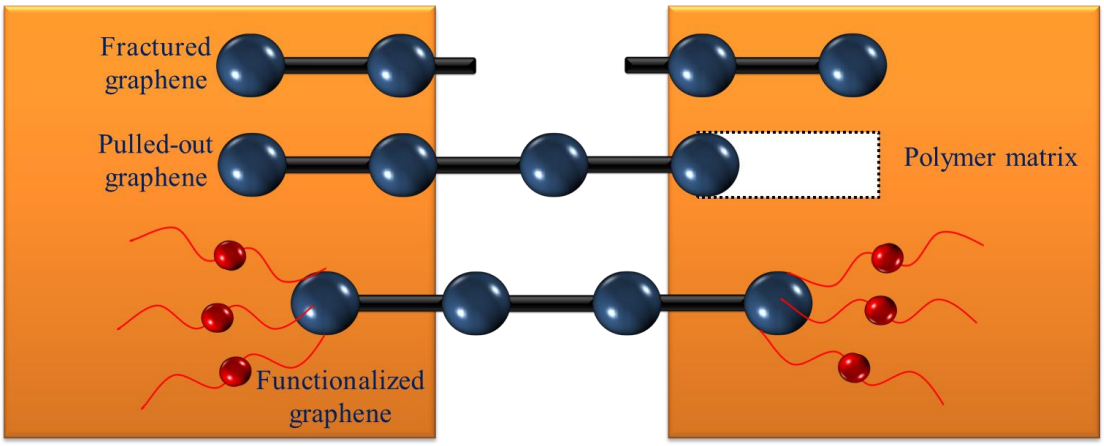

Figure 1: Graphene-polymer interfacial interactions: either C-C covalent bond breaks or graphene pull-out takes place. Interfacial interactions can be improved by functionalization.

nanocomposites have found applications in aerospace, automotive, and construction due to ease of processing and high strength to weight ratio. In many applications, the composite system undergoes external loadings. The relationship between loads acting on a system and the response of the system towards the applied loads is studied in terms of mechanical properties. Therefore, epoxy based nanocomposites are supposed to have superior mechanical properties. There are various tests to measure mechanical properties such as tensile testing, bend testing, creep testing, fatigue testing, and hardness testing, to name a few. These tests usually take specimens of specific geometries and subject to loading at certain rate. In general, the industrial scale samples contain porosity and notches which act as stress concentrators and are deleterious to mechanical properties of nanocomposites. And sometimes it becomes difficult to control the maximum flaw size. The shape of the flaw is another very important parameter as pointed notch (V-notch) is more detrimental than round notch (U-shaped). Due to the pronounced effect of defects on nanocomposite properties, it is important to understand how a system will tolerate the external loading in the presence of a flaw under operating conditions, and how a system will resist the propagation of cracks from these flaws. Therefore, how the material will behave in reality will only be determined when the test specimen contains possible flaws such as a notch. To deal with this issue in a pragmatic way, an intentional notch is produced in the specimen and resistance to fracture is measured and is termed as fracture toughness. Different specimens are used for fracture toughness such as notched tension, three point bend, and compact tension specimen as shown in Figure 2. The toughness is usually measured in three different modes namely (1) mode-I (tensile mode), (2) mode-II (shearing mode), and (3) mode-III (tearing mode) as shown in Figure 3. Most of the literature on epoxy nanocomposites reported mode-I fracture toughness.

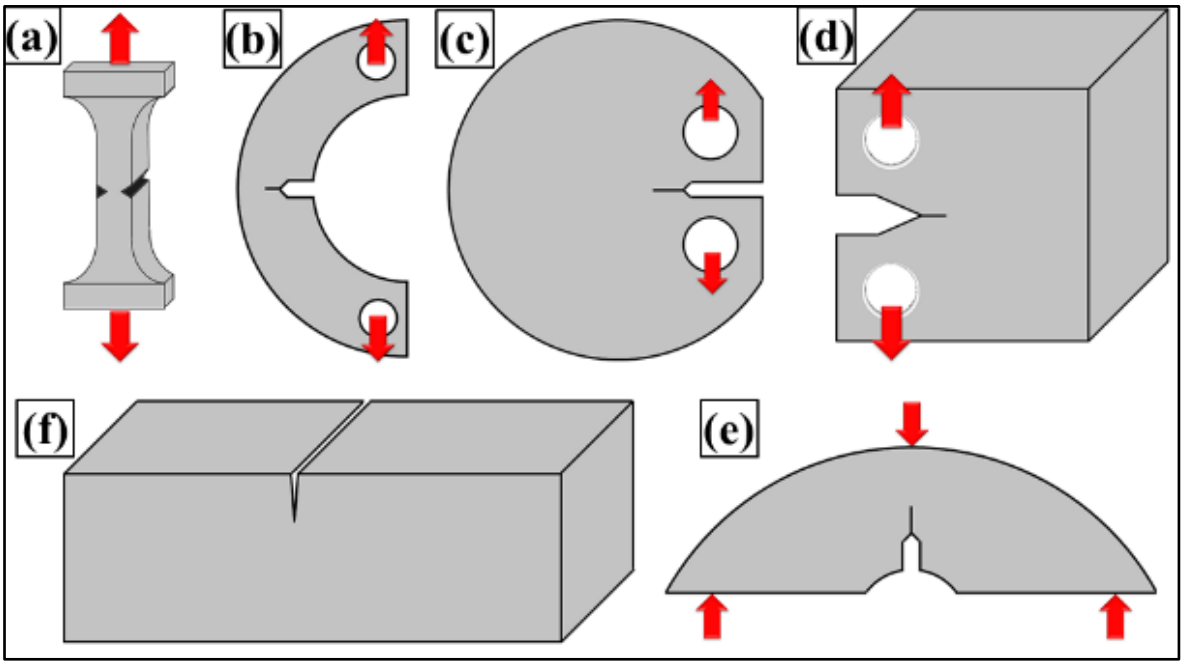

Figure 2: Various fracture toughness test specimen geometries: (a) notched tensile, (b-d) compact tension, (e) compact bend, and (f) single-edge notched three point bend specimens.

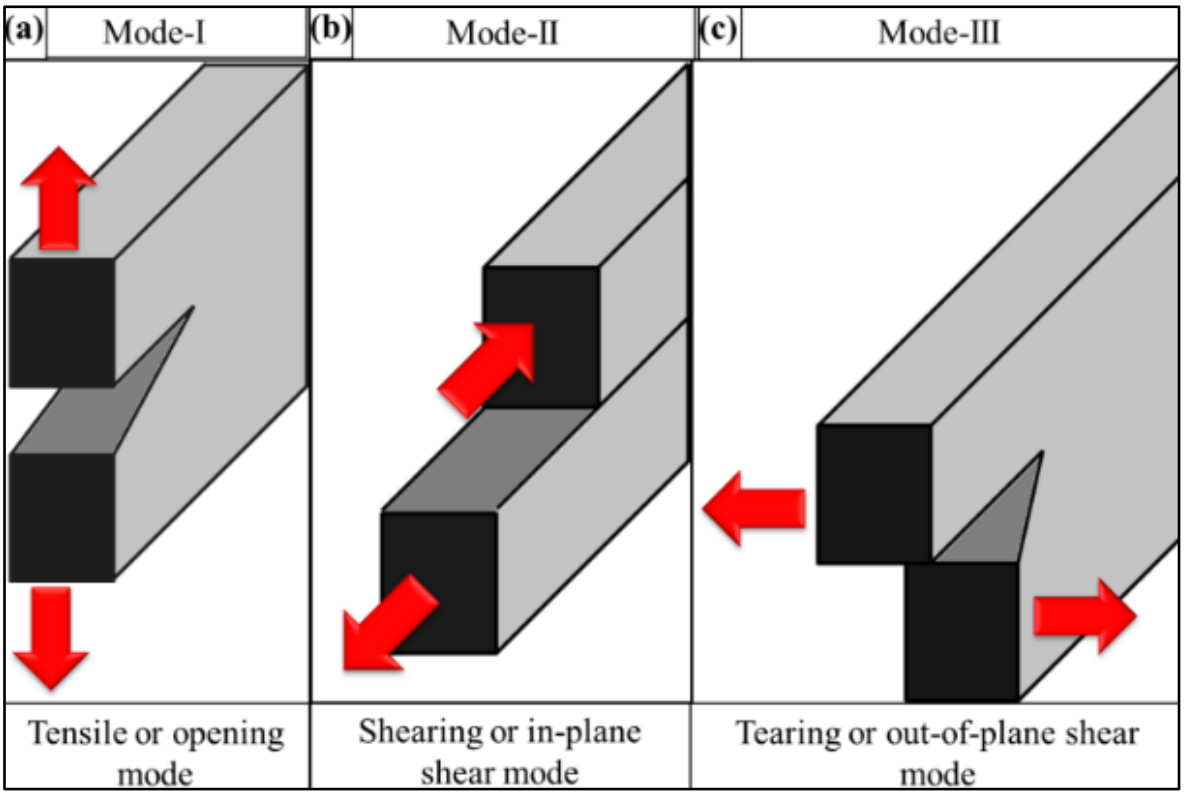

Figure 3: Fracture modes: Various fracture toughness test specimen geometries: (a) notched tensile, (b-d) compact tension, (e) compact bend, and (f) single-edge notched three point bend specimens.

Some of the fracture toughness tests include double torsion, indentation, double cantilever tests, and Chevron notch method. Chevron notch method is popular as it uses a relatively small amount of material and no material constants are needed for the calculations. The technique is also suitable for high-temperature testing as flaw healing is not a concern. However, it requires a complex specimen shape that incurs an extra machining cost. The most commonly used specimen is single-edge notched beam subjected to three or four point bending. Unfortunately, it has been reported that the results of this test are very sensitive to the notch width and depth. Therefore, a pre-notched or molded beam is preferred. As polymers and polymer nanocomposites can be molded into desired shape, a specific kind of notch can be replicated in multiple specimens. Due to reproducibility of notch dimensions, the single-edge notched beam test can give reproducible values of fracture toughness in polymers and polymer nanocomposites. These are the reasons that most of the literature published on polymers and polymer nanocomposites used single-edge notch beams (subjected to three point bend loading) to determine fracture toughness values (K_{1C}). Impact loading methods, such as Charpy and Izod impact tests, are also used to determine impact fracture toughness. Fracture toughness values obtained through different techniques cannot be directly compared [88]. Fracture can be defined as the mechanical separation of a solid owing to the application of stress.

Ductile and brittle are the two broad modes of fracture, and fracture toughness is related to the amount of energy required to create fracture surfaces. In ideally brittle materials, such as glass, the energy required for fracture is simply the intrinsic surface energy of the materials, as demonstrated by Griffith [89]. For structural alloys at room temperature, considerably more energy is required for fracture because plastic deformation accompanies the fracture process. In polymer nanocomposites, the fracture path becomes more tortuous

as cracks detour around strong reinforcement. This increase in crack tortuosity provides additional work to fracture and, therefore, an increase in fracture toughness. In polymers, the fracture process is usually dominated by crazing or the nucleation of small cracks and their subsequent growth [90].

Toughness is defined as the ability of a material to absorb energy before fracture takes place. It is usually characterized by the area under a stress-strain curve for a smooth (unnotched) tension specimen loaded slowly to fracture. The term fracture toughness is usually associated with the fracture mechanics methods that deal with the effect of defects on the load-bearing capacity of structural components. The fracture toughness behavior for polymers usually falls into two kinds; below the glass transition temperature T_g, and above T_g. Above T_g, the deformation is non-linear and fracture behavior is stable cracking. Below T_g, the deformation is nearly linear elastic and fracture is unstable with a single-point toughness value. As epoxy based nanocomposites are mostly used in temperatures below T_g, therefore, mostly the fracture toughness values below T_g are reported.

The fracture toughness of materials is of great significance in engineering design because of the high probability of flaws being present. Defined another way, it is the critical stress intensity at which final fracture occurs. The plane strain fracture toughness (critical stress intensity factor, K_{1C}) can be calculated using eq. (1), where P_{max} is maximum load of load-displacement curve (N), f(a/w) is a constant related to the geometry of the sample and is calculated using eq. (2), B is sample thickness (mm), W is sample width (mm), and a is crack length (should be kept between 0.45W and 0.55W according to ASTM D5045) [68]. The critical strain energy release rate (G_{1C}) can be calculated using eq. (3), where E is the Young's modulus obtained from the tensile tests (MPa), and ν is the Poisson's ratio of the

polymer. The geometric function f(a/W) strongly depends on the a/W ratio as shown in Figure 4 [91].

The fracture toughness is dependent on many factors such as type of loading and environment in which the system will be loaded. However, the key defining factor is the microstructure. With the help of optical and electron microscopy, the dispersed reinforcement and polymer matrix can be observed in qualitative and quantitative manners, respectively. However, in this binary system integrated at nanoscale, there are myriad of factors that expound the overall performance of produced nanocomposites. One constituent of the overall microstructure is particle size distribution. The mechanical properties are improved when load is efficiently transferred from matrix to reinforcement. One of the controlling factors for load transfer mechanism is networking of reinforcement. The load can only be transferred from the matrix to the reinforcement if a connected network of

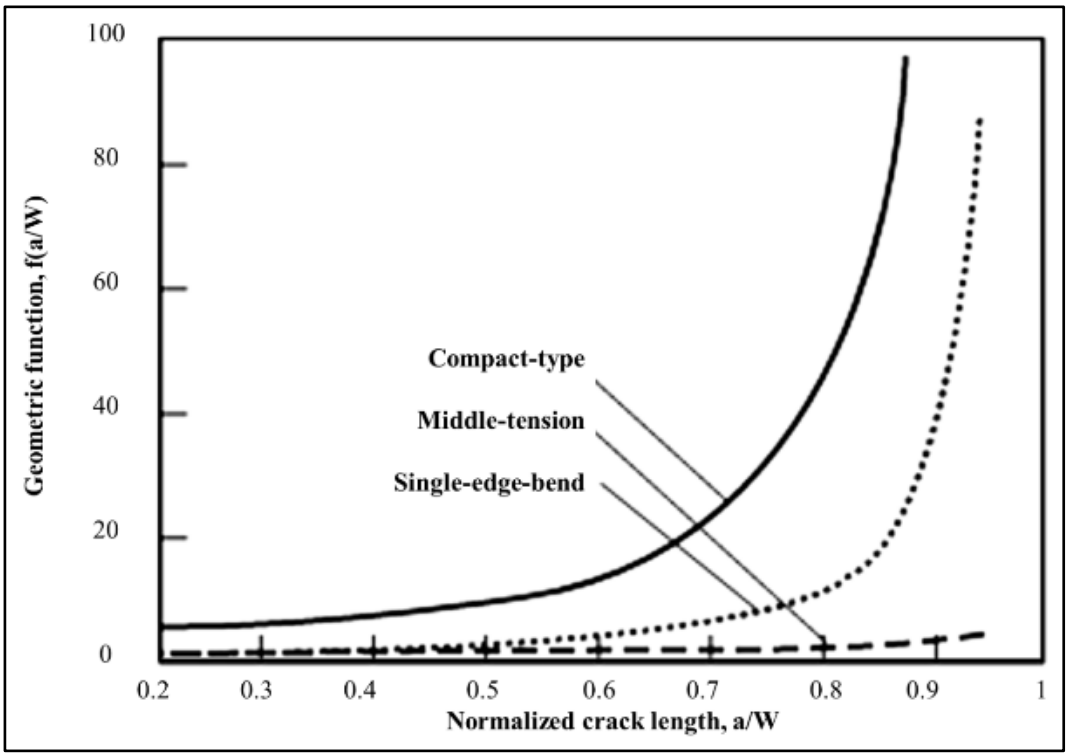

Figure 4: Variation in geometric function f(a/W) with normalized crack length (a/W) [91]**.**

reinforcing particles is available. Any disjoint in the network will act as the weakest link for load transfer and polymer matrix will be prone to external loading. One of the factors influencing network formation is filling ratio (or packing density). When particle size distribution is narrow, the voids between the particles would not be filled and those empty locations will be a preferred route for the cracks to surmount the reinforcement particles. On the other hand, when reinforcement has wide size distribution, the finer particles can occupy the empty spaces in between large particles. It increases the filling ratio and makes an efficiently connected network of reinforcement. Sohn and Moreland have shown that packing density is dependent on particle size distribution and shows direct relationship, i.e. packing density increases as the particle size distribution is extended [92]. It was also found that packing density is independent of particle size. They further reported that particle shape also influences packing density. It is obvious as perfect cubes will have 100% packing while voids will be certain in spherical particles which will lower the packing density. Therefore, a wide size distribution is helpful in improving the mechanical properties as strong networking of reinforcing particles can take place because of high packing density.

The properties of nanocomposites are also significantly dependent on filler shape and size. The graphene size, shape, and topography can be controlled simultaneously as shown in Figure 5 [93]. Chen et al. synthesized well-aligned millimeter-sized tetragon-shaped and hexagon-shaped graphene on a polycrystalline copper substrate using low pressure CVD [93]. CVD is an efficient approach to produce high quality and large surface area graphene on metallic substrates [94,95]. Graphene can be grown epitaxially on single crystal copper substrate [96–99]. Graphene shape and orientation strongly depend on crystallographic orientation of copper substrate [100,101]. The dendritic graphene with multiple branches

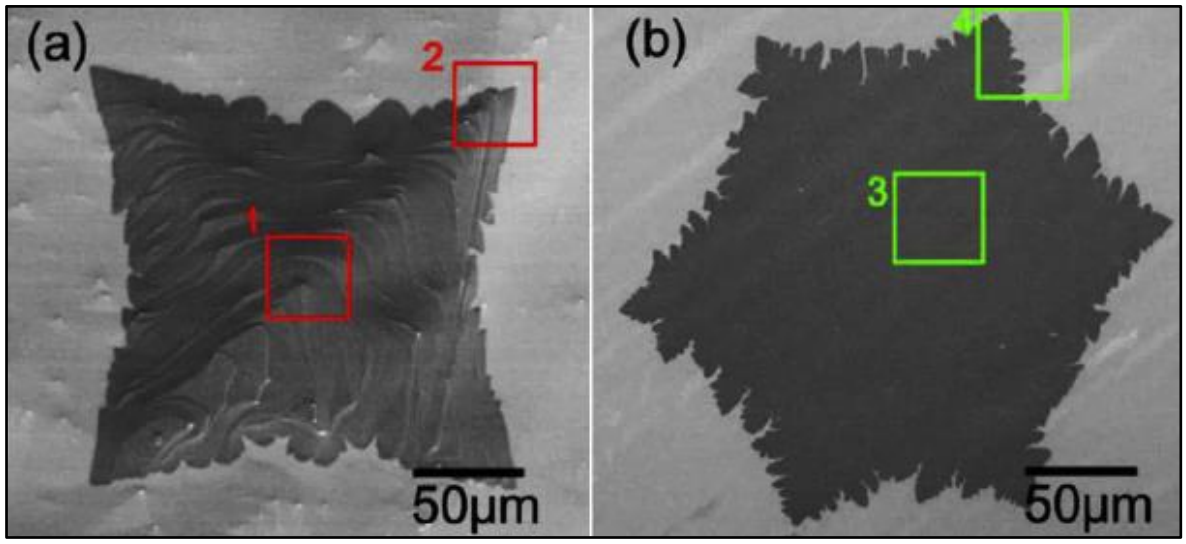

Figure 5: SEM images of topographically controlled (a) tetragon-shaped graphene and (b) hexagonal graphene [93]**.**

can be obtained by diffusion- limited growth dynamics [102]. The graphene shape can also be controlled using surface condition of substrate. For example, wet-loaded samples produce tetragonal shaped and dry-loaded samples produce hexagonal shaped graphene [93]. The graphene shape can also be controlled by controlling the processing temperature [103,104].

$$K_{1C} = \frac{P_{max} f(\frac{a}{W})}{BW^{1/2}} \quad \textbf{(1)}$$

$$f(a/W) = \frac{\left[\left(2+\frac{a}{W}\right)\left\{0.0866+4.64\left(\frac{a}{W}\right)-13.32\left(\frac{a}{W}\right)^2+14.72\left(\frac{a}{W}\right)^3-5.6\left(\frac{a}{W}\right)^4\right\}\right]}{\left(1-\frac{a}{W}\right)^{3/2}} \quad \textbf{(2)}$$

$$G_{1c} = \frac{K_{1c}^2(1-\nu^2)}{E} \quad \textbf{(3)}$$

It is the type of bonding present between the phases that imparts unique mechanical properties to the whole system. Therefore, interfacial interactions count a lot toward

overall performance of epoxy based nanocomposites. It is well established that dispersion state is a crucial factor in defining the properties of nanocomposites. In addition, the orientation of reinforcement and polymer chains and the degree of crosslinking significantly influence the mechanical, thermal, and electrical properties of graphene based polymer nanocomposites [105]. Additionally, the porosity is another important influential factor and two kinds of porosity are commonly observed: round porosity which is attributed to fluids and air entrapment as fluids exert equal pressure in all sides, and irregular porosity which can be because of reinforcement bridging and relative movement of reinforcement and matrix [106]. One of the factors that define the interfacial interactions is the interphase and the properties of nanocomposites are significantly influenced by interphase properties [107]. Another factor that is not an integral part of microstructure but can significantly influence the microstructure is thermal fluctuation [108]. Thermal fluctuations can cause phase transformation and influence surface roughness features of graphene.

8 Structure and fracture toughness

Graphene has honeycomb lattice having sp^2 bonding which is much stronger than sp^3 bonding found in diamond [109]. There is sp^2 orbital hybridization between P_x and P_y that forms σ-bond [51]. The orbital P_z forms π-bond with half-filled band that allows free motion of electrons. When bombarded with pure carbon atoms, hydrocarbons, or other carbon containing molecules, the graphene directs the carbon atoms into vacant seats thereby self-repairing the holes in the graphene sheet. Through their crack deflection modeling, Faber and Evans showed that maximum improvement in fracture toughness,

among all other nano-reinforcements, can be obtained using graphene mainly because of its better capability of deflecting the propagating cracks [110,111].

As graphene is a 2D structure, each carbon atom can undergo chemical reaction from the sides resulting in high chemical reactivity. The carbon atoms on the edge of graphene sheet have three incomplete bonds (in single layer graphene) that impart especially high chemical reactivity to edge carbon atoms. In addition, defects within graphene sheet are high energy sites and preferable sites for chemical reactants. All these factors make the graphene a very high chemical reactive entity. The Raman and XPS spectra of graphite, GO, and thermally Reduced Graphene Oxide (RGO) are shown in Figure 6 (a) and (b), respectively. The graphene structure can be studied using Transmission Electron Microscopy (TEM) and other high resolution tools. Wrinkles were observed in graphene flat sheet which were due to the instability of 2D lattice structure [68].

Wrinkling is a large and out-of-plane deflection caused by compression (in-plane) or shear. Wrinkling is usually found in thin and flexible materials such as cloth fabric [112]. Graphene Nanosheets (GNSs) were also found to undergo wrinkling phenomenon [113]. When wrinkling takes place, strain energy is stored within GNSs which is not sufficient to allow the GNSs to regain their shape. Wrinkling can be found on GNSs as well as exfoliated graphite. A typical wrinkling pattern can be observed on exfoliated graphite as shown in Figure 7. The wrinkles in GNSs are sundering apart at different locations while getting closer at other regions. As GNSs do not store sufficient elastic strain energy, wrinkling is an irreversible phenomenon but can be altered by external agency [114]. The surface roughness varies depending on graphene sheets owing to their dissimilar surface roughness features such as wrinkles' size and shape. Therefore, the ability of sheets to

mechanical interlock with other sheets and polymer chains is dissimilar. Wang *et al.* showed that wrinkle's wavelength and amplitude are directly proportional to sheet size (length, width, and thickness) as it is clear from eq. (4) and eq. (5) where λ is wrinke wavelength, ν is Poisson's ratio, L is graphene sheet size, t is thickness of graphene sheet, ε is edge contraction on a suspended graphene sheet, and A is the wrinkle amplitude [56].

Palmeri *et al.* showed that the graphene sheets have a coiled structure that helps them to store sufficient amount of energy [115]. The individual sheet and chunk of sheets together are subjected to plastic deformation at the application of external load. The applied energy is utilized in undertaking plastic work that enhanced the material's ability to absorb more energy. It is believed that large graphene sheets have large size wrinkles [116]. These wrinkles twist, bend, and fold the graphene sheets. The wrinkles and other induced defects remain intact while curing of polymer matrix. This reduces geometric continuity and regularity of graphene and lowers load transfer efficiency and can cause severe localized stress concentration.

9 Surface area and fracture toughness

The K_{1C} strongly depends upon the surface area of the reinforcement as it influences the matrix-reinforcement interfacial interactions. When the reinforcement has large surface area, the interfacial area increases which increases the number of routes for the transport of load from matrix to reinforcement [83]. On the contrary, when agglomeration takes place, not only the agglomerates act as stress raisers, but also the net surface area is decreased that further drops the fracture toughness and other mechanical properties of nanocomposites [117]. One reason that graphene supersedes other reinforcements is its high surface area [118]. The surface area of graphene is

$$\lambda^4 \approx \frac{4\pi^2 \nu L^2 t^2}{3(1-\nu^2)\varepsilon} \tag{4}$$

$$A^4 \approx \frac{16\nu L^2 t^2 \varepsilon}{3\pi^2(1-\nu^2)} \tag{5}$$

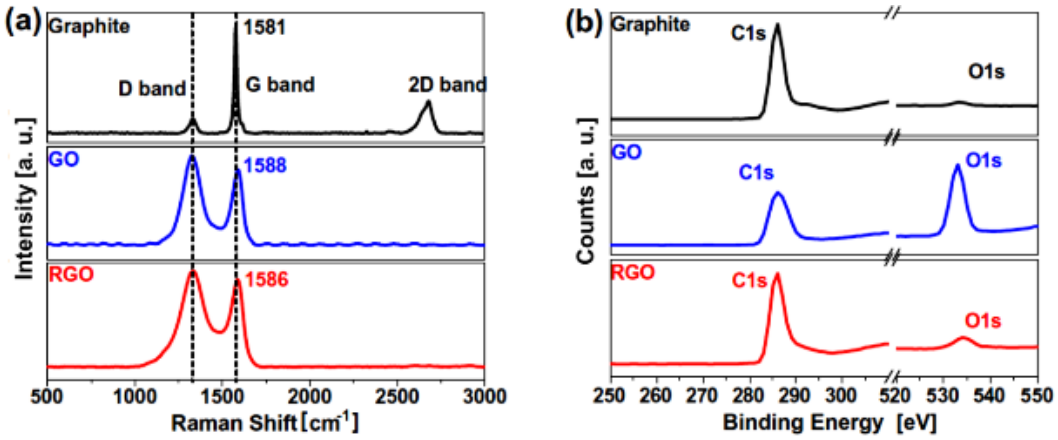

Figure 6: (a) Raman spectra and (b) XPS survey scans of graphite, GO, and RGO [68].

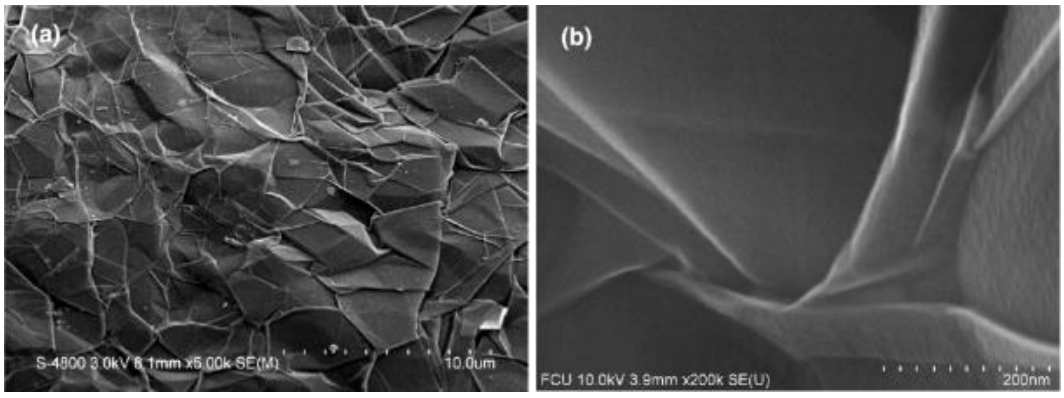

Figure 7: Wrinkling of GNSs: (a) A typical wrinkling pattern. (b) A closer view of the wrinkled GNS [114]**.**

even higher than that of CNTs [119]. To make a comparison, the surface areas of short carbon fiber and graphene are calculated. The surface area of carbon fiber is calculated using the formula for the solid cylinder while surface area of graphene is calculated using the formula for the rectangular sheet. The thickness of graphene is considered variable so that the same relation can be used for multiple layers of graphene sheets stacked together

in the form of graphene nanosheets. The length of short carbon fiber is taken 1 μm and diameter 0.1 μm. The dimensions of graphene are ℓ× w× t = 1 μm× 0.1 μm× 10 nm. The density of both short carbon fiber and graphene is taken 2.26 to make comparison based on dimensions only. The surface area of 1 g of carbon fibers is 19 m^2 and that of graphene is 98 m^2. It can be observed that although the lengths of both reinforcements are the same and the width of graphene is equal to the diameter of a short carbon fiber, there is a large difference in surface areas when the thickness of graphene is kept 10 nm. This difference will further increase if graphene dimensions are reduced. The specific surface area of graphene is as high as 2600 m^2/g [120,121]. It shows that graphene having much larger surface area, can significantly improve the fracture toughness of the epoxy nanocomposites. The chain mobility and curing reactions can be tailored by taking advantage of increased graphene surface area to improve K_{1C} of its composites [122,123]. There is also improved thermal conduction among graphene-graphene links that significantly improve the overall thermal conductivity of the nanocomposites [124,125]. The electrical conductivity also increases with graphene as graphene sheets form links and provide a passageway for electrical conduction [126].

10 Size and fracture toughness

Zhao and Hoa used theoretical computer simulation approach to study the improvement in toughness when epoxy is reinforced with 2D nano-reinforcement of different particle size [127,128]. The simulation results showed that there is direct relation between particle size and stress concentration factor up to 1 μm after which the stress concentration factor was impervious to any further size increase. However, Chatterjee *et al.* [78] showed that

fracture toughness was improved by increasing the graphene size which is in negation with simulation results by Zhao and Hoa.

The increase in the fracture toughness of epoxy was found to be strongly dependent upon the graphene sheet size [56]. An inverse relation was found in most of the cases between sheet size and fracture toughness for the nanocomposites. The increase in fracture toughness with decrease in sheet size can be explained on the basis of stress concentration factor as discussed above. Although graphene acts as reinforcement, however, it has associated stress and strain fields which arise from the distortion of the structure of polymer matrix. When sheet size or weight fraction or both are increased beyond certain value, the stress concentration factor dominates the reinforcing character. As a result, fracture toughness and other mechanical properties, such as tensile and flexural strength and stiffness, start decreasing which is in accordance with Zhao and Hoa's simulation results [127].

Wang *et al.* used Graphene Oxide (GO) of three different sizes namely GO-1, GO-2, GO-3, having average diameters, 10.79 µm, 1.72 µm, and 0.70 µm, respectively, to produce nanocomposites using an epoxy matrix [56]. The influence of GO size on fracture toughness is shown in Figure 8. It can be observed that fracture toughness is strongly dependent on GO sheet size. The maximum increase in fracture toughness was achieved with the smallest sheet size GO. The K_{1C} values dropped when weight fraction was increased beyond 0.1 wt%. This decrease in K_{1C} with increasing weight fraction can be correlated with crack generation and dispersion state (sec. 11-12).

11 Weight fraction and fracture toughness

As shown in Figure 8, the K_{1C} first increases with GO and then starts decreasing in all the three cases shown. The increase in K_{1C} is due to reinforcing effect of GO while the drop in K_{1C} is due to crack generation and agglomeration. Addition of high GO weight fraction generates cracks that reduce the fracture toughness of the nanocomposite [56]. The other reason for such behavior is due to high probability of agglomeration at higher weight fractions due to Van der Waals forces [56].

The weight fractions of reinforcements at which maximum K_{1C} was achieved for different epoxy-graphene nanocomposites are shown in Figure 9. All the published research articles stated that the maximum K_{1C} values were achieved at or below 1 wt% of graphene and K_{1C}

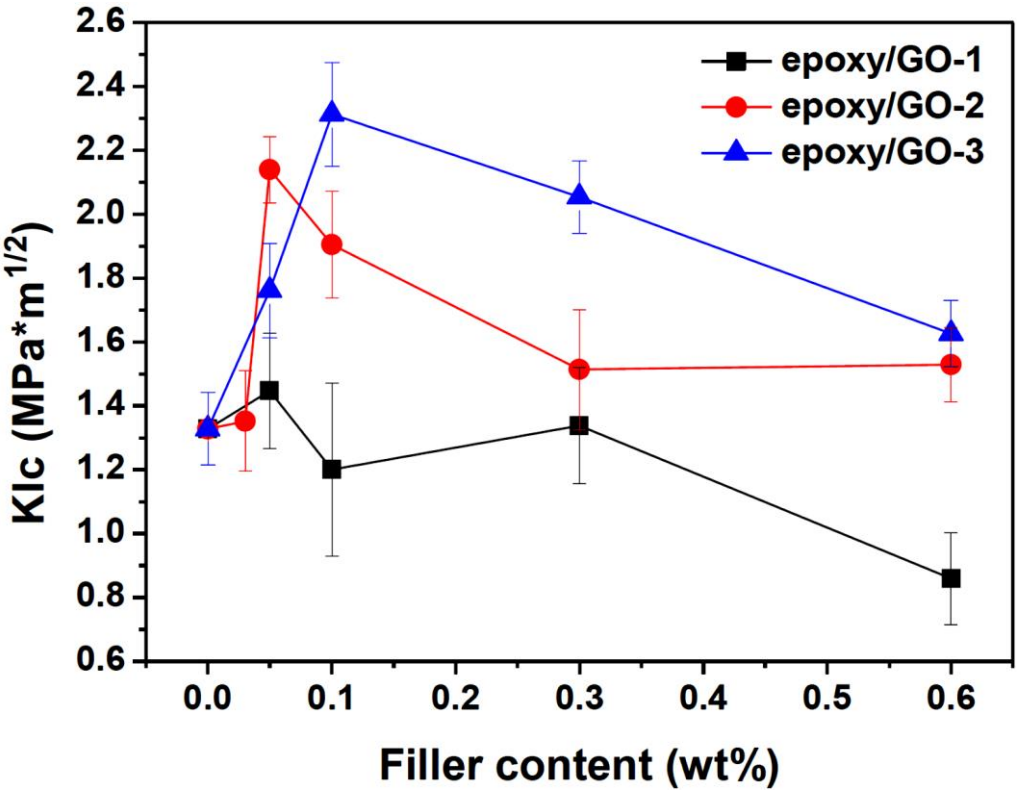

Figure 8: K_{1C} versus GO content for the epoxy nanocomposites. The error bars represent standard deviations [56]**.**

dropped when weight fraction of graphene was raised beyond 1 wt%. The decrease in K_{1C} with higher weight fraction of graphene can be correlated with the dispersion state of graphene (sec. 12). As graphene weight fraction increases beyond 1 wt%, the dispersion state becomes inferior. The maximum increase in K_{1C} was 131% which is achieved at 1 wt% of graphene. However, it is worth discussing the dispersion mode adopted [62]. The graphene was dispersed using a combination of sonication and mechanical stirring. This combination provides an efficient way of dispersing the graphene into epoxy. In addition to that, sonication causes exfoliation, delayering, and length shortening of graphene sheets. These aspects help alleviating the stress concentration factor and cracks associated with large graphene sheets. These factors result in K_{1C} improvement up to 131% which is the maximum among the maximum improvements in K_{1C} values reported in epoxy-graphene nanocomposites.

It can be observed from Figure 9 that there is no fixed value of GNPs weight % at which maximum increase in K_{1C} is achieved. In addition, the increase in K_{1C} at fixed GNP wt% is not the same. For example, at 0.5 wt%, the % increase in K_{1C} is reported up to 45% by Chandrasekaran et al [63] and about 110% by Ma et al. [76]. Therefore, it can be concluded that the wt% of GNPs is not the sole factor defining the influence of GNPs on mechanical properties of nanocomposites. There are other influential factors as well such as dispersion method, use of dispersant, and functionalization. It was observed that lower improvement in K_{1C} was observed when dispersion was carried out with only sonication and higher improvement in K_{1C} was observed when sonication was assisted with secondary dispersion method especially mechanical stirring (see Figure 11 for details). In addition, the use of organic solvent is another important parameter in defining the improvement in mechanical properties.

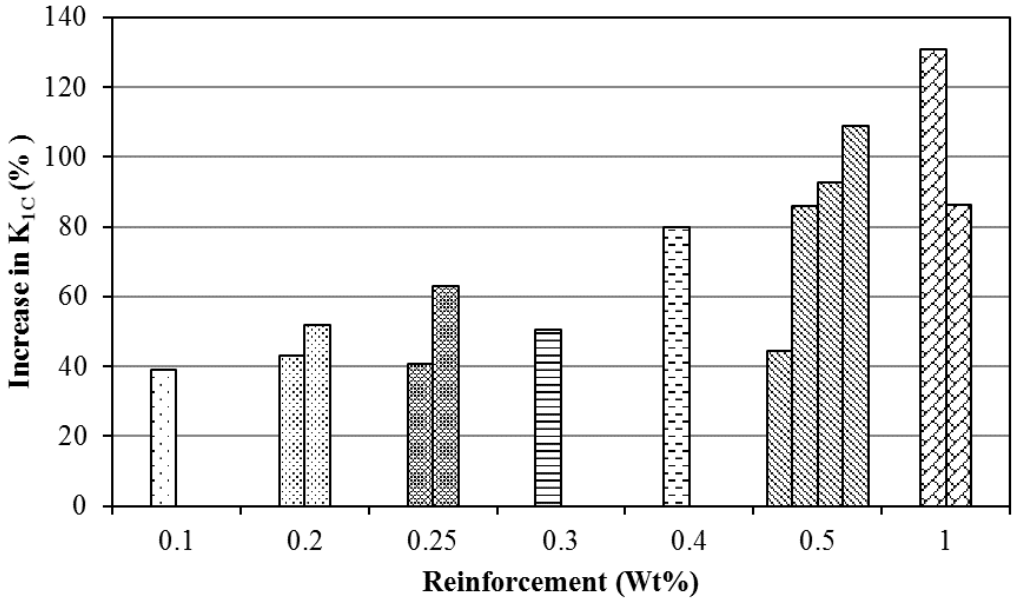

Figure 9: The weight fractions of reinforcements at which maximum K_{1C} was achieved in different epoxy/graphene nanocomposites and corresponding improvement (%) in K_{1C} (See references in Table 1).

The solvent as dispersion medium is used for two main characteristics; (1) low viscosity of solvent and (2) ability to lower the viscosity of polymer matrix as dispersion becomes easier in a low viscosity medium. However, lower mechanical properties were reported in some cases when organic solvent was used as dispersion medium [129–133]. Loos et al. produced epoxy samples with varied amount of acetone (0, 7, 10, 13 wt%) [134]. They reported significant drop in Young's modulus, tensile strength, and fracture strain as a result of residual acetone. The drop in mechanical properties was directly proportional to the amount of acetone used [134]. The traces of organic solvents influence cure kinetics and restrict cross-linking process [135]. Hong and Wu mentioned that residues of organic solvents result in lower curing exotherm, reaction rate, initial curing rate, glass transition temperature (T_g), and reaction order [136]. They also reported that organic solvents with higher boiling points have greater effect on cure kinetics and mechanical properties of epoxy [136].

Therefore, the use of solvent is not completely propitious which can be attributed to four main reasons; (1) some organic solvents are not efficient dispersants for graphene, (2) the remnants of organic solvent adversely affect the cure kinetics, (3) any residues of the solvent cause porosity which is detrimental to the mechanical properties, and additionally, (4) the solvent needs to be evaporated after dispersion which delays the process and increases the cost. Previously, the organic solvents were used as dispersion medium especially for carbon nanotubes (CNTs) to improve their dispersion state in polymer matrix [137–141]. This practice was justified as the cylindrical shape and very high aspect ratio of CNTs caused them to entangle severely. Also, dispersing them in polymer resin with relatively high viscosity was quite difficult as well. Therefore, the use of organic solvents was inevitable.

12 Dispersion state and fracture toughness

The end product of most of the graphene synthesis methods is agglomerated graphene [34]. In addition, graphene tends to agglomerate due to the weak intermolecular Van der Waals forces [122]. Therefore, dispersing graphene in epoxy matrix is always a challenge. The relationship between dispersion state and nature of crack advancement is schematically shown in Figure 10. Figure 10 (a) is a schematic of poorly dispersed agglomerated graphene in epoxy matrix. As graphene sheets have a stress concentration factor associated with them, (micro-) cracks are generated around the graphene agglomerates. These (micro-) cracks may propagate under the application of external load and may lead to fracture. If there is a pre-existing crack in the matrix, it will propagate when load is applied. If the crack faces the agglomerate, it will either be restrained by the agglomerate or detour/bifurcate to circumvent the agglomerate in case of higher loads.

However, as graphene is present in the form of agglomerates, a major portion of the epoxy matrix is not reinforced at all. Therefore, a crack can easily propagate through the brittle epoxy until fracture occurs. This is possibly the reason why poorly dispersed graphene was not found efficient in improving the fracture toughness of epoxy [68]. On the contrary, if graphene is uniformly dispersed, it would be difficult for the crack to move. Figure 10 (b) shows a schematic diagram for an ideal situation in which graphene of nearly same dimensions is homogeneously dispersed in epoxy matrix. In this case, as sheet size is relatively smaller than that of graphene agglomerate, the stress concentration factor associated with the graphene sheets is benign and there is almost no (micro-) cracking around individual graphene sheets. If there is a pre-existing crack in the matrix and it starts propagating under the influence of external load, it has to come across graphene sheets at each step. If the external load is high enough, each crack will split into multiple sub-cracks. There is required energy at each division and sub-division of crack to generate new surfaces. Therefore, extensive energy will be dissipated before the crack covers long displacement from its initial position to cause fracture. This will significantly improve the fracture toughness of the epoxy. Therefore, uniformly dispersed graphene is preferred to improve the fracture toughness of the epoxy-graphene nanocomposites.

Tang et al. produced highly dispersed and poorly dispersed RGO-epoxy nanocomposites using solution casting technique. The high dispersion of RGO in epoxy was achieved using ball milling process [68]. The RGO dispersed in epoxy using sonication process and not subjected to ball milling was termed as poorly dispersed. They studied the influence of graphene dispersion on mechanical properties of produced nanocomposite. The highly dispersed RGO-epoxy showed 52% improvement in K_{1C} while poorly dispersed RGO-

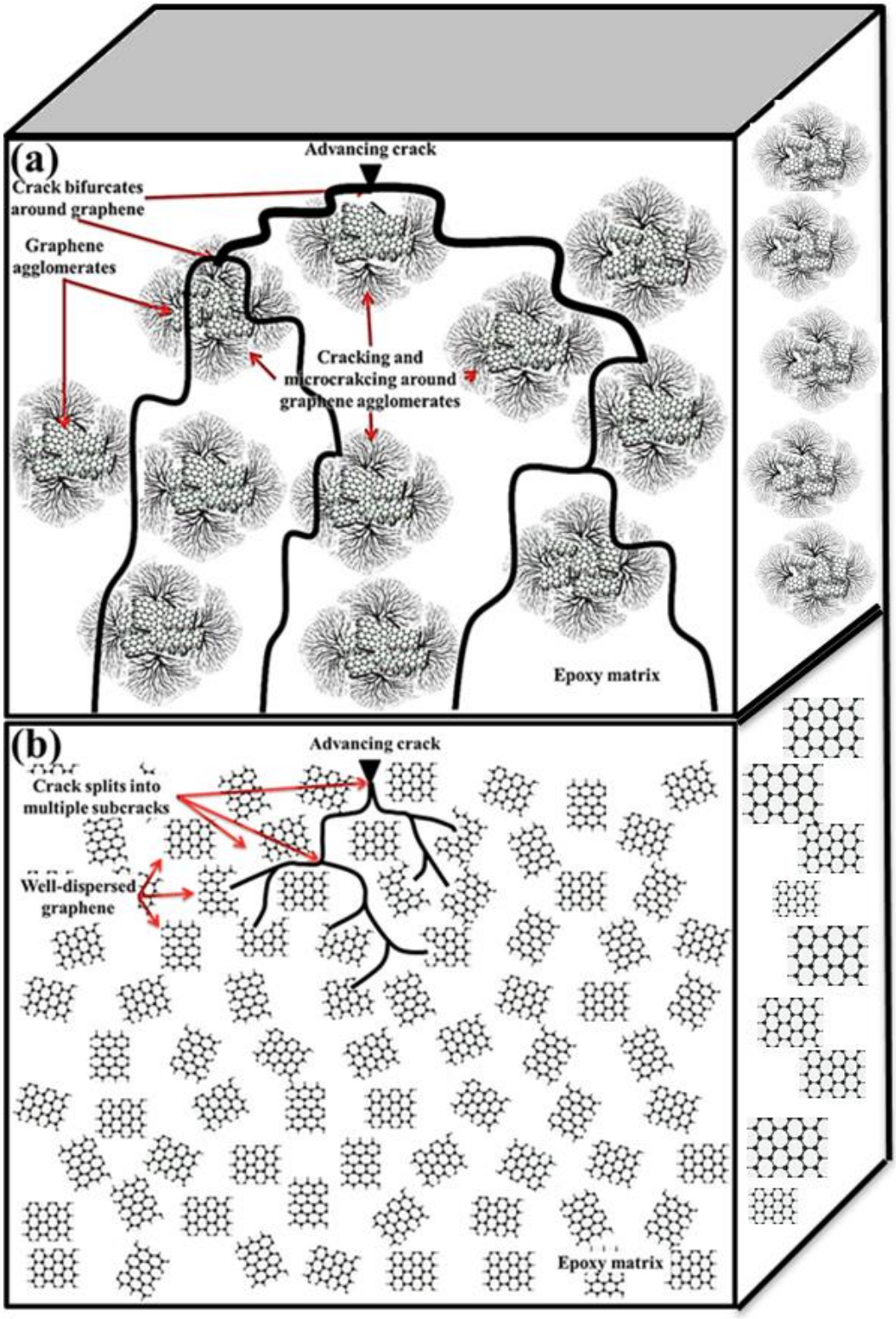

Figure 10: Influence of graphene dispersion on crack propagation method; (a) poorly dispersed graphene; (b) Ideally uniformly dispersed graphene.

epoxy showed only 24% improvement in K_{1C}. It shows that better dispersion of graphene can significantly improve the fracture toughness of epoxy nanocomposites [68].

Several dispersion modes to disperse reinforcement into epoxy matrix were successfully adopted (see references in Table 1). The maximum % increase in K_{1C} as a function of dispersion mode is shown in Figure 11. In most of these articles, sonication is the main mode of dispersing reinforcement in epoxy matrix. It can be observed that when sonication is assisted by a supplementary dispersion technique like mechanical stirring and magnetic stirring, the K_{1C} values were significantly increased. The maximum improvement in K_{1C} of 131% was achieved when a combination of sonication and mechanical stirring was

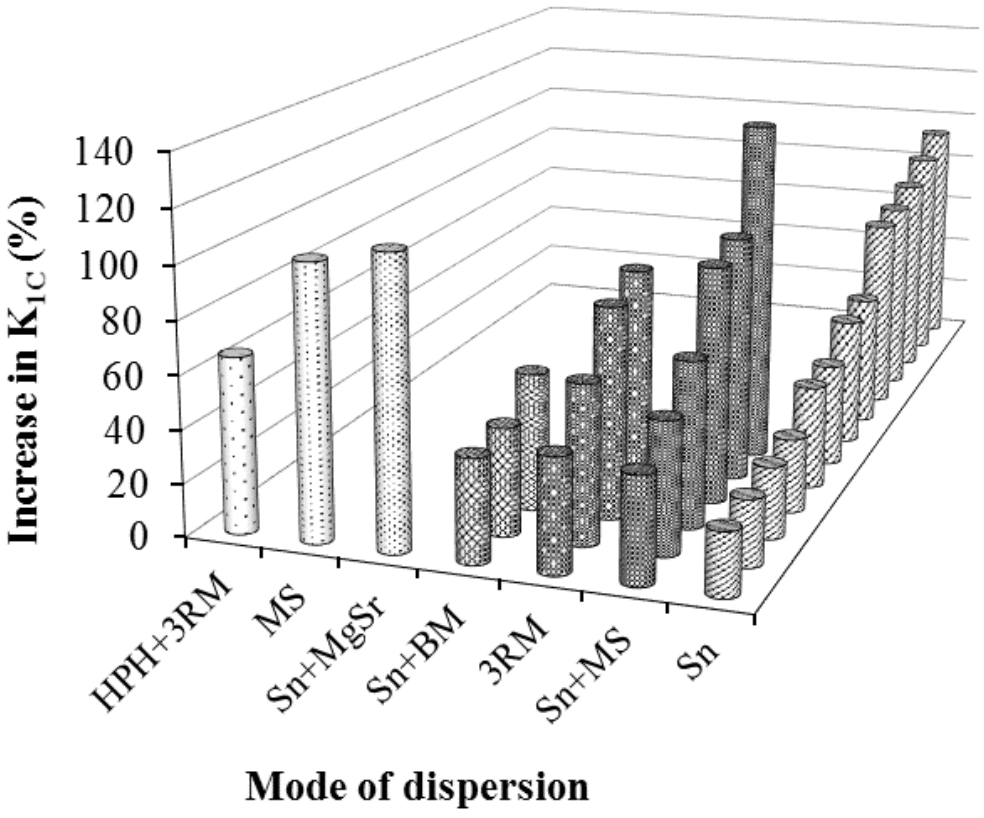

Figure 11: The maximum improvement in K1C as a function of dispersion mode. (See references in Table 1).

employed [62]. The second highest improvement in K_{1C} is achieved with a combination of sonication and magnetic stirring and K_{1C} increased by 109% [76]. The minimum values in K_{1C} improvements are achieved when sonication is coupled with ball milling [59,87,111]. Since both the sonication and ball milling processes reduce the sheet size and produce surface defects [142–156], we believe that the surface defects significantly increased and sheet size reduced below the threshold value and therefore higher K_{1C} improvement was not achieved. Although three roll milling (calendering process) is an efficient way of dispersing the reinforcement into polymer matrix due to high shear forces, however, the maximum improvement in K_{1C} using three roll mill was reported 86% [73] which is lower than achieved with a combination of sonication and mechanical stirring (131% [62]).

13 Functionalization and fracture toughness

As described previously, graphene tends to agglomerate due to the weak Van der Waals interactions and its smoother surface texture inhibits achieving strong interfacial interactions. To tackle limited dispersibility and interfacial bonding of graphene, surface modifications are carried out [157–161]. In fact, introduction of functional groups on graphene surface can induce novel properties [162–166]. Various methods to modify graphene surface were employed and can be categorized into two main groups namely: (1) chemical functionalization; and (2) physical functionalization.

In chemical functionalization, chemical entities are typically attached covalently. For example, in defect functionalization, functional groups are attached at the defect sites of graphene such as –COOH (carboxylic acid) and –OH (hydroxyl) groups. Defects can be any departure from regularity including pentagons and heptagons in hexagonal structure of graphene. Defects may also be produced by reaction with strong acids such as HNO_3,

H_2SO_4 or their mixture, strong oxidants including $KMnO_4$, ozone and reactive plasma [167]. The functional groups attached at the defect sites of graphene can do further chemical reactions including but not limited to silanation, thiolation, and esterification [168]. Unlike chemical functionalization, physical functionalization has non-covalent functionalization where the supermolecular complexes of graphene are formed as a result of wrapping of graphene by surrounding polymers [34]. Surfactants lower the surface tension of graphene thereby diminishing the driving force for the formation of aggregates. The graphene dispersion can be enhanced by non-ionic surfactants in case of water-soluble polymers [34].

The different functionalization methods adopted to study their influence on K_{1C} values with corresponding improvements (%) in K_{1C} values are shown in Figure 12. The minimum improvement was achieved for amino-functionalized graphene oxide (APTS-

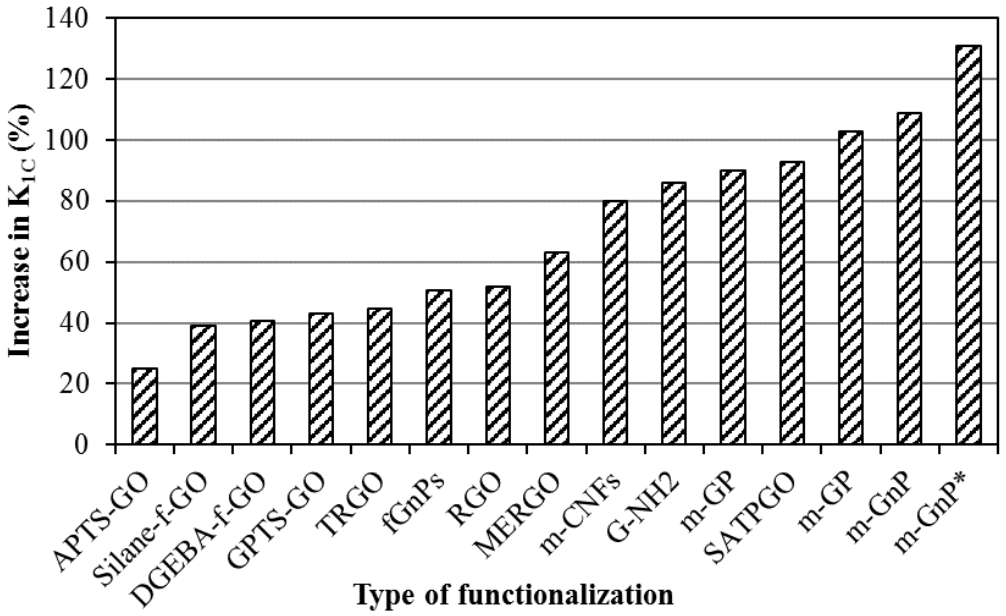

Figure 12: The maximum improvement in K_{1C} as a function of functionalization method. (See references in Table 1).

GO) [70] while maximum improvement was recorded for surfactant modified graphene nanoplatelets [62]. This could be attributed to the dispersion improvement of the graphene in the epoxy matrix when surfactants were used in addition to the improving interactions without causing reduction in graphene sheet size or imparting surface defects on graphene sheets.

14 Other mechanical properties

The literature showed an absence of consensus of graphene role in improving other mechanical properties of nanocomposites. Some authors reported significant improvement in the mechanical properties of nanocomposites reinforced with GNPs [169–173]. On the other hand, there was no significant effect due to the incorporation of GNPs into epoxy matrix [174–178] and even worse, the mechanical properties deteriorated by the addition of GNPs [129–133]. The main reasons for the differences in results were discussed in the earlier sections. In general, a major portion of literature has shown that GNPs can significantly improve the mechanical properties of epoxy nanocomposites. The percent improvements in tensile strength and tensile modulus are shown in Figure 13. The maximum improvement in tensile strength is as high as 108% [179] and tensile modulus up to 103% [180]. GNPs were also found to improve flexural properties of nanocomposites. Naebe *et al.* produced covalent functionalized epoxy-graphene nanocomposites and reported 18% and 23% increase in flexural strength and modulus, respectively [181]. Qi *et al.* produced graphene oxide-epoxy nanocomposites and reported increase up to 53% in flexural strength [182]. The impact strength and hardness were also significantly improved by graphene in epoxy nanocomposites. For example, Ren *et al.* applied a combination of bath sonication, mechanical mixing, and shear mixing to disperse

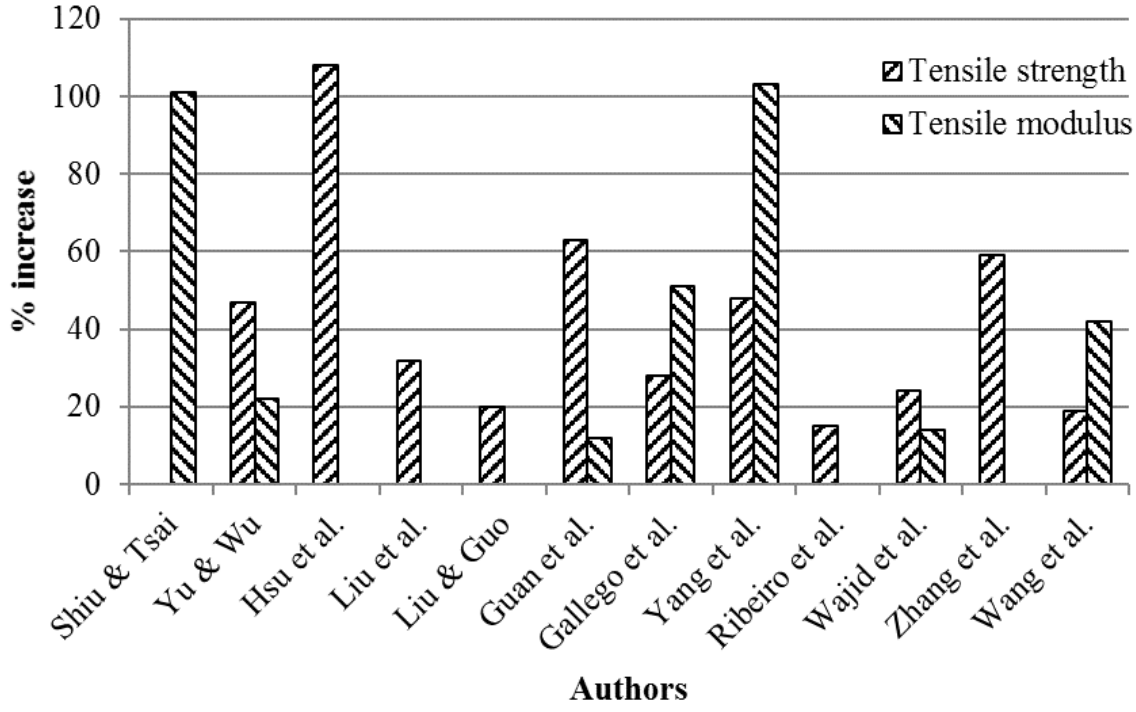

Figure 13: The percentage increase in tensile properties of epoxy/graphene nanocomposites [179,180,183–192]**.**

GO in cyanate ester-epoxy and produced nanocomposites using in-situ polymerization [193]. They reported an increase of 31% in impact strength. Qi *et al.* produced graphene oxide-epoxy nanocomposites and reported an increase in impact strength up to 96% [194] whereas Lu *et al.* produced GO-epoxy nanocomposites and reported an increase in impact strength up to 100% [195]. Shen *et al.* produced GNS-epoxy nanocomposites and reported an increase in impact strength up to 11% [196] and Bao *et al.* reported increase in hardness up to 35% [197]. The G_{1C} also improved with the incorporation of graphene in epoxy nanocomposites. Meng *et al.* produced epoxy-graphene nanocomposites and reported increase in G_{1C} up to 597% [198].

15 Thermal properties

Due to the superior thermal conductivity of graphene, graphene based polymer nanocomposites are promising candidates for high-performance thermal interface materials. The dissipation of heat from electronic devices may also be barricaded when the high thermal conductivity of graphene is efficiently utilized. The graphene has shown higher efficiency in increasing the thermal conductivity of polymers than CNTs [199]. It has been found experimentally that the Effective Thermal Conductivity (K_{eff}) of graphene based polymer nanocomposites has a non-linear dependence on graphene weight fraction [200–202]. Xie et al. proposed an analytical model to determine K_{eff} of graphene based nanocomposites [203]. Their model proposed very high thermal conductivity values as the model did not take into account the interfacial thermal resistance. Lin et al. developed a model based on Maxwell-Garnett effective medium approximation theory to determine effective thermal conductivity of graphene based nanocomposites [204,205]. They showed that the enhancement in thermal conductivity is strongly influenced by aspect ratio and orientation of graphene. Hu et al. used molecular dynamics approach to show that the agglomeration of graphene is of major concern in increasing the thermal conductivity of the system [206]. The variation in thermal conductivity with various forms of graphene and graphite nanocomposites is summarized in Table 2 and influence of dispersion mode on the improvement of thermal conductivity is shown in Figure 14. The maximum improvement in thermal conductivity was observed in case of mechanical stirring. In general, sonication caused a lower improvement in thermal conductivity. However, maximum improvement in thermal conductivity (not shown in Figure 14) was observed in case of sonication which is 1.6×10^{4}% [207].

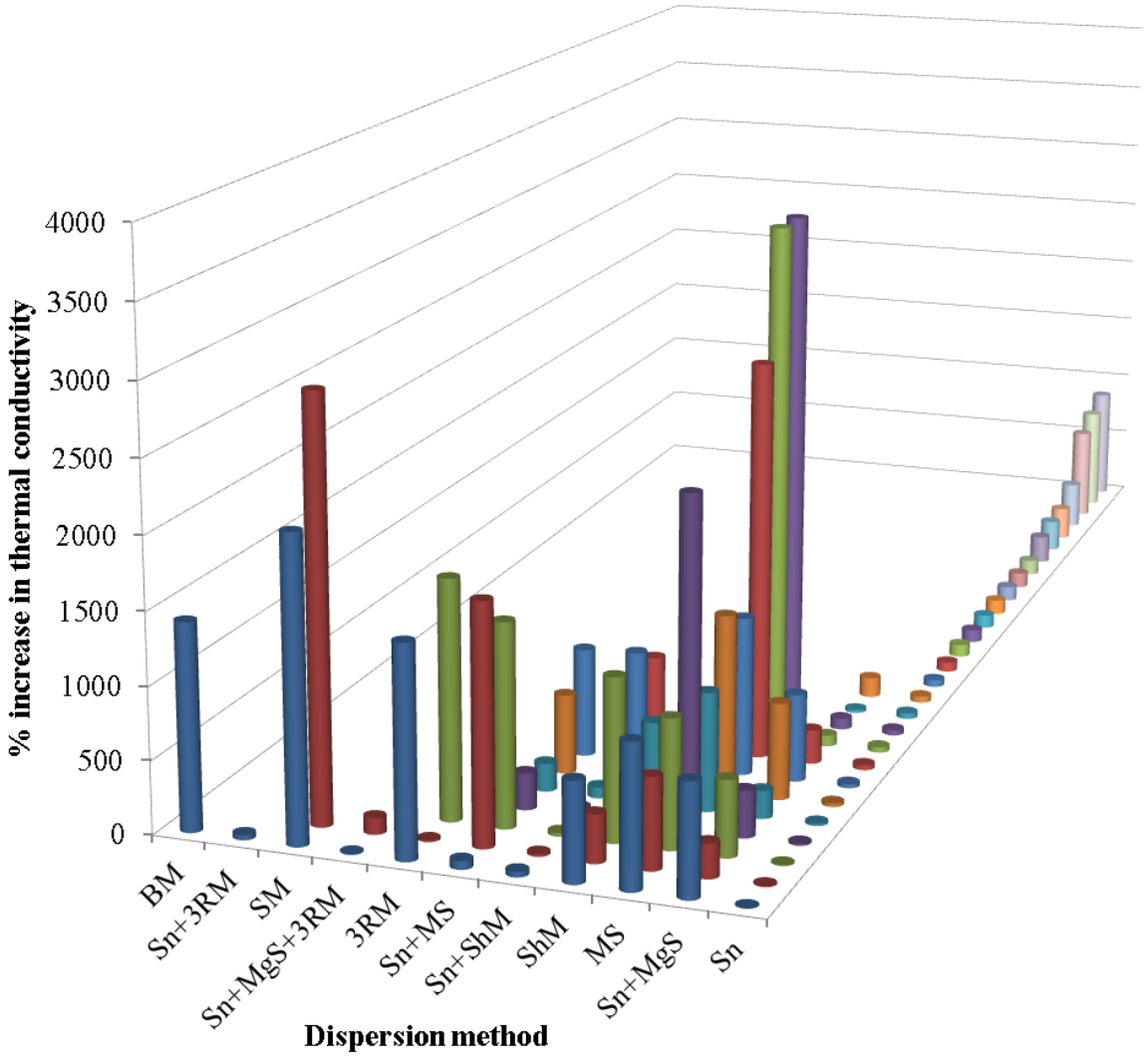

Figure 14: % increase in thermal conductivity as a function of dispersion method (see reference in Table 2).

The theoretical calculations predict thermal conductivity values of polymer nanocomposites far greater than the experimental values [208]. It can be explained on the basis of Thermal Boundary Resistance (TBR, also known as Kapitza resistance) between graphene and polymer chains [209]. The heat transfer in composite system is restricted by interfacial thermal resistance arising from weak phonon-phonon coupling which leads to backscattering of phonons at the boundary region. The interfacial thermal resistance increases with increasing interfacial area. Therefore, this resistance becomes quite

significant in case of graphene because of its high surface area. The heat transfer takes place as a consequence of Brownian motion of discrete thermal walkers [210]. In Brownian motion, the thermal walkers exhibit random changes in motion in each time step and can be modeled using random algorithm [211–214]. In each space direction, these position changes take values from a normal distribution with a zero mean and a standard deviation depending on the thermal diffusivity (D_m) and the time increment (Δt) as given in eq. (6) [208].

$$\sigma = \sqrt{2D_m \Delta t} \quad \textbf{(6)}$$

The TBR (R_{bd}) is introduced at graphene-polymer interface by a phonon transmission probability ($f_{m\text{-}GA}$) which can be measured according to acoustic mismatch theory as given in eq. (7) [215],

$$f_{m-GA} = \frac{4}{\rho_m C_{\rho m} \nu_m R_{bd}} \quad \textbf{(7)}$$

where ρ_m, $C_{\rho m}$, and ν_m are the density of, specific heat of, and sound velocity in polymer matrix, respectively. The improvement in thermal conductivity can be theoretically described by the percolation theory using a power law relationship as given in eq. (8) [216–221],

$$\sigma_c = \sigma_f [(\varphi - \varphi_c)/(1 - \varphi_c)]^t \quad \textbf{(8)}$$

where σ_f and φ are thermal conductivity and volume fraction of graphene, respectively, φ_c is percolation threshold, and t is universal critical exponent. A comparative infrared microscopy technique can be used to measure thermal properties of nanocomposites [208]. The thermal properties can be approximated by Fourier's law [222,223]. The variation in

thermal conductivity of graphene-PMMA nanocomposites with varying graphene content is shown in Figure 15 [208]. The thermal conductivity increases up to 3.5 times of pure PMMA at 2.5 vol% of graphene. The increase in thermal conductivity may be attributed to large contact area and strong interface between graphene and matrix. As there are strong π-π interactions between graphene-graphene, the TBR between graphene-graphene can be neglected. However, the TBR between graphene-PMMA must be considered and taken as $1.906*10^{-8}$ m^2K/W [224]. When graphene is oriented along the heat flux, higher K_{eff} values are obtained due to efficient heat transfer channel provided by graphene. However, when graphene is oriented perpendicular to the direction of heat flux, lower K_{eff} values are

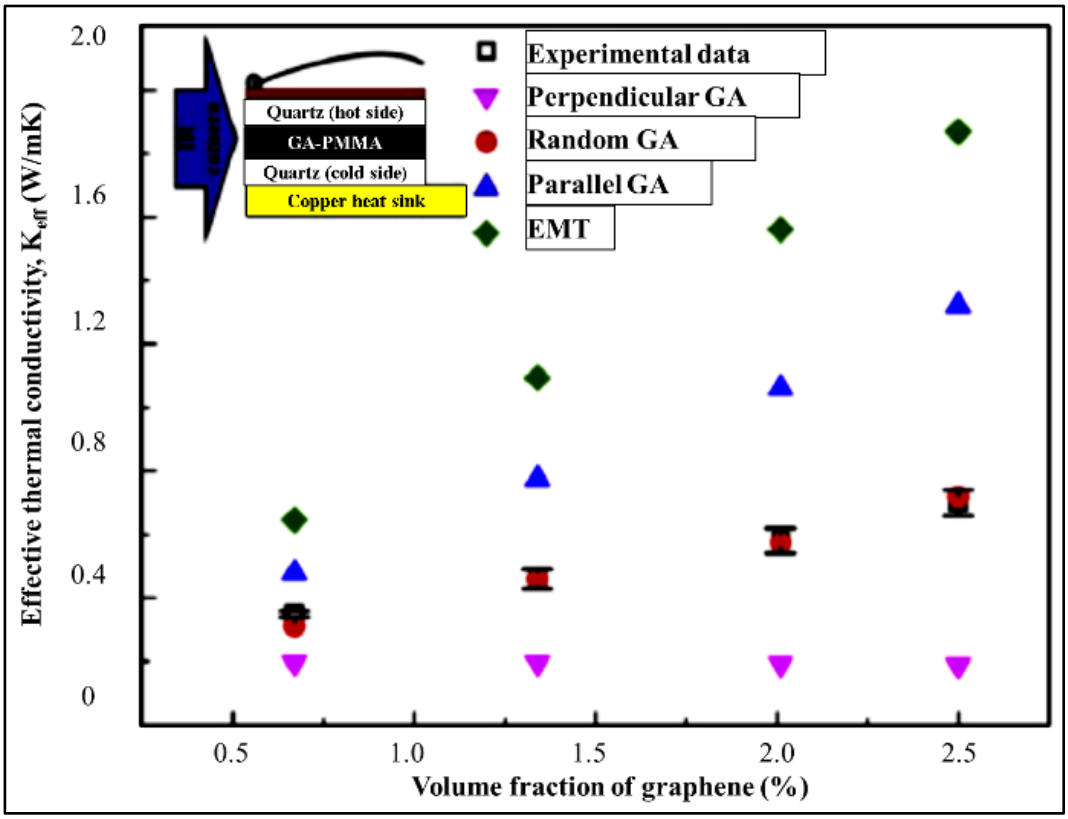

Figure 15: The thermal conductivity of GA-PMMA composites as a function of graphene volume fraction. Inset is the set-up scheme for comparative infrared microscopy technique, where the amorphous quartz is used as reference material [208]**.**

obtained due to TBR. The modified effective medium theory to estimate K_{eff} is given in eq. (9) [208],

$$K_{GA-PMMA} = K_{rGO}\left[\frac{3K_{PMMA} + 2f(K_{rGO} - K_{PMMA})}{(3-f)K_{rGO} + K_{PMMA}f + \frac{R_{bd}K_{PMMA}K_{rGO}f}{H}}\right] \quad \textbf{(9)}$$

where R_{bd} is TBR between graphene and PMMA, H is thickness of Functionalized Reduced Graphene Oxide (m-rGO) sheets, K_{rGO} is thermal conductivity of graphene, K_{PMMA} is thermal conductivity of PMMA, and f is volume fraction of graphene. The results show that the values predicted by EMT are greater than experimental values. One main reason for this is the particle size distribution which EMT does not take into account. In general, a large particle size distribution can increase the filling ratio as the finer particles can fill in the interstitial sites created by larger particles. The higher filling ratio helps in making strong networks of graphene which can significantly increase the thermal conductivity values compared with narrow size distribution.

Chu et al. proposed an analytical model based on Differential-Effective-Medium (DEM) theory to determine the thermal properties of graphene based nanocomposites [225]. The DEM theory can be used to effectively describe the thermal properties of composites [226–228]. Chu et al. considered the Graphene Nanoplatelets (GNPs) as oblate spheroid with very large aspect ratio and considered the isotropic two phase composite system. The composite system was considered with temperature field $\vec{T}$ and heat flux $\vec{Q}$ which are given by eq. (10) and eq. (11) [225], respectively, where d(T) is temperature distribution function.

$$\vec{T} = -\nabla d(T) \quad \textbf{(10)}$$

$$\vec{Q} = K\vec{T} \quad \textbf{(11)}$$

The solution for the temperature fields, T_p and T_m, within the dispersed particles and surrounding matrix, respectively, is given by eq. (12) [225],

$$\frac{T_p}{T_m} = \frac{1}{1 + H_j\left(\frac{K_j}{K_m} - 1\right)} \quad \textbf{(12)}$$

where H_j is the depolarization factor of the ellipsoidal particles along j-axis, k_m is the thermal conductivity of matrix, and k_j is thermal conductivity of GNP along j-axis [225]. The depolarization factor (H) obeys the following equation, $2H_x + H_z = 1$, where,

$$H_x = \frac{p^2}{2(p^2-1)} - \frac{p^2}{2(p^2-1)^{3/2}}\cos h^{-1}p \quad \textbf{(13)}$$

eq. (12) can be used to approximate the dependency of effective thermal conductivity of nanocomposites on the reinforcement volume fraction as given in eq. (14) [226,228],

$$\frac{dK^*}{df} = \frac{f}{3}\sum_{j=x,y,z(x=y)} \frac{K^* - K_j}{K^* + H_j(K_j - K^*)} \quad \textbf{(14)}$$

when the initial condition is kept $k^* = k_m$ at GNP volume fraction f = 0, eq. (14) can be written after integration as eq. (15) [225],

$$9(1-f)\frac{K^* - K_m}{2K^* + K_m} = f\left[\frac{K_z - K^*}{K^* + H_Z(K_z - K^*)} + \frac{2(K_x - K^*)}{K^* + H_x(K_x - K^*)}\right] \quad \textbf{(15)}$$

where K_z and K_x are the thermal conductivity values of GNP along longitudinal and transverse axes, respectively. At a very large aspect ratio (a >> c), the values of H_x and H_z can be taken as zero and unity, respectively. Therefore, eq. (15) can be simplified as eq. (16) [225].

$$9(1-f)\frac{K^*-K_m}{2K^*+K_m} = f\left[\frac{2K_x}{K^*} - \frac{K^*}{K_z} - 1\right] \quad \textbf{(16)}$$

To consider interfacial thermal resistance, Chu et al. considered GNP as core-shell structure as shown in Figure 16 [225]. The interfacial boundary layer has thickness c and thermal conductivity values of k_s and the effective thermal conductivity can be written as eqs. (17- (19) [205], where Θ is the dipolar factor of shelled GNPs [229]. When interfacial thermal resistance is incorporated, the effective thermal conductivity of graphene based nanocomposites is given by eq. (20) [225].

Liu et al. also proposed the model based on Effective Medium Approximation (EMA) theory to determine effective thermal conductivity of graphene based nanocomposites as given in eqs. (21- (23) [204]. When interfacial thermal resistance is incorporated, the model takes the form as eq. (24) with comparison of the results shown in Figure 17 [225].

$$K_j^{eff} = \frac{K_j}{1 + {\Theta_j H_j K_j}/{K_m}} \quad \textbf{(17)}$$

$$K_x^{eff} = \frac{K_x}{2R_K K_x/L + 1} \quad \textbf{(18)}$$

$$K_z^{eff} = \frac{K_z}{2R_K K_z/t + 1} \quad \textbf{(19)}$$

$$9(1-f)\frac{K^*-K_m}{2K^*+K_m}$$

$$= f\left[\frac{2K_x}{2K^*\left({}^{R_K K_x}/_{L}+1\right)}-\frac{K^*\left({}^{2R_K K_z}/_{t}+1\right)}{K_z}-1\right] \quad \textbf{(20)}$$

$$\frac{K^*}{K_m}=\frac{\{2A_x(H_x-1)+A_z(H_z-1)\}/_{3f}-1}{(2A_xH_x+A_ZH_z)f/_{3}-1} \quad \textbf{(21)}$$

$$A_x=\frac{K_x-K_m}{K_m+H_x(K_x-K_m)} \quad \textbf{(22)}$$

$$A_z=\frac{K_z-K_m}{K_m+H_z(K_z-K_m)} \quad \textbf{(23)}$$

$$\frac{K^*}{K_m}=\frac{1+{}^{2f\left\{{}^{K_x}/_{K_m}\left({}^{2R_K K_x}/_{L}+1\right)\right\}}/_{3}}{1-{}^{f}/_{3}} \quad \textbf{(24)}$$

16 Electrical properties

Tailoring the electrical properties of graphene can unlock many potential electronic applications of graphene [230,231]. For example, effective gauge fields are introduced when lattice deformation of graphene takes place. Like the effective magnetic field, the produced effective gauge fields influence the Dirac fermions [232]. The Fermi level in undoped graphene lies at the Dirac point where the minimum conductivity values are achieved [233]. By adding free charge carriers, i.e. dopants, the electrical properties of graphene can be improved and conductivity increases linearly with carrier density

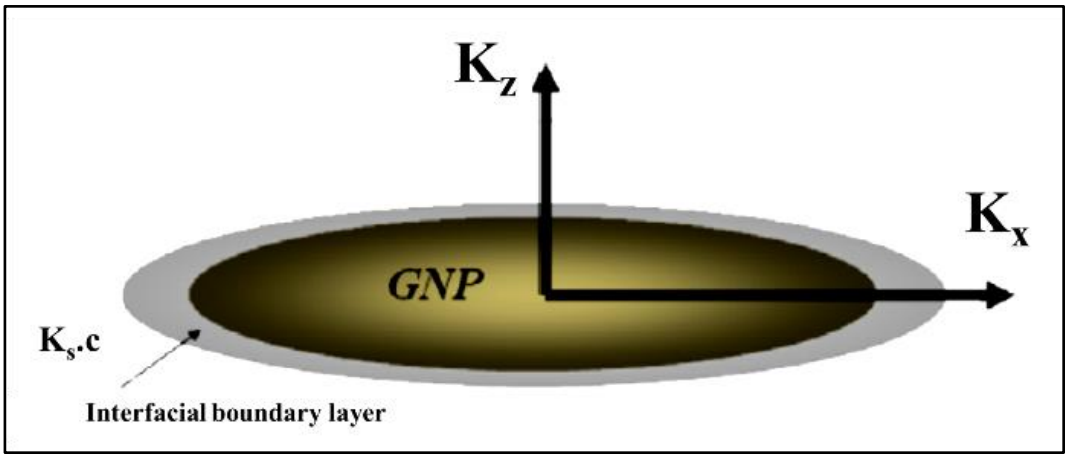

Figure 16: A core-shell GNP with coating with a very thin interfacial boundary layer [225]**.**

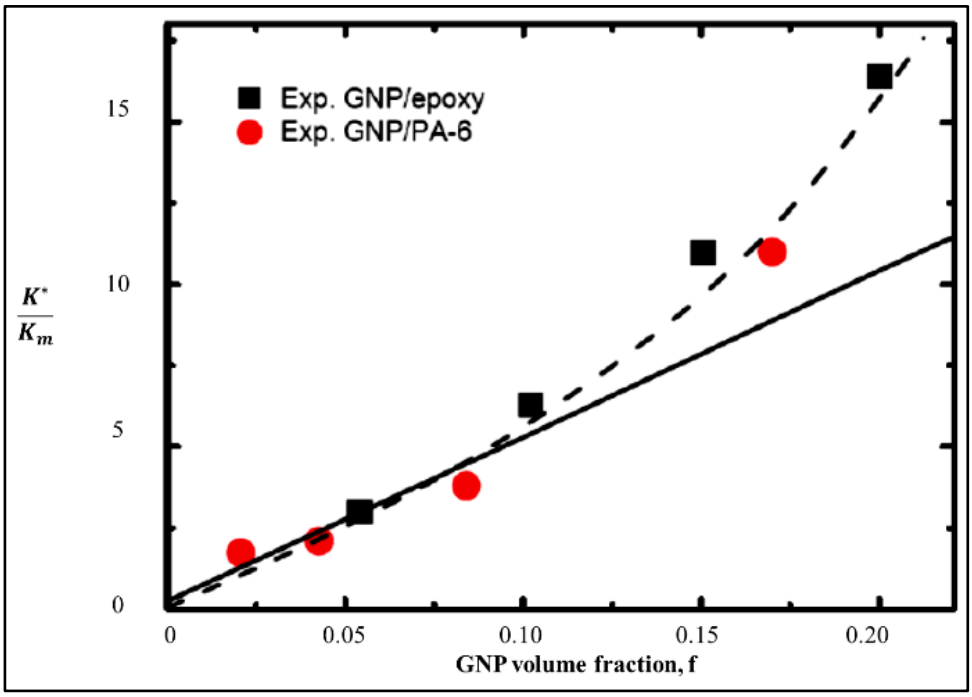

Figure 17: Comparison between the theoretical and experimental results [225]**.**

[234,235]. For example, boron as dopants can contribute ~0.5 carriers per dopant in graphene sheet [236]. Dopants can be introduced during the synthesis of graphene using Chemical Vapor Deposition (CVD) [237]. The variation in electrical conductivity with various forms of graphene and graphite nanocomposites is summarized in Table 3. The maximum improvement in electrical conductivity was observed in case of a combination

of ball milling and mechanical stirring. Therefore, both thermal and electrical conductivities improved in case of mechanical stirring.

Due to graphitic composition, graphene exhibits excellent electrical conductivity. The charge carrier mobility of graphene at room temperature is as high as 15000 cm^2/Vs [238]. When graphene is uniformly dispersed in the polymer matrix, graphene can provide efficient pathways for conduction which can boost electrical conductivity of nanocomposites. At a certain graphene loading, the electrical conductivity of graphene based polymer nanocomposites shows a drastic increase and they lose their insulating character and start behaving like conductors. This graphene loading is called as percolation threshold and is usually taken at thirteen orders of magnitude increase in the electrical conductivity of produced nanocomposite [239–241]. The percolation threshold should be as low as possible in order to decrease the use of graphene. The dispersion state or degree of agglomeration of graphene is known to have a significant influence on the percolation threshold and electrical conductivity of graphene based polymer nanocomposites [242]. The key factors influencing the percolation threshold include, dispersion state, physicochemical interactions between the matrix and the reinforcement, shape of the reinforcement, and method to produce nanocomposite. The conductivity models can be classified into three main categories: (1) structure- oriented [243], (2) thermodynamic [244], and (3) statistical [239,245]. The structure-oriented models consider the microstructure of nanocomposites before and after the processing. As properties are strongly dependent on microstructure, therefore the structure-oriented models give a more realistic approach to predict conductivity behavior of nanocomposites.In certain cases, when achieving the actual microstructure is difficult, the structure-oriented models replace

the microstructure with fitting parameters. However, these fitting parameters are not a true replacement of actual microstructure especially at nano-scale.

The electrical conductivity of nanocomposites strongly depends on the microstructure. When epoxy is filled with a conducting nano-filler, conduction of the produced nanocomposite depends on how the nano-fillers are aligned [246]. The nano-fillers should make a continuous network to provide a swift conductive pathway for the electrons [247]. Various models have been proposed to approximate percolation threshold for nanocomposites with various nano-fillers such as graphite, CNTs, and graphene. Many proposed models use fitting parameters where achieving actual values is difficult. As microstructure is a key factor in defining the properties of nanocomposites, it should be efficiently incorporated in proposed models to get closer to real-time values. Syurik et al. proposed a modification in McCullough's model with current maps obtained by Conductive Atomic Force Microscopy (CA-AFM) [244].

McCullough's model is a structure-oriented model which assumes that the microstructure and orientation of reinforcement inside the matrix are variables and depend on the reinforcement content [243]. The increase in electrical conductivity can be attributed to the formation of chain-like network of reinforcement. The chain length depends on the size, shape, and volume fraction of reinforcement. Below the percolation threshold, this chain-like network is sporadic and all chains are not connected together. Due to cessation of chain continuity, the conduction is obstructed and the nanocomposites behave as insulators. By the time percolation threshold is achieved, all chains cling together and construct a continuous network which acts as a highway for electrons and nanocomposites start behaving as conductors. The chain fraction and its dimensions are statistical in nature.

The distribution of chain length can be described by a probability density function η(ν_f,a), where a is the effective aspect ratio and ν_f is the volume fraction of reinforcement. The average value of chain parameter <λ> can be calculated using eq. (25) [244],

$$\langle\lambda\rangle = \int_1^{\infty} n(v_f, a)\lambda(a)da = 1 \quad \textbf{(25)}$$

where λ (a) is a chain parameter dependent on reinforcement shape. When aspect ratio (a) of reinforcement exceeds 1, the chain parameter can be calculated using eq. (26) and eq. (27) [244]. The isotropic distribution of reinforcement in the matrix is given by eq. (28) and eq. (29) [244],

$$\lambda(a) = 1 - A^2\left\{1 - 0.5(A - A^{-1})ln\left(\frac{A+1}{A-1}\right)\right\} \quad \textbf{(26)}$$

$$\text{where, } A^2 = \frac{a}{1-a^2} \quad \textbf{(27)}$$

$$\frac{\sigma_m}{\sigma} = \frac{v_m^2(1 - \langle\lambda\rangle)}{V_m} + \frac{\sigma_m}{\sigma_f}.v_f.\frac{V_m^2 + v_m(1 + V_m)\langle\lambda\rangle}{V_m^2} \quad \textbf{(28)}$$

$$\text{where, } \frac{\sigma_m}{\sigma_f} \ll 1, \qquad V_m = (1 - \langle\lambda\rangle)v_m + \langle\lambda\rangle v_f \quad \textbf{(29)}$$

where σ_m, σ_f, and σ are electrical conductivities of matrix, reinforcement, and composite, respectively. The ν_f and ν_m are volume fractions of reinforcement and matrix, respectively. The experimental determination of η(ν_f,a) and <λ> is quite difficult. Therefore, these factors were taken as fitting parameters. As actual microstructure is not considered, therefore it poses a limitation to McCullough's model exhibiting a semi-empirical character. Syurik et al. used AFM to determine the actual value of <λ> [244]. For ideal

Table 2: A brief record of epoxy based nanocomposites studied for improvement in thermal conductivity values.

Sr.	Authors	Year	Reinforcement (wt%)	Dispersion method	% increase in thermal conductivity	Remarks	Ref
1	Kandre et al.	2015	GnP (1.9wt%)	Sn	9	The simultaneous inclusion of GnPs and SnP/SnW at a combined loading of 1 vol% resulted in about 40% enhancement in the through-thickness thermal conductivity while the inclusion of GnP at the same loading resulted only in 9% improvement. A higher increment with simultaneous addition of GnP and SnP/SnW can be attributed to synergistic effects.	[248]
			SnP/(0.09wt%)		18		
			SnW/(0.09wt%)		8		
			GnP(1.9wt%), SnP(0.09wt%)		38		
			GnP(1.9wt%), SnW(0.09wt%)		40		
2	Tang et al.	2015	Three-dimensional graphene network (3DGNs) (30wt%)	None.	1900	(Composites produced using layer by layer dropping method.) The filler with large size is more effective in increasing the thermal conductivity of epoxy because of continuous transmission of acoustic phonons and minimum scattering at the interface due to reduced interfacial area. High intrinsic thermal conductivity of graphene is the major reason for the obtained high thermal conductivity of nanocomposites.	[249]
			Chemically reduced graphene oxide (RGO) (30wt%)	Sn+MS	1650		
			Natural graphite powder (NG) (30wt%)		1400		
3	Burger et al.	2015	Graphite flakes (12wt%) (GRA-12)	Sn+MgS	237.5	As the filler/matrix interfaces increase, the thermal resistance increases due to phonon scattering. In order to improve the thermal conductivity of a composite, it is better to structure a sample with an adapted morphology than trying to have the best dispersion. A 3D-network was prepared first with graphite foils oriented through the thickness of the sample and then stabilized with DGEBA/DDS resin. The produced composite sample was called as "Network". In 'fibers', all the graphite flakes were aligned through the thickness of sample. When a DGEBA interface layer was applied in 'fiber', the sample was called as 'Fiber+1 interface'. When two DGEBA interface layers was applied in 'fiber' the sample was called as 'Fiber+2 interfaces'.	[250]
			Graphite flakes (15wt%) (GRA-15)		325		
			Graphite flakes (14-15wt%) (Network)		775		
			Graphite flakes (11-12wt%) (Fibers)		666.7		
			Graphite flakes (11-12wt%) (Fiber+1 interface)		608.3		
			Graphite flakes (11-12wt%) (Fiber+2 interface)		237.5		

4	Zeng et al.	2015	Liquid crystal perylene bisimides polyurethane (LCPU) modified reduced graphene oxide (RGO) (1wt%)	Sn	44.4	Along with the increase in thermal conductivity, the impact and flexural strengths increased up to 68.8% and 48.5%, respectively, at 0.7wt% LCPU/RGO.	[251]
5	Wang et al.	2015	GnPs, 1 µm, (GnP-C750)	Sn+MgS+3RM	9.1	The increase in thermal conductivity is higher in case of larger particle size than smaller particle size.	[252]
			GnPs, 5 µm		115		
6	Zhou et al.	2015	Multi-layer graphene oxide (MGO) (2wt%)	Sn	95.5	The thermal conductivity decreases after 2 wt% MGO.	[253]
7	Zeng et al.	2015	Al_2O_3 nanoparticles (30wt%)	Sn	50	The thermal conductivity can be improved by using hybrid fillers.	[254]
			Aminopropyltriethoxy-silane modified Al_2O_3 nanoparticles (Al_2O_3-APS) (30wt%)		68.8		
			Liquid-crystal perylene-bisimide polyurethane (LCPBI) functionalized reduced graphene oxide (RGO) and Al_2O_3-APS (LCPBI/RGO/Al_2O_3-APS)		106.2		
8	Tang et al.	2015	Al_2O_3 (18.4wt%)	Sn+MS	59.1	The increase in thermal conductivity decreases with Al_2O_3 coating of graphite.	[255]
			Graphite (18.4wt%)		254.6		
			Al_2O_3 coated graphite (Al_2O_3-graphite) (18.4wt%)		195.5		
9	Pan et al.	2015	Perylene bisimide (PBI)-hyper-branched polyglycerol (HPG) modified reduced graphene oxide (RGO), (PBI-HPG/RGO) (1wt%)	Sn	37.5	The filler was observed to be uniformly dispersed resulting in strong interfacial thermal resistance.	[256]
10	Wang et al.	2015	SiO_2, 15 nm, (1wt%)	Sn	14.3	SiO_2 nanoparticles are more effective in increasing thermal conductivity than GO. The maximum improvement in thermal conductivity was observed in case of hybrid filler.	[257]
			GO (1wt%)		4.8		
			As-prepared nanosilica/graphene oxide hybrid (m-SGO) (1wt%)		28.6		
11	Zha et al.	2015	GNPs (3.7wt%), Al_2O_3 nanoparticles (ANPs), (65wt%)	Sn+MS	550.4	Al_2O_3 nanofibers are more effective in improving thermal conductivity than Al_2O_3 nanoparticles.	[258]
			GNPs (3.7wt%), Al_2O_3 fibers (Afs) (65wt%)		756.7		

12	Zhou et al.	2015	Multi-layer graphene oxide (MGO) (2wt%)	Sn	104.8	The thermal conductivity decreases after 2wt% MGO.	[259]
13	Wang et al.	2015	GNPs (8wt%)	MS	627	The thermal conductivity increases with GNPs at the loss of Vickers microhardness after 1wt% of GNP.	[260]
14	Pu et al.	2014	RGO (1wt%)	Sn+MgS	21.8	The thermal conductivity decreases after 1 wt% RGO. The silica layer on S-graphene makes electrically conducting graphene insulating, reduces the modulus mismatch between the filler and matrix, and improves the interfacial interactions of the nanocomposites which result in enhanced thermal conductivity.	[261]
			3-aminopropyl triethoxysilane (APTES) functionalized graphene oxide (A-graphene) (8wt%)		47.1		
			Silica-coated A-graphene (S-graphene) (8wt%)		76.5		
15	Fu et al.	2014	Graphite (44.30wt%)	MS	888.2	The maximum improvement in thermal conductivity was observed in case of graphene sheets with thickness of 1.5 nm.	[262]
			Graphite nanoflakes (16.81wt%)		982.3		
			Graphene sheets (10.10wt%)		2258.8		
16	Li et al.	2014	Alighned MLG (AG) (11.8wt%)	Sn	16670	The alignment of MLG causes an exceptional improvement in thermal conductivity and exceeds other filler-based epoxy nanocomposites.	[207]
17	Guo and Chen	2014	GNPs (25wt%)	Sn	780	Ball milling is more effective in improving the thermal conductivity of GNP/epoxy than sonication. The thermal conductivity decreases when ball milling is carried out for more than 30 h.	[148]
			GNPs (25wt%)	BM	1420		
18	Corcione and Maffezzoli	2013	Natural graphite (NG) (1wt%)	Sn	24.1	The thermal conductivity decreases with increasing wt% of NG after 1 wt%. The thermal conductivity decreases after 2wt% of GNPs. The maximum improvement in thermal conductivity was observed with expanded graphite.	[263]
			GNPs (2wt%)		89.8		
			Expanded graphite (EGS) (3wt%)		232.1		
19	Chandrasekaran et al.	2013	GNP (2wt%)	3RM	14	The thermal conductivity increases with increasing temperature	[69]
20	Min et al.	2013	GNPs(5wt%)	Sn	240	High aspect ratio of GNPs and oxygen functional groups play a significant role in improving thermal conductivity of nanocomposites.	[264]
21	Hsiao et al.	2013	Silica (1wt%)	Sn+ShM	19	The existance of the intermediate silica layer	[265]

			Thermally reduced graphene oxide (TRGO) (1wt%)		26.5	enhances the interfacial attractions between TRGO and epoxy and improved dispersion state which caused a significant increase in thermal conductivity.
			Silica nanosheets (Silica-NS) (1wt%)		37.5	
			TRGO-silica-NS (1wt%)		61.5	
22	Zhou et al.	2013	Untreated GNPs (12wt%)	Sn+MgS	139.3	Silane functionalization can significantly improve thermal conductivity of GNP/epoxy. [266]
			Silane-treated COOH-MWCNTs (6wt%)		192.9	
			Silane-treated GNPs (6wt%)		525	
23	Raza et al.	2012	GNPs, 5 µm, 30wt%, in rubbery epoxy	MS	818.6	The thermal conductivity increases with increasing particle size. The particle size distribution significantly influences the thermal conductivity. GNPs with a broad particle size distribution gave higher thermal conductivity than the particles with a narrow particle size distribution due to the availability of smaller particles which can bridge gaps between larger particles. [267]
			GNPs, 5 µm, 20wt%, in rubbery epoxy	ShM	332.6	
			GNPs, 15 µm, 25wt%, in rubbery epoxy	MS	1228.4	
			GNPs, 15 µm, 25wt%, in rubbery epoxy	ShM	1118.2	
			GNPs, 20 µm, 20wt%, in rubbery epoxy	ShM	684.6	
			GNPs, 20 µm, 12wt%, in glassy epoxy	ShM	567.6	
			GNPs, 15 µm, 20wt%, in glassy epoxy	MS	683	
24	Kim et al.	2012	GO (3wt%)	Sn	90.4	The increase in thermal conductivity decreases with $Al(OH)_3$ coating on GO. [268]
			$Al(OH)_3$-coated graphene oxide (Al-GO) (3wt%)		35.1	
25	Chatterjee et al.	2012	Amine functionalized expanded graphene nanoplatelets (EGNPs) (2wt%)	Sn+3RM	36	The EGNPs form a conductive network in the epoxy matrix allowing for increased thermal conductivity. [79]
26	Im and Kim	2012	Thermally conductive graphene oxide (GO) (50wt%)	Sn	111	The thermal conductivity decreases after 50wt% which can be attributed to residual epoxy that forms an insulting layer on reinforcement. MWCNT helps formation of 3D network structure. [269]
			Thermally conductive graphene oxide (GO) (50wt%), MWCNTs (0.36wt%)		203.4	
27	Heo et al.	2012	Al_2O_3 (80wt%), GO (5wt%)	3RM	1650	The increase in thermal conductivity decreases with [270]

			$Al(OH)_3$-coated GO (5wt%)		1450	$Al(OH)_3$ coating of GO.
28	Huang et al.	2012	MWNTs (65wt%)	MS	1100	GNPs are more effective in improving the thermal conductivity than MWNTs. The maximum improvement in thermal conductivity was observed in cse of hybrid fillers. [271]
			GNPs (65wt%)		2750	
			MWNTs (38wt%), GNPs (38wt%)		3600	
29	Teng et al.	2011	MWNT (4wt%)	Sn	160	GNPs showed a significant higher increase in thermal conductivity than MWNTs. The maximum improvement in thermal conductivity is shown by non-covalent functionalized GNS which can be attributed to high surface area and uniform dispersion of GNS. [123]
			GNPs(4wt%)		700	
			Poly(glycidyl methacrylate containing localized pyrene groups (Py-PGMA) functionalized GNPs (Py-PGMA-GNS)		860	
30	Gallego et al.	2011	MWNTs (1wt%) in nanofluids	ShM	66.7	The layered structure of MWNTs enables an efficient phonon transport through the inner layers, while SWNTs present a higher resistance to heat flow at the interface due to its higher surface area. The f-MWNTs have functional groups on their surface acting as scattering points for the phonon transport. [272]
			f-MWNTs (0.6wt%) in nanofluids		20	
			SWNTs (0.6 wt%) in nanofluids		20	
			Functionalized graphene sheet (FGS) (1 wt%) in nanofluids		0	
			GO (1wt%) in nanofluids		0	
			MWNTs(1wt%) in nanocomposites		72.7	
			Functionalized graphene sheet (FGS) (1 wt%) in nanocomposites		63.6	
31	Tien et al.	2011	Graphene flakes (12wt%)	Sn	350	The thermal conductivity increases exponentially with increasing wt% of graphene flakes. [273]
32	Ganguli et al.	2008	Exfoliated graphite flakes (20wt%)	SM	2087.2	The thermal conductivity increases with chemical functionalization [201]
			Chemically functionalized graphite flakes(20wt%)		2907.2	
33	Yu et al.	2008	Carbon black (CB) (10wt%)	Sn+ShM	75	The hybrid filler demonstrates a strong synergistic effect and surpasses the performance of the individual SWNT and GNP filler. [274]
			SWNTs (10wt%)		125	
			GNPs (10wt%)		625	
			GNPs (7.5 wt%),SWNTs (2.5 wt%)		775	

Table 3: A brief record of epoxy based nanocomposites studied for improvement in electrical conductivity values.

Sr.	Authors	Year	Reinforcement/wt%	Dispersion method	% increase in electrical conductivity	Remarks	Ref.
1	Wu et al.	2015	GNPs (1.5wt%), transverse to alighnment	Sn+3RM	1.00E+07	The maximum thermal conductivity was observed in case of aligned GNPs.	[275]
			GNPs (3wt%), randomly oriented		1.00E+08		
			GNPs (3wt%), parallel to alignment		1.00E+10		
2	Liu et al.	2015	Graphene woven fabric (GWF) (0.62wt%)	None.	1.00E+13	(Samples were produced using resin infiltration.) The average number of graphene layers in GWFs varied between 4 and 12.	[276]
3	Ming et al.	2015	Graphene foam (GF) (80wt%)	None.	8.00E+02	(Samples were produced using hot pressing.) The electrical conductivity of pure graphene foam (GF) is 2.9 Scm-1 which is much lower than graphene which can be because of the presence of structural defects.	[277]
5	Ghaleb et al.	2014	GNPs (1.1wt%)	Sn	1.39E+06	GNPs are more effective in improving the thermal conductivity of epoxy than MWCNTs.	[129]
			MWCNTs (1.9wt%)		1.62E+05		
6	Tang et al.	2014	GO (5wt%)	Sn+HSM	1.92E+09	The surface functionalization of GO can significantly improve the electrical conductivity of GO-epoxy.	[278]
			Diamine polyetheramine functionalized GO (GO-D230) (5wt%)		1.92E+12		
7	Dou et al.	2014	Silver plated graphene (Ag-G) (25wt%)	Sn+MS	4.13E+02	Ag-graphene can be used in electronic applications due to high electrical conductivity.	[279]
8	Tang et al.	2014	GO (3.6wt%)	Sn	1.00E+18	The surface functionalization significantly improves electrical conductivity	[280]
			Polyetheramine refluxed GO (GO-D2000) (3.6wt%)		1.00E+17		
9	Monti et al.	2013	GNPs (3wt%)	Sn+MS	2.08E+05	The samples were produced using chloroform	[281]
			GNPs (3wt%)		1.16E+05	The samples were produced using tetrahydrofuran.	
10	Wajid et al.	2013	GNPs (0.24wt%)	Sn+MS	2.22E+03	The samples were produced using dimethylformamide.	[190]
11	Chandrakekaran et al.	2013	GNPs (1wt%)	Sn+ShM	1.00E+04	3RM is more effective in improving the electrical conductivity of epoxy than sonication and high speed shear mixing.	[69]
			GNPs (2wt%)	3RM	1.00E+08		
12	Suherman et al.	2013	GNPs (80wt%), CNTs	BM+MS	7.30E+17	The electrical conductivity significantly increases with hybrid filler.	[282]

			(5wt%), through-plane				
			GNPs (80wt%), CNTs (5wt%), in-plane		1.80E+18		
			GNPs (80wt%), through-plane		4.00E+17		
			GNPs (80wt%) in-plane		5.00E+17		
13	Mancinelli et al.	2013	GO (0.5wt%)	Sn	2.40E+02	The conductivity was measured before post curing.	[283]
			GO (0.5wt%)		7.30E+02	The conductivity was measured after post-curing.	
			Octadecylamine (ODA) treated partially reduced and chemically modified GO (MGO) (0.5wt%)		5.50E+02		
			GO (0.5wt%)	Two phase extraction	2.40E+02		
			GO (0.5wt%)		7.80E+03	The conductivity significantly increased after post-curing.	
14	Al-Ghamdi et al.	2013	Foliated graphite nanosheets (FGNs) (40wt%)	Centrifugal mixing	9.90E+03	Dielectric properties of epoxy-FGN composites decreased with an increase in frequency.	[284]
15	Kim et al.	2012	$Al(OH)_3$ functionalized GO (Al-GO) (3wt%)	MS+MgS	7.50E+01	The increase in electrical conductivity decreases with $Al(OH)_3$ functionalization of GO.	[285]
			GO (3wt%)		1.15E+02		
16	Heo et al.	2012	Al_2O_3 (80wt%), $Al(OH)_3$ functionalized GO (Al-GO) (5wt%)	3RM	2.90E+03	The increase in electrical conductivity with $Al(OH)_3$ functionalization decreased. The electrically insulating $Al(OH)_3$ on the graphene oxide nanosheet can prevent electron tunneling and act as ion traps which block ion mobility, resulting in a decrease in the electrical properteis of nanocomposites.	[270]
			Al_2O_3 (80wt%), GO (5wt%)		4.90E+03		
17	Tien et al.	2011	Graphite flakes (14wt%)	Sn	4.00E+07	The percolation threshold was 8wt%	[273]
18	Fan et al.	2009	GNPs (5wt%)	Sn+MS	5.50E+10	The maximum electrical conductivity was observed in case of hybrid fillers.	[286]
			GNPs (4.5wt%), carbon black (CB) (0.5 wt%)		5.50E+12		
19	Jovic et al.	2008	Expanded graphite (EG) (8wt%)	Sn	5.50E+17	The electrical conductivity further increases with the application of electric field.	[287]
20	Li et al.	2007	MWCNTs (1wt%)	Sn	4.63E+07	The samples were produced using acetone.	[288]
21	Pecastaings et al.	2004	MWCNTs (20wt%)	Sn+MS	4.53E+03	The samples were produced using acetone.	[289]

where n is the number of conductive chains, ℓ_i is length of i^{th} chain, d_i is diameter of i^{th} chain, $<\ell>$ and $<d>$ are average length and average diameter of chain, respectively. Therefore, eq. (28) can be reduced to eq. (30), and density of composite can be calculated using rule of mixture as given in eq. (31) [244],

$$\frac{\sigma_m}{\sigma} = \frac{v_m^2(1-\langle\lambda\rangle)}{V_m} \quad \textbf{(30)}$$

$$\rho = \rho_f v_f + \rho_m(1-v_f) \quad \textbf{(31)}$$

where ρ, ρ_f, ρ_m, are specific densities of composite, reinforcement, and matrix, respectively. During production of nanocomposites, porosity is inevitable due to, (1) air entrapment, (2) evaporation of volatiles, (3) any shrinkage during curing, and (4) the relative movement of reinforcement and polymer chains. The porosity influences the conductivity which can be considered using an apparent density (ρ_{ap}) connected with specific density through the pore coefficient as given in eq. (32) [244].

When the nanocomposites are produced by a reproducible technology, such as latex technology, in which conductivity trends remain the same when samples are reproduced using the same parameters [290], the K_ρ can be taken as constant and needs to be measured only once. From eq. (32), eq. (31) can be written as eq. (33) where the coefficient K_ρ depends on geometry of the reinforcement [244]. The value of ρ_{ap} can be defined experimentally if the reinforcement fraction (w), sample's volume (V) and mass (m) are known as given in eq. (34), and the volume fraction of reinforcement can be calculated using eq. (35) where volume fraction can be converted to weight fraction using eq. (36), and G can be calculated by combining eq. (37) and eq. (38) [244]. The eq. (37) and eq. (38) show the conductivity behavior with respect to reinforcement fraction. The CA-AFM image of Graphene Nanoplatelet Reinforced Polystyrene (GNP/PS) nanocomposites is

$$\rho = \frac{\rho_f v_f}{K_p} + \rho_m(1 - v_f) \quad \textbf{(33)}$$

$$K_p = {\rho_f}/{\rho_{ap}} \quad \textbf{(32)}$$

$$\frac{\rho_f}{K_p} = \frac{m.w}{V - \frac{m(1-w)}{\rho_m}} \quad \textbf{(34)}$$

$$v_f = \frac{\rho - \rho_m}{\frac{\rho_f}{K_p} - \rho_m} \quad \textbf{(35)}$$

$$G = \frac{v_f}{w_f} \quad \textbf{(36)}$$

$$\frac{\sigma_m}{\sigma} = \frac{G^2(1 - w_f)^2(1 - \langle\lambda\rangle)}{V_m} \quad \textbf{(37)}$$

$$V_m = (1 - \langle\lambda\rangle)G(1 - w_f) + \langle\lambda\rangle G w_f \quad \textbf{(38)}$$

shown in Figure 18 (a) and corresponding image of the grains is shown in Figure 18 (b) where 368 grains are shown with size distribution of the GNP clusters shown in Figure 18 (c) [244]. The GNP/PS nanocomposites were prepared by latex technology which allows the reproducible percolation threshold [290]. Most of the GNPs had a thickness of 2-3 atomic layers and average surface area 1-3 μm^2. The weight fractions of GNPs were 0, 0.6, 0.9, 1.5, and 2.0 wt%. Electrical conductivity measurements in Direct Current (DC) mode were performed in a direction parallel to the sample top surface using a 2-probe configuration and a Keithley 2602 system source meter. Conductivity was calculated from the obtained I/V characteristics using eq. (39) [244],

$$\sigma = \frac{b.I}{V.A} \quad \textbf{(39)}$$

where V is applied voltage and I is current value through a cross-section (A) and between the distance (b). The values of <λ> for all composites are in the range 0<λ<1 and lie in the restrictions of McCullough's model [243]. Figure 19 shows the variation in conductivity values measured using: (a) CA-AFM (curve 1), (b) 2-point DC method (curve 2), (c) McCullough's model (curve 3), and (d) with varying GNP loading (curve 4) [244]. The relationship between <λ> and $\sqrt{< \grave{a} >^2}$ is shown in Figure 20 [244]. The conductivities by CA-AFM and 2-point DC measurements are in accordance. The conductivity of polymer at low GNP loading is close to that of dielectric polymer matrix as no continuous pathways of GNPs are available for conduction. The percolation threshold of 0.9 wt% is suggested by DC measurements and is corroborated by Scanning Electron Microscopy (SEM) and CA-AFM. At the percolation threshold marked by DC measurements, the conductivity increases sharply by five orders of magnitude. This can be explained by the presence of

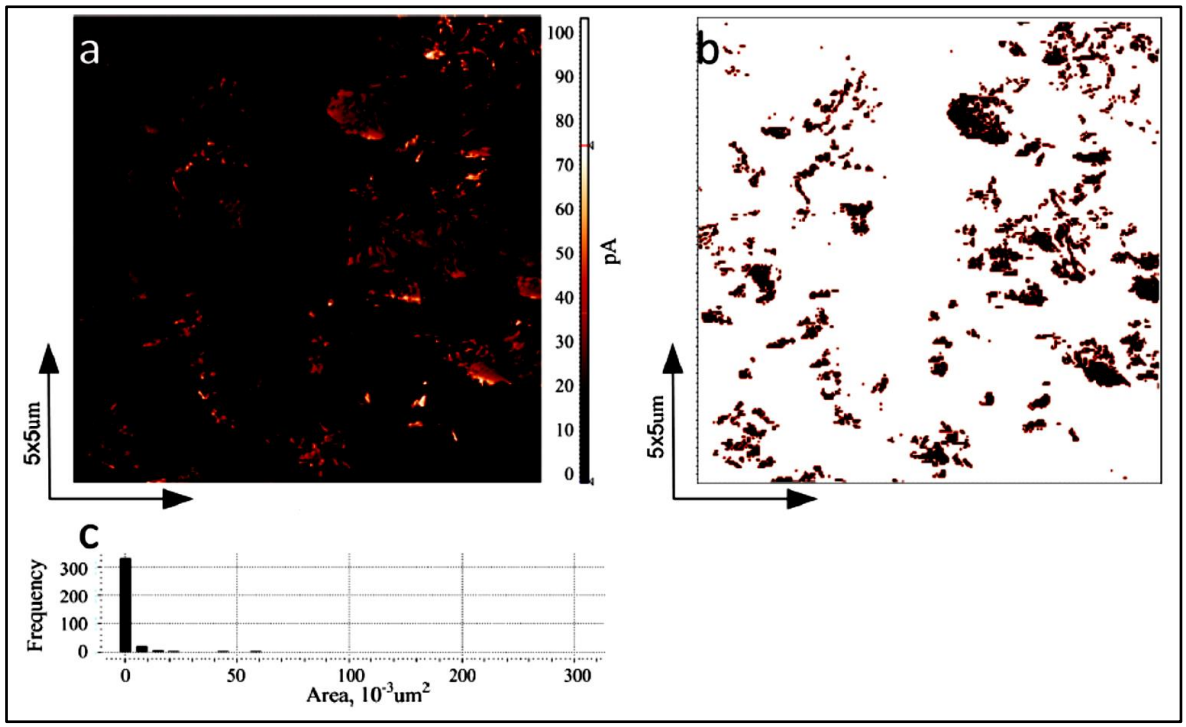

Figure 18: An overview of the process of cluster analyzing: (a) CA-AFM image of the GNPs/PS composite, the scan size in 5×5 µm, (b) the corresponding image of the grains, (c) the histogram presenting a size distribution of the GNPs clusters [244].

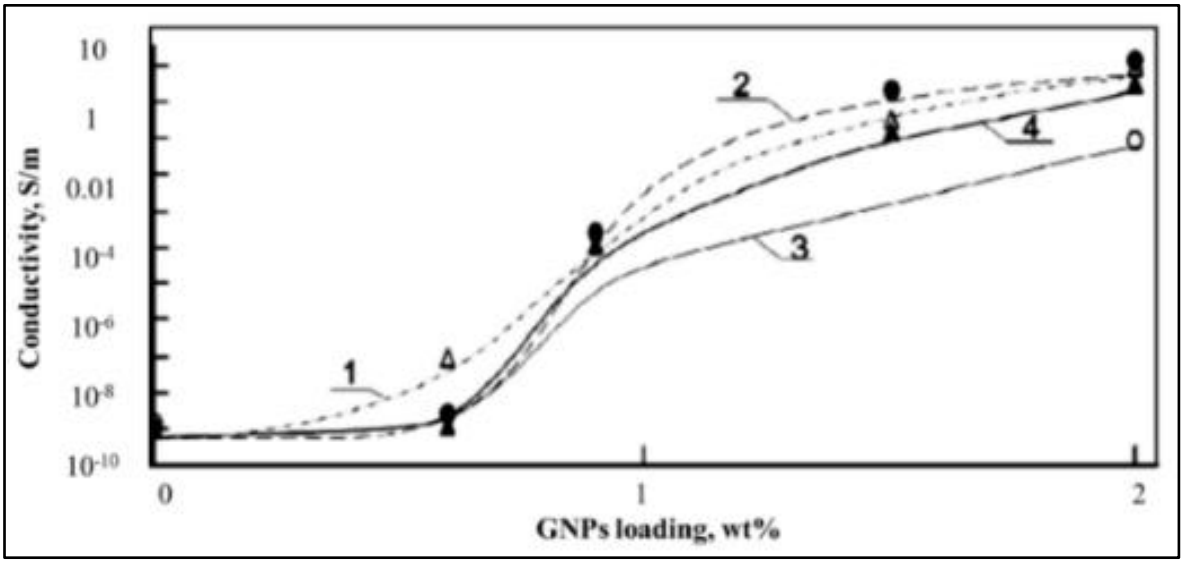

Figure 19: The experimentally obtained dependencies of the conductivity of the GNPs/PS nanocomposite via GNP loading obtained via CA-AFM (curve 1) and macro conductivity measurements (curve 2) and a comparison with the McCullough's model (curve 3) and the developed model (curve 4) [244]**.**

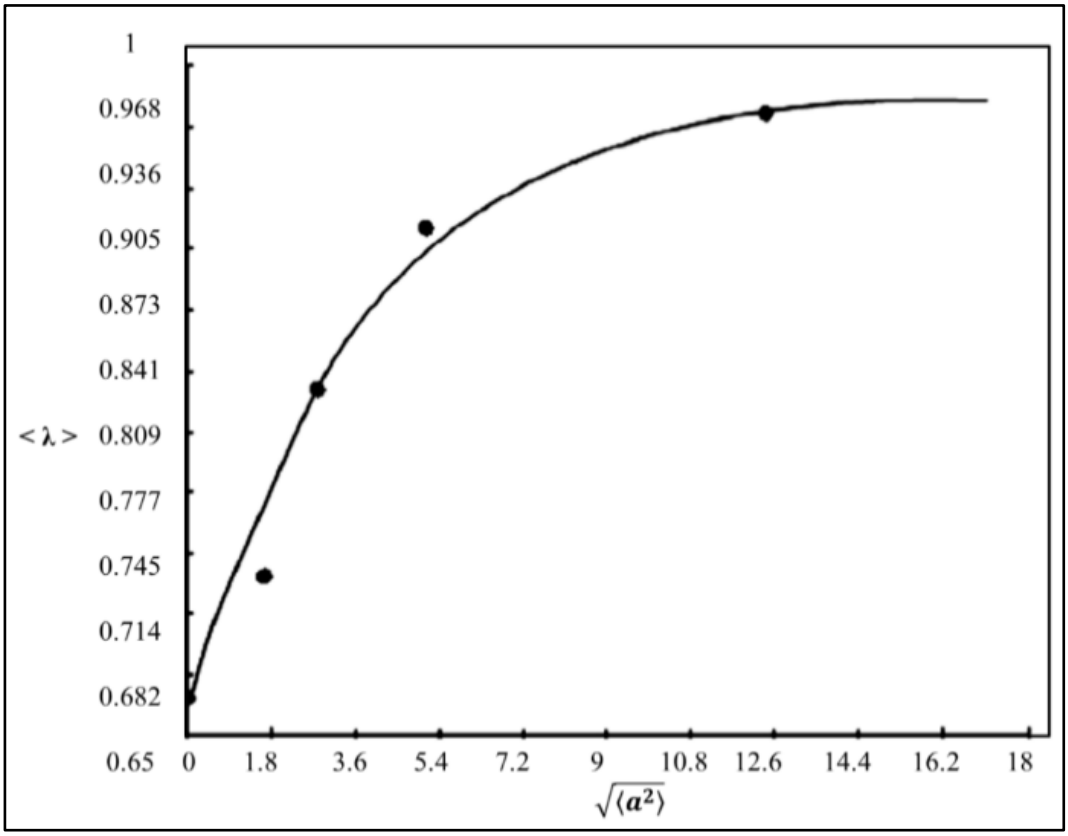

Figure 20: The dependence of the average chain parameter on the mean-square value of the aspect ratio [244]**.**

microscopic conductive sub-networks of GNPs. However, these sub-networks do not create continuous network. Therefore, these sub-networks are not initially detected by DC measurements until a continuous network is established. The network if nanofiller is defined by the dispersion state of the nanofiller in the polymer matrix. Therefore, a detailed analysis is required to study various factors that can influence the dispersion state of nanofillers. The next chater discusses about the reasons and remedies of nanofillers (MLG and CNT) in polymers.

The tribological protection of stiff technical polymers, such as epoxy, is finding proliferating interest to employ them in mechanical engineering applications [291–295]. To grasp phenomenological understanding of tribology and fracture mechanics, it is of foremost importance to study the interplay between surface roughness features and bulk properties [296]. To improve the wear resistance of monolithic polymers, surface coatings are applied. It is because the preferential growth of crystallites in subsequent deposition closes the cracks and gives the option to tailor the surface roughness features as per the design/service requirements [297–300]. Various coating techniques include galvanic/electrochemical deposition and plasma and thermal spraying that can yield thick coatings of high load support [301].

Although efficient adhesion strength between coating and substrate may be achieved in as-coated samples, however, delamination takes place when subjected to external loading. It is because the coatings have too high stiffness and too low plastic deformability to follow the substrate deformation. This disparity may be exacerbated in the presence of thermal stresses or elevated temperatures due to disparate coefficient of thermal expansion (CTE) of coating and the substrate. For example, epoxy may show ten times more thermal expansion than most of the thin film materials studied [301]. Alternatively, polymer

coatings on polymer substrate may have comparable stiffness and CTE; however, they fail in tribological applications. Therefore, even if coated, it is highly likely that the polymers will suffer from wear in applications where sliding contact is inevitable. Hence, it becomes essential to study the behavior of monolithic polymers for tribological applications. The tribology primarily deals with the surface condition and topography.

The various features of topography include: (1) surface roughness, (2) surface waviness, (3) surface form, and (4) lay, as shown in Figure 21 [302]. As various factors influence surface roughness features, therefore it is conventional to study them separately during the analysis. In general, component performance related to topography (e.g., friction reflectivity, wear characteristics, lubrication properties, and resistance to stress failure) is studied evaluating the surface roughness parameter. And component performance related to abrasive tool (e.g., vibration or noise generation) is studied by analyzing the surface waviness parameter [302].

The topography is not only important in monolithic polymers, but also in case of Polymer Matrix Composites (PMCs) [303–305]. Epoxy is an excellent matrix for composites because of its many features superior to that of competition including but not limited to handling characteristics, improvement in composite mechanical properties, acceptable cost, and processing flexibility [1]. A plethora of research has been dedicated to improve the performance of polymer nanocomposites. Gao et al. have shown that interfacial interactions and mechanical properties of carbon fiber-epoxy composites can be improved by increasing the surface roughness of the filler [306]. They also showed that surface roughness in a few tens of nanometer scale does not contribute significantly in increasing the interfacial adhesion from the “mechanical interlocking” [306]. Surfaces can be made rough or porous to enhance the extent of mechanical interlocking [302]. Karger-Kocsis et

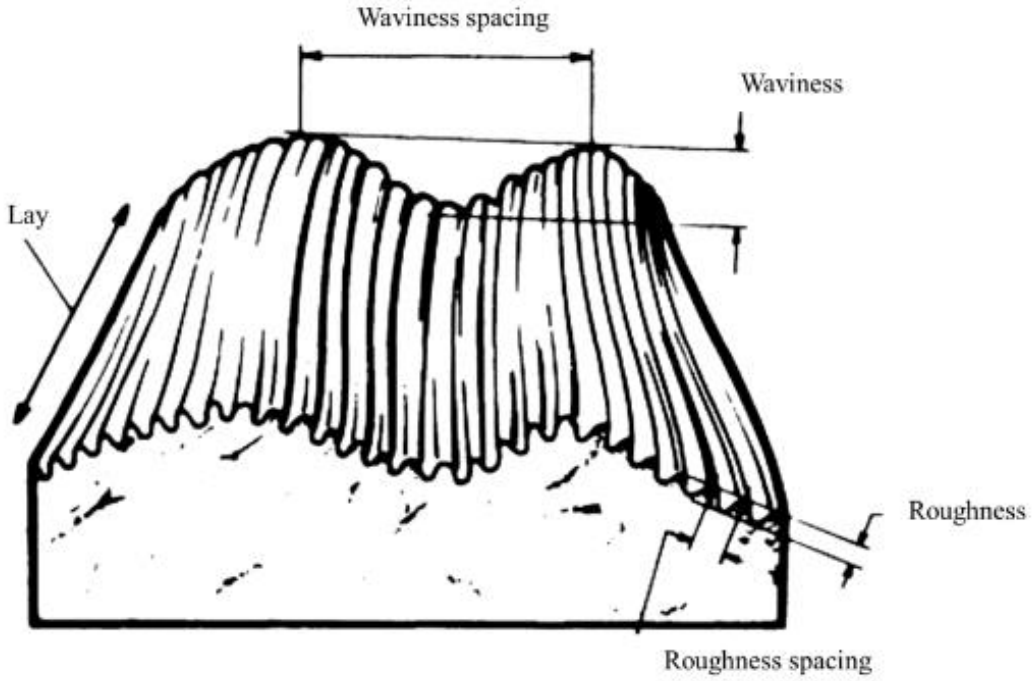

Figure 21: Illustration of the roughness, waviness, and general form of a surface [302].

al. have reported that hierarchical and hairy fillers have high surface area and capillary wetting by the polymers [307]. The textured fillers also exhibit mechanical interlocking with the polymers and cause local reinforcement of the fiber-matrix interphase [307]. Moon and Jang studied the mechanical interlocking and wetting at the interface between argon plasma treated ultra-high modulus polyethylene (UHMPE) fiber reinforced vinylester resin composite [308].

They observed a significant increase in interlaminar shear strength. It has been shown that plasma etching of UHMPE produces micro-pittings on fiber surface and this spongy surface structure helps improve mechanical interlocking with the polymer matrix and causes a significant increase in interlaminar shear strength [309–312]. The topography can be controlled during synthesis such as using a combination of UV lithography and electro-deposition [313]. The surface roughness features may also be tailored by texturing the mold surface when the production route is the casting.

Any regular or irregular spacing on the surface tend to form a texture or pattern [302]. The surface textures are formed during the casting, manufacturing, or machining processes. Another important factor is microstructure of the material as internal stresses, released after machining, can also contribute to surface deformation, and may form a specific topography. The machining processes can significantly influence the topography. A major factor is the action of the abrasive tool on the material. Elements such as tool speed, feed, shape, and cutting fluids can affect the topography. Other influential factors can be instability of the abrasive tool due to chatter or imbalance in the grinding wheel, and errors in the machine tool guideway [302]. In next chapter, mechanical properties of nanoclay-MLG-EP nanocomposites with modified surface roughness are discussed.

Chapter-2

Influence of Macro-Topography on Damage Tolerance and Fracture Toughness of MLG-Nanoclay-Epoxy Nanocomposites

---

17 Abstract

Influence of surface roughness features on mechanical properties of MLG-nanoclay-epoxy samples has been studied. The surface roughness features studied include waviness (W_a), roughness average (R_a), root mean square value (R_q), and maximum roughness height (R_{max} or R_z). The R_z of as-cast monolithic epoxy samples was 13.93 µm. By treating with velvet cloth, the R_z value significantly decreased to 2.28 µm. The R_z value of samples treated with abrasive paper 1200P was 4.85 µm which is also lower than that of as-cast samples. However, R_z values significantly increased by treating with abrasive papers 320P and 60P and became 20.32 µm and 39.32 µm, respectively. It is interesting to note that although R_a, W_a, and R_q, all increased by treating the samples with abrasive paper 1200P, however, R_z decreased by abrasive paper 1200P. A weight loss of up to 17% was observed in the samples after the treatment with the abrasive papers. Both V-shaped and U-shaped notches were produced on the surfaces of the samples. The mechanical properties were significantly degraded due to surface notches mainly because of the associated stress concentration effect.

Keywords: Surface roughness; fracture toughness; MLG-nanoclay-EP; mechanical properties.

18 Introduction

The primary reason to study the surface roughness features is to try to forecast the performance of the system. For example, the surface of a bearing should be textured such that it allows lubricant to be retained in small pockets and at the same time allows the bearing movement with a minimum of friction. If the surface has high roughness, wear will be expedited; however, if the surface has low roughness, poor lubrication and seizure may take place. Therefore, a compromise between smoothness and roughness is essential to maintain. The other reason to measure the surface roughness features is to control the manufacturing process as the operator can detect variation in surface finish and adjust the controllables to ensure that the process remains in limit [302].

A simple and common method to measure surface roughness features is the surface texture recorder whose principle is schematically shown in Figure 22 [302]. The stylus is moved across the surface with the help of a guiding mechanism to produce the "traced profile," which is produced by the interaction of the stylus with the surface of the sample. The transducer generates a signal which is produced from the difference between a "reference profile" or "datum profile" and the traced profile. The transducer signal is converted into a digital signal using an analog-to-digital converter. At this point, the transducer contains only the vertical or Z-component of the profile. The traversing component generates the

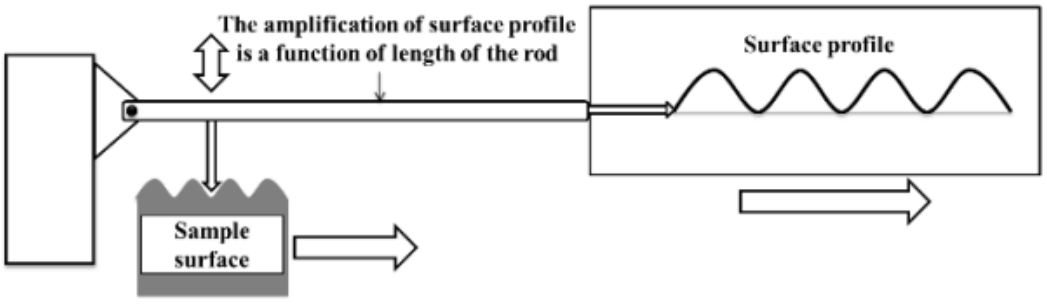

Figure 22: Basic principle of a surface texture recorder.

horizontal or X-component which is combined with the Z-component to acquire the “total profile.” The total profile is then filtered to omit unnecessary information which generates a “primary profile.” The filtering techniques can further be employed to separate the waviness, roughness, and form features of the surface [302].

For effective analysis of surface roughness features, the obtained profile needs to be analyzed according to internationally recognized mathematical formulae which are called parameters. A certain number can be given to a certain aspect of surface roughness features to compare it with another pattern or reference and to remove the need for subjective operator assessment. A single parameter is not enough to characterize the surface roughness completely. Therefore, multiple parameters are usually used.

The parameters can be divided into four basic types: (1) Amplitude parameters measure the vertical characteristics of topography. (2) Spacing parameters measure the irregularity spacings along the surface, regardless of the amplitude of these irregularities. (3) Hybrid parameters measure a combination of the spacing and amplitude of the surface irregularities. (4) Extended parameters are not only defined by the profile data and require further attributes or inputs [302]. The most common use of engineering surfaces is to provide a bearing surface for another component moving relative to it, resulting in wear. The material ratio (Figure 23) parameter T_p (in %) is commonly used to study the effect of wear on a surface [302]. Material ratio is defined as the ratio of the length of the surface to the evaluation length at a specified depth in the profile [302]. The parameter T_p can thus be used to control bearing surfaces as well as surfaces requiring lubrication [302].

The damage tolerance is the ability of a critical structure to withstand a level of service or manufacturing-induced damage or flaws while maintaining its function [1]. The damage tolerance of aircraft components is necessarily studied to avoid any catastrophic in-flight

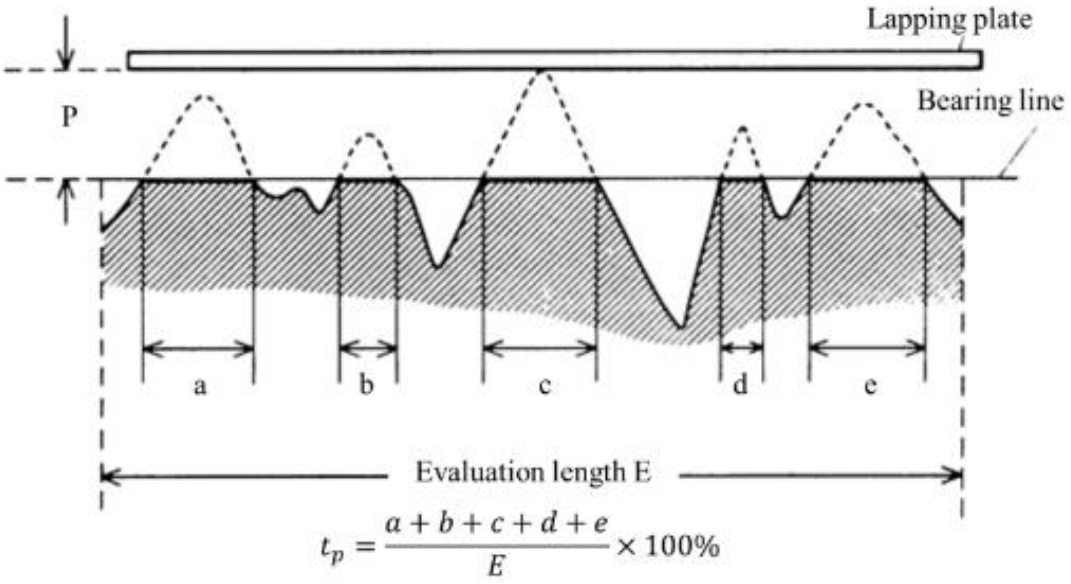

Figure 23: Illustration showing the derivation of material ratio, T_p [302]**.**

failure. The damage tolerance tests ensure that the component under inspection does not undergo functional impairment during its service life or within the duration between two scheduled maintenances. The functional impairment is defined as the presence of damage in a part that requires maintenance action [1]. The PMCs have found extensive applications in aerospace, automotive, and construction owing to ease of processing and high strength to weight ratio which is an important property required for aerospace applications [16]. Among different polymers, epoxy is the most commonly used thermosetting polymer matrix in PMCs [1].

In current study, epoxy was reinforced with nanoclay/MLG and surface roughness of produced nanocomposites was varied by treating with abrasive papers of different surface roughness values. An Alicona optical microscope was used to study the surface roughness values of produced samples. The mechanical and dynamic mechanical properties of produced samples were studied. The results showed that surface roughness can significantly influence the above-stated properties of MLG/nanoclay/epoxy samples.

19 Experimental section

19.1 Materials

Bisphenol A-epichlorohydrin based epoxy having density of ~1.3 g/cm^3 and dimethylbenzylamine isophorone diamine based low viscosity fast curing hardener with ~1.1 g/cm^3 density were used in current study. The epoxy matrix used consisted of EPOPHENTM EL5 bisphenol A based liquid epoxy and EPOPHENTM EHA57 diamine hardener, purchased from Polyfibre, UK. This epoxy system is a multi-purpose resin offering good all-round properties with the epoxy group content of 4.76-5.25 mol/kg. The viscosity of liquid epoxy and hardener are 12000-15000 cps and 45 cps at room temperature, respectively. To prepare monolithic epoxy samples, the mix proportions are 50 parts by weight of hardener to 100 parts by weight of liquid epoxy. The gelation time of the resin was 43 min at room temperature.

MLG of 12 nm average thickness and 4.5 µm average lateral size with specific surface area of 80 m^2/g and purity 99.2% was purchased from Graphene Supermarket. Halloysite nanoclay was used as second filler and purchased from Sigma-Aldrich. The diameter is between 30-70 nm with length 1-4 µm and has a tube-like morphology. The density of halloysite nanoclay is 2.53 g/cm^3 and surface area is 64 m^2/g. It has low electrical and thermal conductivities and strong hydrogen interactions, on account of which the inner hydroxyl groups show greater stability than the surface hydroxyl groups in halloysite. The tube-like morphology, high aspect ratio, and low percolation make halloysite nanoclay a potential reinforcement for epoxy and other polymers.

19.2 Samples production

The fillers were dispersed in resin using tip sonication for 3 h. The sonication was carried out using tip sonicator of power 750 W and frequency 250 kHz (Vibra-cell model VC 750, USA). The operation mode was 70% power with 10 s vibration and 5 s break. Although the sonication was carried out at room temperature, however, temperature of the system rose due to high energy vibration produced by tip sonicator. The epoxy and hardener were degassed separately for 1 h. The two parts were mixed in epoxy: hardener ratio of 2:1. Following thorough hand mixing for 10 min, vacuum degassing was again carried out for 15 min. The resin was poured into silicone molds (without any release agent) and cured at room temperature for 6 h followed by post-curing at 150 °C for overnight to ensure completion of the crosslinking. The top and bottom surfaces of each sample were treated with abrasive papers for 1 min on rotating wheels at rotational speed of 150 rpm.

19.3 Characterization

The densification of samples was calculated according to ASTM Standard D792. The densities of epoxy, hardener, and water were, 1.3, 1.1, and 0.9975 g/cm^3, respectively. Experimental density and densification were calculated using Eqs. (1) and (2), respectively.

$$Experimental\ density = \frac{Weight\ in\ Air}{Weight\ in\ Air - Weight\ in\ Water} \times Density\ of\ water \quad \textbf{(1)}$$

$$Densification\ (\%) = \frac{Experimental\ Density}{Theoretical\ Density} \times 100 \quad \textbf{(2)}$$

Vickers microhardness test was conducted using Buehler Micromet II to determine the hardness values of the samples. The load applied was 200 g for 10 seconds. Tensile, three-point bending, and fracture toughness tests were conducted using Instron Universal Testing Machine (Model 3382). The displacement rate was kept 0.5 mm/min for tensile

and fracture toughness tests and 1 mm/min for three-point bending test. Five specimens were tested for each composition. The schematics of the specimens are shown in Figure 24.

Tensile properties were measured according to ASTM D638 Type-V geometry with specimen thickness 4 mm. Three-point bending test was conducted according to ASTM D790 with specimen dimensions 3 × 12.7 × 48 mm. A single-edge-notch three-point bending (SEN-TPB) specimen was used to determine mode-I fracture toughness (K_{1C}) according to ASTM D5045. The specimen dimensions were 3 × 6 × 36 mm with a crack of length 3 mm. The notch was made at the mid of sample and tapped to sharpen by a fresh razor blade. The K_{1C} was calculated using Eq. (3),

$$K_{1C} = \frac{P_{max} f\left(\frac{a}{w}\right)}{BW^{1/2}} \quad \textbf{(3)}$$

where, P_{max} is maximum load of load-displacement curve (N), f(a/w) is constant related to geometry of the sample and was calculated using Eq. (4), B is sample thickness (mm), W is sample width (mm), and a is crack length (kept between 0.45W and 0.55W). The critical strain energy release rate (G_{1C}) was calculated using Eq. (5) where E is the Young's modulus obtained from the tensile tests (MPa), and ν is the Poisson's ratio of the polymer, taken to be 0.35.

$$f(a/w) = \frac{\left[\left(2+\frac{a}{w}\right)\left\{0.0866+4.64\left(\frac{a}{w}\right)-13.32\left(\frac{a}{w}\right)^2+14.72\left(\frac{a}{w}\right)^3-5.6\left(\frac{a}{w}\right)^4\right\}\right]}{\left(1-\frac{a}{w}\right)^{3/2}} \quad \textbf{(4)}$$

$$G_{1c} = \frac{K_{1c}^2(1-\nu^2)}{E} \quad \textbf{(5)}$$

Charpy impact toughness test was carried out according to ASTM D6110 using notched specimen with dimensions 3.2 × 12.7 × 64 mm. A V-notch (45°) was made in the middle

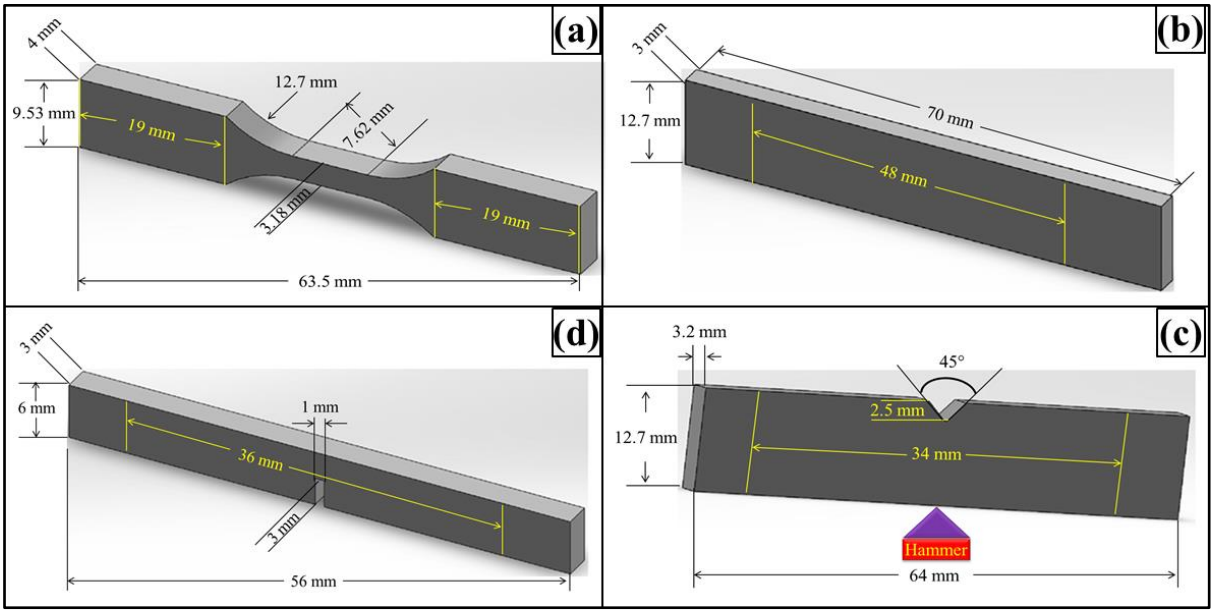

Figure 24: Schematics of mechanical test specimens: (a) tensile, (b) three point bend, (c) fracture toughness, and (d) Charpy impact toughness test specimens.

of the specimen whose depth was 2.5 mm and tip of radius 0.25 mm. The specimen was placed as simply supported beam and hit by hammer from behind the notch. The impact toughness was calculated using Eq. (6),

$$Impact\ toughness = \frac{mgh(\cos\beta - \cos\alpha)}{wt} \quad \textbf{(6)}$$

where, m is hammer mass (kg), g is standard gravity (9.8 m/s^2), h is length of hammer arm (m), β is hammer swing up angle after test piece breaks (rad), α is hammer lifting up angle (rad), w is sample width (mm), and t is sample thickness (mm).

An Alicona Infinite Focus optical microscope (G4) was used to generate optical micrographs and measure topographical features. The Alicona optical microscope is a non-contact method (focus-follow method) for topography measurement. The focus-follow method (Figure 25) involves the use of a moving lens which keeps a spot of light focused on the surface. The vertical movement of the lens is controlled by an electric motor and correlates to the surface profile [302]. The analog electrical signal is generated to drive the

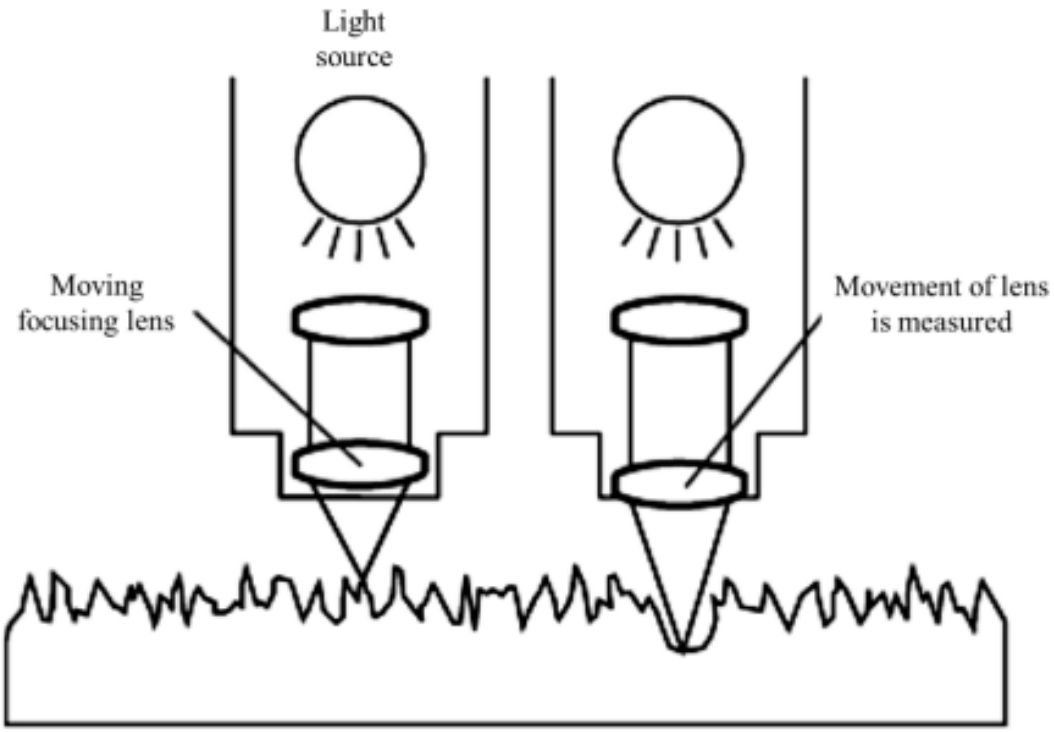

Figure 25: Focus-follow method for non-contact measurement of roughness [302]**.**

motor which is then digitized and processed in the same manner as a contact stylus. A separate transducer may also be used to monitor the position of the lens. Non-contact techniques are getting increasingly popular to measure topographical features, especially for surfaces that may be subject to damage using contact techniques. The results obtained are very similar to those of stylus techniques and can use the same parameter definitions. Some non-contact techniques, such as diffraction measurements, can measure topographical features easily and quickly and can potentially be used on the machining tool.

The non-contact methods have certain limitations. For example, in high slope surfaces, an insufficient intensity of light reaches the detector and the focus lens begins to follow inaccurately. In addition, when the contaminated surfaces are studied, the contamination is measured as part of topographical features as there is no external agency to remove the contaminations from the surface [302]. Considering these limitations, it was ensured that

samples are placed flat and surface is clean to obviate any artefacts in surface roughness profiles.

DMA (Model 8000, PerkinElmer) was used to determine dynamic storage modulus (E'), and loss modulus (E") of the samples. The loss factor (Tanδ) was calculated as the ratio (E"/ E'). Rectangular test specimens of dimensions 2.5 × 8 × 30 mm were used with a single cantilever clamp. All tests were carried out by temperature sweep method (temperature ramp from 30 °C to 180 °C at 5 °C/min) at a constant frequency of 1 Hz. The maximum force of DMA was 10 N and applied during all tests. The glass transition temperature (T_g) was taken as the temperature value at the peak of Tanδ curves. Scanning electron microscopy analysis using a SEM FEI Quanta 200, was carried out of the fractured surfaces of tensile specimens to evaluate the fracture modes in the samples. The fractured portions were cut from the specimens and a layer of gold was applied using Emscope sputter coater model SC500A.

20 Results and discussion

The SEM images of MLG and nanoclay are shown in Figure 26. Due to wrinkled structure of MLG, stronger interfacial interactions may be expected with MLG than with the smooth tubular structure of nanoclay. The SEM images of abrasive papers are shown in Figure 27. SEM images of velvet cloth (Figure 27a-c) show that fibers are vertically aligned with localized intermingling of the fibers. The individual fiber consists of multiple small fibers stacked together (Figure 27c). The abrasive particles on abrasive paper 1200P (Figure 27d-f) are relatively smaller in size and nearly uniformly dispersed with small debris spread on the surface. The abrasive particles on abrasive paper 320P (Figure 27g-i) are relatively coarser in size than that of abrasive paper 1200P. The individual particles have rough

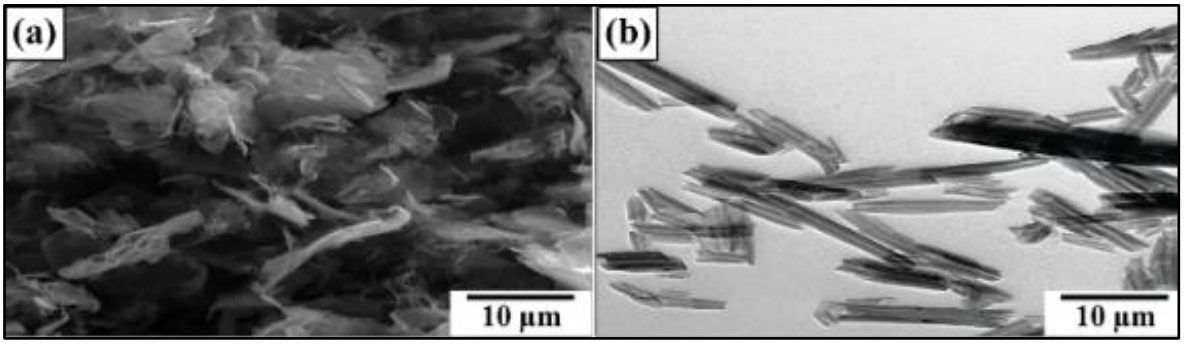

Figure 26. SEM images: (a) MLG, and (b) nanoclay.

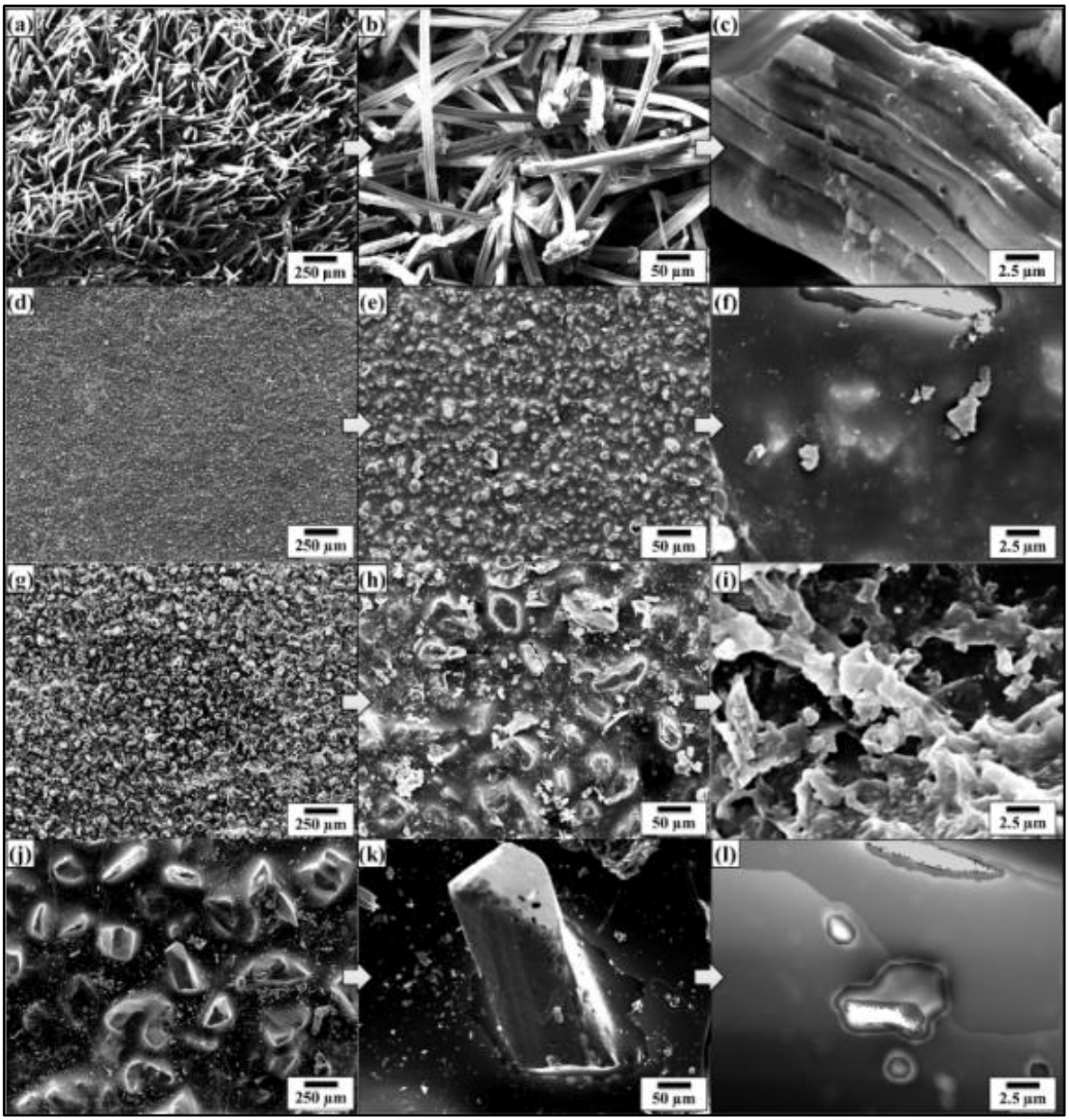

Figure 27: SEM images of abrasive papers: (a-c) Velvet cloth, (d-f) 1200P, (g-i) 320P, and (j-l) 60P.

geometry (Figure 27i). Therefore, surface roughness on the treated samples should be expected of very wide size distribution. The abrasive particles on abrasive paper 60P (Figure 27j-k) are the largest in size with sharp edges (Figure 27k) like a machining tool. Therefore, the coarsest surface roughness should be expected in samples treated with abrasive paper 60P.

The Energy Dispersive Spectroscopy (EDS) spectrum of abrasive paper is shown in Figure 28. The peak at 0 keV represents noise. The peak at 1.7 keV represents gold (Au) which comes due to the sputter coating of gold layer on the sample. The highest peaks are of C, Si, and O which show that the abrasive papers primarily consist of SiC and certain amount of oxides. The abrasive paper is produced by a high temperature reaction between SiO_2 and C producing SiC and unreacted Si, C, and O. Besides, Ca and Cu peaks are also observed which may be the constituents of the glue used to fix the abrasive particles on the surface.

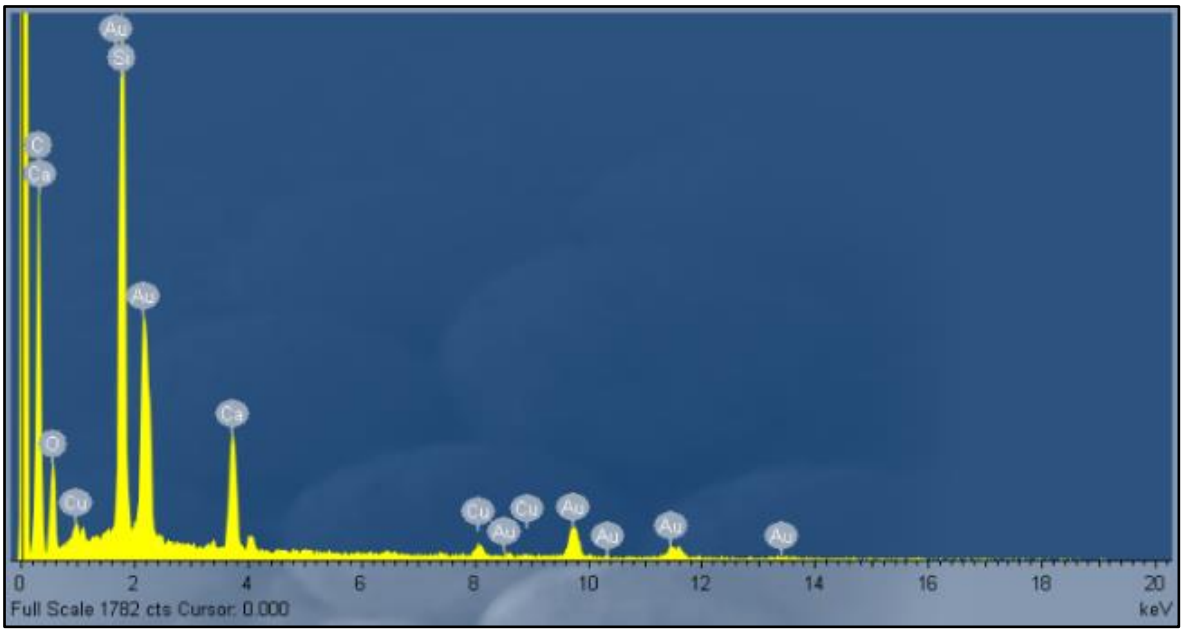

Figure 28: EDS spectrum of abrasive paper.

The variation in weight loss in MLG-nanoclay-EP samples when treated with abrasive surfaces of varying surface roughness values is shown in Figure 29 (a). The weight loss significantly increased as the coarseness of the abrasive paper increased. The values shown are the average of 20 different samples. A relatively large standard deviation was observed. This scatter can be attributed to the non-uniform surface roughness of the abrasive paper. It is because the abrasive particles were of different morphology as shown in Figure 29 (b). This scatter would be helpful in producing some useful results as the in-service components also come in contact with surfaces having non-uniform surface roughness. In addition, when the epoxy is cast in machined mold or cavity, the mold or cavity also contains corrugations of varying depth and shape due to machine vibrations and possible wobbling of the machining tool.

The surface roughness features of the samples were measured using an Alicona optical microscope. The 3D images of abrasive papers and their surface roughness values are shown in Figure 30. Surface roughness refers to high frequency irregularities which are produced when the sample is exposed to abrasive tool [302]. The surface roughness values significantly increased from abrasive paper 1200P to abrasive paper 60P. The surface

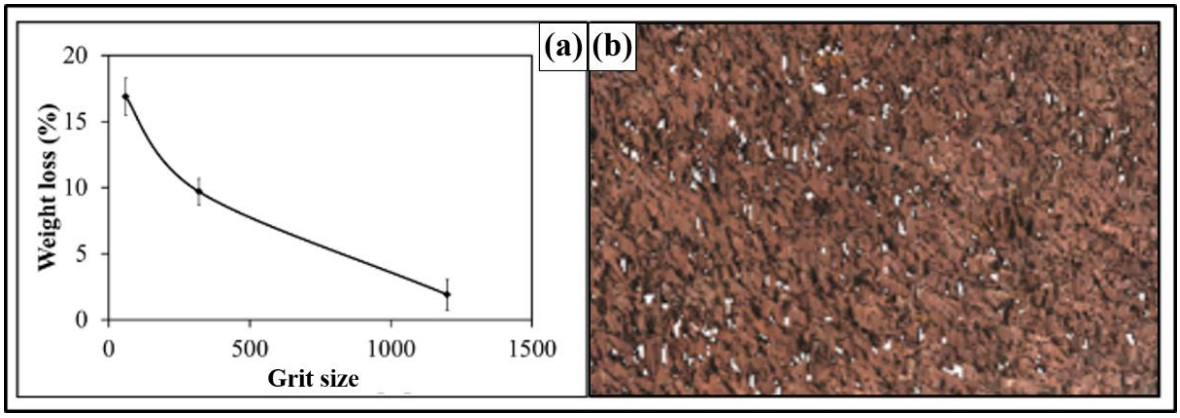

Figure 29: (a) Weight loss (%) in MLG/nanoclay/EP samples after treatment with abrasive papers for 1 min at 150 rpm. (b) Optical micrograph of velvet cloth.

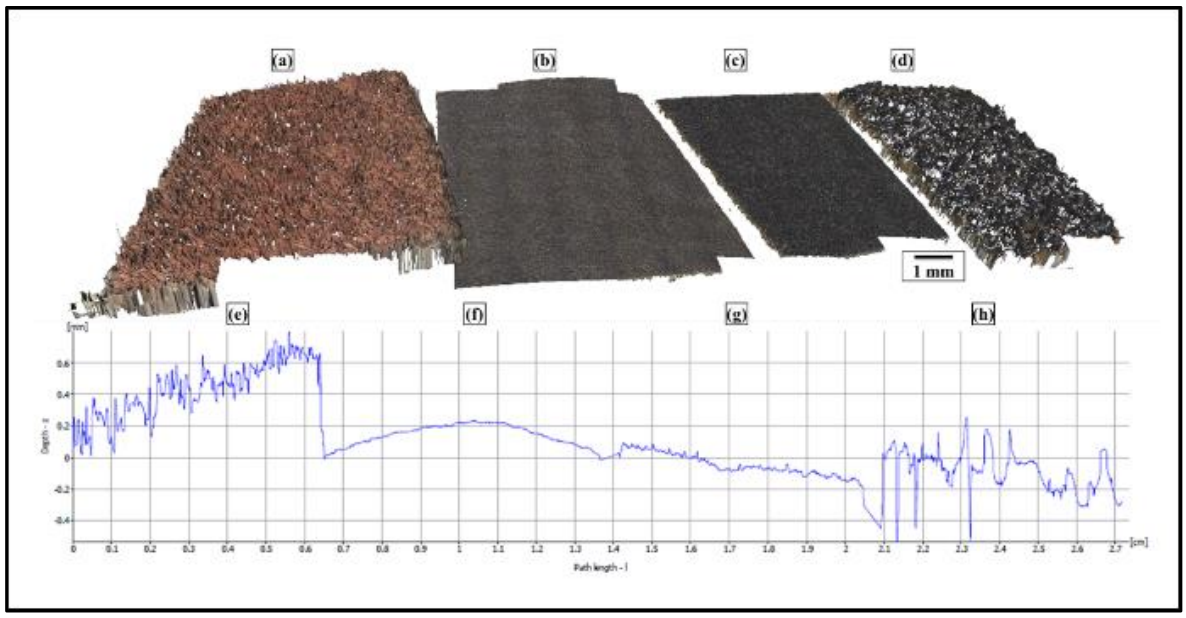

Figure 30: 3D images of abrasive papers: (a) Velvet cloth, (b) 1200P, (c) 320P, and (d) 60P, with corresponding surface roughness shown in (e-h), respectively.

roughness of velvet cloth is also very high. However, it should be noted that the velvet cloth is soft, and therefore, its impression on the sample will be the softest. Hence, minimum surface roughness is expected on the samples treated with the velvet cloth. The other three abrasive papers are hard and would leave the impression on the samples commensurate with the actual surface roughness of the abrasive papers.

The topographical features of abrasive papers are summed up in Figure 31. Surface waviness refers to the medium-frequency irregularities on the sample surface with wave-like structure comprising of series of crests and toughs [302]. Surface waviness is produced by errors in the machine tool guideway and/or the instability of the abrasive tool [302]. The waviness (W_a) of velvet cloth was 1.44 µm. By treating with velvet cloth, the W_a value decreased to 1.40 µm. The W_a value of abrasive paper 1200P is 1.07 µm. The abrasive papers 320P and 60P have W_a values of 1.68 µm and 1.33 µm, respectively.

A similar trend was observed in case of surface roughness (R_a). The R_a is defined as the mean height of the roughness profile and is superimposed on the surface waviness [302]. The R_a is one of the most commonly used roughness amplitude parameters. It assesses the coarseness of the surfaces such as those produced by turning, milling, and grinding operations. The R_a value of velvet cloth was 0.88 µm. The R_a value of abrasive paper 1200P was 0.71 µm. The abrasive papers 320P and 60P had R_a values of 2.84 µm and 5.78 µm, respectively.

As the averages of numbers 2 & 4 and 1 & 5 are the same, similarly, being an average value, R_a therefore cannot give accurate information about the topographical features. The disparate profiles can have the same R_a value and yet have very different performance characteristics [302]. Another average parameter, R_q states the root mean square of the profile and is more sensitive to surface variation [302]. The R_q value of velvet cloth was 1.2 µm. The R_q value of abrasive paper 1200P was 0.87 µm. The abrasive papers 320P and 60P had R_q values to 4.12 µm and 7.44 µm, respectively.

The maximum roughness height is another important parameter and was varied by treatment with abrasive papers. Sometimes, it becomes desirable to specify the maximum roughness height (R_{max}) or peak-to-valley height (R_z), rather than using R_a [302]. The R_z parameter measures the highest and lowest points of the profile and is valuable when products are subject to elevated stresses. Any large peak-to-valley heights may be areas likely to suffer from crack propagation due to stress concentration and possible triaxial state of stress generated at the notch tip [302]. However, as R_z is very susceptible to scratches or dirt, it is an unstable parameter [302]. The R_z of velvet cloth was 103.52 µm. The R_z value of abrasive paper 1200P was 12.85 µm. However, R_z values were

significantly higher for abrasive papers 320P and 60P and recorded 52.32 µm and 103.46 µm, respectively.

The topographical details of abrasive papers are shown in Figure 32. Figure 32 (ai) shows the optical micrograph of velvet cloth where protruded fibers can be observed. Any black spots are artefacts in the optical images as these regions are either above or below the focus range. The fiber structure is more prominent in Figure 30 (a) with 3D image of the fibers. Due to the protruded fibers, the profile showed high waviness and surface roughness. The waviness of velvet cloth is shown in Figure 32 (aii). Although roughness amplitude is very important parameter, the spacing (waviness) of the roughness peaks can be equally important [302]. The upper bound of W_a is about ± 100 µm. The R_a of velvet cloth is shown in Figure 32 (aiii). The surface roughness alters abruptly between ± 100 µm. It is because the fibers of velvet cloth are oriented in random orientations. The Gaussian distribution of surface roughness of velvet cloth is shown in Figure 32 (aiv). The distribution shows typical bell-shaped curve that indicates that surface roughness is varied and most of the surface roughness values are concentrated between ±100 µm with the maximum extension up to ±120 µm. The roughness profile of complete velvet cloth sample, as shown in Figure 30 (a), was determined and is shown in Figure 32 (av). The distribution shows that R_z is about ±120 µm.

The optical micrograph of abrasive paper 1200P is shown in Figure 32 (bi). The abrasive particles are nearly uniformly distributed on the surface except a few rarefied regions. In addition, it was observed that the abrasive paper is not perfectly flat and contains waviness to a certain degree which is evident in Figure 32 (bii). The waviness varies between ±10 µm. Apart from waviness, the abrasive particles are also of non-uniform size which affects the surface profile as shown in Figure 32 (biii). The roughness alters sharply with distance

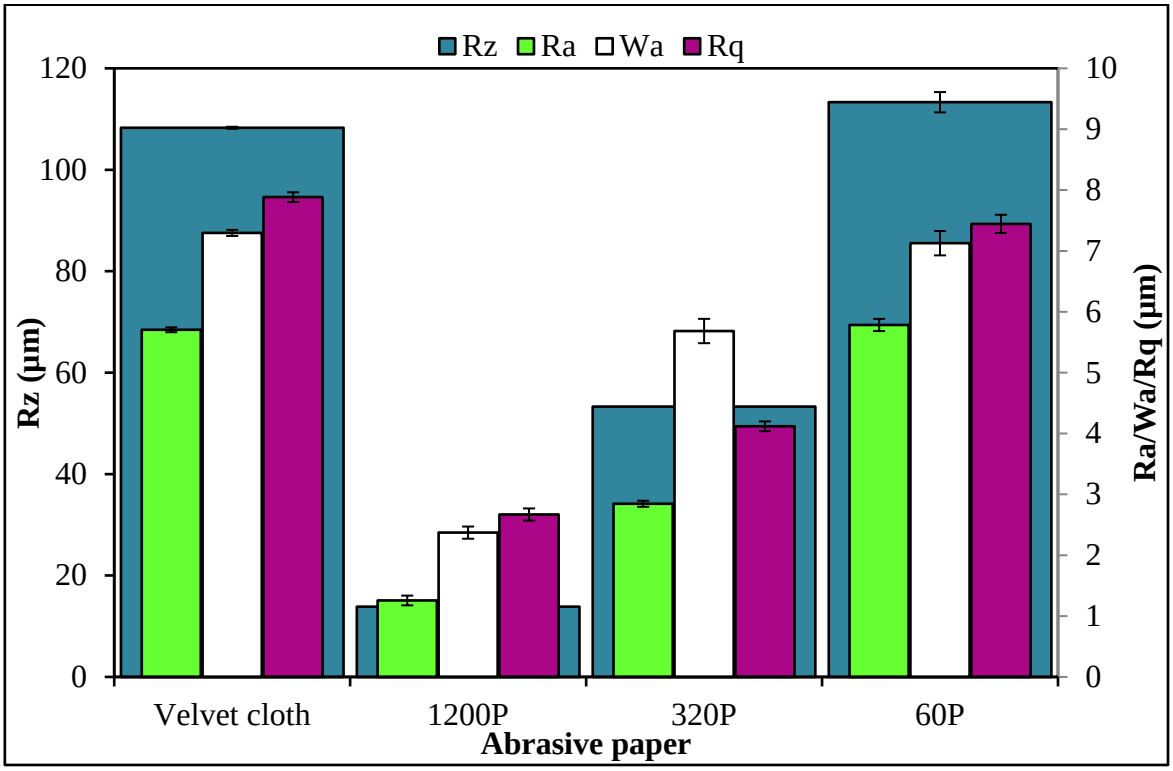

Figure 31: Surface roughness parameters of abrasive papers.

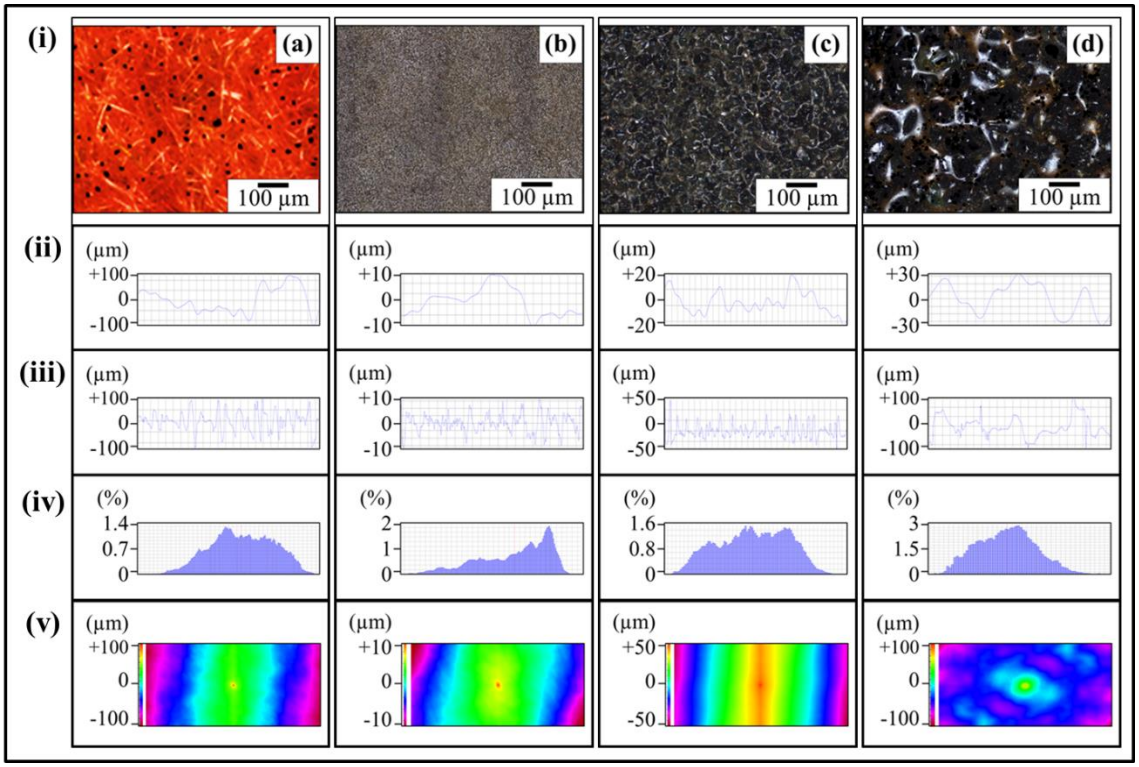

Figure 32: Topography profiles of abrasive papers: (a) Velvet cloth, (b) 1200P, (c) 320P, and (d) 60P. In all cases, (i) optical image, (ii) waviness, (iii) surface roughness of selected line, (iv) percentage vs. topographical dimensions, and (v) surface profile of selected rectangular specimen.

and lies in the range of ±10 µm. The Gaussian distribution of surface roughness of abrasive paper 1200P is shown in Figure 32 (biv). The roughness profile of abrasive paper 1200P is shown in Figure 32 (bv). A major fraction of roughness is ±13 µm. As the optical micrograph (Figure 32bi) showed that 1200P is not perfectly flat, this is also evident in roughness profile (Figure 32bv).

The optical micrograph of abrasive paper 320P is shown in Figure 32 (ci). The abrasive powder of relatively wide size distribution is nearly uniformly distributed over the surface. The waviness (Figure 32cii) varies between ±20 µm and roughness varies between ±50 µm to -20 µm. It can also be observed that certain roughness peaks (Figure 32ciii) are pointed and other are curved that show that certain particles are sharp and other angular. Using this roughness profile, samples can be produced containing V-shaped and U-shaped notches, simultaneously. As V-shaped notches have higher associated stress concentration effect at the notch tip than that of U-shaped notches, therefore, V-shaped notches will influence the mechanical properties more strongly than U-shaped notches. The Gaussian distribution of surface roughness of abrasive paper 320P is shown in Figure 32 (civ). There is large size distribution and maximum concentration of roughness values reaches up to 1.6%. The roughness profile of abrasive paper 320P is shown in Figure 32 (cv). There is large variation of particle size with no domination of one particular size.

The optical micrograph of abrasive paper 60P is shown in Figure 32 (di). The abrasive particles can clearly be seen being separated by a brown phase which can be the glue to adhere the particles with the surface. As the particle size is very large, large waviness and roughness are certain. The waviness varies between ±30 µm (Figure 32dii) and roughness varies between ±100 µm (Figure 32diii). The Gaussian distribution of surface roughness is shown in Figure 32 (civ). A typical bell-shaped curve is obtained with ends at ±110 µm.

The roughness profile of abrasive paper 60P is shown in Figure 32 (dv). A coarse profile is obtained due to large particle size. The R_z value goes as high as ±110 µm.

The surface roughness features of monolithic epoxy samples are summed up in Figure 33. The waviness (W_a) of as-cast monolithic epoxy samples was 1.44 µm. By treating with velvet cloth, the W_a value decreased to 0.3 µm. The W_a value of monolithic epoxy samples treated with abrasive paper 1200P increased to 2.37 µm. The abrasive papers 320P and 60P further increased the W_a values to 5.68 µm and 7.13 µm, respectively. A similar trend was observed in case of surface roughness (R_a). The R_a value of as-cast monolithic epoxy samples was 0.87 µm. By treating with velvet cloth, the R_a value decreased to 0.70 µm. The R_a value of monolithic epoxy samples treated with abrasive paper 1200P increased to 1.26 µm. The abrasive papers 320P and 60P further increased the R_a values to 2.84 µm and

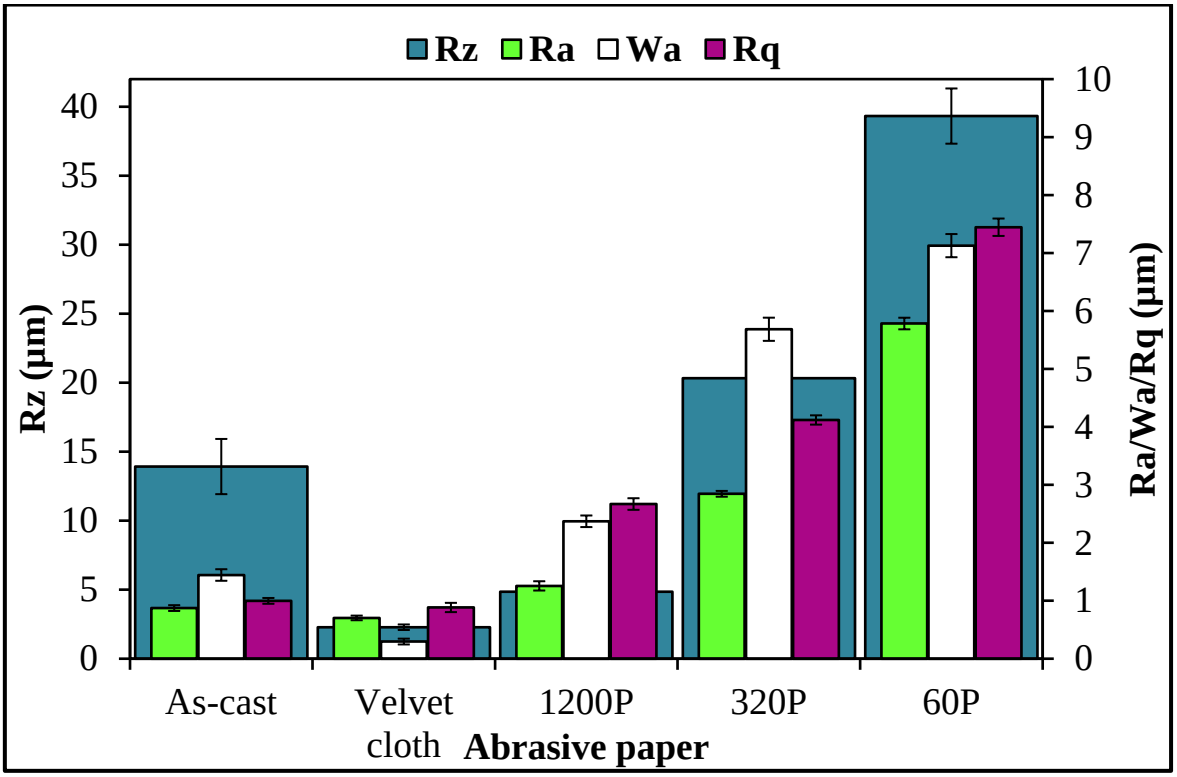

Figure 33: Surface roughness parameters of monolithic epoxy samples after treatment with abrasive papers for 1 min at 150 rpm.

5.78 µm, respectively.

The treatment of monolithic epoxy samples treated with abrasive papers also influenced the R_q values. The R_q value of as-cast monolithic epoxy samples was 1.0 µm. By treating with velvet cloth, the R_q value decreased to 0.88 µm. The R_q value of monolithic epoxy samples treated with abrasive paper 1200P increased to 2.67 µm. The abrasive papers 320P and 60P further increased the R_q values to 4.12 µm and 7.44 µm, respectively.

The R_z of as-cast monolithic epoxy samples was 13.93 µm. By treating with velvet cloth, the R_z value significantly decreased to 2.28 µm. The R_z value of monolithic epoxy sample treated with abrasive paper 1200P was 4.85 µm which is also lower than that of as-cast monolithic epoxy samples. However, R_z values significantly increased by treating with abrasive papers 320P and 60P and became 20.32 µm and 39.32 µm, respectively. It is interesting to note that although R_a, W_a, and R_q, all increased by treating the monolithic epoxy samples with abrasive paper 1200P, however, R_z decreased by abrasive paper 1200P.

The surface roughness features of 0.1 wt% MLG-EP nanocomposites are shown in Figure 34 and Figure 35. The roughness parameters were decreased by treatment with velvet cloth and 1200P while increased with 320P and 60P. Figure 35 (ai) shows the optical micrograph of as-cast 0.1 wt% MLG-EP sample. The waviness (Figure 35aii) of the sample varies between ±15 µm while the surface roughness (Figure 35aiii) varies between ±40 µm. This surface roughness is coming from the mold surface. The surface roughness graph shows that pointed notches of about 40 µm are present on the as-cast 0.1 wt% MLG-EP samples. The Gaussian distribution (Figure 35aiv) shows that the roughness size is distributed with dominant size fraction of 2%. The roughness profile (Figure 35av) shows that most of the roughness lies within ±40 µm with a deep notch (red region). (bi) shows

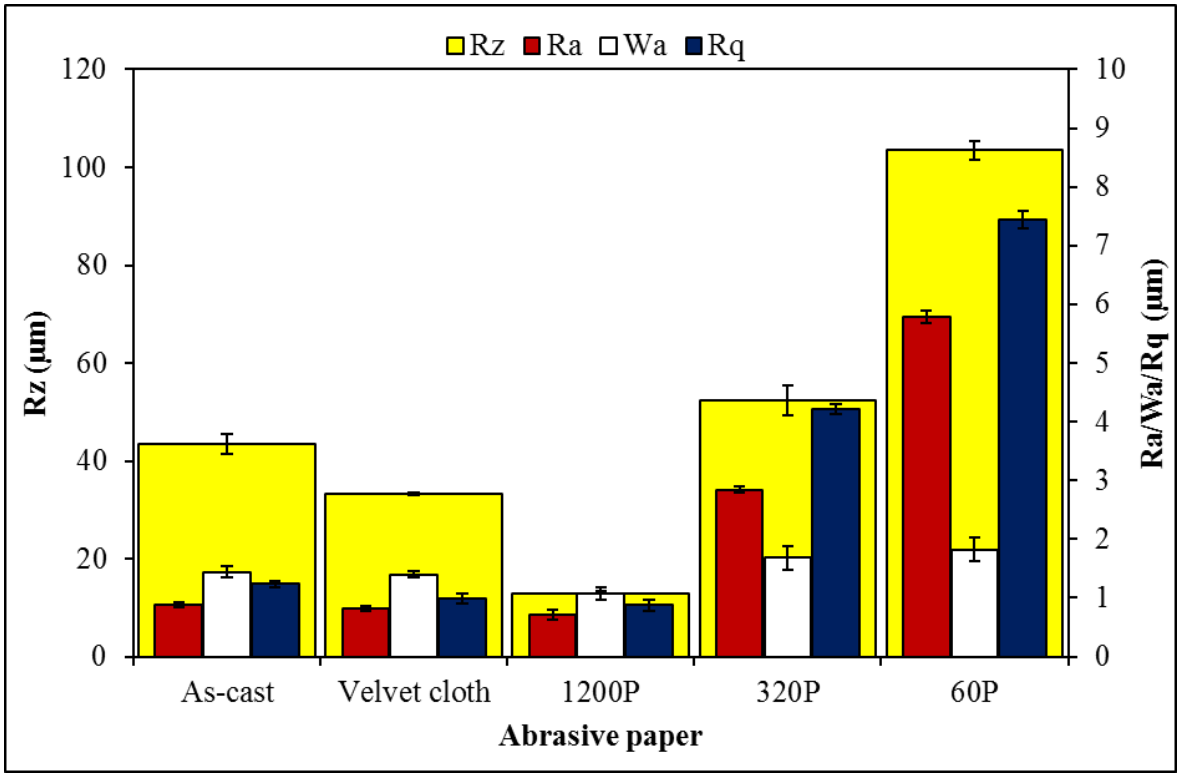

Figure 34. Surface roughness features of 0.1 wt% MLG-EP nanocomposites after treatment with abrasive papers for 1 min at 150 rpm.

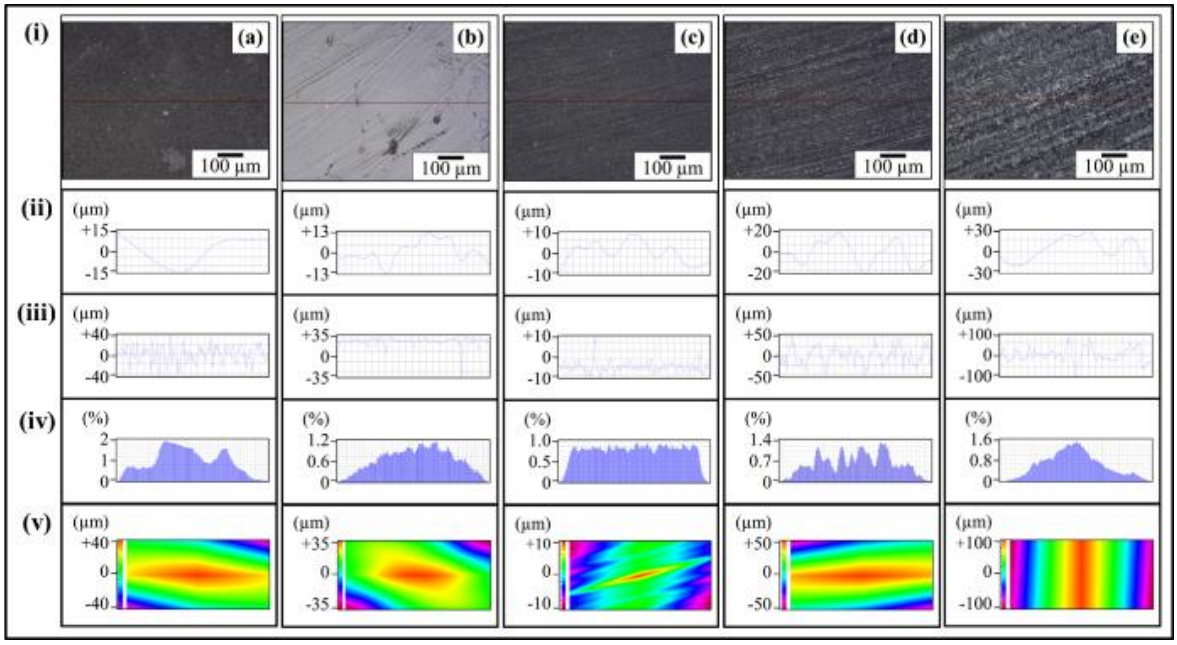

Figure 35. Surface roughness profiles of 0.1 wt% MLG-EP nanocomposites after treatment with abrasive papers for 1 min at 150 rpm: (a) as-cast, (b) Velvet cloth, (c) 1200P, (d) 320P, and (e) 60P. In all cases, (i) optical image, (ii) waviness, (iii) surface roughness of selected line, (iv) percentage vs. topographical dimensions, and (v) surface profile of selected rectangular specimen.

the optical micrograph of 0.1 wt% MLG-EP sample treated with velvet cloth for 1 min (each side) on rotating wheels with rotational speed of 150 rpm. The waviness (Figure 35bii) varies between ±13 µm while the surface roughness (Figure 35biii) varies between ±35 µm. The Gaussian distribution (Figure 35biv) shows that the roughness size is nearly uniformly distributed with dominant size fraction of 1.2%. The large range of surface roughness can be explained on the basis of diamond paste. The diamond paste had average particle size of 3 µm. Therefore, remnant dispersed and agglomerated diamond particles contributed toward surface roughness. The roughness profile (Figure 35bv) shows that the surface roughness slightly decreased compared to as-cast sample (Figure 35av). Figure 35 (ci) shows the optical micrograph of 0.1 wt% MLG-EP sample treated with abrasive paper 1200P. The waviness (Figure 35cii) varies between ±10 µm while the surface roughness (Figure 35ciii) varies between ±10 µm. The surface roughness fluctuates more quickly than in as-cast and velvet treated samples. However, the sharp notches have decreased. The Gaussian distribution (Figure 35civ) shows that a nearly uniform distribution of roughness was obtained with dominant size fraction of 1%. The roughness profile (Figure 35cv) shows that there are no deep surface notches. Figure 35 (di) shows that the optical micrograph of 0.1 wt% MLG-EP sample treated with abrasive paper 320P. The scratches of different size and orientation can be observed. The waviness (Figure 35dii) varies between ±20 µm while the surface roughness (Figure 35diii) varies between ±50 µm. The Gaussian distribution (Figure 35div) shows that the dominant roughness fraction is 1.4%. The roughness profile (Figure 35dv) shows that deep notches emerge on sample surface by treatment with 320P. Figure 35 (ei) shows the optical micrograph of 0.1 wt% MLG-EP sample treated with abrasive paper 60P. A coarse topography can be observed. The waviness (Figure 35eii) varies between ±30 µm while the surface roughness (Figure 35eiii) varies between ±100 µm. The deep pointed notches can be observed which can later

influence the mechanical properties of the samples. The Gaussian distribution (Figure 35eiv) shows that dominant roughness fraction is 1.6%. The surface profile of larger sample (Figure 35ev) shows that coarse topography is present with abruptly changing roughness.

The surface roughness features of 0.1 wt% nanoclay-EP nanocomposites are shown in Figure 36 and details shown in Figure 37. The roughness parameters were decreased by treatment with velvet cloth and 1200P while increased with 320P and 60P. Figure 37 (ai) shows the optical micrograph of as-cast 0.1 wt% nanoclay-EP sample. The waviness (Figure 37aii) of the sample varies between ±15 µm while the surface roughness (Figure 37aiii) varies between ±40 µm. This surface roughness is coming from the mold surface. The surface roughness graph shows that pointed notches of about 40 µm are present on the as-cast 0.1 wt% nanoclay-EP samples. The Gaussian distribution (Figure 37aiv) shows that the roughness size is distributed with dominant size fraction of 1%. The roughness profile (Figure 37av) shows that most of the roughness lies within ±40 µm with a deep notch. Figure 37 (bi) shows the optical micrograph of 0.1 wt% nanoclay-EP sample treated with velvet cloth for 1 min (each side) on rotating wheels with rotational speed of 150 rpm. The waviness (Figure 37bii) varies between ±15 µm while the surface roughness (Figure 37biii) varies between ±35 µm. The Gaussian distribution (Figure 37biv) shows that the roughness size is nearly uniformly distributed with dominant size fraction of 2%. The roughness profile (Figure 37bv) shows that the surface roughness slightly decreased compared to as-cast sample (Figure 37av). Figure 37 (ci) shows the optical micrograph of 0.1 wt% nanoclay-EP sample treated with abrasive paper 1200P. The waviness (Figure 37cii) varies between ±10 µm

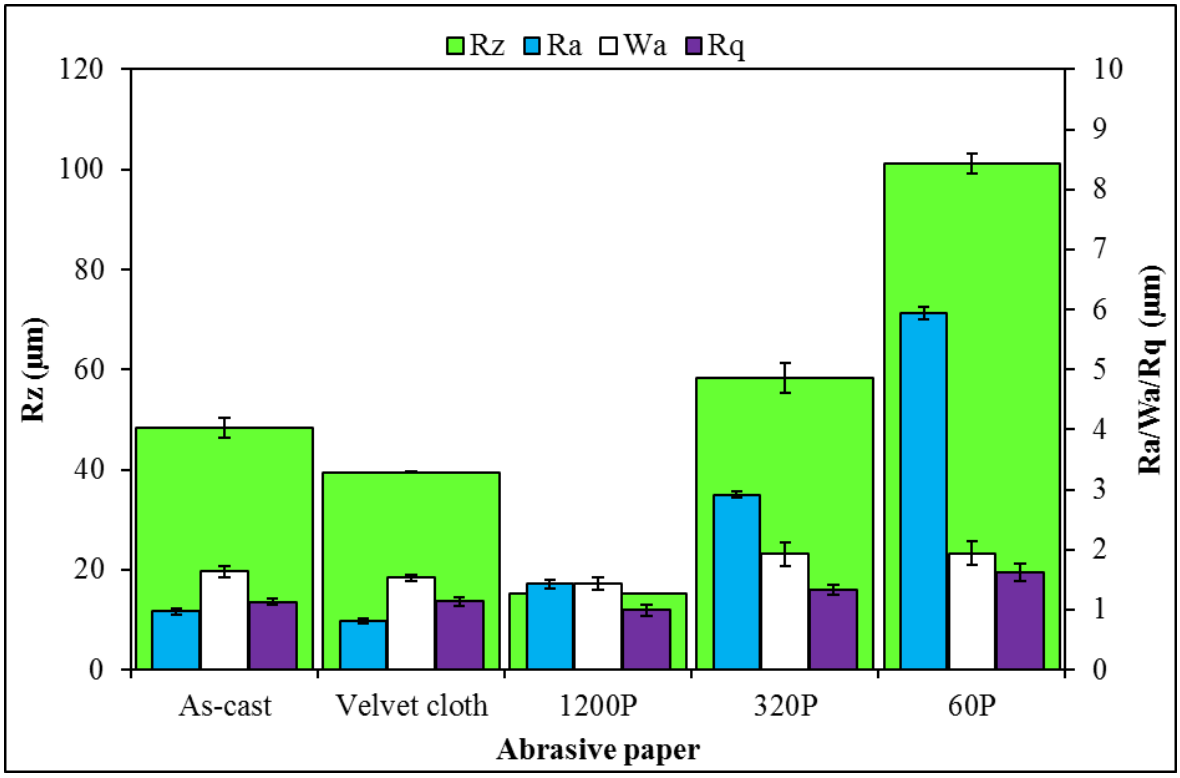

Figure 36. Surface roughness features of 0.1 wt% nanoclay-EP nanocomposites after treatment with abrasive papers for 1 min at 150 rpm.

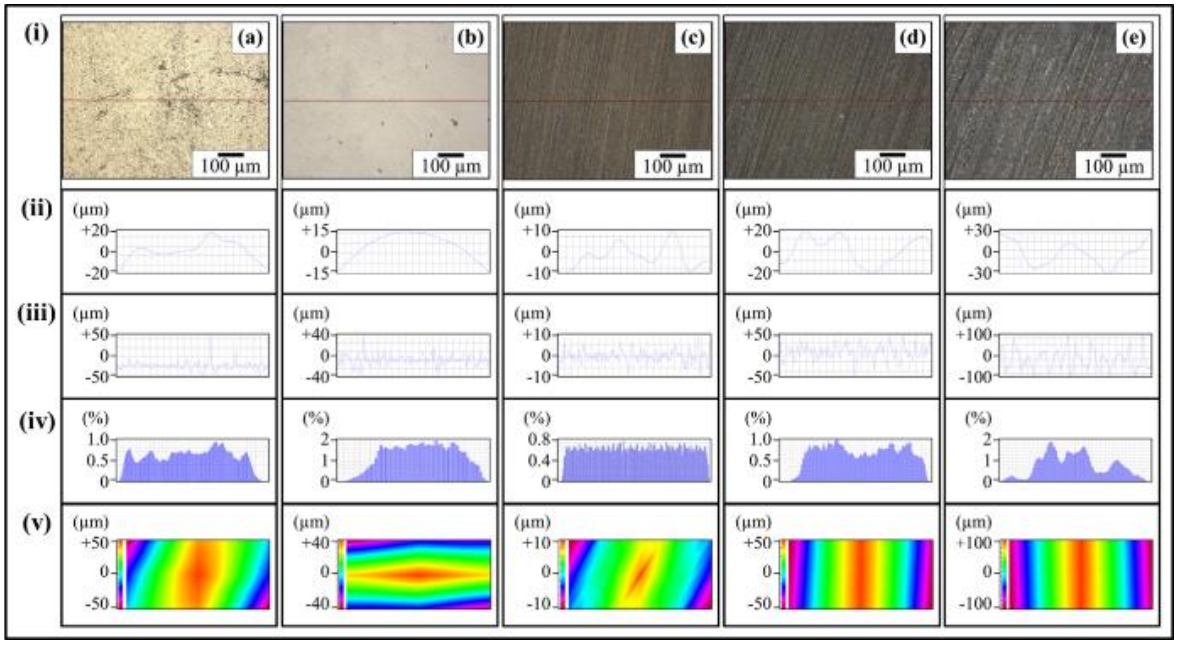

Figure 37. Surface roughness profiles of 0.1 wt% nanoclay-EP nanocomposites after treatment with abrasive papers for 1 min at 150 rpm: (a) As-cast; (b) Velvet cloth; (c) 1200P; (d) 320P; and (e) 60P. In all cases, (i) Optical image; (ii) Waviness; (iii) Surface roughness of selected line; (iv) Percentage vs. topographical dimensions; and (v) Surface profile of selected rectangular specimen.

while the surface roughness (Figure 37ciii) varies between ±10 µm. The surface roughness fluctuates more quickly than in as-cast and velvet treated samples. However, the sharp notches have decreased. The Gaussian distribution (Figure 37civ) shows that a nearly uniform distribution of roughness was obtained with dominant size fraction of 0.8%. The roughness profile (Figure 37cv) shows that there are no deep surface notches. Figure 37 (di) shows that the optical micrograph of 0.1 wt% nanoclay-EP sample treated with abrasive paper 320P. The scratches of different size and orientation can be observed. The waviness (Figure 37dii) varies between ±20 µm while the surface roughness (Figure 37diii) varies between ±50 µm. The Gaussian distribution (Figure 37div) shows that the dominant roughness fraction is 1%. The roughness profile (Figure 37dv) shows that deep notches emerge on sample surface by treatment with 320P. Figure 37 (ei) shows the optical micrograph of 0.1 wt% nanoclay-EP sample treated with abrasive paper 60P. A coarse topography can be observed. The waviness (Figure 37eii) varies between ±30 µm while the surface roughness (Figure 37eiii) varies between ±100 µm. The deep pointed notches can be observed which can later influence the mechanical properties of the samples. The Gaussian distribution (Figure 37eiv) shows that dominant roughness fraction is 2%. The surface profile of larger sample (Figure 37ev) shows that coarse topography is present with abruptly changing roughness.

The surface roughness features of 0.05 wt% MLG-0.05 wt% nanoclay-EP nanocomposites are shown in Figure 38 and details shown in Figure 39. The roughness parameters were decreased by treatment with velvet cloth and 1200P while increased with 320P and 60P. Figure 39 (ai) shows the optical micrograph of as-cast 0.05 wt% MLG-0.05 wt% nanoclay-EP sample. The waviness (Figure 39aii) of the sample varies between ±15 µm while the surface roughness (Figure 39aiii) varies between ±40 µm. This surface roughness is coming from the mold surface. The surface roughness graph shows that pointed notches of

about 40 µm are present on the as-cast 0.05 wt% MLG-0.05 wt% nanoclay-EP samples. The Gaussian distribution (Figure 39aiv) shows that the roughness size is distributed with dominant size fraction of 1%. The roughness profile (Figure 39av) shows that most of the roughness lies within ±40 µm with a deep notch. Figure 39 (bi) shows the optical micrograph of 0.05 wt% MLG-0.05 wt% nanoclay-EP sample treated with velvet cloth for 1 min (each side) on rotating wheels with rotational speed of 150 rpm. The waviness (Figure 39bii) varies between ±15 µm while the surface roughness (Figure 39biii) varies between ±35 µm. The Gaussian distribution (Figure 39biv) shows that the roughness size is nearly uniformly distributed with dominant size fraction of 2%. The roughness profile (Figure 39bv) shows that the surface roughness slightly decreased compared to as-cast sample (Figure 39av).Figure 39 (ci) shows the optical micrograph of 0.05 wt% MLG-0.05 wt% nanoclay-EP sample treated with abrasive paper 1200P. The waviness (Figure 39cii) varies between ±10 µm while the surface roughness (Figure 39ciii) varies between ±10 µm. The surface roughness fluctuates more quickly than in as-cast and velvet treated samples. However, the sharp notches have decreased. The Gaussian distribution (Figure 39civ) shows that a nearly uniform distribution of roughness was obtained with dominant size fraction of 0.8%. The roughness profile (Figure 39cv) shows that there are no deep surface notches. Figure 39 (di) shows that the optical micrograph of 0.05 wt% MLG-0.05 wt% nanoclay-EP sample treated with abrasive paper 320P. The scratches of different size and orientation can be observed. The waviness (Figure 39dii) varies between ±20 µm while the surface roughness (Figure 39diii) varies between ±50 µm. The Gaussian distribution (Figure 39div) shows that the dominant roughness fraction is 1%. The roughness profile (Figure 39dv) shows that deep notches emerge on sample surface by treatment with 320P. Figure 39 (ei) shows the optical micrograph of 0.05 wt% MLG-0.05

wt% nanoclay-EP sample treated with abrasive paper 60P. A coarse topography can be observed. The waviness

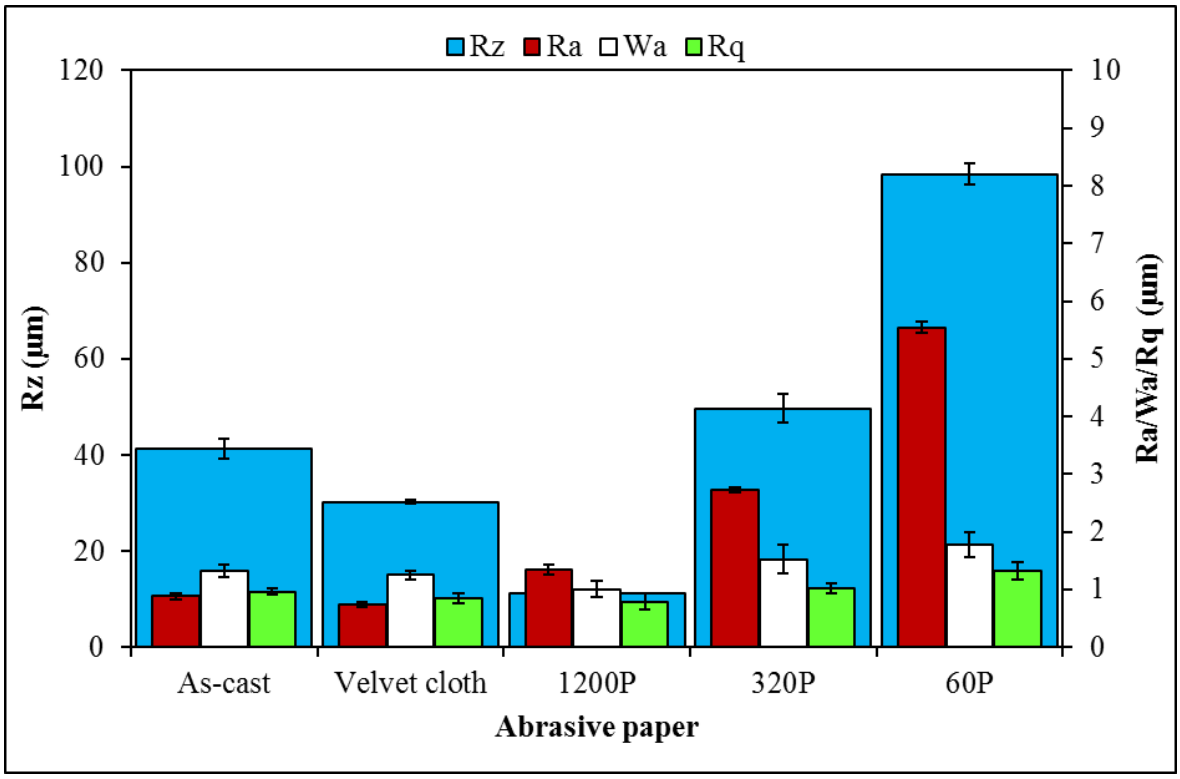

Figure 38. Surface roughness features of 0.05 wt% MLG-0.05 wt% nanoclay-EP nanocomposites after treatment with abrasive papers for 1 min at 150 rpm.

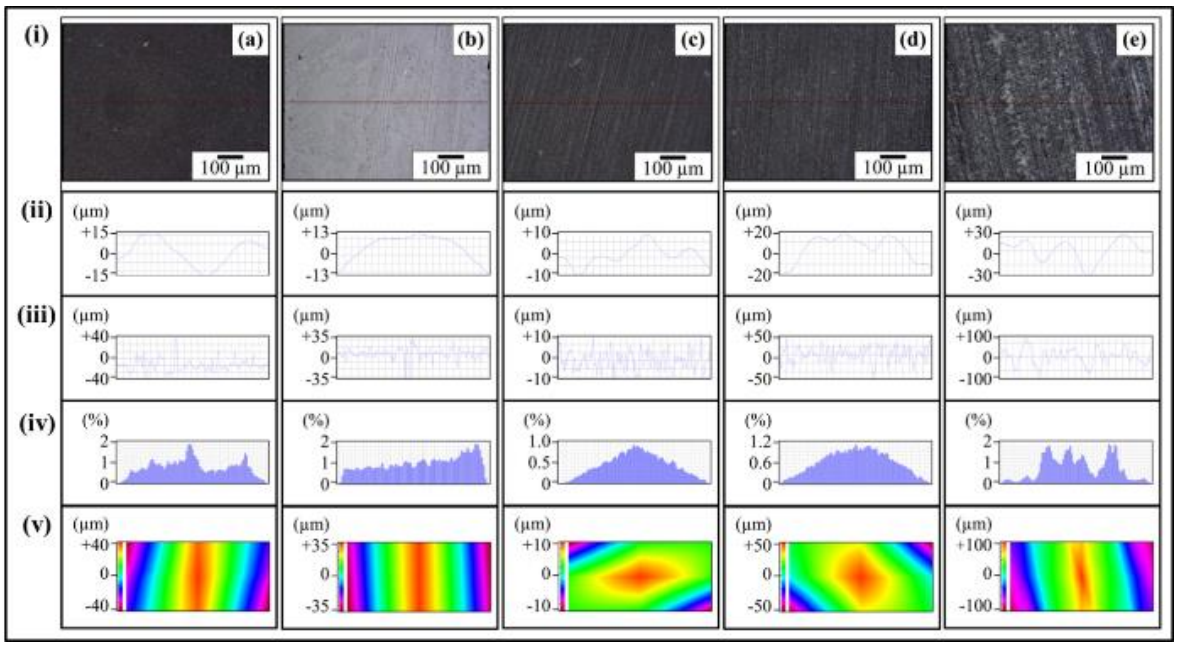

Figure 39. Surface roughness profiles of 0.05 wt% MLG-0.05 wt% nanoclay-EP samples after treatment with abrasive papers for 1 min at 150 rpm: (a) As-cast; (b) Velvet cloth; (c) 1200P; (d) 320P; and (E) 60P. In all the cases, (i) optical image, (ii) waviness, (iii) surface roughness of selected line, (iv) percentage vs. topographical dimensions, and (v) surface profile of selected rectangular specimen.

(Figure 39eii) varies between ±30 µm while the surface roughness (Figure 39eiii) varies between ±100 µm. The deep pointed notches can be observed which can later influence the mechanical properties of the samples. The Gaussian distribution (Figure 39eiv) shows that dominant roughness fraction is 2%. The surface profile of larger sample (Figure 39ev) shows that coarse topography is present with abruptly changing roughness.

The topographical features of 0.5 wt% MLG-EP nanocomposites are shown in Figure 40 and Figure 41. The roughness parameters were decreased by treatment with velvet cloth and 1200P while increased with 320P and 60P. Figure 41 (ai) shows the optical micrograph of as-cast 0.5 wt% MLG-EP sample. The waviness (Figure 41aii) of the sample varies between ±15 µm while the surface roughness (Figure 41aiii) varies between ±40 µm. This surface roughness is coming from the mold surface. The surface roughness graph shows that pointed notches of about 40 µm are present on the as-cast 0.5 wt% MLG-EP samples. The Gaussian distribution (Figure 41aiv) shows that the roughness size is distributed with dominant size fraction of 3%. The roughness profile (Figure 41av) shows that most of the roughness lies within ±40 µm with a deep notch. Figure 41 (bi) shows the optical micrograph of 0.5 wt% MLG-EP sample treated with velvet cloth for 1 min (each side) on rotating wheels with rotational speed of 150 rpm. The waviness (Figure 41bii) varies between ±13 µm while the surface roughness (Figure 41biii) varies between ±35 µm. The Gaussian distribution (Figure 41biv) shows that the roughness size is nearly uniformly distributed with dominant size fraction of 3%. The roughness profile (Figure 41bv) shows that the surface roughness slightly decreased compared to as-cast sample

(Figure 41av). Figure 41 (ci) shows the optical micrograph of 0.5 wt% MLG-EP sample treated with abrasive paper 1200P. The waviness (Figure 41cii) varies between ±10 µm while the surface roughness (Figure 41ciii) varies between ±10 µm. The surface roughness fluctuates more quickly than in as-cast and velvet treated samples. However, the sharp notches have decreased. The Gaussian distribution (Figure 41civ) shows that a nearly uniform distribution of roughness was obtained with dominant size fraction of 1.4%. The roughness profile (Figure 41cv) shows that there are no deep surface notches. Figure 41 (di) shows that the optical micrograph of 0.5 wt% MLG-EP sample treated with abrasive paper 320P. The scratches of different size and orientation can be observed. The waviness (Figure 41dii) varies between ±20 µm while the surface roughness (Figure 41diii) varies between ±50 µm. The Gaussian distribution (Figure 41div) shows that the dominant roughness fraction is 1.8%. The roughness profile (Figure 41dv) shows that deep notches emerge on sample surface by treatment with 320P. Figure 41 (ei) shows the optical micrograph of 0.5 wt% MLG-EP sample treated with abrasive paper 60P. A coarse topography can be observed. The waviness (Figure 41eii) varies between ±30 µm while the surface roughness (Figure 41eiii) varies between ±100 µm. The deep pointed notches can be observed which can later influence the mechanical properties of the samples. The Gaussian distribution (Figure 41eiv) shows that dominant roughness fraction is 3.4%. The surface profile of larger sample (Figure 41ev) shows that coarse topography is present with abruptly changing roughness.

The topographical features of 0.5 wt% nanoclay-EP nanocomposites are shown in Figure 42 and details shown in Figure 43. The roughness parameters were decreased by treatment with velvet cloth and 1200P while increased with 320P and 60P. Figure 43 (ai) shows the optical micrograph of as-cast 0.5 wt% nanoclay-EP sample. The waviness (Figure 43aii) of the sample varies between ±15 µm while the surface roughness (Figure 43aiii) varies

between ±40 µm. This surface roughness is coming from the mold surface. The surface roughness graph shows that pointed notches of about 40 µm are present on the as-cast 0.5 wt% nanoclay- EP samples. The Gaussian distribution (Figure 43aiv) shows that the roughness size is distributed with dominant size fraction of 4%. The roughness profile (Figure 43av) shows

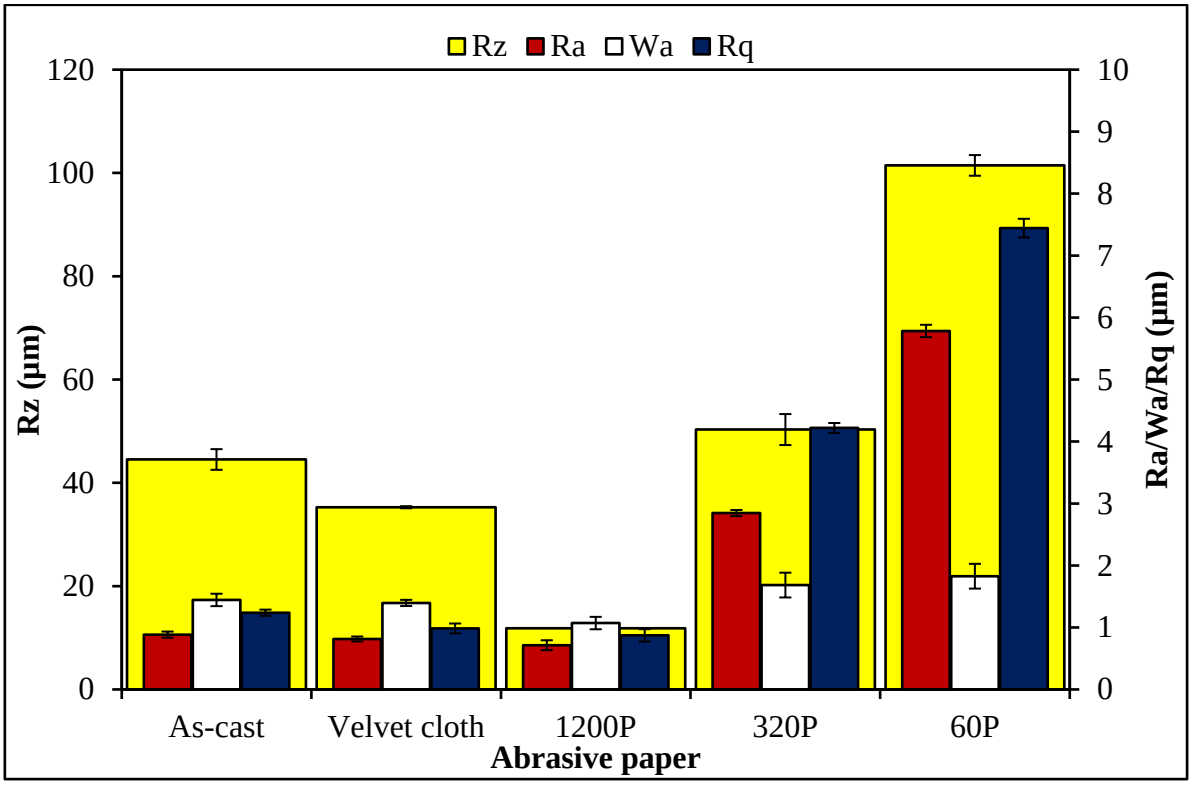

Figure 40. Topographical features of 0.5 wt% MLG-EP nanocomposites.

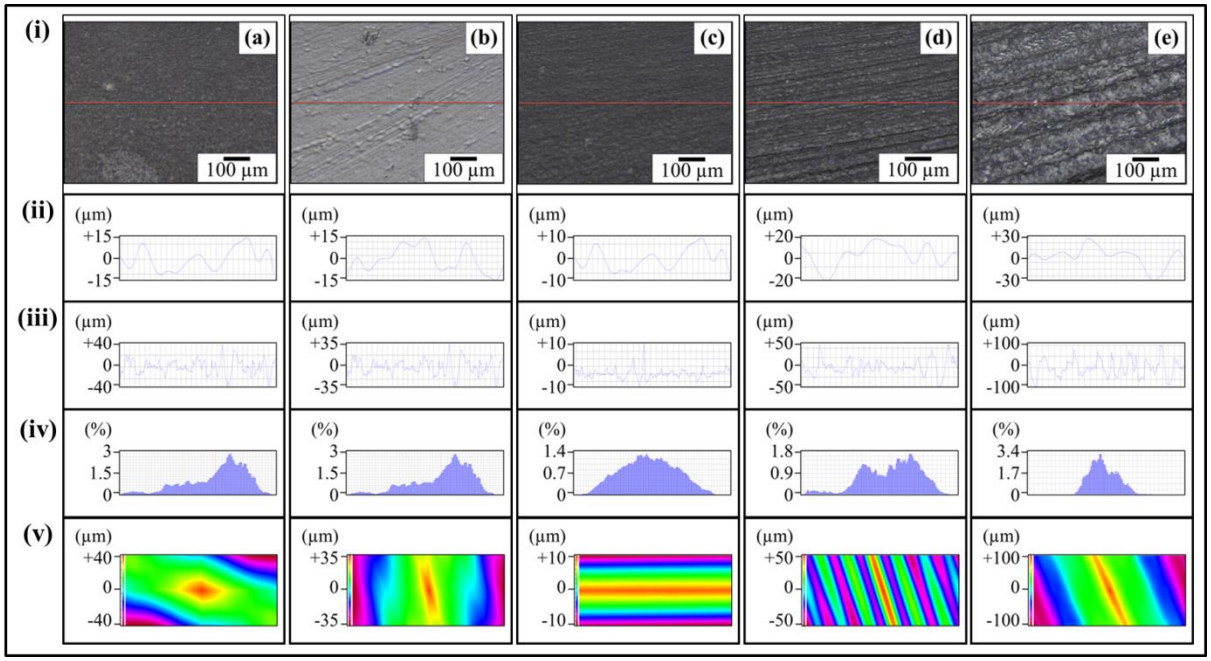

Figure 41. Topography profiles of 0.5 wt% MLG-EP nanocomposites treated with: (a) as-cast, (b) Velvet cloth, (c) 1200P, (d) 320P, and (e) 60P. In all cases, (i) optical image, (ii) waviness, (iii) surface roughness of selected line, (iv) percentage vs. topographical dimensions, and (v) surface profile of selected rectangular specimen.

that most of the roughness lies within ±40 µm with a deep notch. Figure 43 (bi) shows the optical micrograph of 0.5 wt% nanoclay-EP sample treated with velvet cloth for 1 min (each side) on rotating wheels with rotational speed of 150 rpm. The waviness (Figure 43bii) varies between ±15 µm while the surface roughness (Figure 43biii) varies between ±35 µm. The Gaussian distribution (Figure 43biv) shows that the roughness size is nearly uniformly distributed with dominant size fraction of 1.8%. The roughness profile (Figure 43bv) shows that the surface roughness slightly decreased compared to as-cast sample (Figure 43av).

Figure 43 (ci) shows the optical micrograph of 0.5 wt% nanoclay-EP sample treated with abrasive paper 1200P. The waviness (Figure 43cii) varies between ±10 µm while the surface roughness (Figure 43ciii) varies between ±10 µm. The surface roughness fluctuates more quickly than in as-cast and velvet treated samples. However, the sharp notches have

decreased. The Gaussian distribution (Figure 43civ) shows that a nearly uniform distribution of roughness was obtained with dominant size fraction of 2.2%. The roughness profile (Figure 43cv) shows that there are no deep surface notches. Figure 43 (di) shows that the optical micrograph of 0.5 wt% nanoclay-EP sample treated with abrasive paper 320P. The scratches of different size and orientation can be observed. The waviness (Figure 43dii) varies between ±20 µm while the surface roughness (Figure 43diii) varies between ±50 µm. The Gaussian distribution (Figure 43div) shows that the dominant roughness fraction is 2%. The roughness profile (Figure 43dv) shows that deep notches emerge on sample surface by treatment with 320P. Figure 43 (ei) shows the optical micrograph of 0.5 wt% nanoclay-EP sample treated with abrasive paper 60P. A coarse topography can be observed. The waviness (Figure 43eii) varies between ±30 µm while the surface roughness (Figure 43eiii) varies between ±100 µm. The deep pointed notches can be observed which can later influence the mechanical properties of the samples. The Gaussian distribution

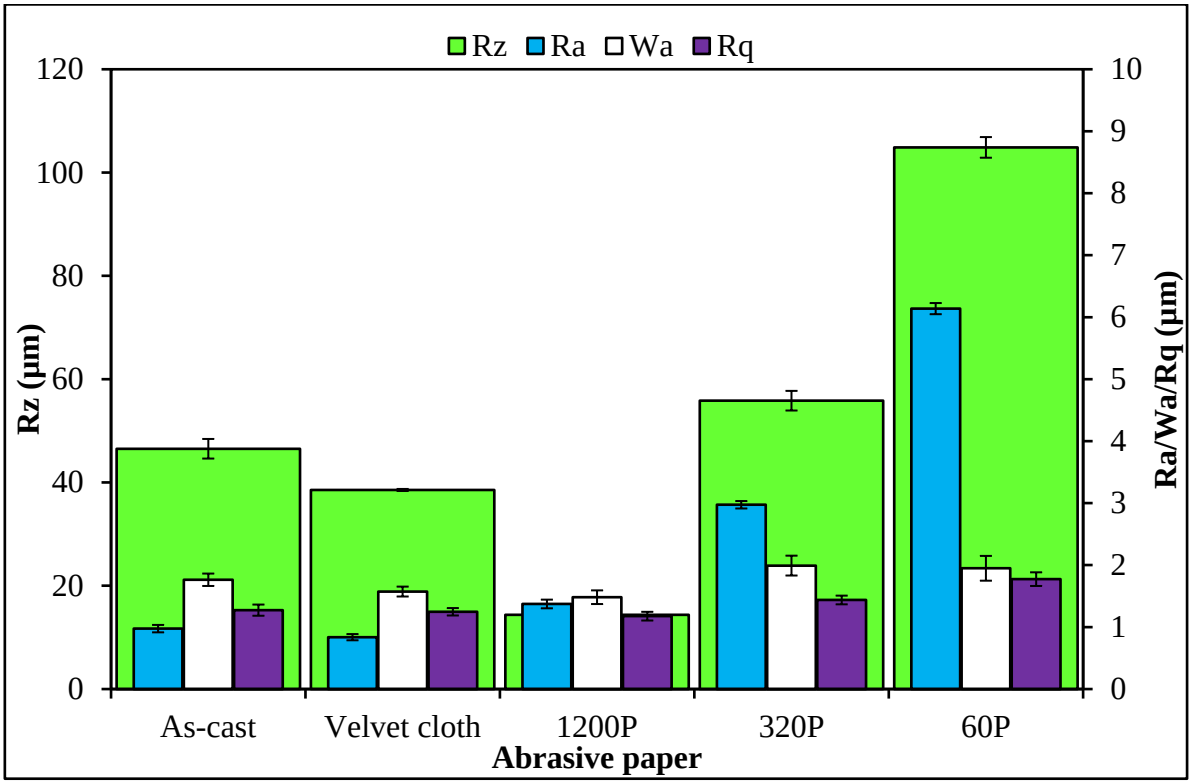

Figure 42. Topographical features of 0.5 wt% nanoclay-EP nanocomposites.

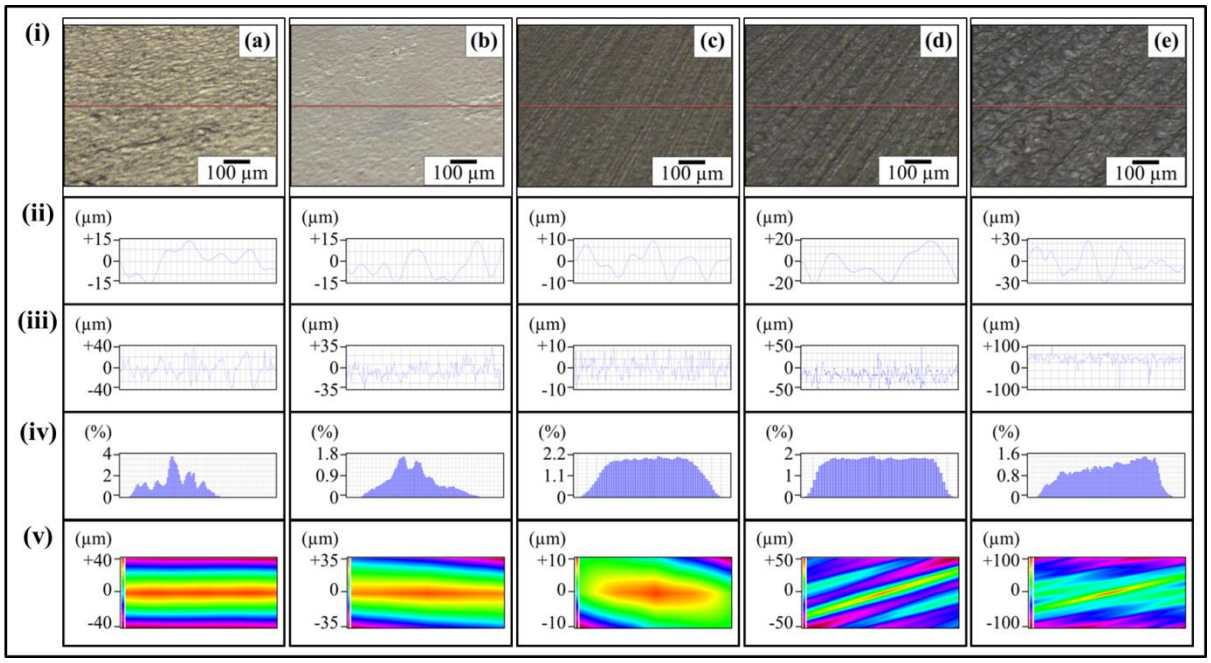

Figure 43. Topography profiles of 0.5 wt% nanoclay-EP nanocomposites treated with: (a) As-cast; (b) Velvet cloth; (c) 1200P; (d) 320P; and (e) 60P. In all cases, (i) Optical image; (ii) Waviness; (iii) Surface roughness of selected line; (iv) Percentage vs. topographical dimensions; and (v) Surface profile of selected rectangular specimen.

(Figure 43eiv) shows that dominant roughness fraction is 1.6%. The surface profile of larger sample (Figure 43ev) shows that coarse topography is present with abruptly changing roughness.

The topographical features of 0.25 wt% MLG-0.25 wt% nanoclay-EP nanocomposites are shown in Figure 44 and details shown in Figure 45. The roughness parameters weredecreased by treatment with velvet cloth and 1200P while increased with 320P and 60P. Figure 45 (ai) shows the optical micrograph of as-cast 0.25 wt% MLG-0.25 wt% nanoclay-EP sample. The waviness (Figure 45aii) of the sample varies between ±15 µm while the surface roughness (Figure 45aiii) varies between ±40 µm. This surface roughness is coming from the mold surface. The surface roughness graph shows that pointed notches of about 40 µm are present on the as-cast 0.25 wt% MLG-0.25 wt%

nanoclay-EP samples. The Gaussian distribution (Figure 45aiv) shows that the roughness size is distributed with dominant size fraction of 1%. The roughness profile (Figure 45av) shows that most of the roughness lies within ±40 µm with a deep notch. Figure 45 (bi) shows the optical micrograph of 0.25 wt% MLG-0.25 wt% nanoclay-EP sample treated with velvet cloth for 1 min (each side) on rotating wheels with rotational speed of 150 rpm. The waviness (Figure 45bii) varies between ±15 µm while the surface roughness (Figure 45biii) varies between ±35 µm. The Gaussian distribution (Figure 45biv) shows that the roughness size is nearly uniformly distributed with dominant size fraction of 2.2%. The roughness profile (Figure 45bv) shows that the surface roughness slightly decreased compared to as-cast sample (Figure 45av). Figure 45 (ci) shows the optical micrograph of 0.25 wt% MLG-0.25 wt% nanoclay-EP sample treated with abrasive paper 1200P. The waviness (Figure 45cii) varies between ±10 µm while the surface roughness (Figure 45ciii) varies between ±10 µm. The surface roughness fluctuates more quickly than in as-cast and velvet treated samples. However, the sharp notches have decreased. The Gaussian distribution (Figure 45civ) shows that a nearly uniform distribution of roughness was obtained with dominant size fraction of 2%. The roughness profile (Figure 45cv) shows that there are no deep surface notches. Figure 45 (di) shows that the optical micrograph of 0.25 wt% MLG-0.25 wt% nanoclay-EP sample treated with abrasive paper 320P. The scratches of different size and orientation can be observed. The waviness (Figure 45dii) varies between ±20 µm while the surface roughness (Figure 45diii) varies between ±50 µm. The Gaussian distribution (Figure 45div) shows that the dominant roughness fraction is 1.4%. The roughness profile (Figure 45dv) shows that deep notches emerge on sample surface by treatment with 320P. Figure 45 (ei) shows the optical micrograph of 0.25 wt% MLG-0.25 wt% nanoclay-EP sample treated with abrasive paper 60P. A coarse topography can be observed. The waviness (Figure 45eii) varies between ±30 µm while the surface

roughness (Figure 45eiii) varies between ±100 µm. The deep pointed notches can be observed which can later influence the mechanical properties of the samples. The Gaussian distribution (Figure 45eiv) shows that dominant roughness fraction is 1.6%. The surface profile of larger sample (Figure 45ev) shows that coarse topography is present with abruptly changing roughness.

The surface roughness features of 1.0 wt% nanoclay-EP nanocomposites are shown in Figure 46 and details shown in Figure 47. The roughness parameters were decreased by treatment with velvet cloth and 1200P while increased with 320P and 60P. Figure 47 (ai) shows the optical micrograph of as-cast 1.0 wt% nanoclay-EP sample. The waviness (Figure 47aii) of the sample varies between ±15 µm while the surface roughness (Figure 47aiii) varies between ±40 µm. This surface roughness is coming from the mold surface. The surface roughness graph shows that pointed notches of about 40 µm are present on the as-cast 1.0 wt% nanoclay-EP samples. The Gaussian distribution (Figure 47aiv) shows that the roughness size is distributed with dominant size fraction of 2.2%. The roughness profile (Figure 47av) shows that most of the roughness lies within ±40 µm with a deep notch. Figure 47 (bi)

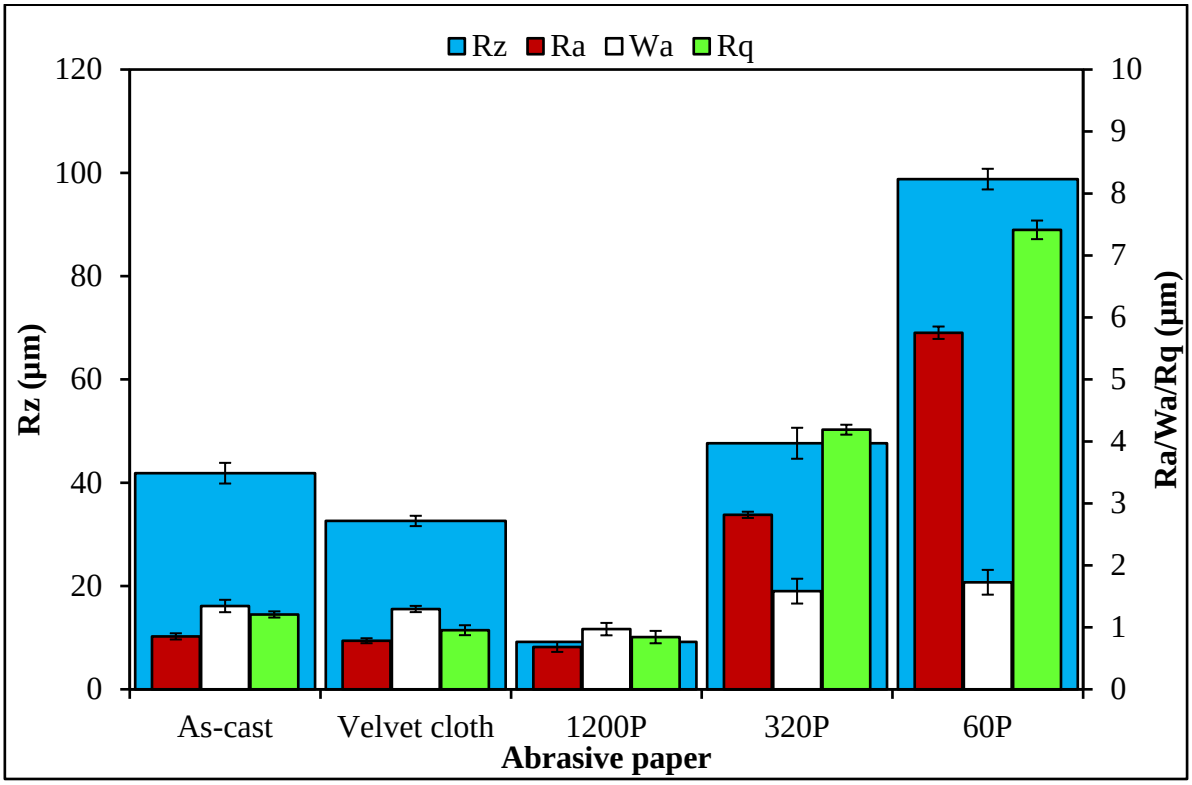

Figure 44. Topographical features of 0.25 wt% MLG-0.25 wt% nanoclay-EP nanocomposites.

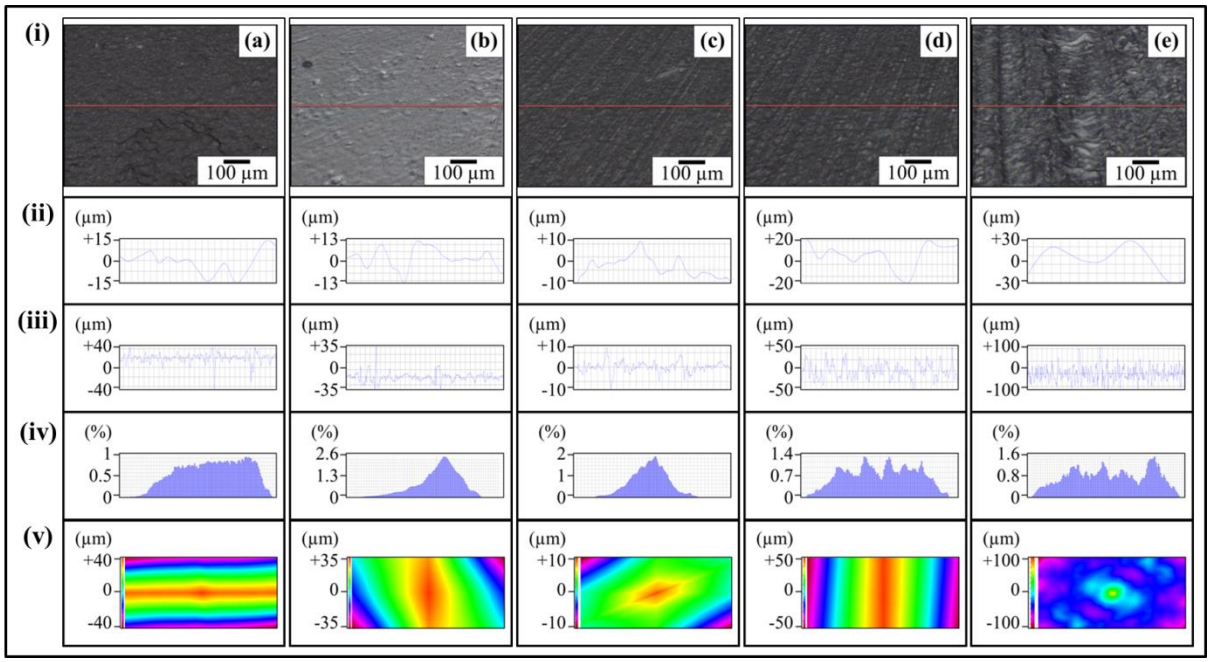

Figure 45. Topography profiles of 0.25 wt% MLG-0.25 wt% nanoclay-EP samples: (a) As-cast; (b) Velvet cloth; (c) 1200P; (d) 320P; and (E) 60P. In all the cases, (i) optical image, (ii) waviness, (iii) surface roughness of selected line, (iv) percentage vs. topographical dimensions, and (v) surface profile of selected rectangular specimen.

shows the optical micrograph of 1.0 wt% nanoclay-EP sample treated with velvet cloth for 1 min (each side) on rotating wheels with rotational speed of 150 rpm. The waviness (Figure 47bii) varies between ±15 µm while the surface roughness (Figure 47biii) varies between ±35 µm. The Gaussian distribution (Figure 47biv) shows that the roughness size is nearly uniformly distributed with dominant size fraction of 1%. The roughness profile (Figure 47bv) shows that the surface roughness slightly decreased compared to as-cast sample (Figure 47av). Figure 47 (ci) shows the optical micrograph of 1.0 wt% nanoclay-EP sample treated with abrasive paper 1200P. The waviness (Figure 47cii) varies between ±10 µm while the surface roughness (Figure 47ciii) varies between ±10 µm. The surface roughness fluctuates more quickly than in as-cast and velvet treated samples. However, the sharp notches have decreased. The Gaussian distribution (Figure 47civ) shows that a nearly uniform distribution of roughness was obtained with dominant size fraction of 0.8%. The roughness profile (Figure 47cv) shows that there are no deep surface notches. Figure 47 (di) shows that the optical micrograph of 1.0 wt% nanoclay-EP sample treated with abrasive paper 320P. The scratches of different size and orientation can be observed. The waviness (Figure 47dii) varies between ±20 µm while the surface roughness (Figure 47diii) varies between ±50 µm. The Gaussian distribution (Figure 47div) shows that the dominant roughness fraction is 2%. The roughness profile (Figure 47dv) shows that deep notches emerge on sample surface by treatment with 320P. Figure 47 (ei) shows the optical micrograph of 1.0 wt% nanoclay-EP sample treated with abrasive paper 60P. A coarse topography can be observed. The waviness (Figure 47eii) varies between ±30 µm while the surface roughness (Figure 47eiii) varies between ±100 µm. The deep pointed notches can be observed which can later influence the mechanical properties of the samples. The Gaussian distribution (Figure 47eiv) shows that dominant roughness fraction is 1.4%. The surface profile of larger sample (Figure 47ev) shows that coarse topography is present with

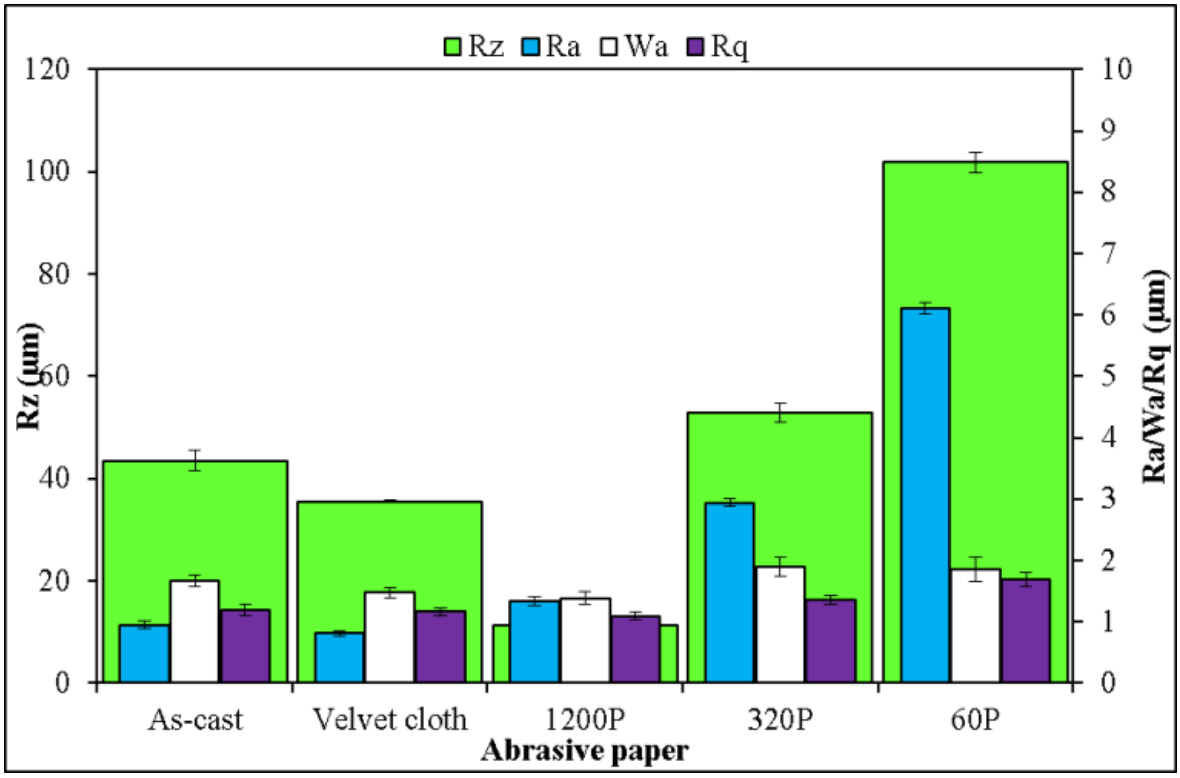

Figure 46: Surface roughness features of 1.0 wt% nanoclay-EP nanocomposites after treatment with abrasive papers for 1 min at 150 rpm.

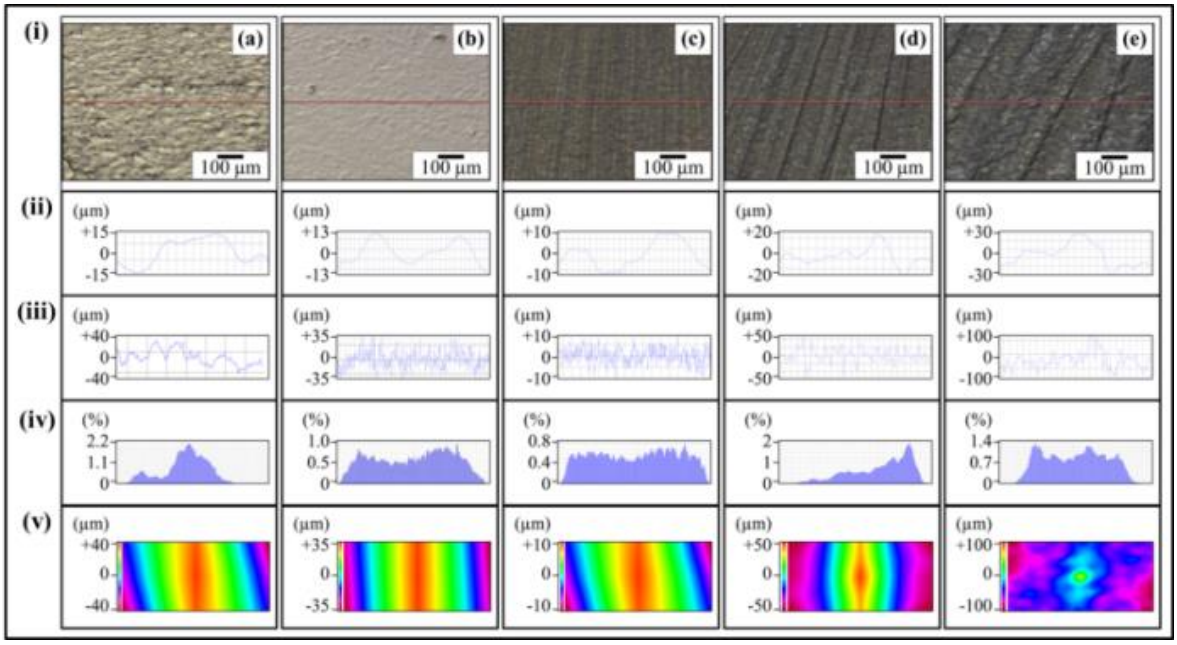

Figure 47: Surface roughness profiles of 1.0 wt% nanoclay-EP nanocomposites after treatment with abrasive papers for 1 min at 150 rpm: (a) As-cast; (b) Velvet cloth; (c) 1200P; (d) 320P; and (e) 60P. In all cases, (i) Optical image; (ii) Waviness; (iii) Surface roughness of selected line; (iv) Percentage vs. topographical dimensions; and (v) Surface profile of selected rectangular specimen.

abruptly changing roughness. sample.

The surface roughness features of 1.0 wt% MLG-EP nanocomposites are shown in Figure 48 and Figure 49. The roughness parameters were decreased by treatment with velvet cloth and 1200P while increased with 320P and 60P. Figure 49 (ai) shows the optical micrograph of as-cast 1.0 wt% MLG-EP sample. The waviness (Figure 49aii) of the sample varies between ±15 µm while the surface roughness (Figure 49aiii) varies between ±40 µm. This surface roughness is coming from the mold surface. The surface roughness graph shows that pointed notches of about 40 µm are present on the as-cast 1.0 wt% MLG-EP samples. The Gaussian distribution (Figure 49aiv) shows that the roughness size is distributed with dominant size fraction of 2%. The roughness profile (Figure 49av) shows that most of the roughness lies within ±40 µm with a deep notch. Figure 49 (bi) shows the optical micrograph of 1.0 wt% MLG-EP sample treated with velvet cloth for 1 min (each side) on rotating wheels with rotational speed of 150 rpm. The waviness (Figure 49bii) varies between ±13 µm while the surface roughness (Figure 49biii) varies between ±35 µm. The Gaussian distribution (Figure 49biv) shows that the roughness size is nearly uniformly distributed with dominant size fraction of 2%. The large range of (Figure 45diii) varies between ±50 µm. The Gaussian distribution (Figure 45div) shows that the dominant roughness fraction is 1.4%. The roughness profile (Figure 45dv) shows that deep notches emerge on sample surface by treatment with 320P. Figure 45 (ei) shows the optical micrograph of 0.25 wt% MLG-0.25 wt% nanoclay-EP sample treated with abrasive paper 60P. A coarse topography can be observed. The waviness (Figure 45eii) varies between ±30 µm while the surface roughness (Figure 45eiii) varies between ±100 µm. The deep pointed notches can be observed which can later influence the mechanical properties of the samples. The Gaussian distribution (Figure 45eiv) shows that dominant roughness fraction is 1.6%. The surface profile of larger sample (Figure 45ev) shows that coarse

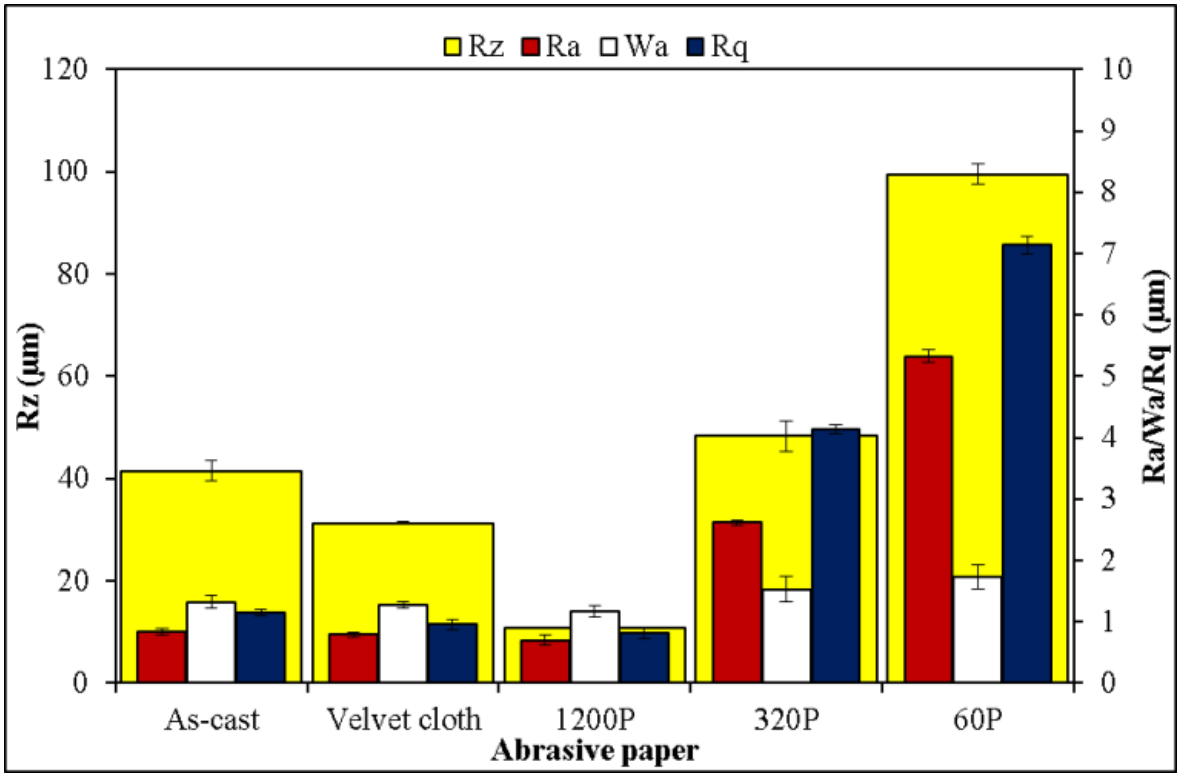

Figure 48: Surface roughness features of 1.0 wt% MLG-EP nanocomposites after treatment with abrasive papers for 1 min at 150 rpm.

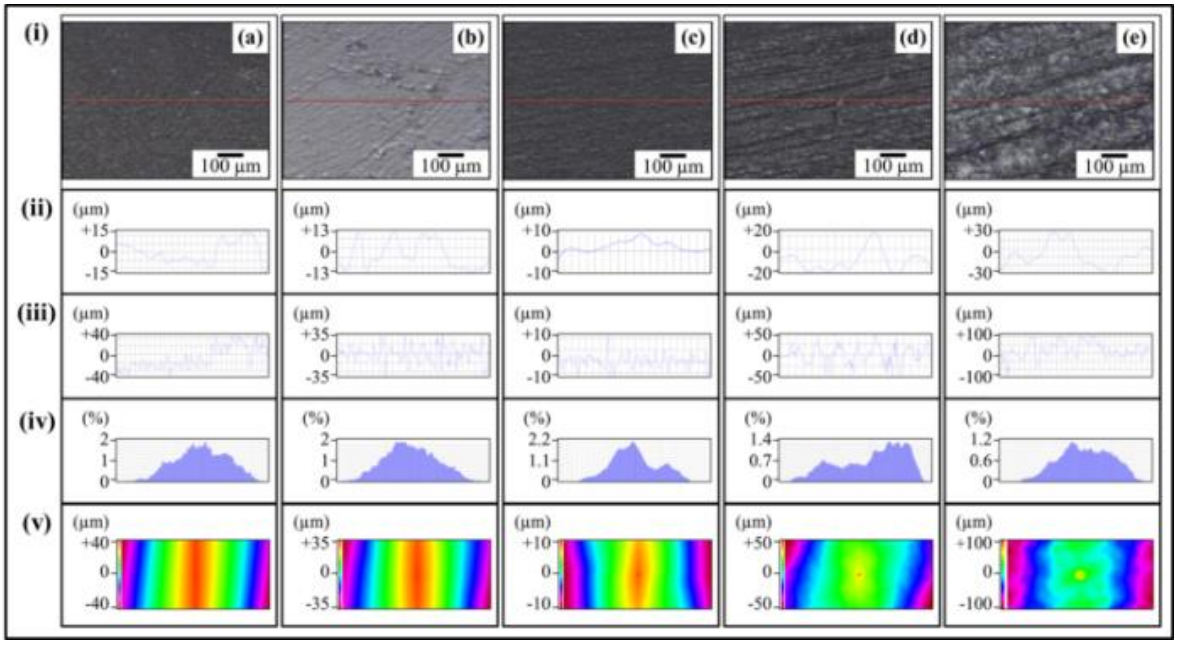

Figure 49: Surface roughness profiles of 1.0 wt% MLG-EP nanocomposites after treatment with abrasive papers for 1 min at 150 rpm: (a) as-cast, (b) Velvet cloth, (c) 1200P, (d) 320P, and (e) 60P. In all cases, (i) optical image, (ii) waviness, (iii) surface roughness of selected line, (iv) percentage vs. topographical dimensions, and (v) surface profile of selected rectangular specimen.

topography is present with abruptly changing roughness.

The surface roughness features of 0.5 wt% MLG-0.5 wt% nanoclay-EP nanocomposites are shown in Figure 50 and details shown in Figure 51. The roughness parameters were decreased by treatment with velvet cloth and 1200P while increased with 320P and 60P. Figure 51 (ai) shows the optical micrograph of as-cast 0.5 wt% MLG-0.5 wt% nanoclay-EP sample. The waviness (Figure 51aii) of the sample varies between ±15 μm while the surface roughness (Figure 51aiii) varies between ±40 μm. This surface roughness is coming from the mold surface. The surface roughness graph shows that pointed notches of about 40 μm are present on the as-cast 0.5 wt% MLG-0.5 wt% nanoclay-EP samples. The Gaussian distribution (Figure 51aiv) shows that the roughness size is distributed with dominant size fraction of 1.6%. The roughness profile (Figure 51av) shows that most of the roughness lies within ±40 μm with a deep notch. Figure 51 (bi) shows the optical micrograph of 0.5 wt% MLG-0.5 wt% nanoclay-EP sample treated with velvet cloth for 1 min (each side) on rotating wheels with rotational speed of 150 rpm. The waviness (Figure 51bii) varies between ±15 μm while the surface roughness (Figure 51biii) varies between ±35 μm. The Gaussian distribution (Figure 51biv) shows that the roughness size is nearly uniformly distributed with dominant size fraction of 4.6%. The roughness profile (Figure 51bv) shows that the surface roughness slightly decreased compared to as-cast sample (Figure 51av). Figure 51 (ci) shows the optical micrograph of 0.5 wt% MLG-0.5 wt% nanoclay-EP sample treated with abrasive paper 1200P. The waviness (Figure 51cii) varies between ±10 μm while the surface roughness (Figure 51ciii) varies between ±10 μm. The surface roughness fluctuates more quickly than in as-cast and velvet treated samples. However, the sharp notches have decreased. The Gaussian distribution (Figure 51civ) shows that a nearly uniform distribution of roughness was obtained with dominant size fraction of 2%. The roughness profile (Figure 51cv) shows that there are no deep surface

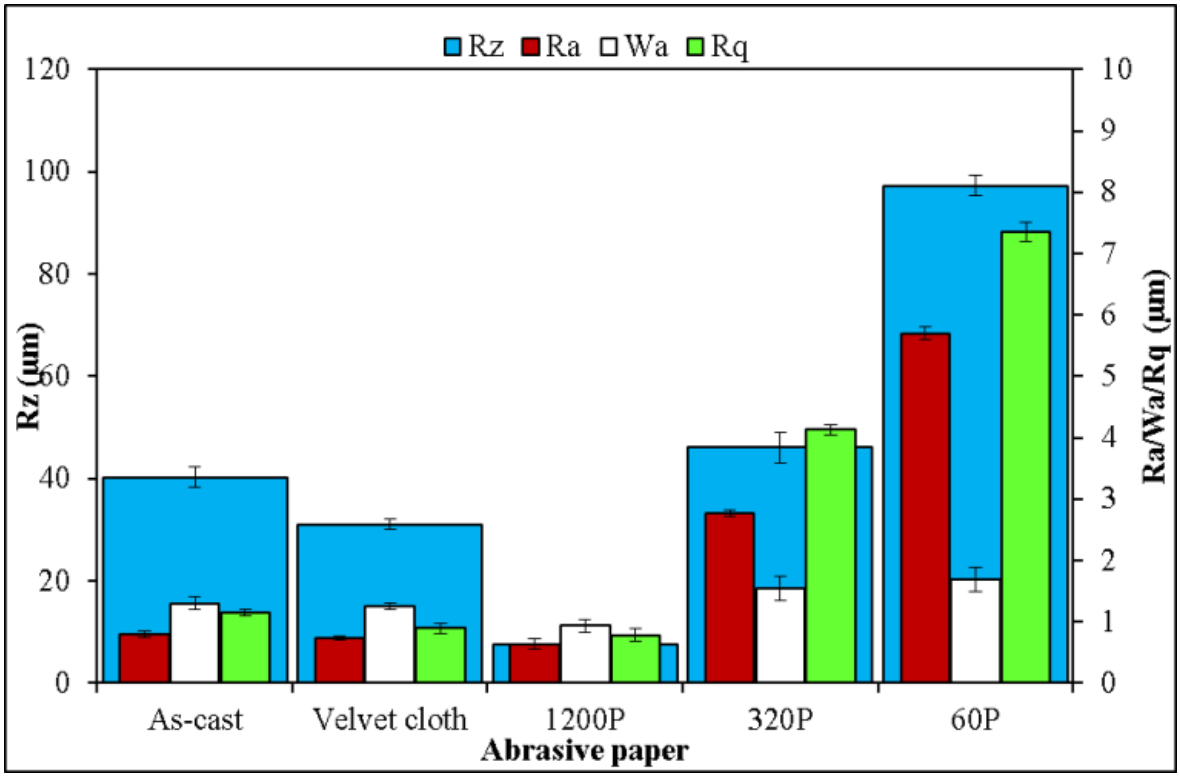

Figure 50: Surface roughness features of 0.5 wt% MLG-0.5 wt% nanoclay-EP nanocomposites after treatment with abrasive papers for 1 min at 150 rpm.

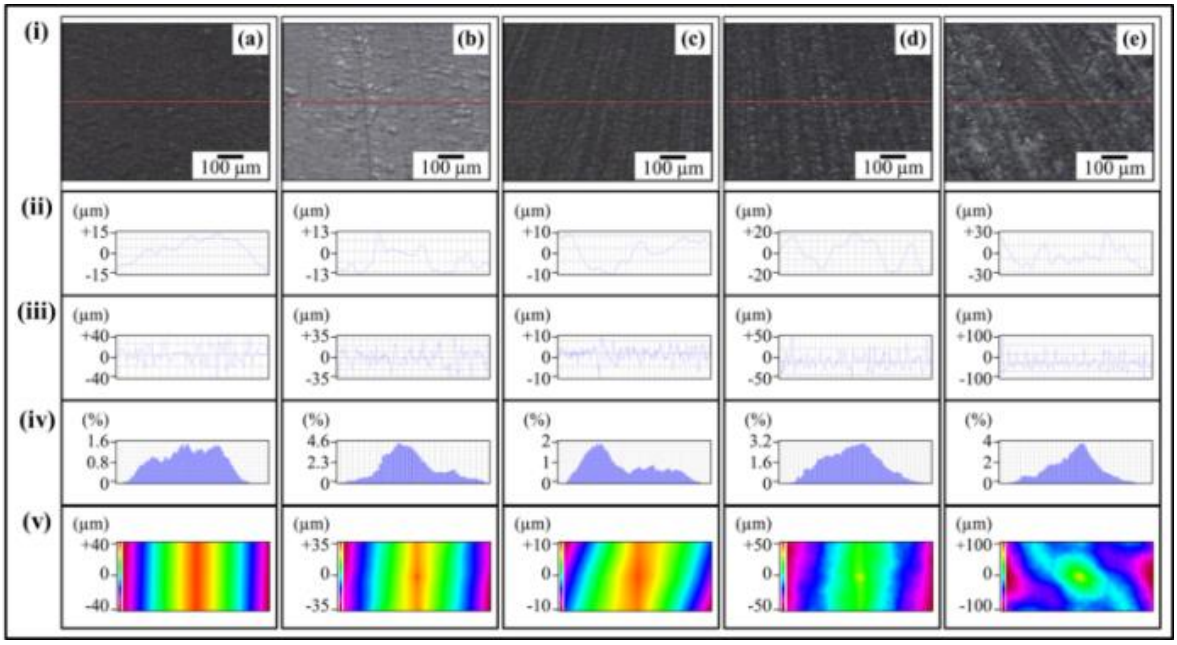

Figure 51: Surface roughness profiles of 0.5 wt% MLG-0.5 wt% nanoclay-EP samples after treatment with abrasive papers for 1 min at 150 rpm: (a) As-cast; (b) Velvet cloth; (c) 1200P; (d) 320P; and (E) 60P. In all the cases, (i) optical image, (ii) waviness, (iii) surface roughness of selected line, (iv) percentage vs. topographical dimensions, and (v) surface profile of selected rectangular specimen.

notches. Figure 51 (di) shows that the optical micrograph of 0.5 wt% MLG-0.5 wt% nanoclay-EP sample treated with abrasive paper 320P. The scratches of different size and orientation can be observed. The waviness (Figure 51dii) varies between ±20 µm while the surface roughness (Figure 51diii) varies between ±50 µm. The Gaussian distribution (Figure 51div) shows that the dominant roughness fraction is 3.2%. The roughness profile (Figure 51dv) shows that deep notches emerge on sample surface by treatment with 320P. Figure 51 (ei) shows the optical micrograph of 0.5 wt% MLG-0.5 wt% nanoclay-EP sample treated with abrasive paper 60P. A coarse topography can be observed. The waviness (Figure 51eii) varies between ±30 µm while the surface roughness (Figure 51eiii) varies between ±100 µm. The deep pointed notches can be observed which can later influence the mechanical properties of the samples. The Gaussian distribution (Figure 51eiv) shows that dominant roughness fraction is 4%. The surface profile of larger sample (Figure 51ev) shows that coarse topography is present with abruptly changing roughness.

The densification of nanoclay-MLG-EP samples is shown in Figure 53. The densification of produced sample is around 99.5% (mean value). The surface roughness features influenced mechanical properties of the samples as shown in Figure 54-Figure 63. However, being intrinsic properties of the materials, surface roughness did not show any visible influence on Young's and fleuxural moduli as shown in Figure 54 and Figure 57, respectively.

The influence of topography on UTS is shown in Figure 55. The UTS of monolithic epoxy treated with velvet cloth increased from 50 MPa to 52 MPa (3% increase). The maximum increase in UTS of monolithic epoxy was observed when monolithic epoxy treated with abrasive paper 1200P and UTS increased to 55 MPa (4% increase). The UTS of monolithic

epoxy treated with abrasive paper 60P decreased to 49 MPa (2% decrease). When treated with abrasive papers 60P, the UTS decreased to 47 MPa (5 % decrease).

The UTS of 0.1 wt% MLG-EP nanocomposites treated with velvet cloth increased from 60 MPa to 62 MPa (2.2% increase). The maximum increase in UTS of 0.1 wt% MLG-EP nanocomposites was observed when 0.1 wt% MLG-EP nanocomposites treated with abrasive paper 1200P and UTS increased to 65 MPa (7.5% increase). The UTS of 0.1 wt% MLG-EP nanocomposites treated with abrasive paper 320P decreased to 59 MPa (1% decrease). When treated with abrasive papers 60P, the UTS decreased to 57 MPa (4.8 % decrease).

The UTS of 0.1 wt% nanoclay-EP nanocomposites treated with velvet cloth increased from 49 MPa to 53 MPa (8% increase). The maximum increase in UTS of 0.1 wt% nanoclay-EP nanocomposites was observed when 0.1 wt% nanoclay-EP nanocomposites treated with abrasive paper 1200P and UTS increased to 58 MPa (20% increase). The UTS of 0.1 wt% nanoclay-EP nanocomposites treated with abrasive paper 320P decreased to 47 MPa (1.5% decrease). When treated with abrasive papers 60P, the UTS decreased to 45.8 MPa (5 % decrease).

The UTS of 0.05 wt% MLG-0.05 wt% nanoclay-EP nanocomposites treated with velvet cloth increased from 48 MPa to 52 MPa (8% increase). The maximum increase in UTS of 0.05 wt% MLG-0.05 wt% nanoclay-EP nanocomposites was observed when 0.05 wt% MLG-0.05 wt% nanoclay-EP nanocomposites treated with abrasive paper 1200P and UTS increased to 58 MPa (20% increase). The UTS of 0.05 wt% MLG-0.05 wt% nanoclay-EP nanocomposites treated with abrasive paper 320P decreased to 47 MPa (1.5% decrease). When treated with abrasive papers 60P, the UTS decreased to 45.8 MPa (5 % decrease).

The UTS of 0.5 wt% MLG-EP nanocomposites treated with velvet cloth increased from 64 MPa to 67 MPa (3.7% increase). The maximum increase in UTS of 0.5 wt% MLG-EP nanocomposites was observed when 0.5 wt% MLG-EP nanocomposites treated with abrasive paper 1200P and UTS increased to 73 MPa (13.3% increase). The UTS of 0.5 wt% MLG-EP nanocomposites treated with abrasive paper 320P decreased to 60 MPa (7% decrease). When treated with abrasive papers 60P, the UTS decreased to 55 MPa (14 % decrease).

The UTS of 0.5 wt% nanoclay-EP nanocomposites treated with velvet cloth increased from 53 MPa to 57 MPa (7% increase). The maximum increase in UTS of 0.5 wt% nanoclay-EP nanocomposites was observed when 0.5 wt% nanoclay-EP nanocomposites treated with abrasive paper 1200P and UTS increased to 63 MPa (19% increase). The UTS of 0.5 wt% nanoclay-EP nanocomposites treated with abrasive paper 320P decreased to 52 MPa (1% decrease). When treated with abrasive papers 60P, the UTS decreased to 50 MPa (4.5% decrease).

The UTS of 0.25 wt% MLG-0.25 wt% nanoclay-EP nanocomposites treated with velvet cloth increased from 68 MPa to 70 MPa (3.5% increase). The maximum increase in UTS of 0.25 wt% MLG-0.25 wt% nanoclay-EP nanocomposites was observed when 0.25 wt% MLG-0.25 wt% nanoclay-EP nanocomposites treated with abrasive paper 1200P and UTS increased to 77 MPa (12% increase). The UTS of 0.25 wt% MLG-0.25 wt% nanoclay-EP nanocomposites treated with abrasive paper 320P decreased to 64 MPa (6% decrease). When treated with abrasive papers 60P, the UTS decreased to 59 MPa (13% decrease).

The UTS of 1.0 wt% MLG-EP nanocomposites treated with velvet cloth increased from 59 MPa to 62 MPa (3.9% increase). The maximum increase in UTS of 1.0 wt% MLG-EP nanocomposites was observed when 1.0 wt% MLG-EP nanocomposites treated with

abrasive paper 1200P and UTS increased to 68 MPa (14.3% increase). The UTS of 1.0 wt% MLG-EP nanocomposites treated with abrasive paper 320P decreased to 55 MPa (7.6% decrease). When treated with abrasive papers 60P, the UTS decreased to 51 MPa (15 % decrease).

The UTS of 1.0 wt% nanoclay-EP nanocomposites treated with velvet cloth increased from 47 MPa to 51 MPa (8% increase). The maximum increase in UTS of 1.0 wt% nanoclay-EP nanocomposites was observed when 1.0 wt% nanoclay-EP nanocomposites treated with abrasive paper 1200P and UTS increased to 57 MPa (21% increase). The UTS of 1.0 wt% nanoclay-EP nanocomposites treated with abrasive paper 320P decreased to 46 MPa (1.5% decrease). When treated with abrasive papers 60P, the UTS decreased to 45 MPa (3 % decrease).

The UTS of 0.5 wt% MLG-0.5 wt% nanoclay-EP nanocomposites treated with velvet cloth increased from 63 MPa to 66 MPa (3.7% increase). The maximum increase in UTS of 0.5 wt% MLG-0.5 wt% nanoclay-EP nanocomposites was observed when 0.5 wt% MLG-0.5 wt% nanoclay-EP nanocomposites treated with abrasive paper 1200P and UTS increased to 72 MPa (13% increase). The UTS of 0.5 wt% MLG-0.5 wt% nanoclay-EP nanocomposites treated with abrasive paper 320P decreased to 59 MPa (7% decrease). When treated with abrasive papers 60P, the UTS decreased to 55 MPa (14% decrease).

The increase in UTS with velvet cloth and abrasive paper 1200P can be attributed to the smoothening of surfaces as as-cast specimens had surface roughness values between ±43 µm. In comparison, the surface roughness of MLG-nanoclay-EP nanocomposites treated with velvet cloth varied between ±33 µm and that of abrasive paper 1200P varied between ±13 µm. Therefore, strength can be increased by treatment with velvet cloth and abrasive paper 1200P. On the contrary, the surface roughness of MLG-nanoclay-EP

nanocomposites treated with 320P varied between ±52 μm and that of abrasive paper 60P varied between ±103 μm. Therefore, it can be concluded that surface roughness beyond about ±20 μm has detrimental effect on tensile strength of MLG-nanoclay-EP nanocomposites. Accordingly, the surface roughness below about ±20 μm is benign for tensile properties of MLG-nanoclay-EP nanocomposites.

The influence of topography on tensile strain is shown in Figure 56. The tensile strain kept increasing with coarser topography which can be attributed to lower stiffness and strength values. The tensile strain did not change much with velvet cloth and slightly increased in case of abrasive paper 1200P. Therefore, overall better tensile properties can be achieved when samples are treated with velvet cloth and abrasive paper 1200P.

The influence of topography on flexural strength is shown in Figure 58. The flexural strength of as-cast monolithic epoxy sample is 53 MPa. When treated with velvet cloth, the flexural strength increases to 57 MPa (7% increase). The flexural strength of sample treated with abrasive paper 1200P is 66 MPa (25% increase). The flexural strength of sample treated with 320P remained high and was 65 MPa (22% increase).

The flexural strength of as-cast 0.1 wt% MLG-EP nanocomposites is 75 MPa. When treated with velvet cloth, the flexural strength increases to 79 MPa (5% increase). The flexural strength of sample treated with abrasive paper 1200P is 88 MPa (18% increase). The flexural strength of sample treated with 320P remained high and was 82 MPa (9% increase).

The flexural strength of as-cast 0.1 wt% nanoclay-EP nanocomposites is 63 MPa. When treated with velvet cloth, the flexural strength increases to 70 MPa (11% increase). The flexural strength of sample treated with abrasive paper 1200P is 81 MPa (29% increase).

The flexural strength of sample treated with 320P remained high and was 68 MPa (8% increase).

The flexural strength of as-cast 0.05 wt% MLG-0.05 wt% nanoclay-EP nanocomposites is 63 MPa. When treated with velvet cloth, the flexural strength increases to 70 MPa (11% increase). The flexural strength of sample treated with abrasive paper 1200P is 81 MPa (29% increase). The flexural strength of sample treated with 320P remained high and was 70 MPa (8% increase).

The flexural strength of as-cast 0.5 wt% MLG-EP nanocomposites is 79 MPa. When treated with velvet cloth, the flexural strength increases to 82 MPa (4% increase). The flexural strength of sample treated with abrasive paper 1200P is 90 MPa (14% increase). The flexural strength of sample treated with 320P remained high and was 76 MPa (4% increase).

The flexural strength of as-cast 0.5 wt% nanoclay-EP nanocomposites is 67 MPa. When treated with velvet cloth, the flexural strength increases to 74 MPa (11% increase). The flexural strength of sample treated with abrasive paper 1200P is 85 MPa (27% increase). The flexural strength of sample treated with 320P remained high and was 72 MPa (7% increase).

The flexural strength of as-cast 0.25 wt% MLG-0.25 wt% nanoclay-EP nanocomposites is 82 MPa. When treated with velvet cloth, the flexural strength increases to 85 MPa (3% increase). The flexural strength of sample treated with abrasive paper 1200P is 93 MPa (14% increase). The flexural strength of sample treated with 320P remained high and was 80 MPa (2% decrease).

The flexural strength of as-cast 1.0 wt% MLG-EP nanocomposites is 70 MPa. When treated with velvet cloth, the flexural strength increases to 73 MPa (4% increase). The flexural strength of sample treated with abrasive paper 1200P is 81 MPa (16% increase). The flexural strength of sample treated with 320P remained high and was 72 MPa (3% increase).

The flexural strength of as-cast 1.0 wt% nanoclay-EP nanocomposites is 62 MPa. When treated with velvet cloth, the flexural strength increases to 69 MPa (10% increase). The flexural strength of sample treated with abrasive paper 1200P is 79 MPa (25% increase). The flexural strength of sample treated with 320P remained high and was 67 MPa (7% increase).

The flexural strength of as-cast 0.5 wt% MLG-0.5 wt% nanoclay-EP nanocomposites is 78 MPa. When treated with velvet cloth, the flexural strength increases to 81 MPa (4% increase). The flexural strength of sample treated with abrasive paper 1200P is 89 MPa (14% increase). The flexural strength of sample treated with 320P remained high and was 80 MPa (3% increase).

In comparison to tensile strength which increased only to 3%, an increase of 22% in flexural strength indicates that surface roughness up to ±20 μm is not detrimental to flexural strength. The flexural strength of sample treated with abrasive paper 60P is 54 MPa which is nearly equal to that of as-cast sample. In comparison to tensile strength which decreased by 2%, the flexural strength value of sample treated with 60P indicates that surface roughness up to ±30 μm has detrimental effect on tensile strength while flexural strength seems impervious.

The influence of topography on flexural strain (%) is shown in Figure 59. The flexural strain nearly remained the same till abrasive paper 320P. However, it increased when sample was treated with abrasive paper 60P. This increase in flexural strain can be explained on the basis of decreased flexural strength.

The influence of topography on fracture toughness (K_{1C}) is shown in Figure 60. No specific trend on K_{1C} was observed and K_{1C} remained nearly the same. One reason can be the orientation of topography with respect to notch and loading axis. The samples were treated with abrasive papers only along wider surfaces and not on the sides of the specimens. Therefore, when the samples were subjected to bending loading, the topographically treated surfaces were parallel to the axis of loading (Figure 52). The deformation and fracture takes place at the tip of notch whose size (3 mm) is much bigger than the surface roughness of topographically modified surfaces. These two reasons may contribute to topography (up to ±30 µm) having no influence on K_{1C}. The values show that standard deviation is different for different samples. It can be because the tip of notch was sharpened manually by a fresh razor blade which may not generate surfaces of equal length and curvature. In addition, the volume fraction, size, and distribution of porosity can be another factor which can influence the mechanical properties.

The variation in G_{1C} of topographically modified monolithic epoxy samples is shown in Figure 61. The trend shows that G_{1C} increases as the coarseness of topography increases. However, as topography did not show significant influence on K_{1C}, the authors are skeptical in believing that this increase in G_{1C} is directly coming from topography. In calculating G_{1C}, K_{1C}^2 is divided by Young's modulus. As Young's modulus decreased with coarse topography, therefore the increase in G_{1C} is possibly stemming from decreased Young's modulus

The Charpy impact toughness values are shown in Figure 62. The Charpy impact toughness value of as-cast monolithic epoxy sample is 0.9 kJ/m^2. After treatment with velvet cloth, the monolithic epoxy sample increased to 1.2 kJ/m^2 (33% increase). The values of samples treated with abrasive papers 1200P, 320P, and 60P are 1, 0.8, and 0.9 kJ/m^2, respectively.

The Charpy impact toughness value of as-cast 0.1 wt% MLG-EP nanocomposites is 1.2 kJ/m^2. After treatment with velvet cloth, the 0.1 wt% MLG-EP nanocomposites increased to 1.3 kJ/m^2 (9% increase). The values of samples treated with abrasive papers 1200P, 320P, and 60P are 1.5, 1.2, and 1.1 kJ/m^2, respectively.

The Charpy impact toughness value of as-cast 0.1 wt% nanoclay-EP nanocomposites is 1.2 kJ/m^2. After treatment with velvet cloth, the 0.1 wt% nanoclay-EP nanocomposites increased to 1.3 kJ/m^2 (9% increase). The values of samples treated with abrasive papers 1200P, 320P, and 60P are 1.5, 1.2, and 1.1 kJ/m^2, respectively.

The Charpy impact toughness value of as-cast 0.05 wt% MLG-0.05 wt% nanoclay-EP nanocomposites is 1.2 kJ/m^2. After treatment with velvet cloth, the 0.05 wt% MLG-0.05 wt% nanoclay-EP nanocomposites increased to 1.3 kJ/m^2 (9% increase). The values of samples treated with abrasive papers 1200P, 320P, and 60P are 1.5, 1.2, and 1.1 kJ/m^2, respectively.

The Charpy impact toughness value of as-cast 0.5 wt% MLG-EP nanocomposites is 1.31 kJ/m^2. After treatment with velvet cloth, the 0.5 wt% MLG-EP nanocomposites increased to 1.45 kJ/m^2 (11% increase). The values of samples treated with abrasive papers 1200P, 320P, and 60P are 1.58, 1.25, and 1.21 kJ/m^2, respectively.

The Charpy impact toughness value of as-cast 0.5 wt% nanoclay-EP nanocomposites is 1.23 kJ/m^2. After treatment with velvet cloth, the 0.5 wt% nanoclay-EP nanocomposites increased to 1.42 kJ/m^2 (9% increase). The values of samples treated with abrasive papers 1200P, 320P, and 60P are 1.33, 1.15, and 1.13 kJ/m^2, respectively.

The Charpy impact toughness value of as-cast 0.25 wt% MLG-0.25 wt% nanoclay-EP nanocomposites is 1.35 kJ/m^2. After treatment with velvet cloth, the 0.25 wt% MLG-0.25 wt% nanoclay-EP nanocomposites increased to 1.49 kJ/m^2 (10% increase). The values of samples treated with abrasive papers 1200P, 320P, and 60P are 1.61, 1.28, and 1.25 kJ/m^2, respectively.

The Charpy impact toughness value of as-cast 1.0 wt% MLG-EP nanocomposites is 1.1 kJ/m^2. After treatment with velvet cloth, the 1.0 wt% MLG-EP nanocomposites increased to 1.2 kJ/m^2 (13.2% increase). The values of samples treated with abrasive papers 1200P, 320P, and 60P are 1.3, 1.0, and 1.0 kJ/m^2, respectively.

The Charpy impact toughness value of as-cast 1.0 wt% nanoclay-EP nanocomposites is 0.8 kJ/m^2. After treatment with velvet cloth, the 1.0 wt% nanoclay-EP nanocomposites increased to 0.8 kJ/m^2 (2% increase). The values of samples treated with abrasive papers 1200P, 320P, and 60P are 0.9, 0.8, and 0.8 kJ/m^2, respectively.

The Charpy impact toughness value of as-cast 0.5 wt% MLG-0.5 wt% nanoclay-EP nanocomposites is 1.29 kJ/m^2. After treatment with velvet cloth, the 0.5 wt% MLG-0.5 wt% nanoclay-EP nanocomposites increased to 1.35 kJ/m^2 (5% increase). The values of samples treated with abrasive papers 1200P, 320P, and 60P are 1.4, 1.2, and 1.2 kJ/m^2, respectively. Although there was no significant difference observed in fracture toughness

values, however, treatment of 0.05 wt% MLG-0.05 wt% nanoclay-EP samples with abrasive papers showed a significant impact on Charpy impact toughness values.

The variation in microhardness is shown in Figure 63. The hardness of as-cast monolithic epoxy sample is 278 HV. When treated with velvet cloth, the microhardness increases to 391 HV (41% increase). And when treated with abrasive paper 1200P, microhardness increases to 438 HV (58% increase).

The hardness of as-cast 0.1 wt% MLG-EP sample is 321 HV. When treated with velvet cloth, the microhardness increases to 348 HV (8% increase). When treated with abrasive paper 1200P, microhardness increases to 368 HV (14% increase). The microhardness values of samples treated with abrasive papers 320P and 60 were 316 HV (3% decrease) and 265 HV (5% decrease).

The hardness of as-cast 0.1 wt% nanoclay-EP sample is 297 HV. When treated with velvet cloth, the microhardness increases to 329 HV (11% increase). When treated with abrasive paper 1200P, microhardness increases to 351 HV (18% increase). The microhardness values of samples treated with abrasive papers 320P and 60P were 296 HV (1% decrease) and 279 HV (6% decrease).

The hardness of as-cast 0.05 wt% MLG-0.05 wt% nanoclay-EP sample is 297 HV. When treated with velvet cloth, the microhardness increases to 329 HV (11% increase). When treated with abrasive paper 1200P, microhardness increases to 351 HV (18% increase). The microhardness values of samples treated with abrasive papers 320P and 60P were 296 HV (1% decrease) and 279 HV (6% decrease).

The hardness of as-cast 0.5 wt% MLG-EP sample is 359 HV. When treated with velvet cloth, the microhardness increases to 372 HV (4% increase). When treated with abrasive

paper 1200P, microhardness increases to 395 HV (10% increase). The microhardness values of samples treated with abrasive papers 320P and 60 were 335 HV (7% decrease) and 298 HV (17% decrease).

The hardness of as-cast 0.5 wt% nanoclay-EP sample is 330 HV. When treated with velvet cloth, the microhardness increases to 363 HV (10% increase). When treated with abrasive paper 1200P, microhardness increases to 384 HV (16% increase). The microhardness values of samples treated with abrasive papers 320P and 60P were 329 HV (1% decrease) and 312 HV (5% decrease).

The hardness of as-cast 0.25 wt% MLG-0.25 wt% nanoclay-EP sample is 365 HV. When treated with velvet cloth, the microhardness increases to 378 HV (4% increase). When treated with abrasive paper 1200P, microhardness increases to 401 HV (10% increase). The microhardness values of samples treated with abrasive papers 320P and 60P were 341 HV (7% decrease) and 304 HV (17% decrease).

The hardness of as-cast 1.0 wt% MLG-EP sample is 372 HV. When treated with velvet cloth, the microhardness increases to 385 HV (4% increase). When treated with abrasive paper 1200P, microhardness increases to 408 HV (10% increase). The microhardness values of samples treated with abrasive papers 320P and 60 were 348 HV (6% decrease) and 265 HV (16% decrease).

The hardness of as-cast 1.0 wt% nanoclay-EP sample is 347 HV. When treated with velvet cloth, the microhardness increases to 380 HV (9% increase). When treated with abrasive paper 1200P, microhardness increases to 401 HV (15% increase). The microhardness values of samples treated with abrasive papers 320P and 60P were 346 HV (1% decrease) and 329 HV (5% decrease).

The hardness of as-cast 0.5 wt% MLG-0.5 wt% nanoclay-EP sample is 391 HV. When treated with velvet cloth, the microhardness increases to 404 HV (3% increase). When treated with abrasive paper 1200P, microhardness increases to 428 HV (9% increase). The microhardness values of samples treated with abrasive papers 320P and 60P were 367 HV (6% decrease) and 330 HV (16% decrease).

The comparison between theoretical modulus and strength values as approximated by rule of mixture and experimental values as determined by tensile testing is shown in Figure 64 and Figure 65. The experimental modulus and strength values are lower than the calculated ones that may mainly be because of the relatively poor dispersion of fillers and porosity present in the samples.

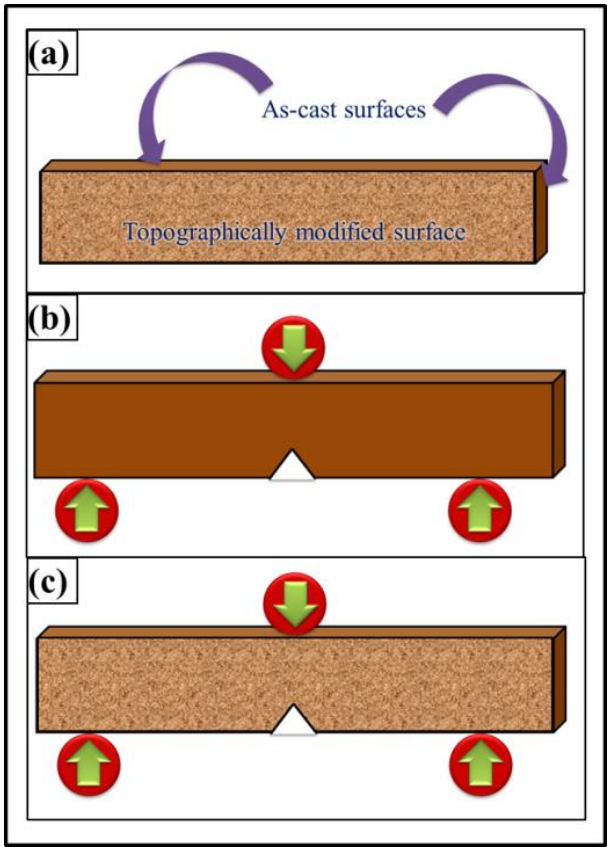

Figure 52: (a) Topographically modified front and back surfaces. The sides were not treated with abrasive papers. (b) As-cast and (c) topographically modified K_{1C} specimen under bending load.

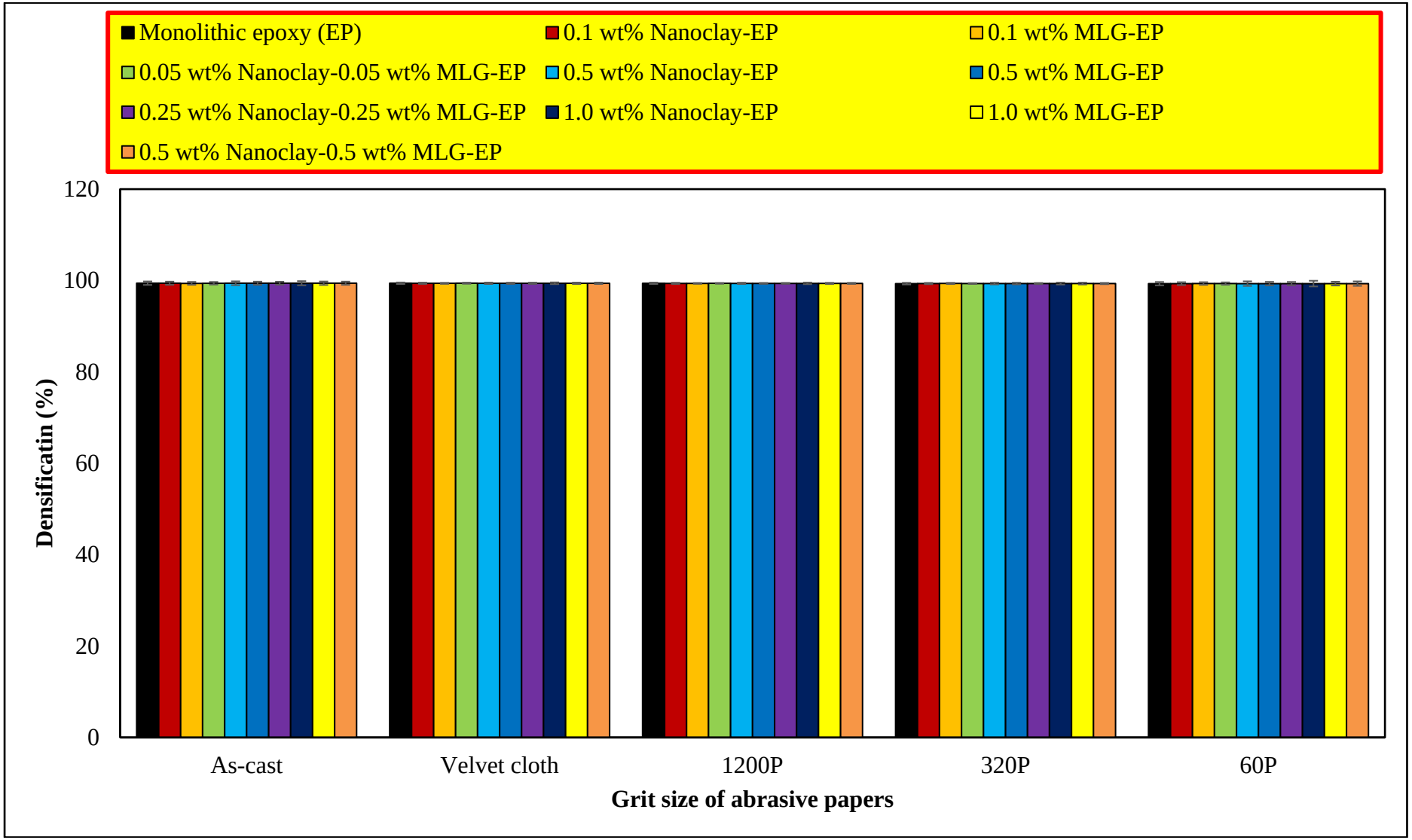

Figure 53: Densification of Nanoclay-MLG-EP nanocomposites after treatment with abrasive papers for 1 min at 150 rpm.

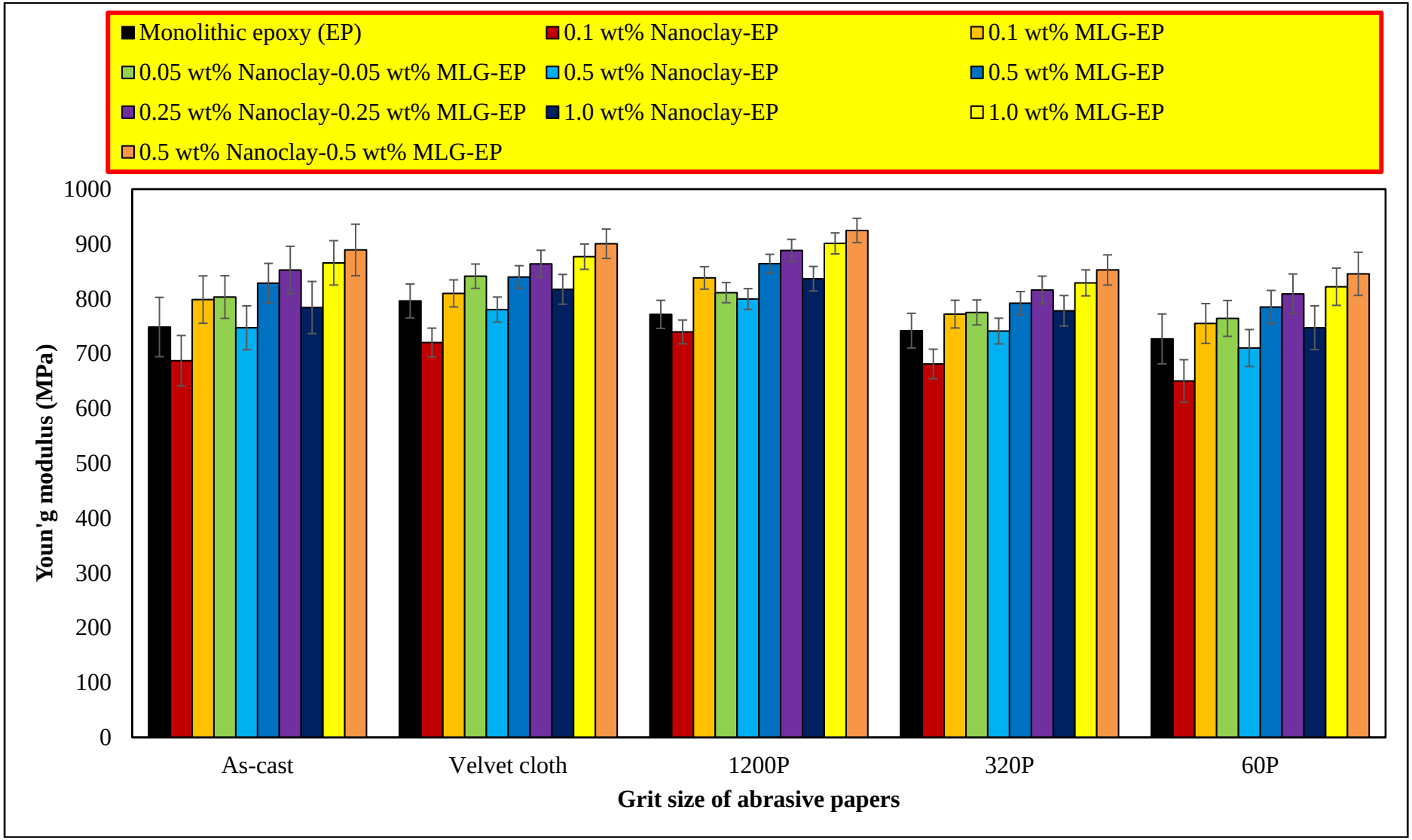

Figure 54: Young's modulus of Nanoclay-MLG-EP nanocomposites after treatment with abrasive papers for 1 min at 150 rpm.

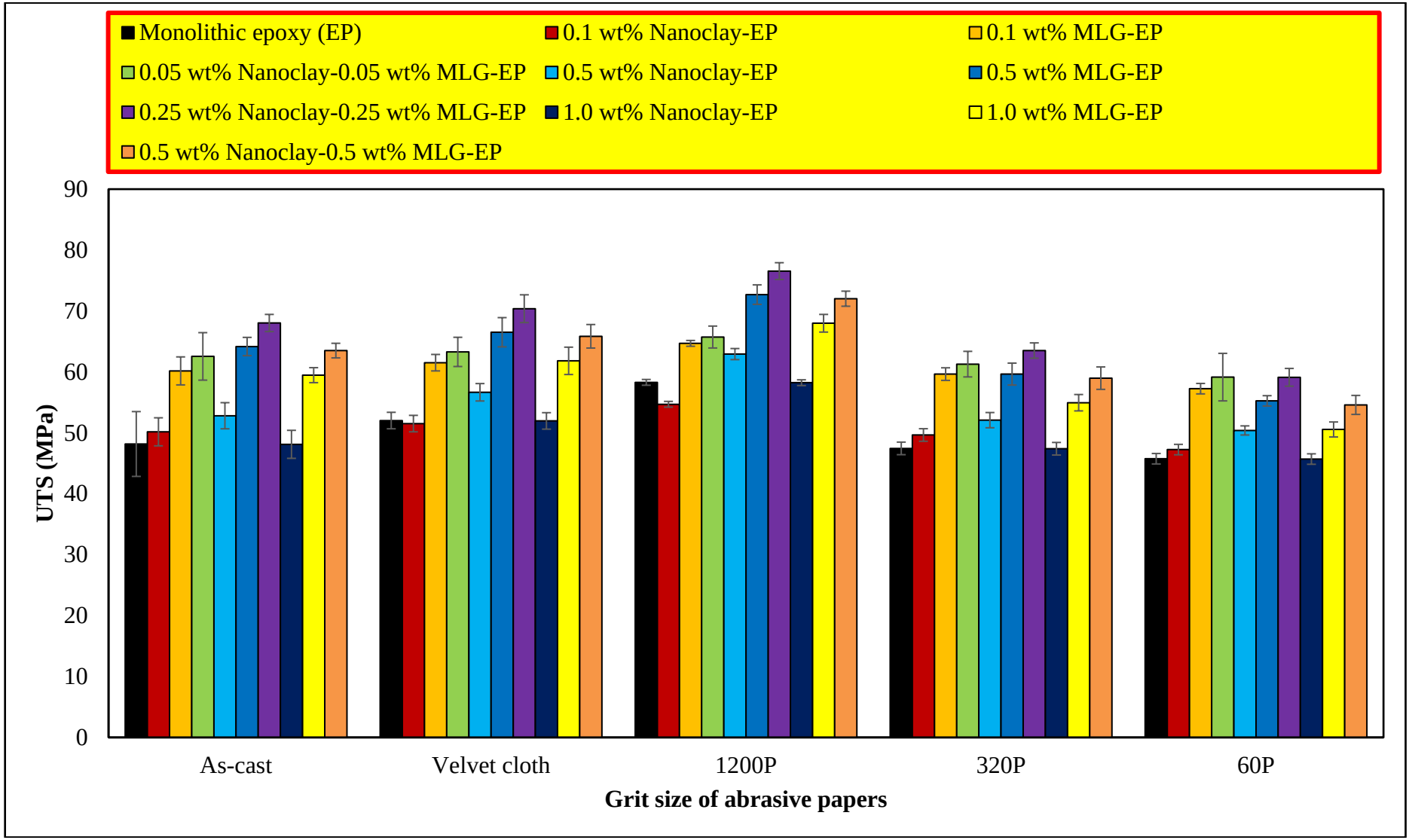

Figure 55: Ultimate tensile strength of Nanoclay-MLG-EP nanocomposites after treatment with abrasive papers for 1 min at 150 rpm.

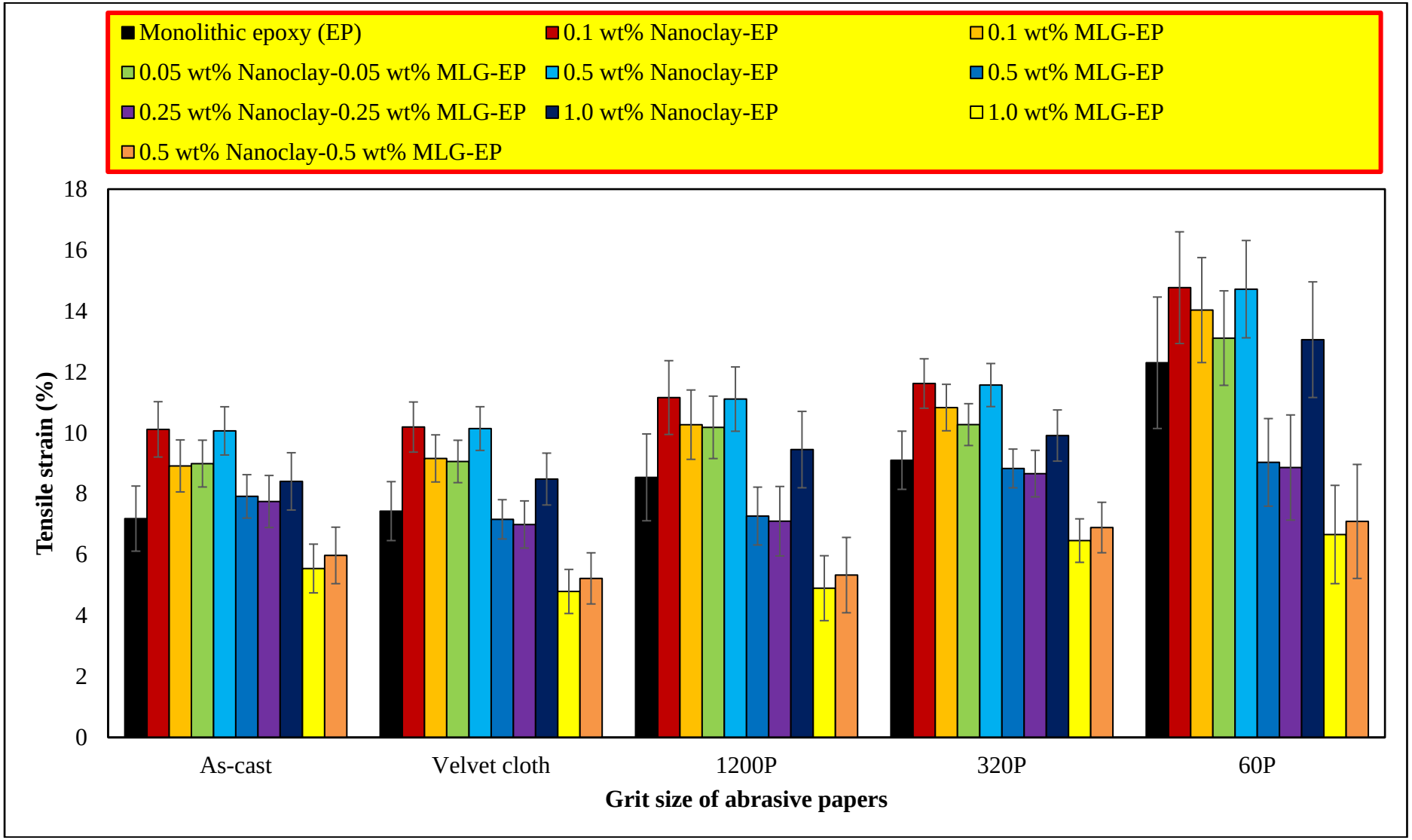

Figure 56: Tensile strain of Nanoclay-MLG-EP nanocomposites after treatment with abrasive papers for 1 min at 150 rpm.

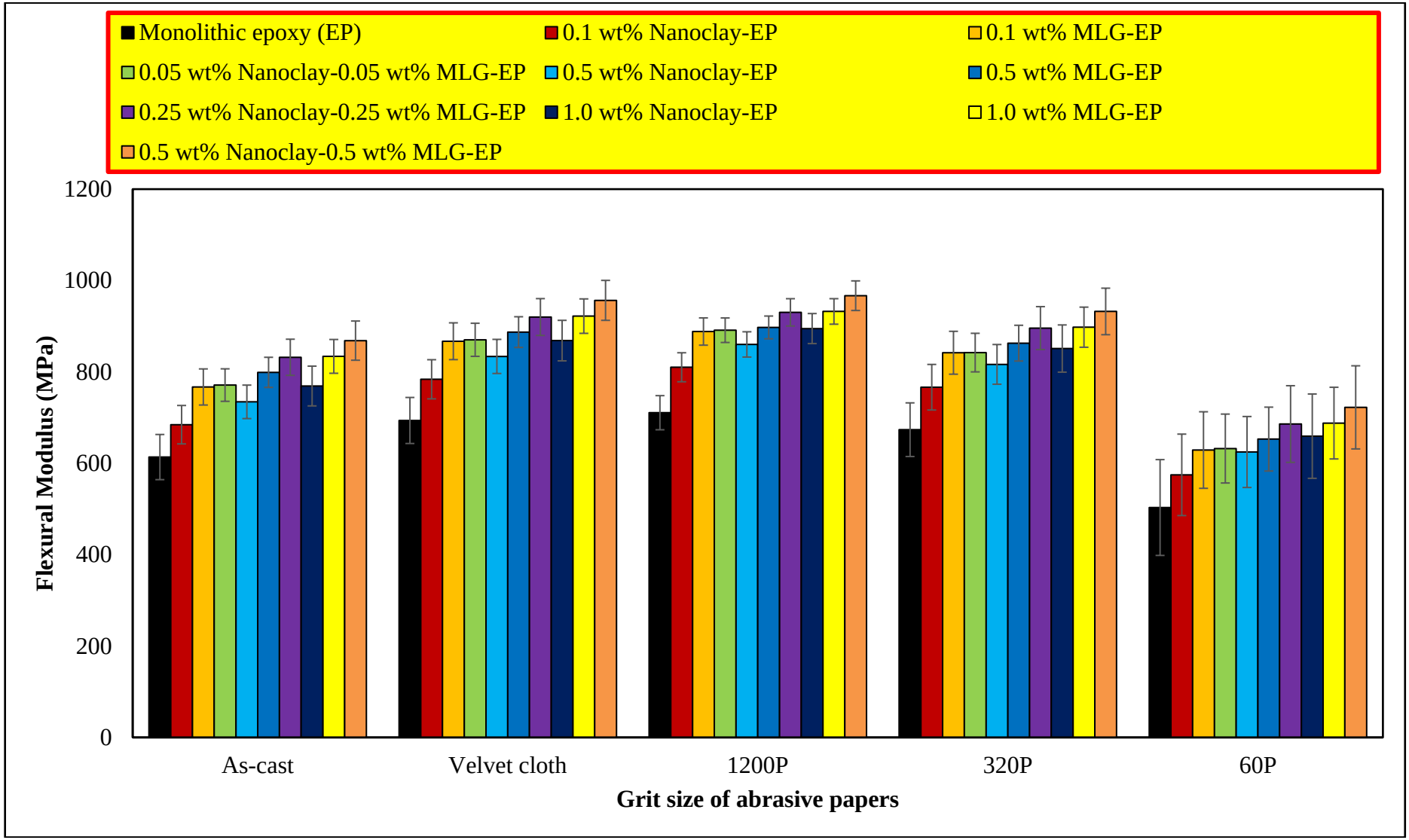

Figure 57: Flexural modulus of Nanoclay-MLG-EP nanocomposites after treatment with abrasive papers for 1 min at 150 rpm.

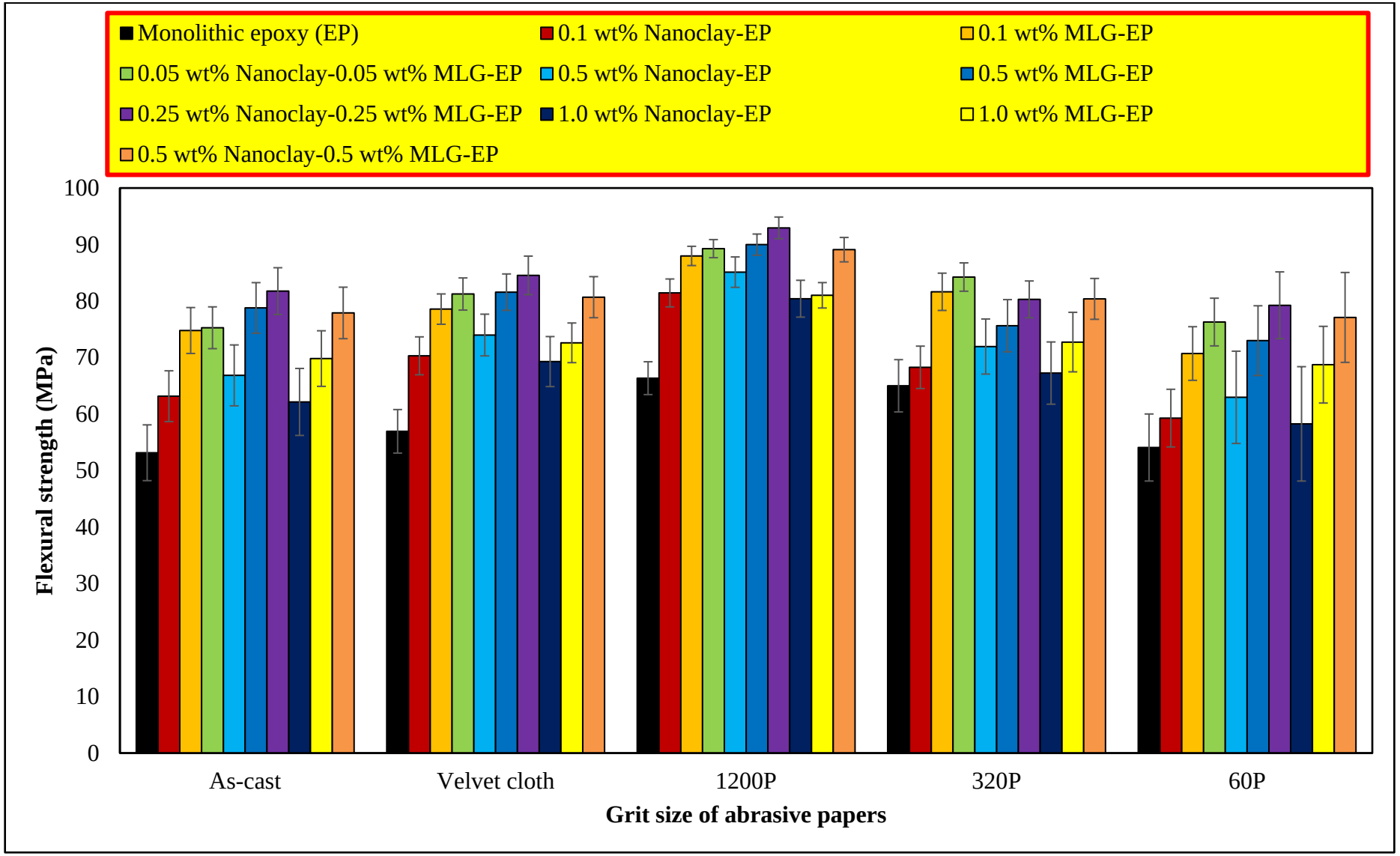

Figure 58: Flexural strength of Nanoclay-MLG-EP nanocomposites after treatment with abrasive papers for 1 min at 150 rpm.

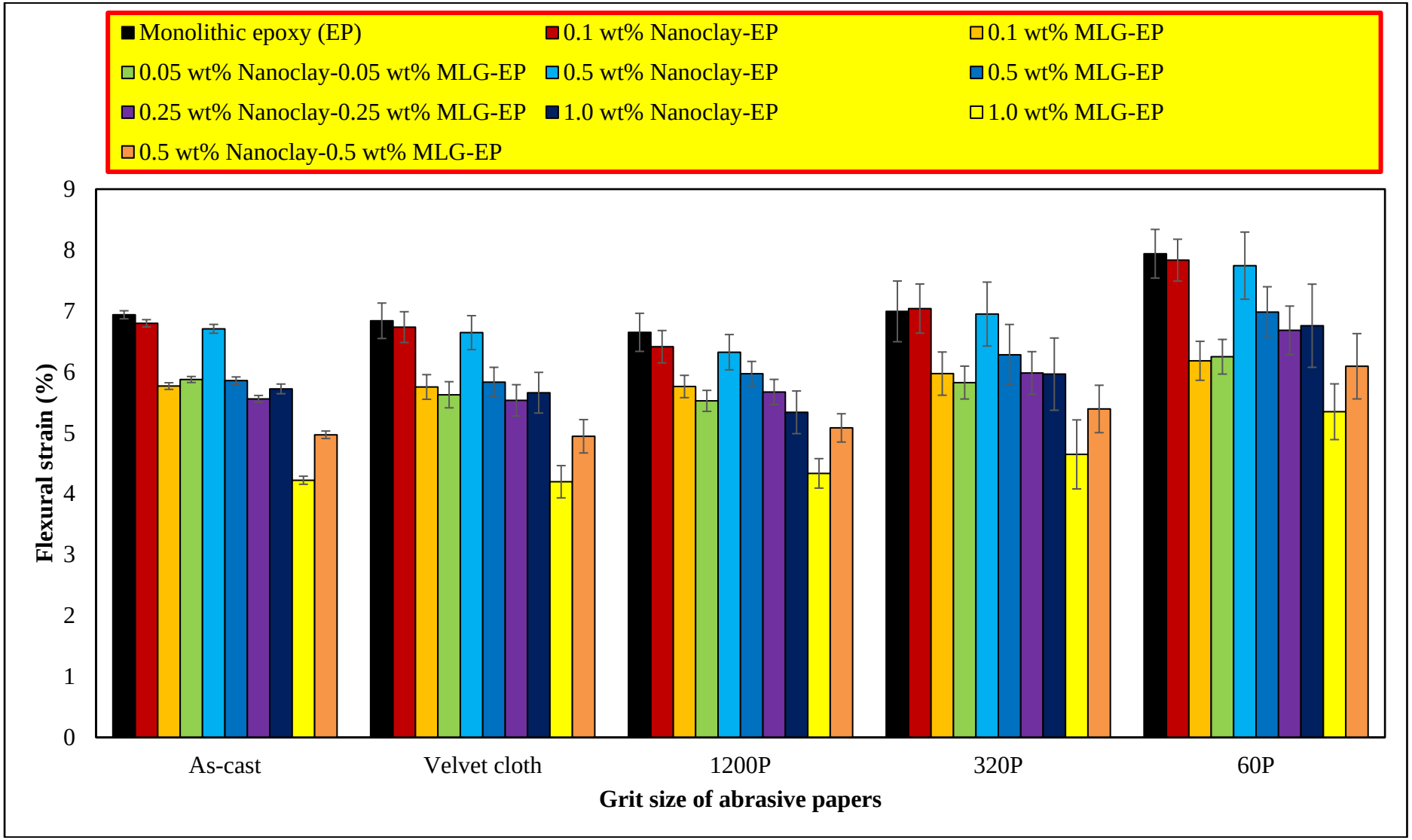

Figure 59: Flexural strain of Nanoclay-MLG-EP nanocomposites after treatment with abrasive papers for 1 min at 150 rpm.

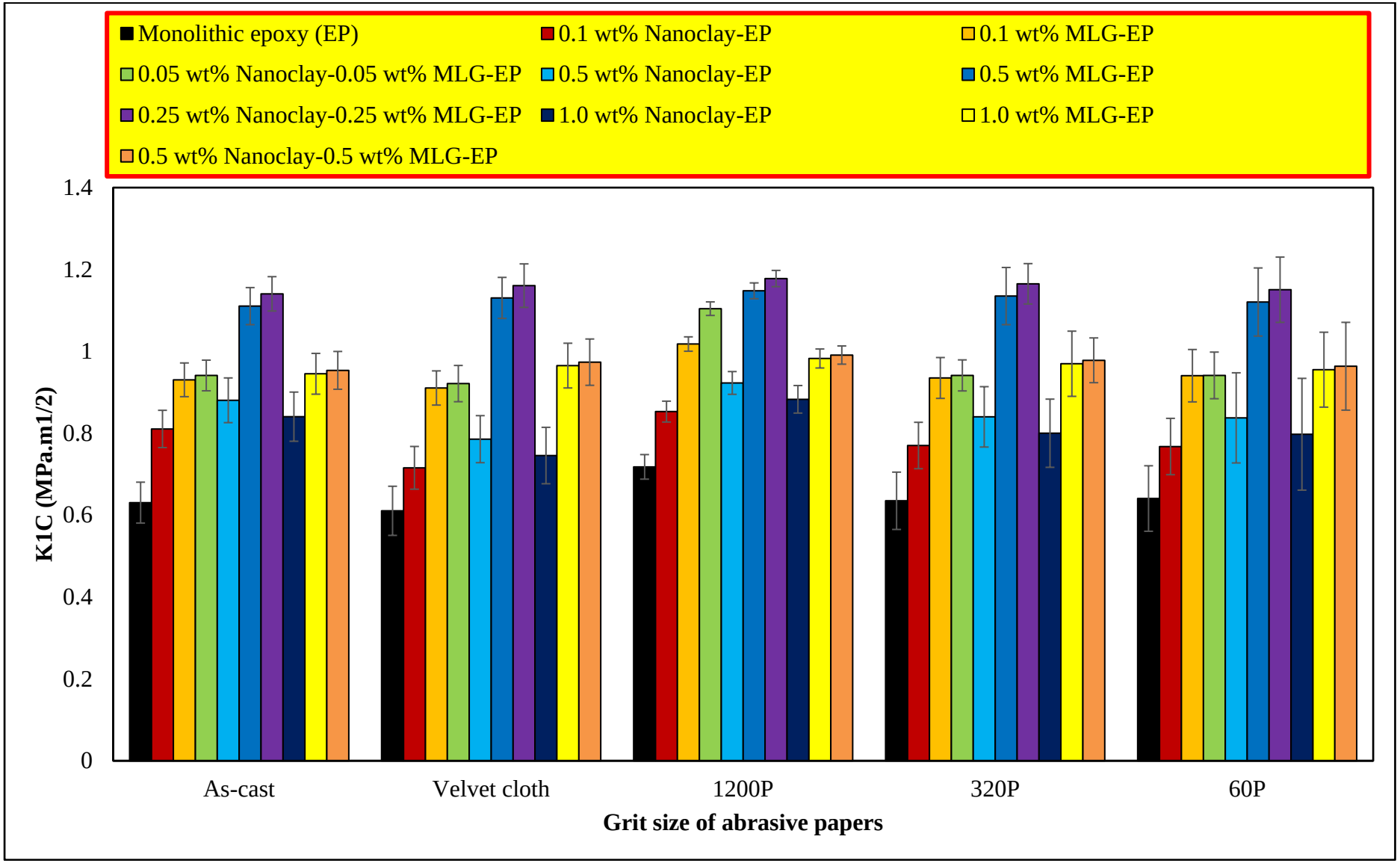

Figure 60: K_{1C} of Nanoclay-MLG-EP nanocomposites after treatment with abrasive papers for 1 min at 150 rpm.

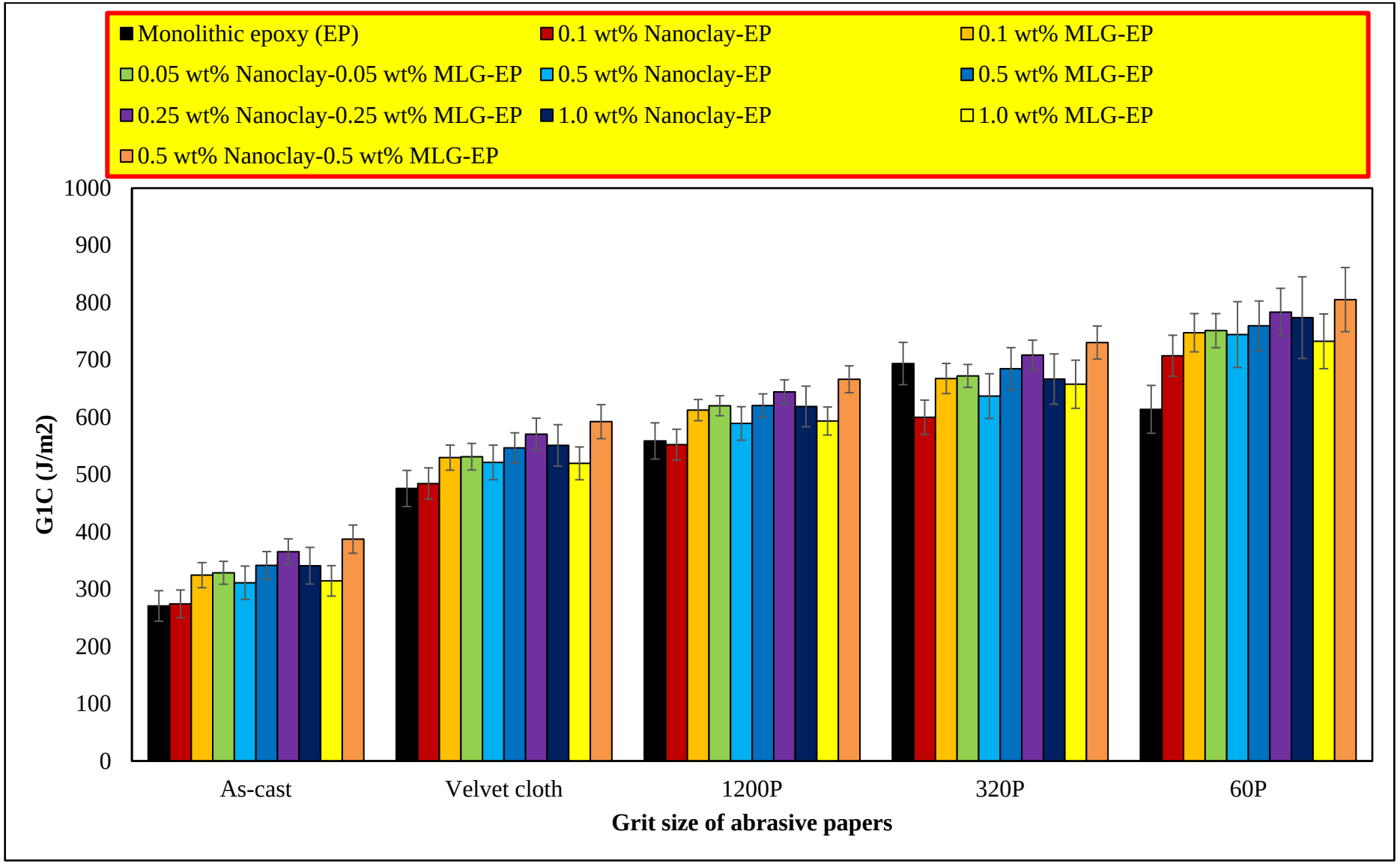

Figure 61: G_{1C} of Nanoclay-MLG-EP nanocomposites after treatment with abrasive papers for 1 min at 150 rpm.

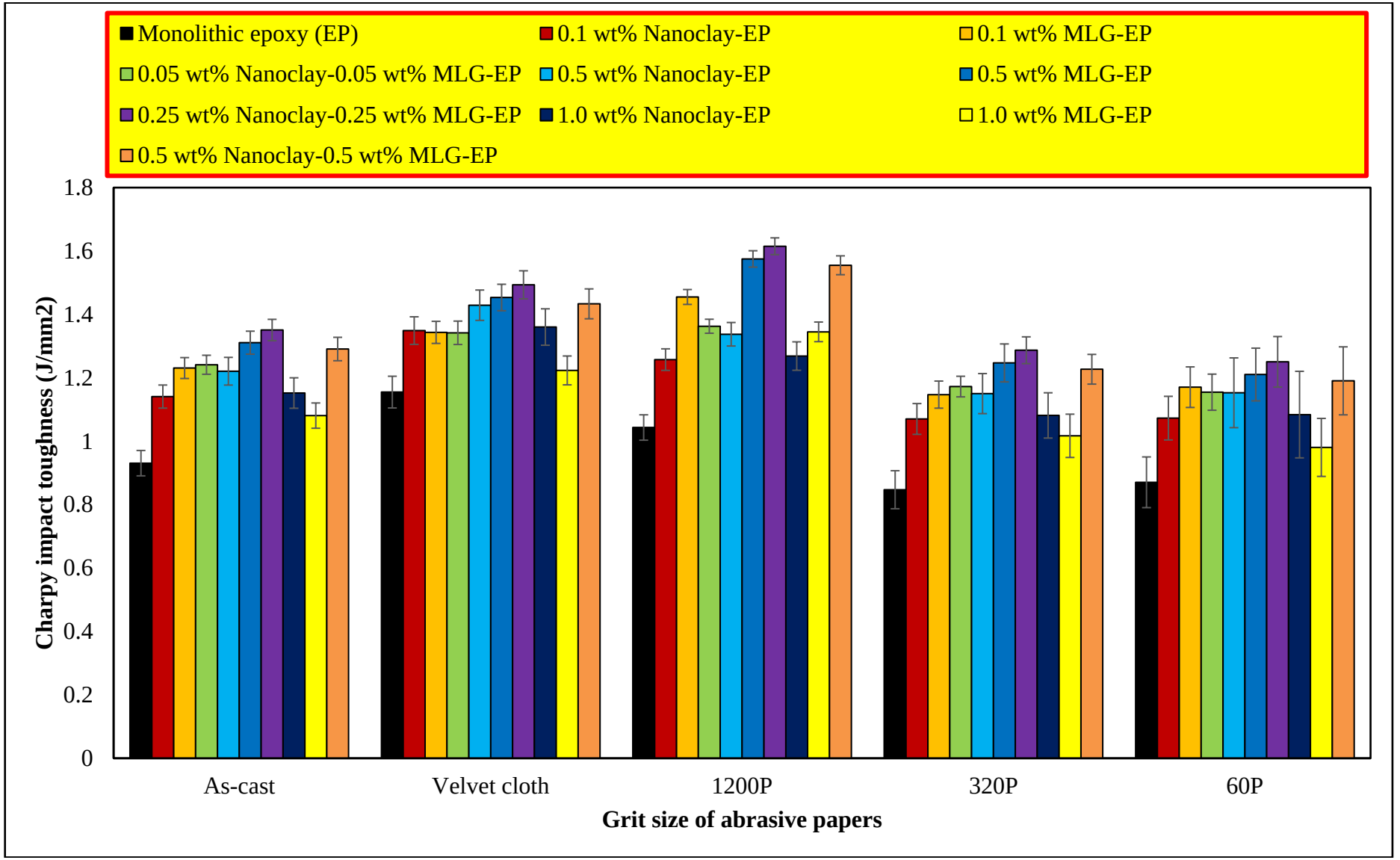

Figure 62: Charpy impact toughness of Nanoclay-MLG-EP nanocomposites after treatment with abrasive papers for 1 min at 150 rpm.

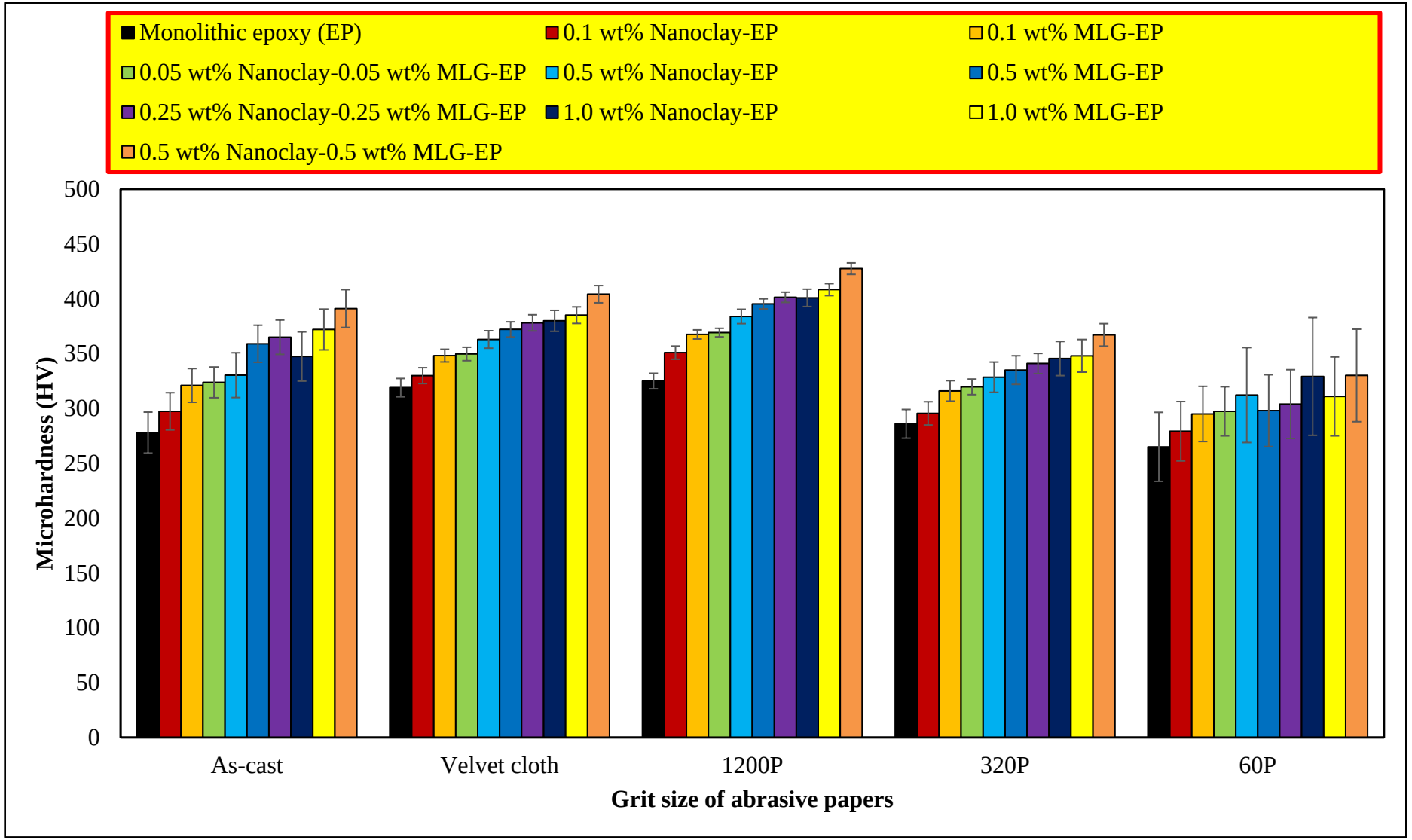

Figure 63: Microhardness of Nanoclay-MLG-EP nanocomposites after treatment with abrasive papers for 1 min at 150 rpm.

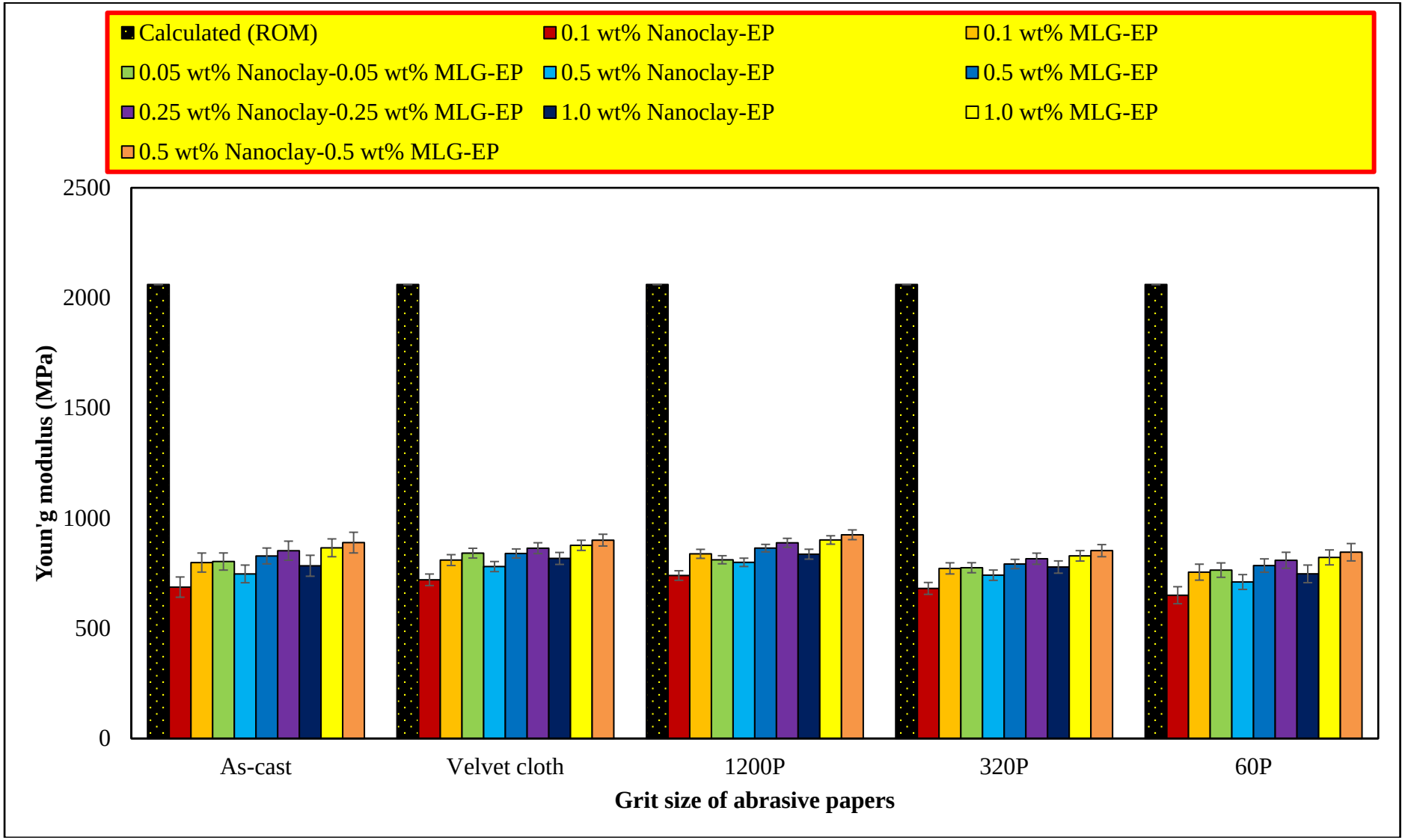

Figure 64: Comparison of Young's modulus with rule of mixture of Nanoclay-MLG-EP nanocomposites after treatment with abrasive papers for 1 min at 150 rpm.

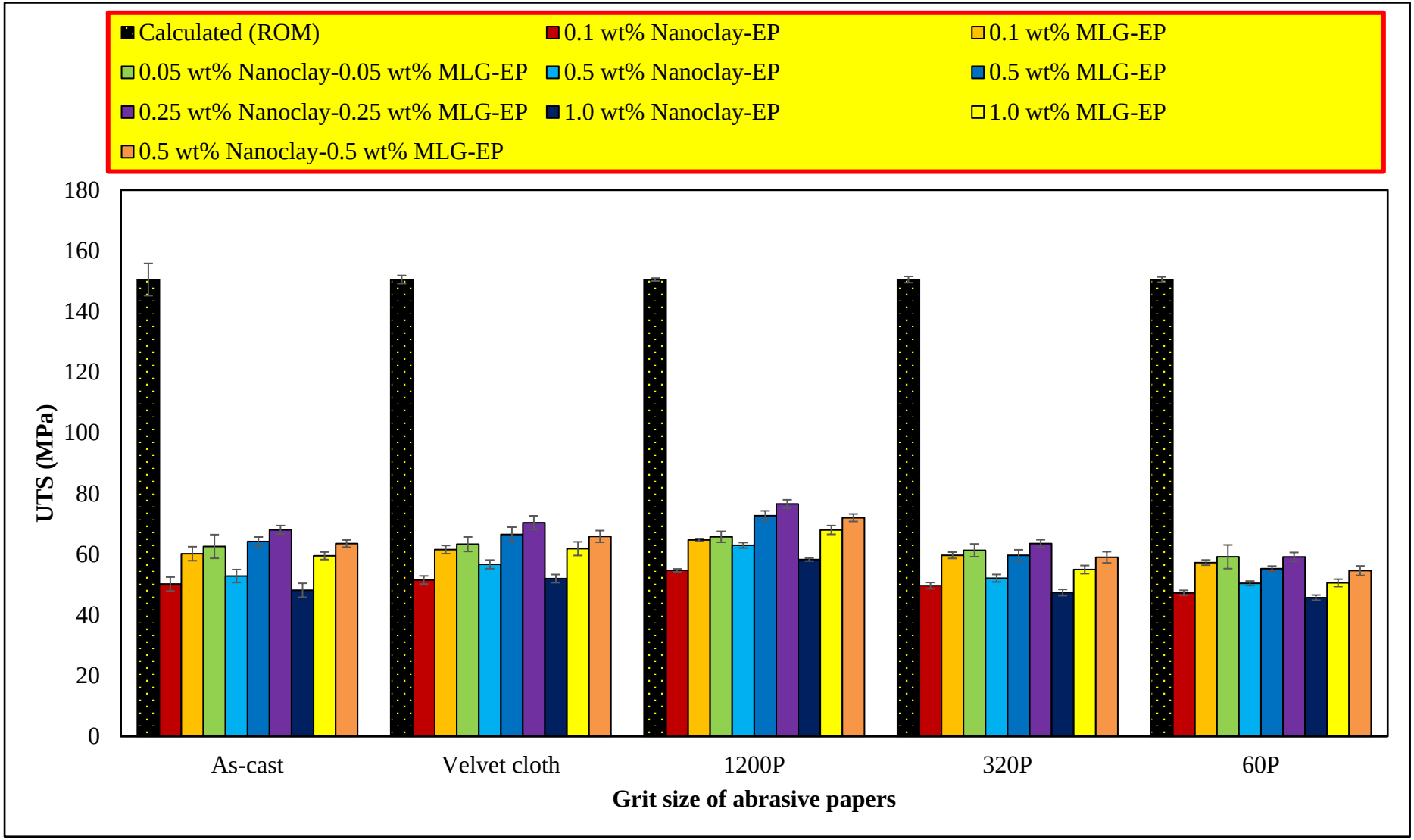

Figure 65: Comparison of UTS with rule of mixture of Nanoclay-MLG-EP nanocomposites after treatment with abrasive papers for 1 min at 150 rpm.

The dynamic mechanical properties are shown in Figure 66-Figure 74. The treatment with abrasive papers has not influenced dynamic mechanical properties of MLG-nanoclay-EP samples. It is because the dynamic mechanical properties are mainly dependent on the structure of sample. As treatment with abrasive papers did not change structure of the nanocomposites, therefore, it did not change the dynamic mechanical properties. It can further be concluded that surface notches up to ±100 µm do not change the dynamic mechanical properties of nanocomposites.

It can be observed that as-cast samples had surface notches stemming from the mold surface. The surface notches in as-cast samples seem inevitable as vibrations and possible wobbling of machine tool yields notches of the surface of mold whose impression is transferred to the surface of samples cast.

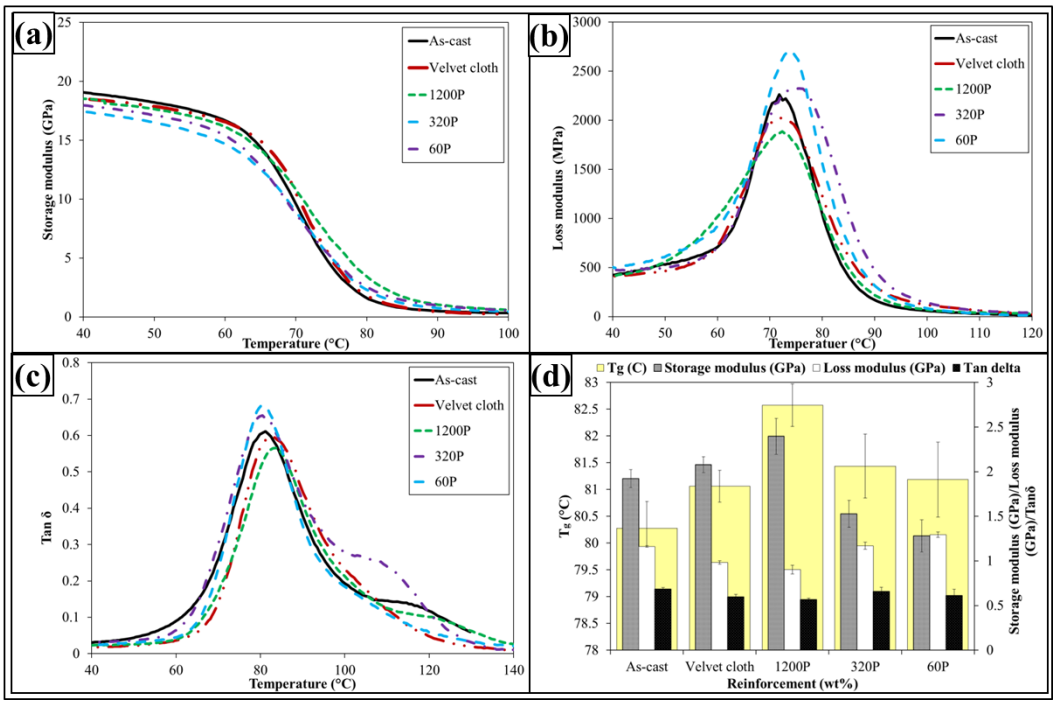

Figure 66: Dynamic mechanical properties: (a) storage modulus, (b) loss modulus, (c) loss factor (Tanδ), and (d) glass transition temperature (T_g), storage modulus, loss modulus, and Tanδ values corresponding to T_g.

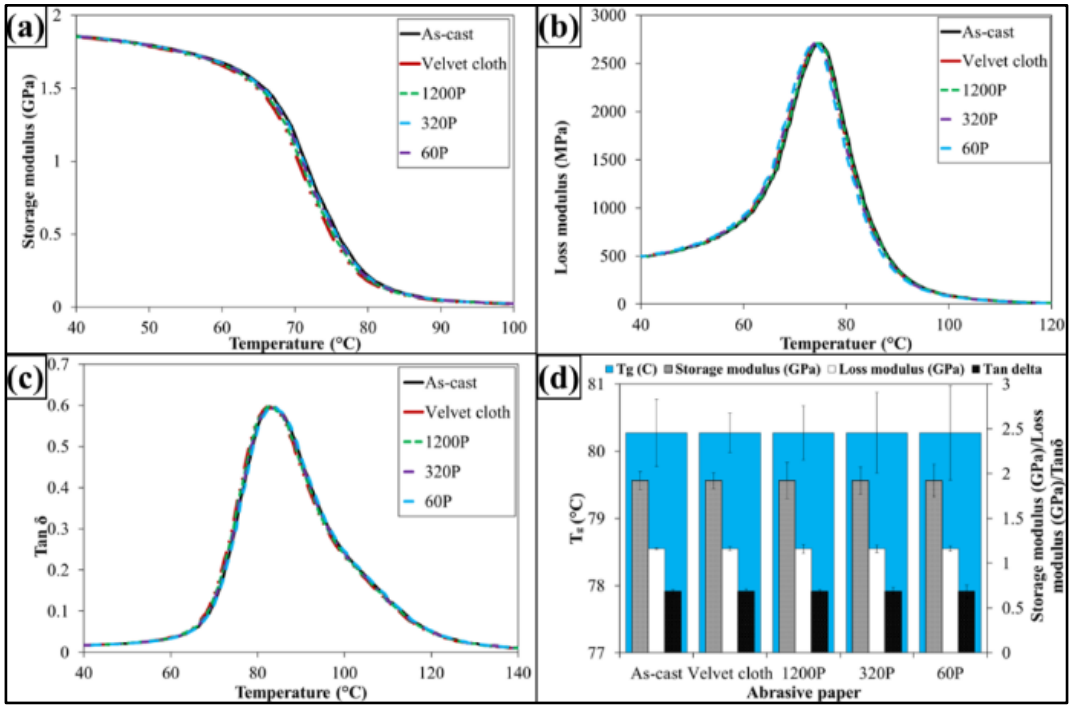

Figure 67. Dynamic mechanical properties of 0.1 wt% MLG-EP nanocomposites: (a) Storage modulus; (b) Loss modulus; (c) Loss factor (Tanδ); and (d) Glass transition temperature (T_g), storage modulus, loss modulus, and Tanδ values corresponding to T_g.

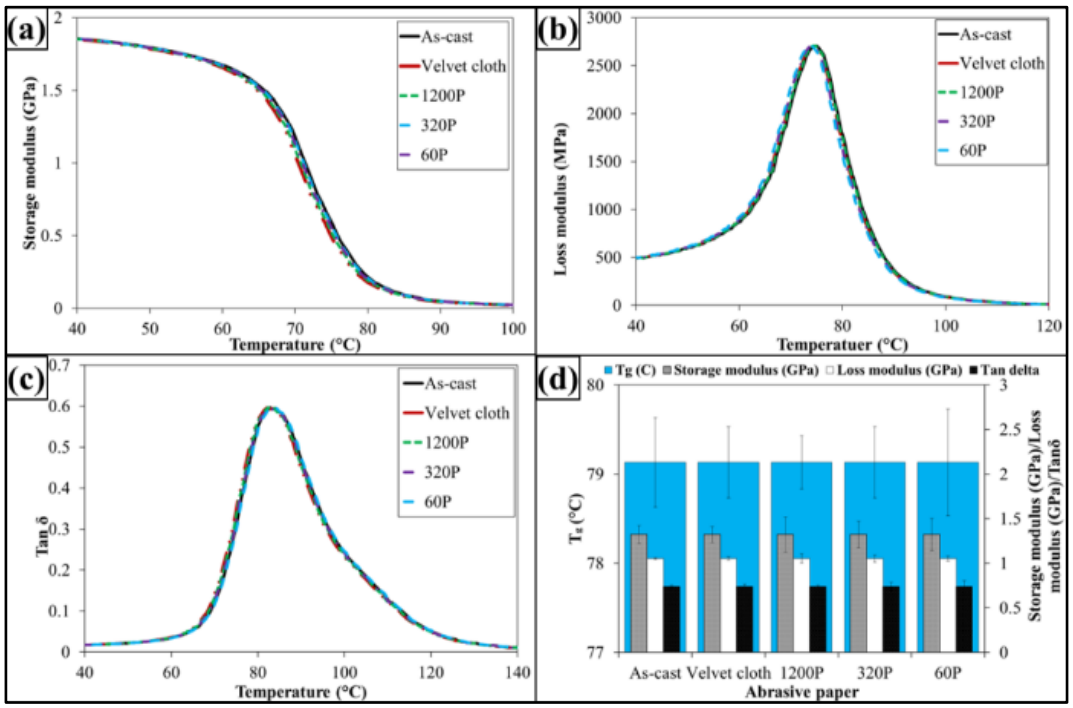

Figure 68. Dynamic mechanical properties of 0.1 wt% nanoclay-EP nanocomposites: (a) Storage modulus; (b) Loss modulus; (c) Loss factor (Tanδ); and (d) Glass transition temperature (T_g); Storage modulus, loss modulus, and Tanδ values corresponding to T_g.

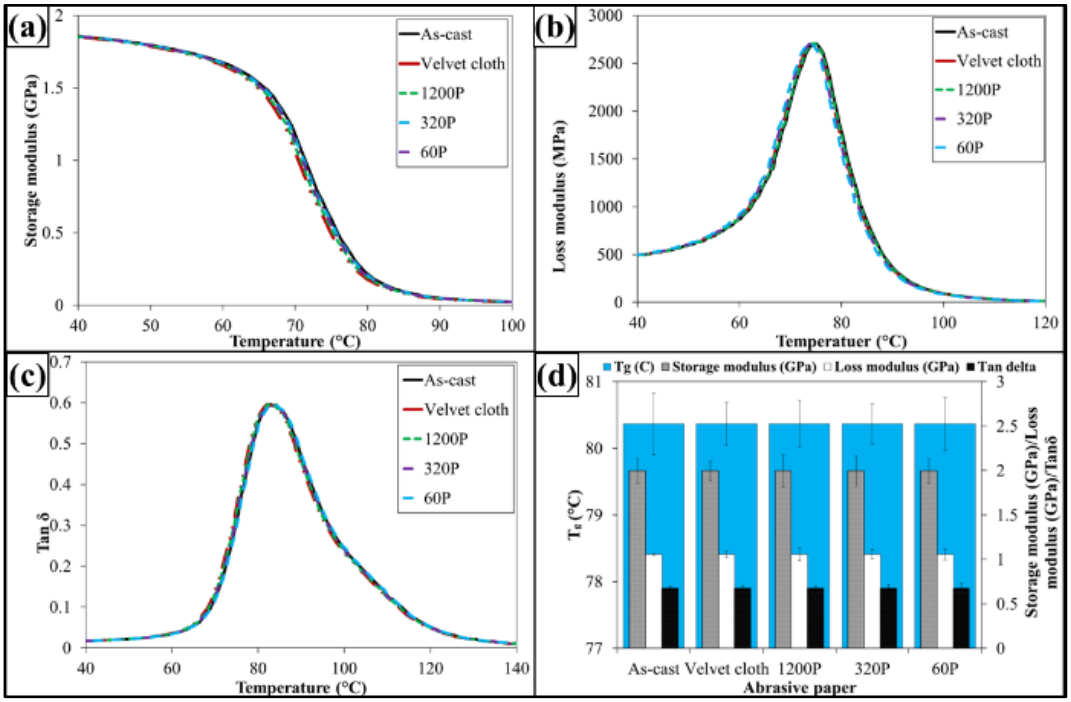

Figure 69: Dynamic mechanical properties of 0.05 wt% MLG-0.05 wt% nanoclay-EP nanocomposites: (a) storage modulus, (b) loss modulus, (c) loss factor (Tanδ), and (d) glass transition temperature (Tg), storage modulus, loss modulus, and Tanδ values corresponding to Tg.

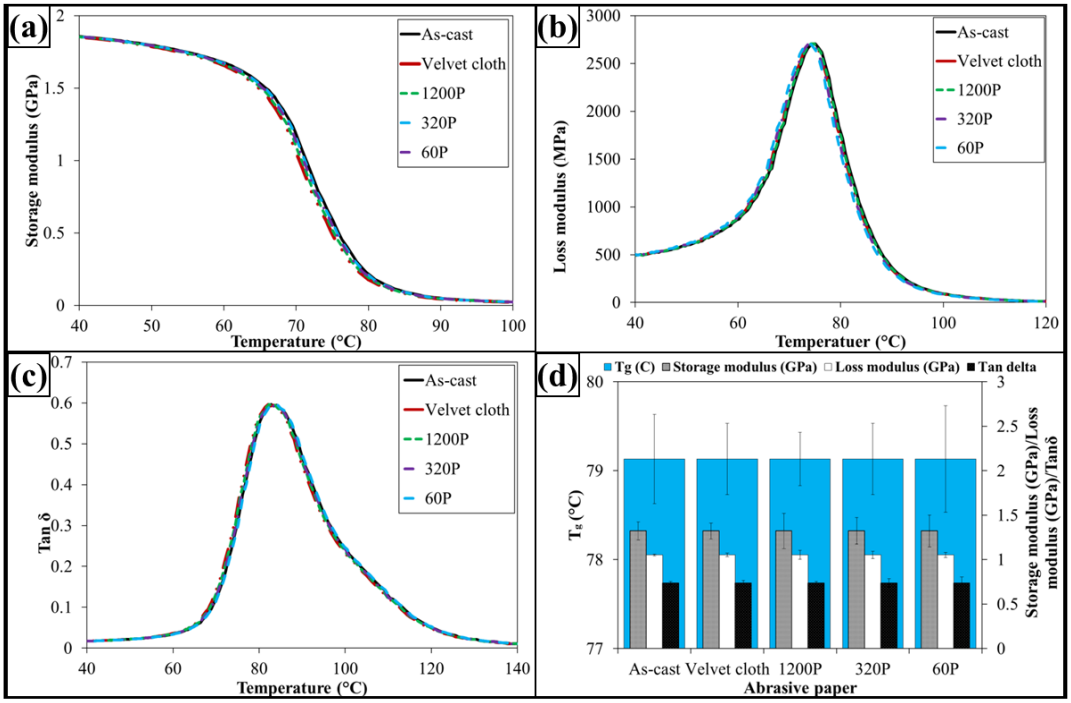

Figure 70. Dynamic mechanical properties of 0.5 wt% nanoclay-EP nanocomposites: (a) Storage modulus; (b) Loss modulus; (c) Loss factor (Tanδ); and (d) Glass transition temperature (T_g); Storage modulus, loss modulus, and Tanδ values corresponding to T_g.

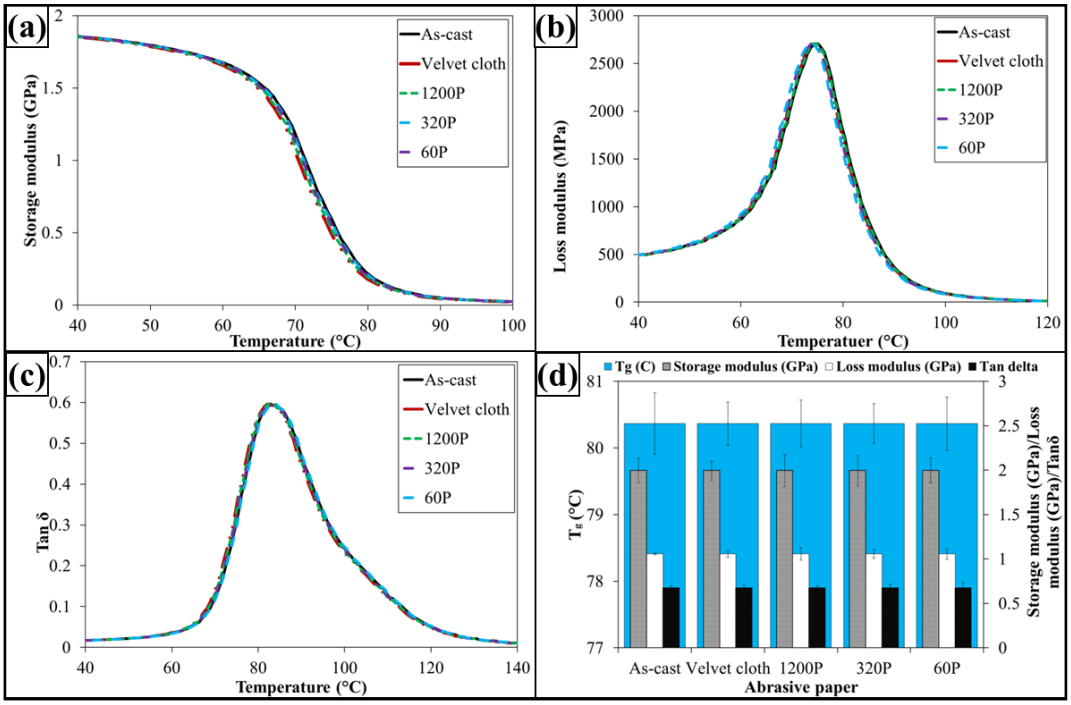

Figure 71. Dynamic mechanical properties of 0.25 wt% MLG-0.25 wt% nanoclay-EP nanocomposites: (a) storage modulus, (b) loss modulus, (c) loss factor (Tanδ), and (d) glass transition temperature (Tg), storage modulus, loss modulus, and Tanδ values corresponding to Tg.

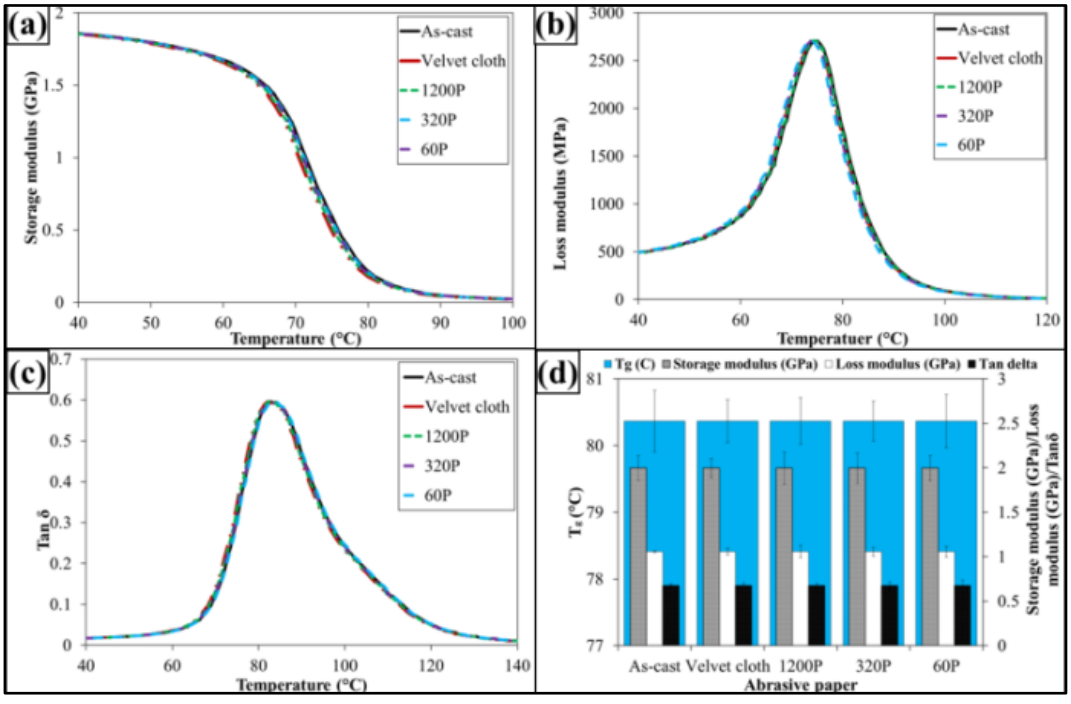

Figure 72: Dynamic mechanical properties of 1.0 wt% MLG-EP nanocomposites: (a) Storage modulus; (b) Loss modulus; (c) Loss factor (Tanδ); and (d) Glass transition temperature (T_g), storage modulus, loss modulus, and Tanδ values corresponding to T_g.

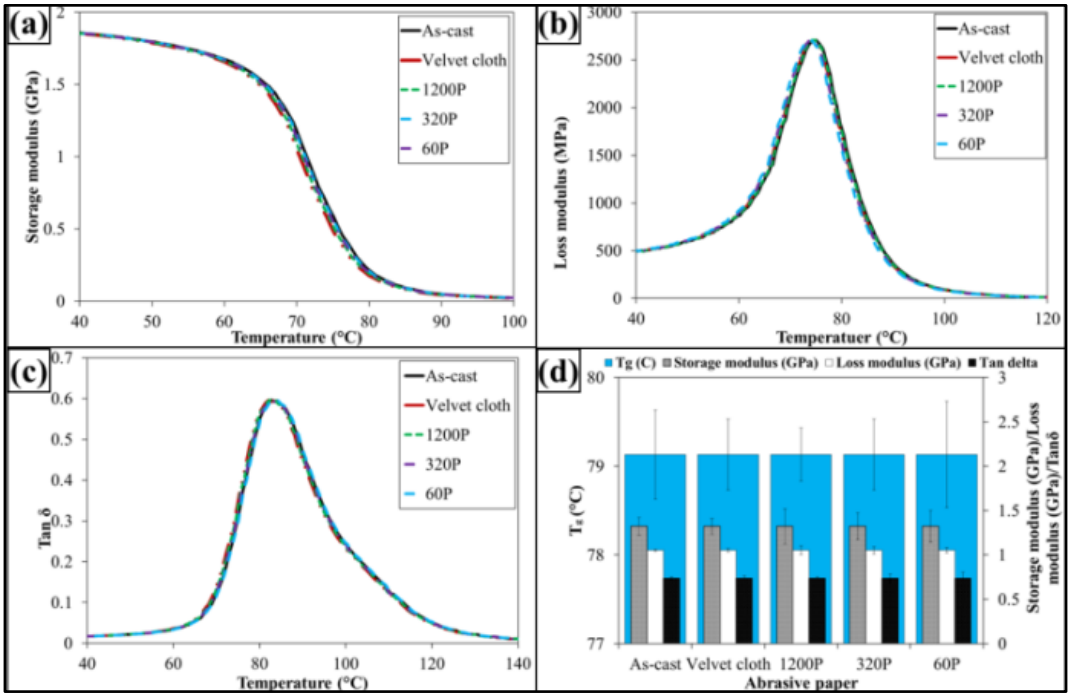

Figure 73: Dynamic mechanical properties of 1.0 wt% nanoclay-EP nanocomposites: (a) Storage modulus; (b) Loss modulus; (c) Loss factor (Tanδ); and (d) Glass transition temperature (T_g); Storage modulus, loss modulus, and Tanδ values corresponding to T_g.

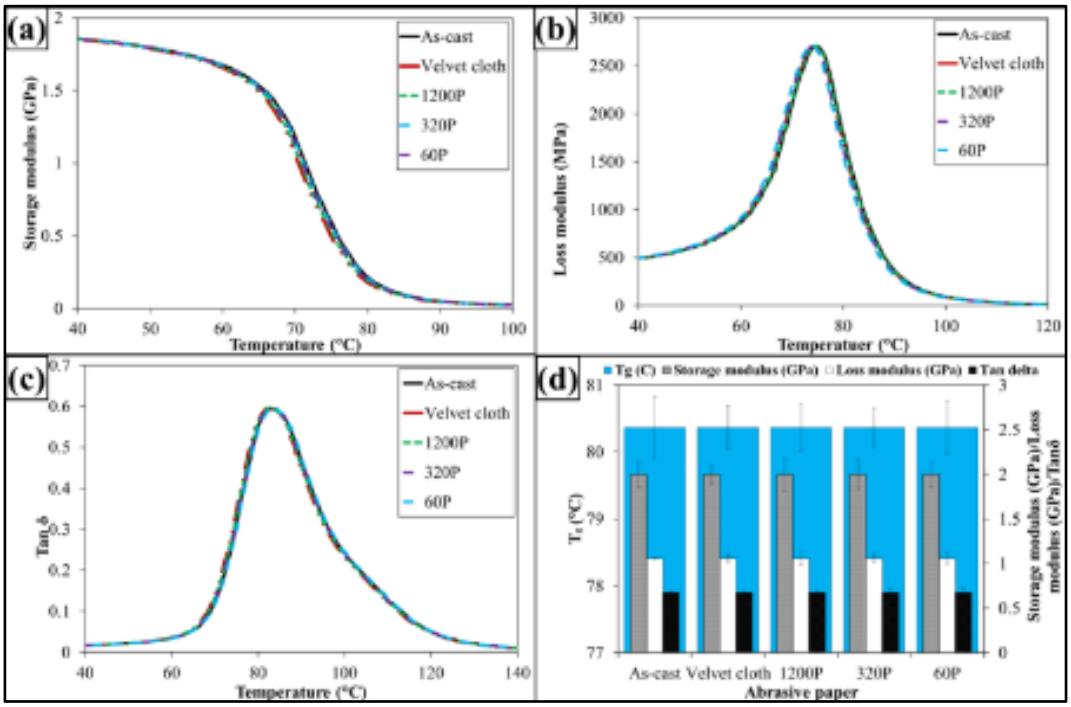

Figure 74: Dynamic mechanical properties of 0.5 wt% MLG-0.5 wt% nanoclay-EP nanocomposites: (a) storage modulus, (b) loss modulus, (c) loss factor (Tanδ), and (d) glass transition temperature (Tg), storage modulus, loss modulus, and Tanδ values corresponding to Tg.

In samples treated with velvet cloth and abrasive paper 1200P, smoothness increased or at least sharp edges were removed. Therefore, an increase in hardness was observed. The hardness decreased in sample treated with abrasive papers 320P and 60P which shows that indenter faces less resistance due to corrugation of the surfaces as shown in Figure 76. The hardness is also a function of applied load. It is known as indentation size effect according to which, "as load increases, the hardness decreases" [314]. It is also defined as, "as impression size decreases, the hardness increases." Jiang et al. produced non-hydrogenated germanium carbide films by magnetron co-sputtering method in a discharge of Ar [315]. They observed that topography significantly influenced by temperature and both hardness and Young's modulus increased with increasing temperature. The compressive stress on the surface increases with increasing temperature [315]. Guo et al. deposited hydrogenated nonocrystalline silicon thin films with high hydrogen dilution ratio by plasma enhanced

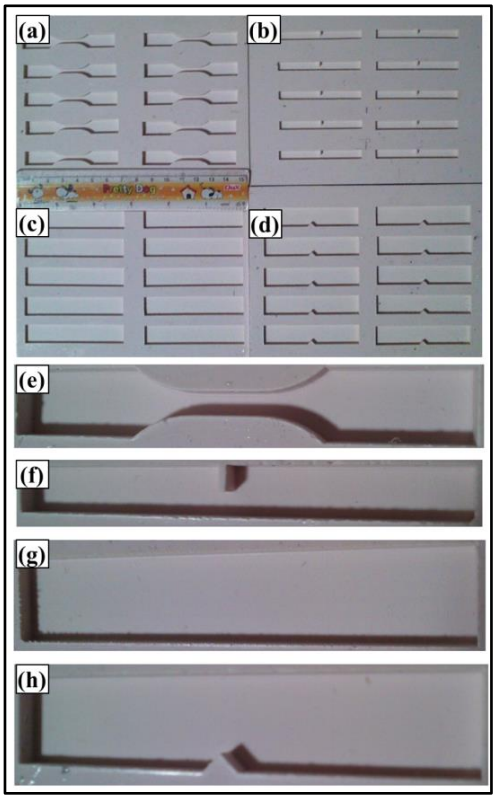

Figure 75: Mold photographs: (a) tensile, (b) K_{1C}, (c) flexural, and (d) Charpy impact toughness molds, and magnified images shown in (e-h), respectively.

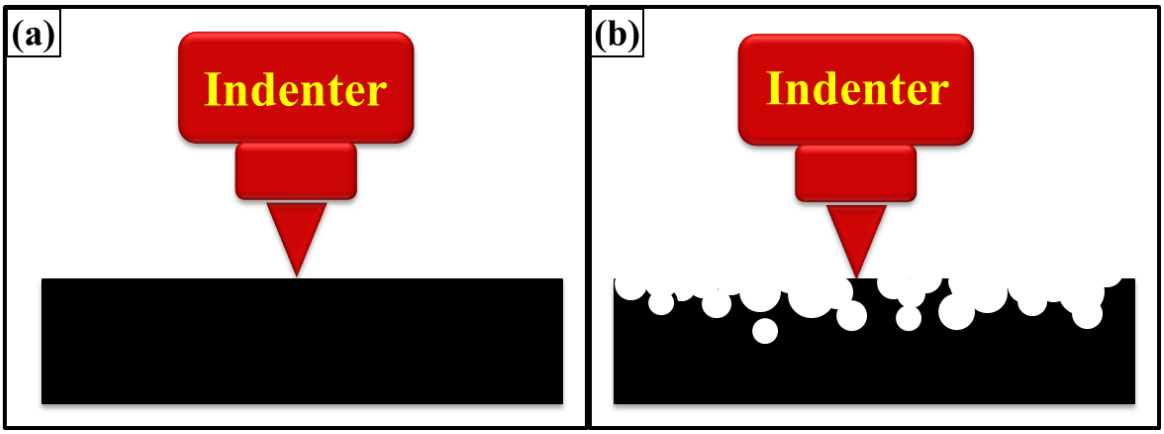

Figure 76: Indenter pressed against (a) smooth and (b) rough surfaces.

chemical vapor deposition technique [316]. The surface roughness decreased with increasing hydrogen dilution ratio. The hardness and Young's modulus increased with finer topography [316]. A similar trend was observed in current study where smooth surfaces (treated with velvet cloth and abrasive paper 1200P) caused increase in modulus and hardness values. On the contrary, the coarser surfaces (treated with abrasive papers 320P and 60P) resulted in decrease in modulus and hardness values. In metals, alloys, and ceramics, the indentation size effect may be attributed to grain size, orientation, and phases in the sample. In polymers, it may be because of degree of crosslinking, orientation of polymer chains, and size and distribution of porosity.

The flexural stress vs. flexural strain response is shown in Figure 77. It should be noted that not all the samples showed the same response as shown in Figure 77. The average values should be considered from Figure 77. As shown in Figure 77, the as-cast monolithic epoxy sample showed a brittle fracture. It is because of the stiff structure of epoxy and presence of any surface notches and porosity. When sample was treated with velvet cloth and abrasive paper 1200P, both flexural strength and flexural modulus were increased. However, treatment with abrasive papers 320P and 60P had detrimental effect on flexural properties.

The images of monolithic epoxy samples are shown in Figure 78. The location of fracture in tensile specimens is different and away from the mid of the gage length. This difference in location of fracture can be attributed to the surface roughness features. The notches caused high localized stress concentration and fracture took place at plane with maximum stress concentration. In fracture toughness and Charpy impact toughness specimens, fracture took place from the notch tip in all cases. It indicates that stress concentration effect caused by surface roughness is very low with respect to stress concentration caused by the main notch.

It can be observed from the topographical analysis above that the treatment of nanocomposites with abrasive papers produced topography with different size, shape, and orientation of notches and corrugations. It can be attributed to varying roughness and particle size distribution of abrasive papers used. Another important feasible mechanism could be the crater formation as shown in Figure 79. When abrasive tool slides against the

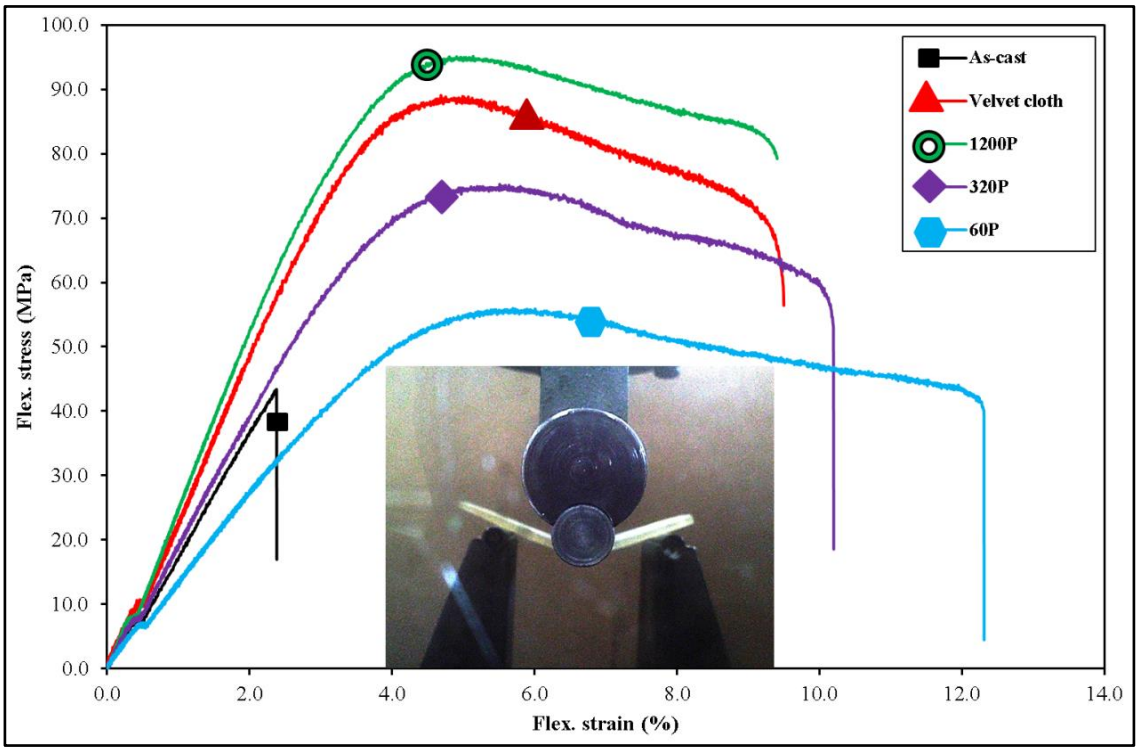

Figure 77: Flex. Stress vs Flex. Strain curves of monolithic samples.

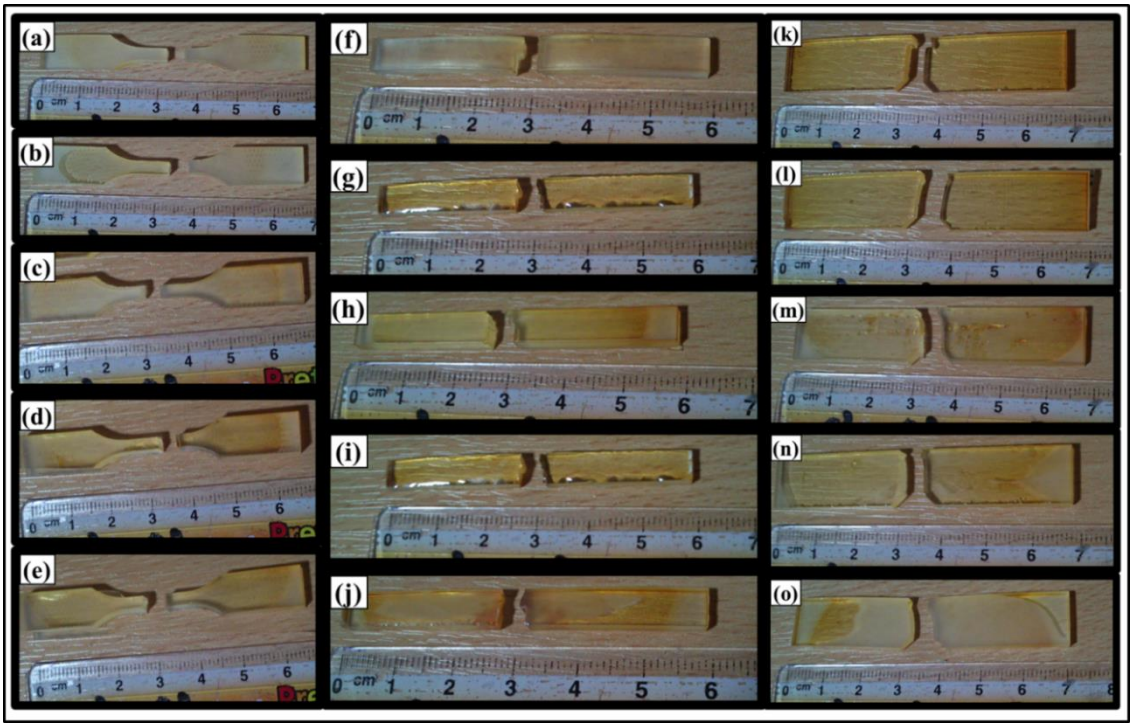

Figure 78: Optical images of broken monolithic epoxy samples. Tensile specimens: (a) As-cast, treated with (b) velvet cloth, (c) 1200P, (d) 320P, and (e) 60P. Flexural specimens: (f) As-cast, treated with (g) velvet cloth, (h) 1200P, (i) 320P, and (j) 60P. Charpy impact toughness specimens: (k) As-cast, treated with (l) velvet cloth, (m) 1200P, (n) 320P, and (o) 60P.

sample surface, elevated temperatures are produced at the contact surface due to frictional forces. The debris produced as a result of wear may coalesce at high temperature. This coalescence may result from diffusion, dissolution, cold-welding, and related possible chemical interactions [317]. The coalesced particles result in crater formation on the surface which may significantly deteriorate the mechanical properties. If crater formation is part of the wear limit criterion, the topography can be analyzed by the depth of the crater or the projected area of the crater [317].

Surfaces are not completely flat at the microscopic level. At high magnification, even the best polished surface will show ridges and valleys, asperities, and depressions. When two surfaces are brought together, they touch intimately only at the tips of a few asperities. At these points, the contact pressure may be close to the hardness of the softer material;

plastic deformation takes place on a very local scale, and cold welding may form strongly bonded junctions between the two materials. When sliding begins, these junctions have to be broken by the friction force, and this provides the adhesive component of the friction. Some asperities may plow across the surface of the mating material, and the resulting plastic deformation or elastic hysteresis contribute to the friction force; additional contributions may be due to wear by debris particles that become trapped between the sliding surfaces [318].

The smooth surfaces are necessary in sliding contact. When the surfaces contain high roughness and are slid against each other, wear takes place. The pointed debris formed as a result of wear, if do not find a place to escape, may cause crater in the surface. The crater may act as high stress concentration site due to notch effect. This stress concentration may

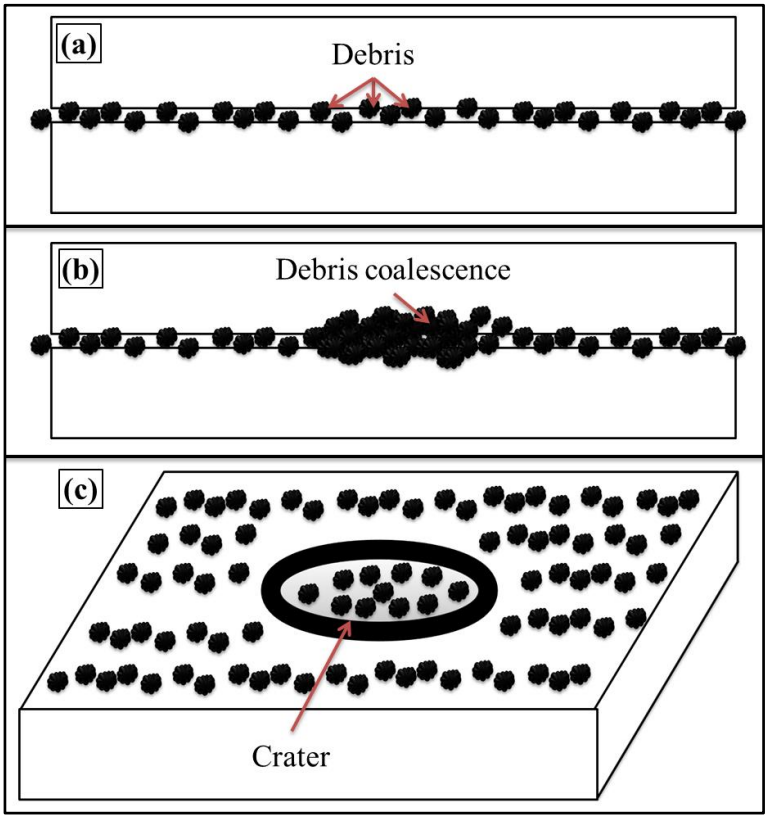

Figure 79: Debris coalescence and crater formation due to frictional forces between two sliding surfaces.

significantly deteriorate mechanical properties of the bulk material. This effect may be further pronounced in case of brittle polymers, such as epoxy, as there are no intrinsic mechanisms available to stop the crack advancement [301]. During sliding contact, thermal stresses are produced which can give rise to peculiar surface roughness features. In case of polymers, the thermal stresses may influence the degree of cross-linking. This altered degree of crosslinking at the surface may influence the overall mechanical properties of polymers [301]. In general, the mechanical properties improve with increasing crosslinking. However, it was shown that fracture toughness decreases with increasing crosslinking [56].

The improvement in mechanical properties with the incorporation of MLG and nanoclay depend on many factors such as dispersion state and interfacial interactions. The maximum improvement in tensile strength is as high as 108% [179] and tensile modulus up to 103% [180]. Graphene was also found to improve flexural properties of nanocomposites. Naebe *et al.* fabricated covalent functionalized epoxy/graphene nanocomposites and reported 18% and 23% increase in flexural strength and modulus, respectively [181]. Qi *et al.* fabricated graphene oxide/epoxy nanocomposites and reported increase up to 53% in flexural strength [182]. The impact strength and hardness were also significantly improved by graphene in epoxy nanocomposites. For example, Ren *et al.* applied a combination of bath sonication, mechanical mixing, and shear mixing to disperse GO in cyanate ester-epoxy and fabricated nanocomposites using in-situ polymerization [193]. They reported an increase of 31% in impact strength. Qi *et al.* fabricated graphene oxide/epoxy nanocomposites and reported increase in impact strength up to 96% [194] whereas Lu *et al.* fabricated GO/epoxy nanocomposites and reported increase in impact strength up to 100% [195]. Shen *et al.* fabricated GNS/epoxy nanocomposites and reported increase in impact strength up to 11% [196] and Bao *et al.* reported increase in hardness up to 35%

[197]. The G_{1C} also improved with the incorporation of graphene in epoxy nanocomposites. Meng *et* al. fabricated epoxy/graphene nanocomposites and reported increase in G_{1C} up to 597% [198].

The nanocomposites can be modeled and simulated to estimate the influence of nanofillers on mechanical, thermal, and electrical properties of nanocomposites. Various theoretical and computational approaches have been employed to explore the effect of nanofillers on the performance of polymer nanocomposites including but not limited to, quantum mechanical-based methods [319], Continuum Mechanics (CM) [320], Molecular Mechanics (MM) [321], Molecular Dynamics (MD) [322], atomistic modeling [323], Density Functional Theory (DFT) [324], and multiscale modeling [325]. For example, some of the authors have shown that MLG is very efficient in scattering and dissipation of thermal flux in epoxy nanocomposites [326].

Because of lighter than epoxy, air bubbles and other volatiles move towards surface to get out of the bulk. However, if bubbles either do not have enough pressure to push epoxy away or the epoxy cures before the escape of air bubbles, the bubbles and volatiles are entrapped within the bulk. If this explanation is true, then it should also be true that air bubbles and volatiles should be concentrated in regions closer to the top surface of the sample exposed to air. In that case, treating the samples with fine abrasive papers may remove bubble-concentrated regions. A similar method is applied in metals and alloys. For example, forged and cast steels are machined to remove oxides, scale, and to achieve desired surface finish. Due to the removal of defect-concentrated regions, the overall stress concentration factor in the samples should decrease which should cause an improvement in the mechanical properties. The segregation of porosity on the sides of the polymer samples is in agreement with the literature [327]. Warrier et al. introduced CNTs in the glass fiber-

epoxy system in three ways: (1) they added CNTs in the epoxy matrix, (2) in the sizing formulation of glass fibers, and (3) combination of the two methods [327]. They produced nanocomposite laminate sheets using vacuum bagging. The voids were present at the borders of the sheet, probably because of entrapped air. The sheets containing CNTs had more voids at borders than that without CNTs. In that case, removing the material from the surface up to a few microns can be helpful in improving the mechanical properties of the samples.

In the next chapter, the fractography of fractured surfaces of the samples are studied and related with the trends observed in the mechanical properties. The Fractography analysis of the samples revealed that MLG significantly influences the fracture patterns. In addition, a careful examination of the surface roughness features of the fractured surfaces suggests that the dispersion state of the fillers, interfacial interactions, and presence of any agglomerates of filler can be estimated based on the surface parameters such as maximum surface roughness (R_z or R_{max}), surface roughness average (R_a), and root mean square parameter of roughness (R_q). For example, a high value of R_z with deep crater and/or trenches indicates the presence of filler agglomerates and concomitant poor mechanical properties of polymer nanocomposites. Similarly, a relatively high surface roughness average with low R_z value indicates the uniform dispersion of the filler and simultaneously improved mechanical properties. However, it was observed that waviness average parameter (W_a) does not have any relation with the weight fraction, dispersion state, or agglomeration of the filler.

Chapter-3

Fractography Analysis with Surface Roughness Features of MLG-Nanoclay-Epoxy Nanocomposites

---

21 Abstract

The stiff and fragile structure of thermosetting polymers, such as epoxy, accomplices the innate cracks to cause fracture and therefore the applications of monolithic epoxy are not ubiquitous. However, it is well established that when reinforced especially by nano-fillers, its ability to withstand crack propagation is propitiously improved. The crack is either deflected or bifurcated when interacts with strong nano-filler such as Multi-Layer Graphene (MLG). Due to the deflection and bifurcation of cracks, specific fracture patterns are observed. These fracture patterns seem aesthetically appealing, and if delved deeper, they can further be used to estimate the influence of nano-filler on the mechanical properties. Here it is shown that, by a meticulous examination of surface roughness features of fractured patterns, various important aspects related to fillers can be approximated such as dispersion state, interfacial interactions, presence of agglomerates, and overall influence of the incorporation of filler on the mechanical properties of nanocomposites.

22 Introduction

The damage tolerance and fracture toughness of epoxy can be enhanced with the incorporation of (nano-) fillers such as metallic oxides [2–4], nanoclays [5–7], carbon nanotubes (CNTs) [8–10], and other carbonaceous materials [11–13,326,328]. After the

groundbreaking experiments on the two dimensional material graphene by Nobel Laureates, Sir Andre Geim and Konstantin Novoselov from the University of Manchester, graphene came into limelight in research field mainly because of its excellent electrical [17], thermal [18], and mechanical properties [19]. Graphene found widespread applications in electronics [20], bio-electric sensors [21], energy technology [22], lithium batteries [23], aerospace [24], bio-engineering [25], and various other fields of nanotechnology [26].

In this chapter, the fractured surfaces of produced nanocomposites are examined using Alicona optical microscope. As related experimental work has already been discussed in Chapter 2, the experimental section is omitted in this chapter and results are shown and discussed in the next section. The surface roughness featues measured and correlated qualitatively with the dispersion state of fillers. It was observed that a high value of R_a (with low R_z value) can be an indicator of smoother samples surfaces, absence of agglomerates and uniform dispersion of nanofillers. On the other hand, a low value of R_a (with high R_z value) indicates the presence of deep surface notches, agglomerates, and non-uniform dispersion of nanofillers. A similar trend was observed in R_q values as in R_a values. However, no specific trend was observed in surface waviness W_a and may not be indicative of dispersion state of nanofillers and surface roughness features.

23 Results and discussion

The SEM images of fractured tensile specimens of as-cast monolithic epoxy are shown in Figure 80 (a-c). Nearly flat surface was obtained with bamboo-like pattern which is typical brittle fracture pattern of monolithic epoxy [68]. A roughly similar but coarser pattern was observed in case of samples treated with velvet cloth Figure 80 (d-f). The coarser fractured

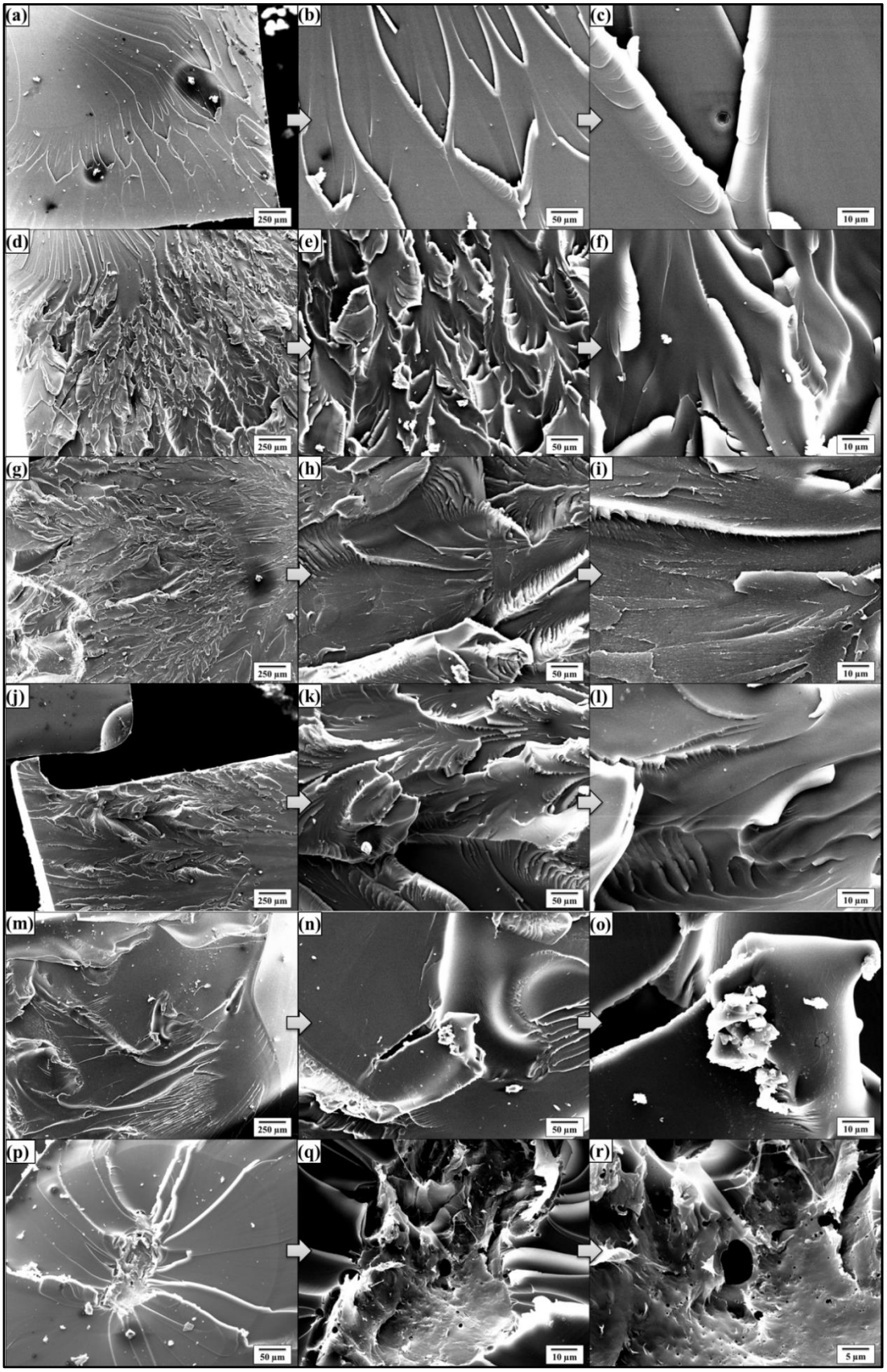

Figure 80: Fractography of monolithic epoxy samples: (a-c) As-cast, treated with: (d-f) velvet cloth, (g-i) 1200P, (j-l) 320P, (m-o) 60P, and (p-r) as-cast epoxy samples.

surface and increase in strength indicate that surface notches were partially removed by velvet cloth which was corroborated by surface profile. It can be observed that the ravines formed are nearly parallel. However, in samples treated with abrasive paper 1200P (Figure 80g-i), not only coarser topography was observed, but also serrations in different orientation were observed within the ravines (Figure 80h). In the samples treated with abrasive paper 320P (Figure 80j-l), the fracture pattern is a combination of those observed in case of as-cast samples and the samples treated with abrasive paper 1200P. The fractured surface was partially rough and partially coarse with serrations in the ravines. It may be attributed to size, shape, and orientation of surface notches produced by abrasive paper.

The influence of topography was clearer in samples treated with abrasive paper 60P (Figure 80m-o). The fractured surface can be divided into three regions: (1) flat surface as observed in case of as-cast samples and those treated with velvet cloth, (2) serrated region as observed in samples treated with abrasive paper 1200P, (3) coarse topography as observed in case of samples treated with abrasive paper 320P. As the abrasive paper 60P had wide size distribution with both pointed and angular edges, therefore it produced notches on the sample surface of various size, shape, and orientation which led to the formation of fracture pattern with disparate features.

Apart from topography, the porosity can also influence fracture behavior as shown in Figure 80 (p-r). The images were taken from next to the edge of the as-cast monolithic epoxy sample. A very fine porosity can be observed (Figure 80r) which produced a kind of crater on the surface. It can further be observed that the porosity is concentrated with pores of varying sizes. The stress concentration is inevitable around the porosity. Therefore, this porous region acted as the epicenter of fracture and fracture lines disseminated in all

directions forming an octopus-like fracture pattern. Therefore, it can be concluded that not only porosity deteriorated mechanical properties, but it also produces a specific fracture pattern which can be called as “octopus-like” fracture pattern caused by porosity. The fracture pattern caused by the porosity extends in all directions. Therefore, it can be more deleterious than surface notch which produces stress concentration along the axis of notch tip. In addition, the fracture lines emanating from the pores may accomplice the innate cracks and may expedite the fracture process.

The fractography surfaces of 0.1 wt% MLG-EP nanocomposites are shown in Figure 81. The monolithic epoxy shows straight bamboo-like fracture pattern indicating the occurrence of typical epoxy brittle fracture. It is because there are no crack bridging mechanisms available in monolithic epoxy. Therefore, once crack is initiated, it propagates without any diversions and results in straight fracture paths. However, with the incorporation of carbonaceous reinforcements, the cracks are deflected resulting in parabolic and non-linear fracture patterns [114]. This was the reason that no specific orientation of crack propagation was observed in 3PBT specimens reinforced with MLG. The fracture became coarser when the samples were treated with velvet cloth and abrasive paper 1200P while trenches and straight and flat fracture patterns were observed when the samples were treated with abrasive papers 320P and 60P. The fracture patterns of K_{1C} specimens differ from those of 3PBT specimens in a way that fracture was originated from the notch tip as the tip generated high levels of stress concentration. As the displacement rate is relatively low in K_{1C} testing, the surface notches showed a significant impact on the topography of fracture surfaces. However, the influence of surface notches and surface roughness features on fracture patterns was marginalized in case of Charpy impact testing where the samples were suddenly impacted at the back of the notch by a heavy and pointed

hammer. Sheer and straight fracture patterns were observed in Charpy impact specimens and fracture took place right from the notch tip in all cases.

The fractography surfaces of 0.1 wt% nanoclay-EP nanocomposites are shown in Figure 82. Overall, a coarser topography of fractured surfaces was observed in case of 0.1 wt% MLG-EP samples than in 0.1 wt% nanoclay-EP samples. No specific orientation of crack propagation was observed in 3PBT specimens reinforced with nanoclay. As in case of 0.1 wt% MLG-EP samples, the fracture patterns of K_{1C} specimens of 0.1 wt% nanoclay-EP samples differ from those of 3PBT specimens in a way that fracture was originated from the notch tip as the tip generated high levels of stress concentration. As the displacement rate is relatively low in K_{1C} testing, nanoclay also showed a significant impact on the topography of fracture surfaces. However, the influence of nanoclay on fracture patterns was marginalized in case of Charpy impact testing where the samples were suddenly impacted at the back of the notch by a heavy and pointed hammer. Sheer and straight fracture patterns were observed in Charpy impact specimens and fracture took place right from the notch tip in all cases. The fractography surfaces of 0.05 wt% MLG-0.05 wt% nanoclay-EP nanocomposites are shown in Figure 83. Overall, the coarsest topography of fractured The surface roughness features of fracture surfaces of tensile specimen of 0.1 wt% MLG/nanoclay-EP nanocomposites are shown in Figure 87-5. The surface waviness (Figure 87-5ii) and Gaussian distribution (Figure 87-5iv) did not show a specific trend of change with the abrasive papers. It can be attributed to the multiple factors affecting the fracture pattern such as surface notches, MLG/nanoclay distribution, orientation, and interfacial interactions. Usually a specific pattern is observed in waviness due to wobbling of machining tool. On the contrary to W_a, a specific variation in surface roughness (Figure 87-5iii) was observed. The surface roughness of as-cast 0.1 wt% Multi-Layer Graphene (MLG)/nanoclay-epoxy (EP) nanocomposites varied between ±6 μm with the presence of

deep crests and troughs. With the treatment with the velvet cloth, the surface roughness changed slightly which became pronounced in samples treated with abrasive paper 1200P. However, in case of samples treated with abrasive papers 320P and 60P, deep trenches can be observed in roughness patterns (Figure 87-5diii and Figure 87-5eiii) that may be attributed to the presence of large notches. The trenches can also be observed in the surface profiles (Figure 87-5dv and Figure 87-5ev).

The surface roughness features are summarized in Figure 96 to Figure 99. This R_z (Figure 96) comes from the ravines formed due to brittle fracture in the thermoset. The R_z values were significantly decreased by the incorporation of nanofillers. As trenches present in monolithic epoxy are removed with the incorporation of nanofillers due to the diversion of advancing cracks, therefore, a decrease in R_z indicates a uniform dispersion of fillers and deflection of the cracks. In addition, an increase in mechanical properties with the incorporation of nanofillers further corroborates the uniform dispersion of nanofillers and energy dissipation at deflection of cracks. The variation in R_z value is in accord with the change in the mechanical properties. Therefore, R_z can be an indicator of the dispersion state of filler.

Apart from R_z, R_a is another important parameter to consider and meansured values are shown in Figure 97. The decrease in R_a with increasing R_z may seem contradicting however can be explained on the basis of observed fractured patterns and surface roughness charts. When treated with velvet cloth and abrasive paper 1200P, no crater was formed due to which lower R_z value was observed. In addition, cracks were deflected quite sharply resulting in sudden variation in surface roughness thereby increasing the R_a value. On the contrary, when treated with abrasive papers 320P and 60P, deep notches were present that caused fracture and increased R_z due to crater formation. However, once a

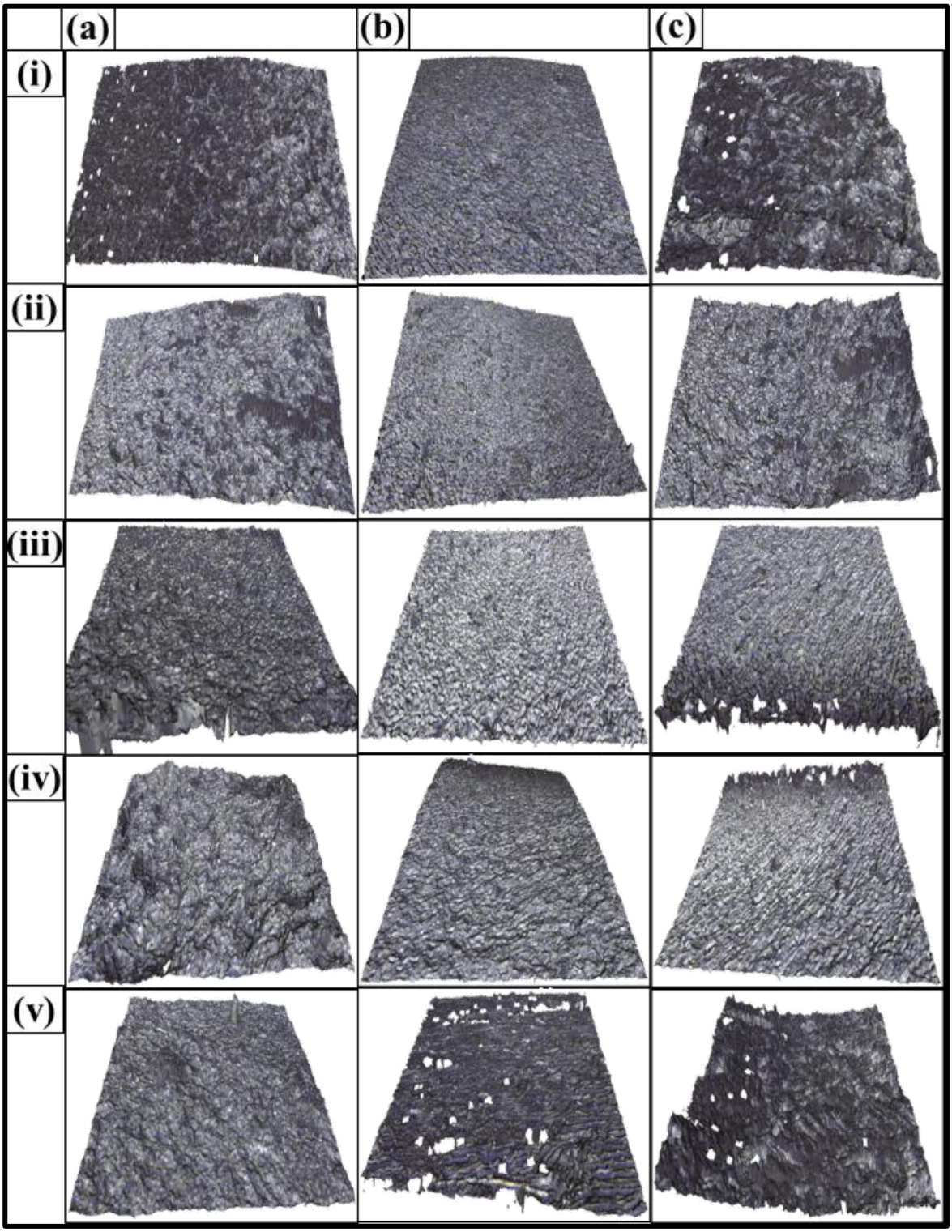

Figure 81: Fracture surfaces of (a) 3PBT, (b) K_{1C}, and (c) Charpy impact test specimens of 0.1 wt% MLG-EP samples after treatment with abrasive papers for 1 min at 150 rpm. From top to bottom: (i) as-cast, (ii) treated with velvet cloth, (iii) 1200P, (iv) 320P, and (v) 60P. The length of bottom edge of each image is 800 nm.

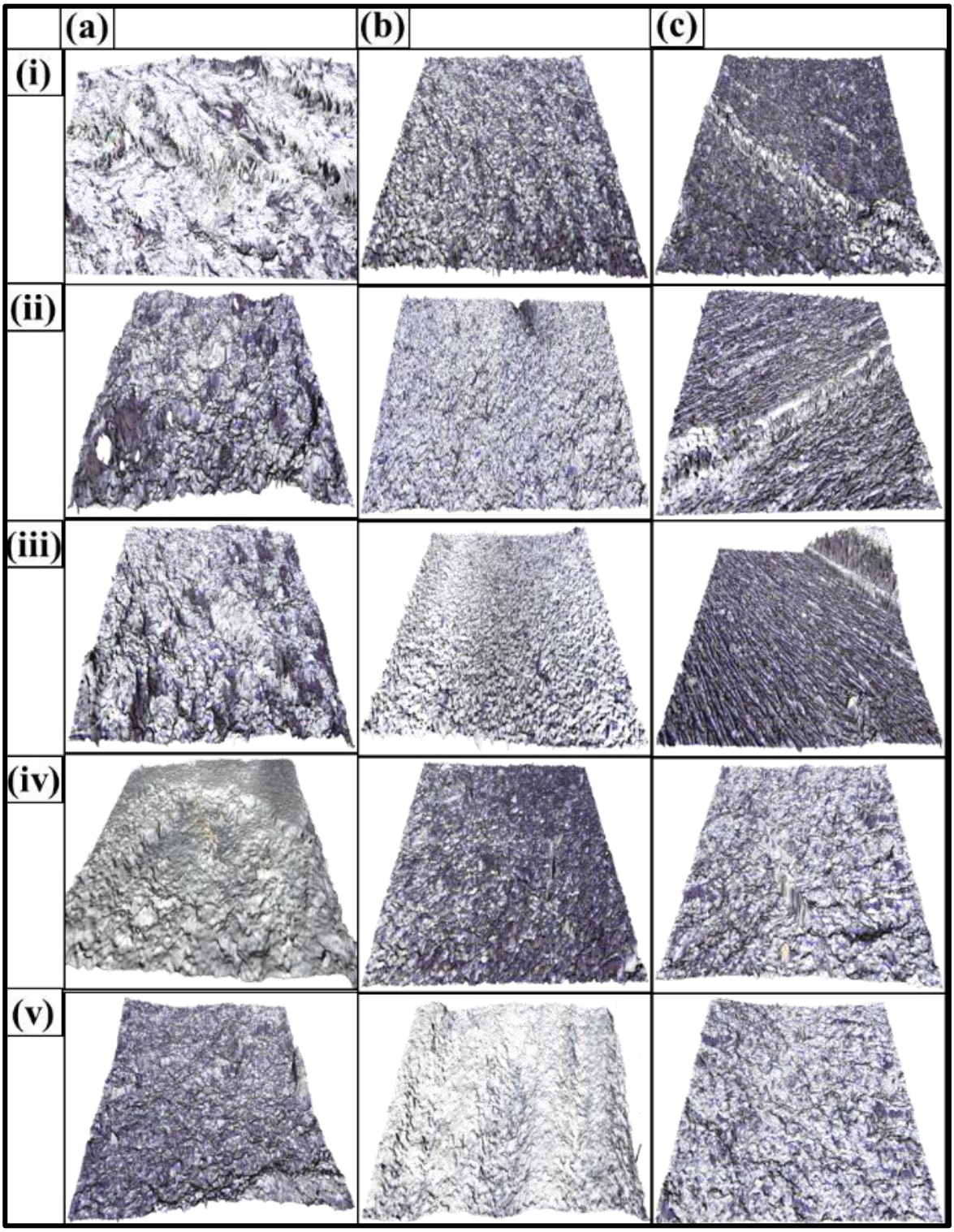

Figure 82: Fracture surfaces of (a) 3PBT, (b) K_{1C}, and (c) Charpy impact test specimens of 0.1 wt% nanoclay-EP samples after treatment with abrasive papers for 1 min at 150 rpm. From top to bottom: (i) as-cast, (ii) treated with velvet cloth, (iii) 1200P, (iv) 320P, and (v) 60P. The length of bottom edge of each image is 800 nm.

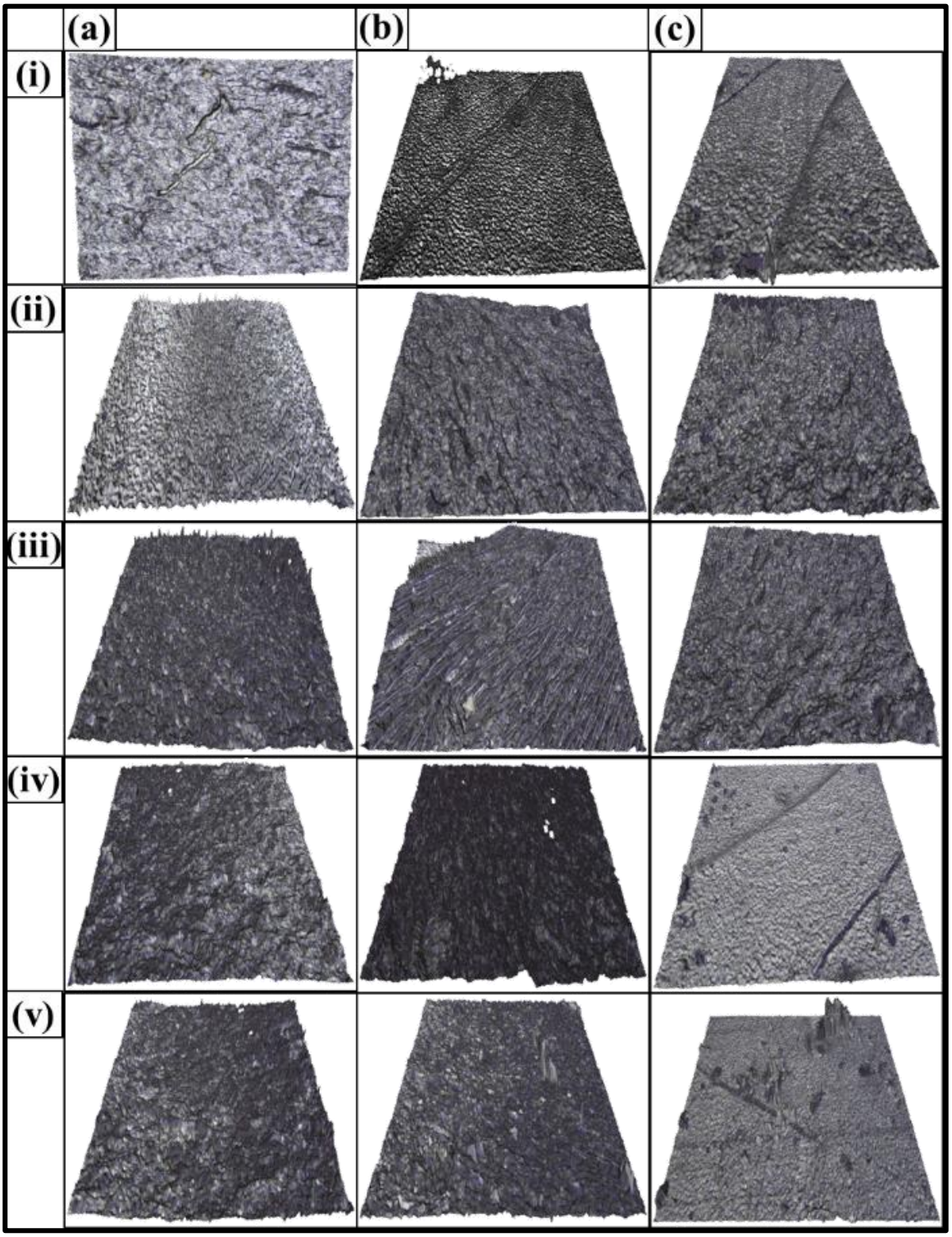

Figure 83: Fracture surfaces of (a) 3PBT, (b) K_{1C}, and (c) Charpy impact test specimens of 0.05 wt% MLG-0.05 wt% nanoclay-EP samples after treatment with abrasive papers for 1 min at 150 rpm. From top to bottom: (i) as-cast, (ii) treated with velvet cloth, (iii) 1200P, (iv) 320P, and (v) 60P. The length of bottom edge of each image is 800 nm.

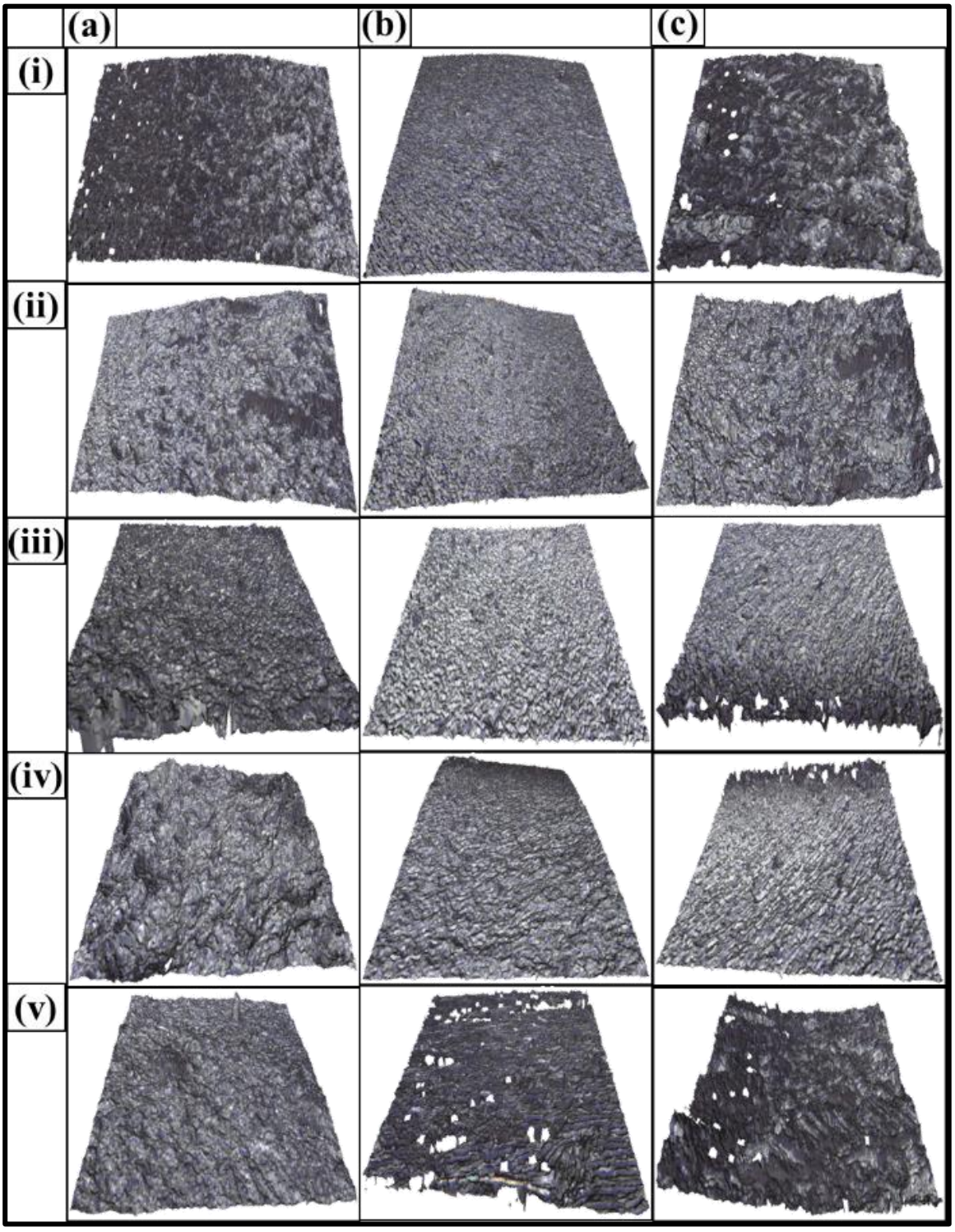

Figure 84: Fracture surfaces of (a) 3PBT, (b) K_{1C}, and (c) Charpy impact test specimens of 1.0 wt% MLG-EP samples after treatment with abrasive papers for 1 min at 150 rpm. From top to bottom: (i) as-cast, (ii) treated with velvet cloth, (iii) 1200P, (iv) 320P, and (v) 60P. The length of bottom edge of each image is 800 nm.

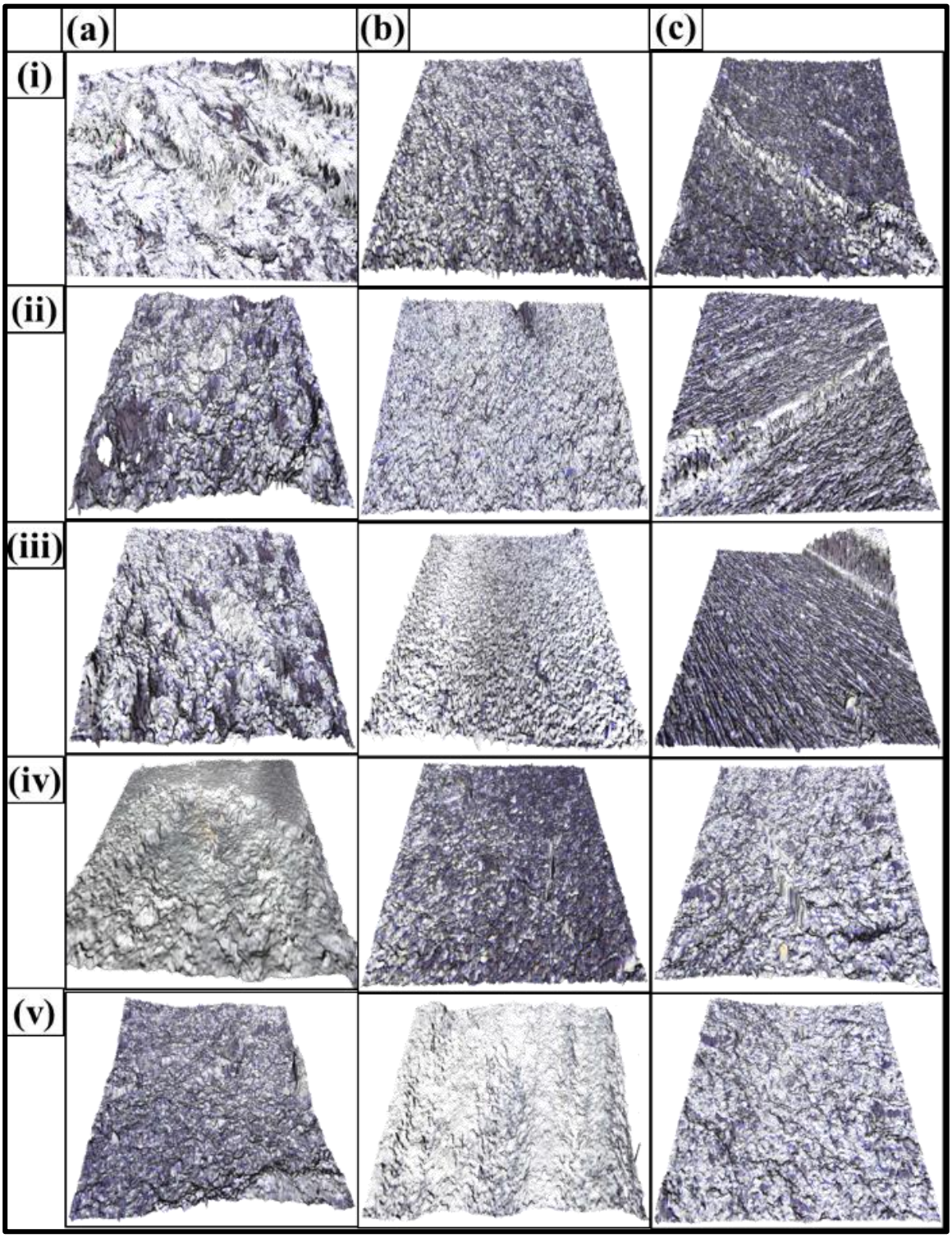

Figure 85: Fracture surfaces of (a) 3PBT, (b) K_{1C}, and (c) Charpy impact test specimens of 1.0 wt% nanoclay-EP samples after treatment with abrasive papers for 1 min at 150 rpm. From top to bottom: (i) as-cast, (ii) treated with velvet cloth, (iii) 1200P, (iv) 320P, and (v) 60P. The length of bottom edge of each image is 800 nm.

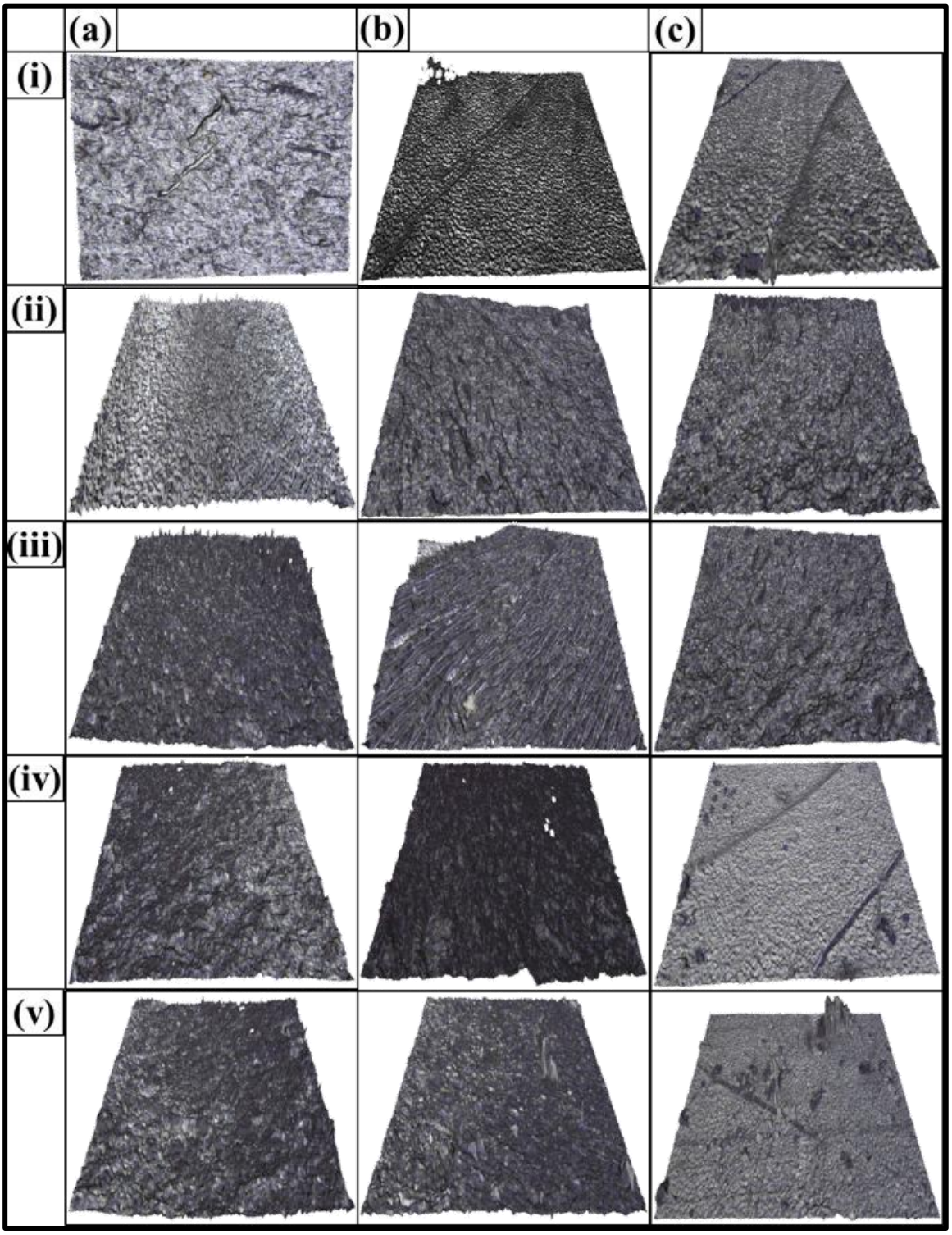

Figure 86: Fracture surfaces of (a) 3PBT, (b) K_{1C}, and (c) Charpy impact test specimens of 0.5 wt% MLG-0.5 wt% nanoclay-EP samples after treatment with abrasive papers for 1 min at 150 rpm. From top to bottom: (i) as-cast, (ii) treated with velvet cloth, (iii) 1200P, (iv) 320P, and (v) 60P. The length of bottom edge of each image is 800 nm.

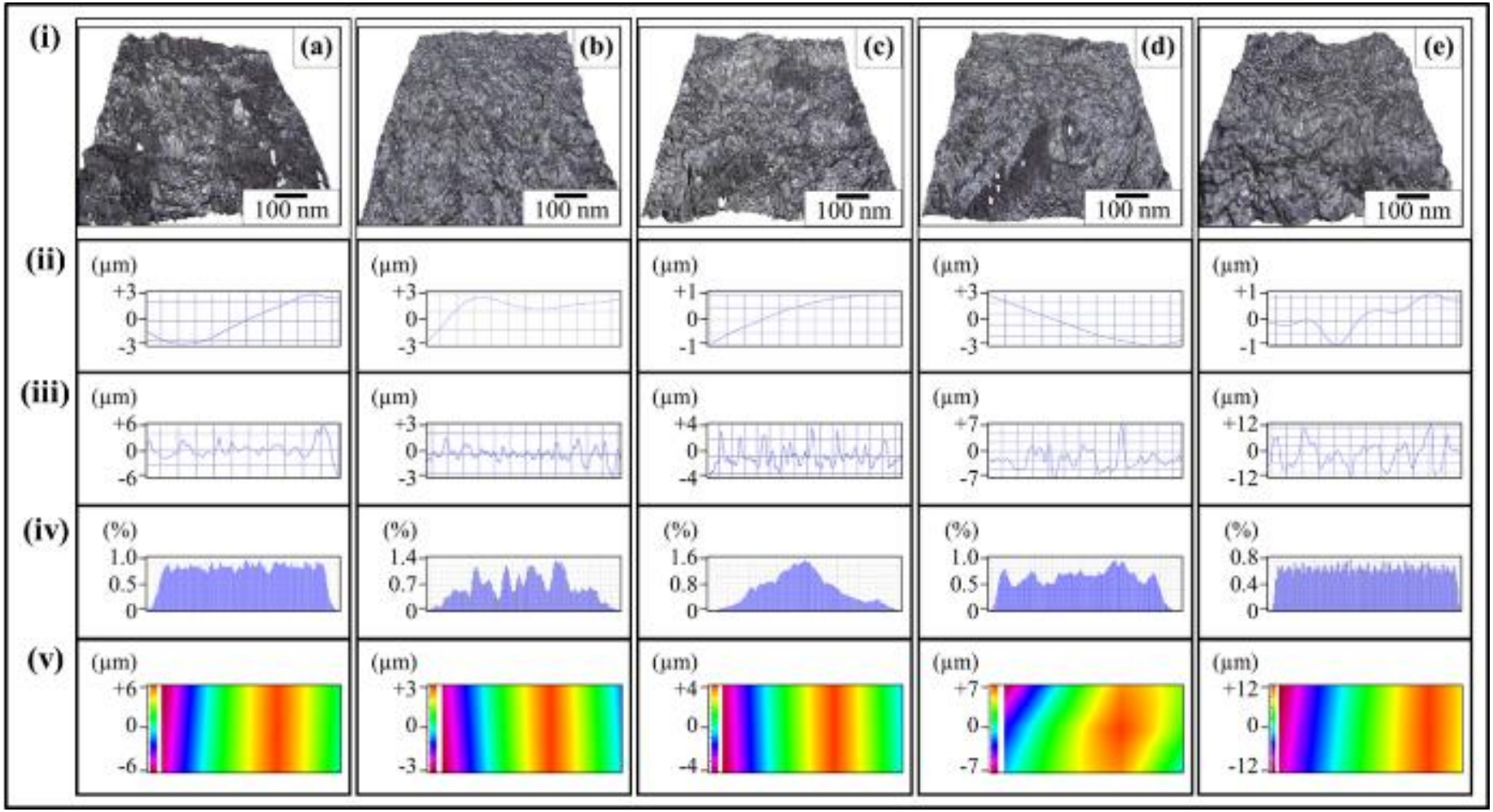

Figure 87: Surface roughness features of 0.1 wt% MLG-EP fractured tensile samples after treatment with abrasive papers for 1 min at 150 rpm: (a) as-cast, (b) treated with velvet cloth, (c) 1200P, (d) 320P, and (e) 60P. From top to bottom in all cases: (i) tensile images (ii) waviness, (iii) roughness, (iv) Gaussian distribution, and (v) surface profile.

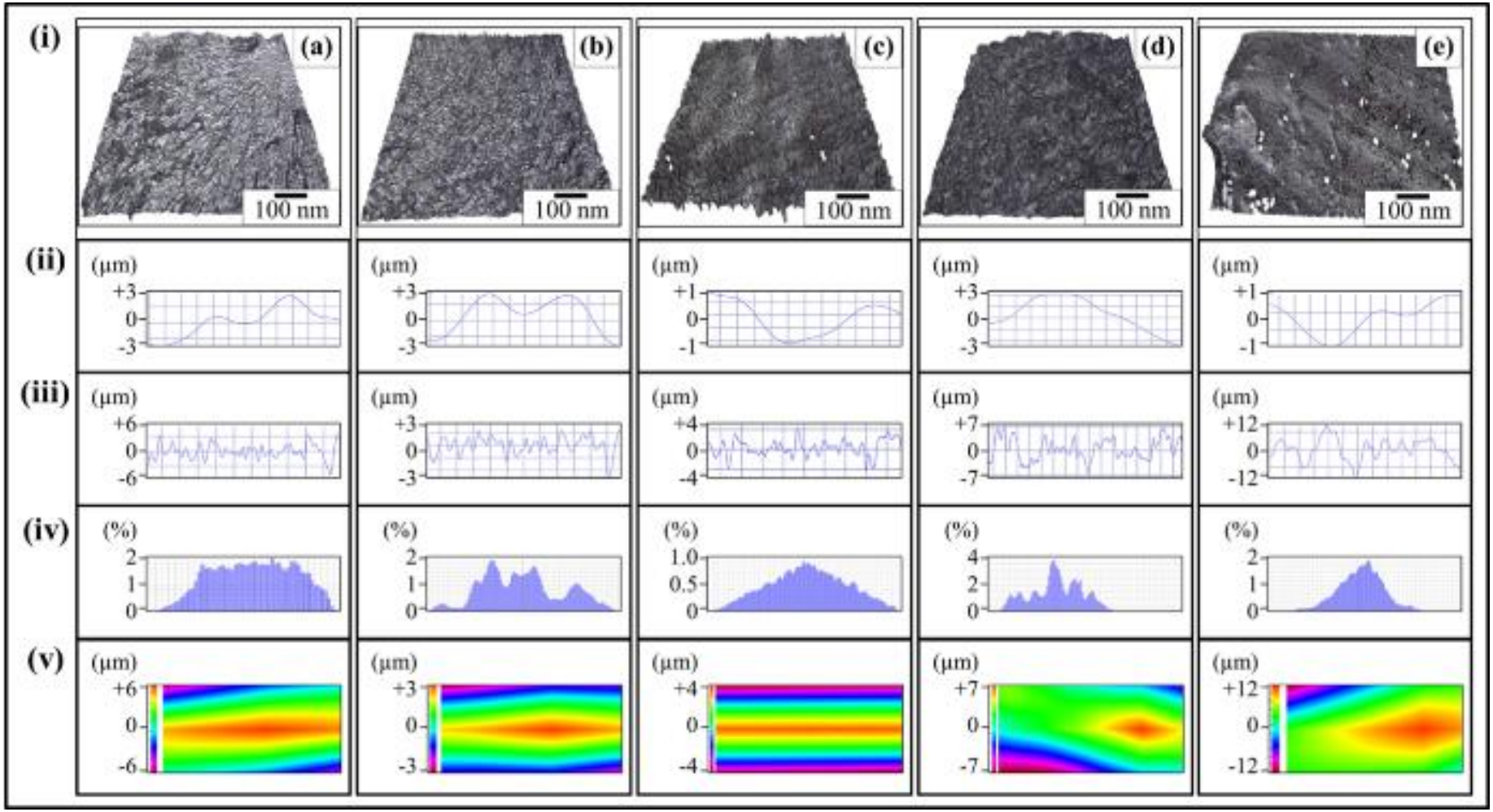

Figure 88: Surface roughness features of 0.1 wt% nanoclay-EP fractured tensile samples after treatment with abrasive papers for 1 min at 150 rpm: (a) as-cast, (b) treated with velvet cloth, (c) 1200P, (d) 320P, and (e) 60P. From top to bottom in all cases: (i) tensile images (ii) waviness, (iii) roughness, (iv) Gaussian distribution, and (v) surface profile.

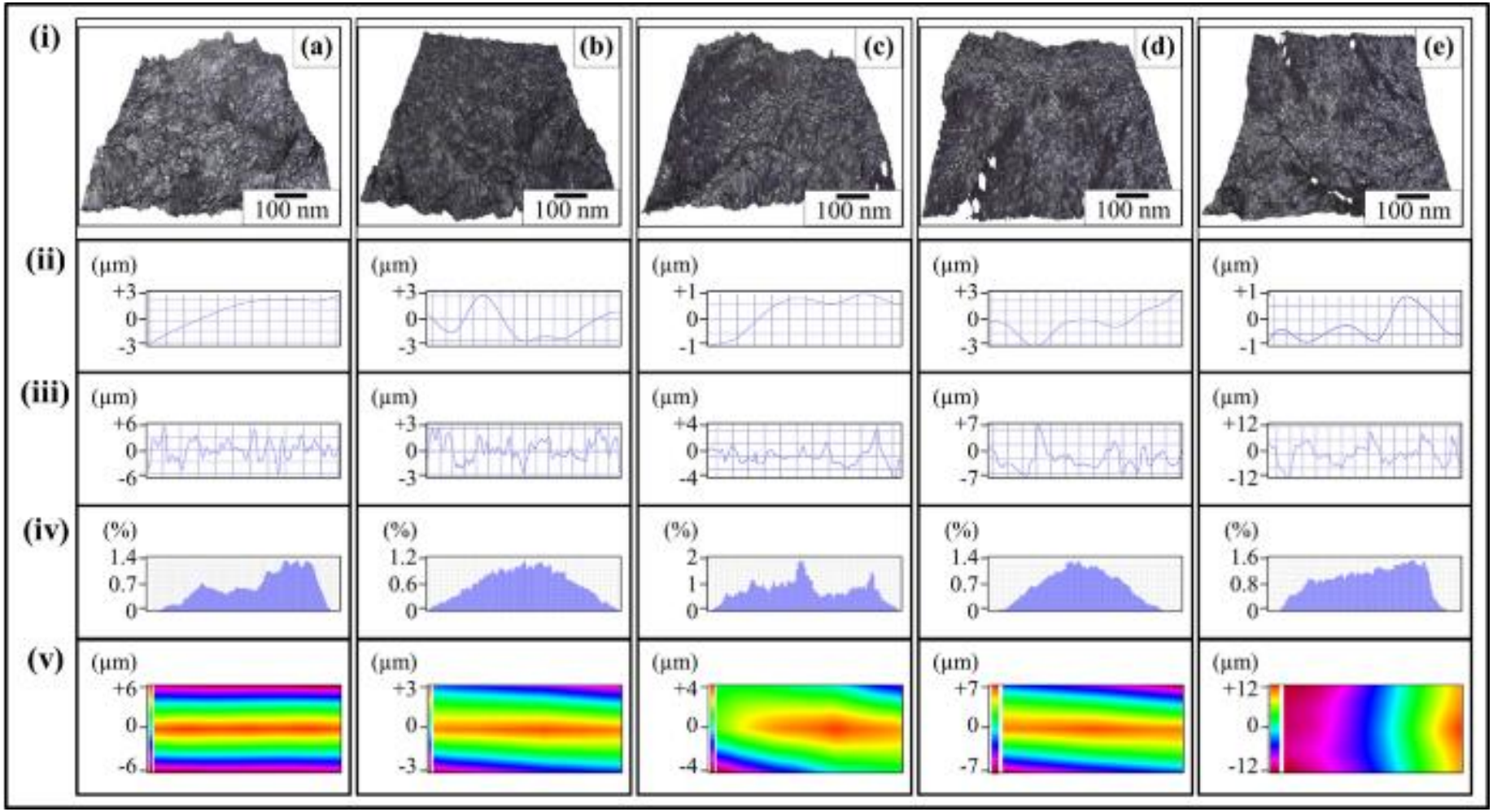

Figure 89: Surface roughness features of 0.05 wt% MLG-0.05 wt% nanoclay-EP fractured tensile samples after treatment with abrasive papers for 1 min at 150 rpm: (a) as-cast, (b) treated with velvet cloth, (c) 1200P, (d) 320P, and (e) 60P. From top to bottom in all cases: (i) tensile images (ii) waviness, (iii) roughness, (iv) Gaussian distribution, and (v) surface profile.surfaces was observed in case of 0.05 wt% MLG-0.05 wt% nanoclay-EP nanocomposites.

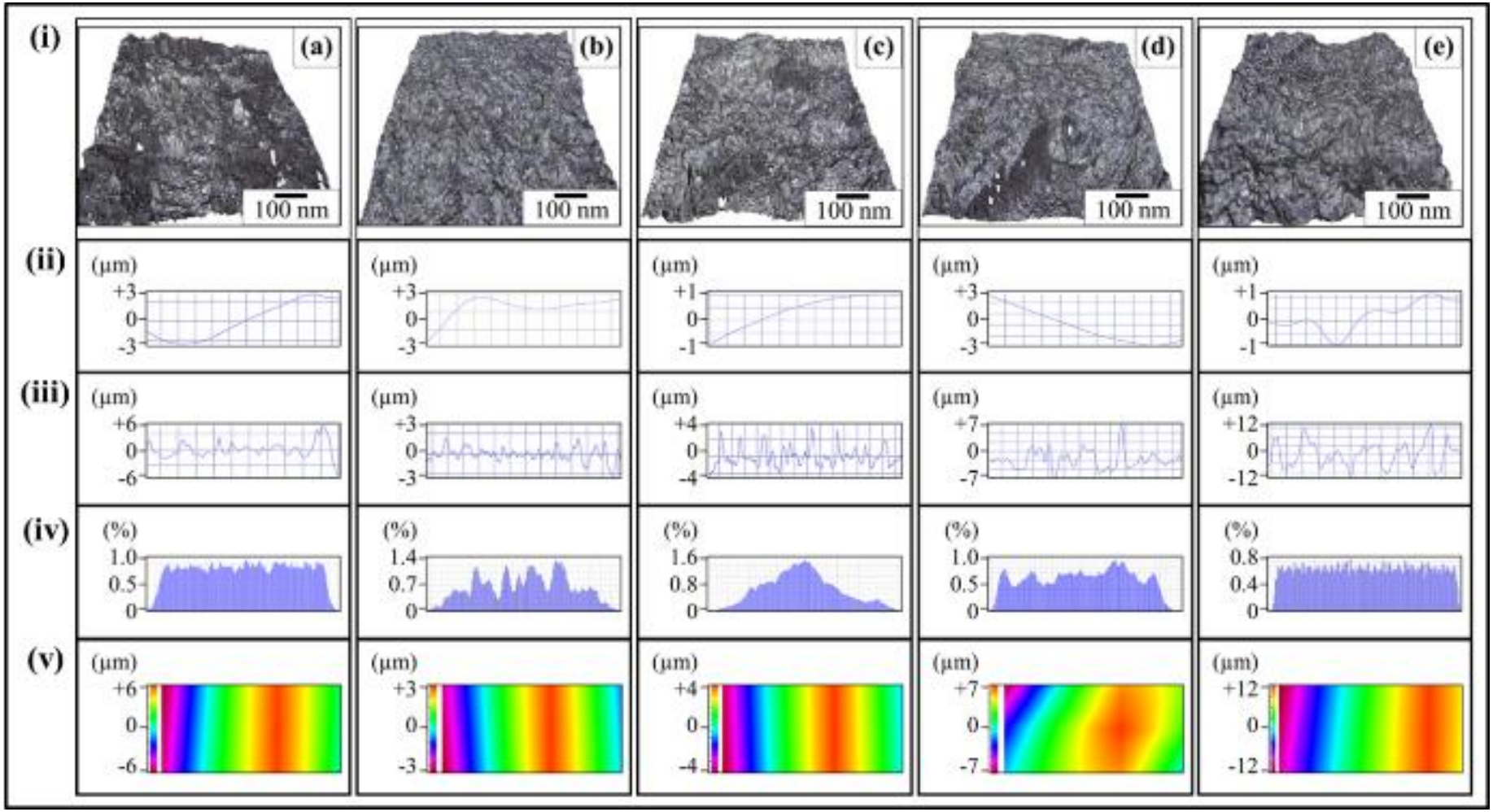

Figure 90: Surface roughness features of 0.5 wt% MLG-EP fractured tensile samples after treatment with abrasive papers for 1 min at 150 rpm: (a) as-cast, (b) treated with velvet cloth, (c) 1200P, (d) 320P, and (e) 60P. From top to bottom in all cases: (i) tensile images (ii) waviness, (iii) roughness, (iv) Gaussian distribution, and (v) surface profile.

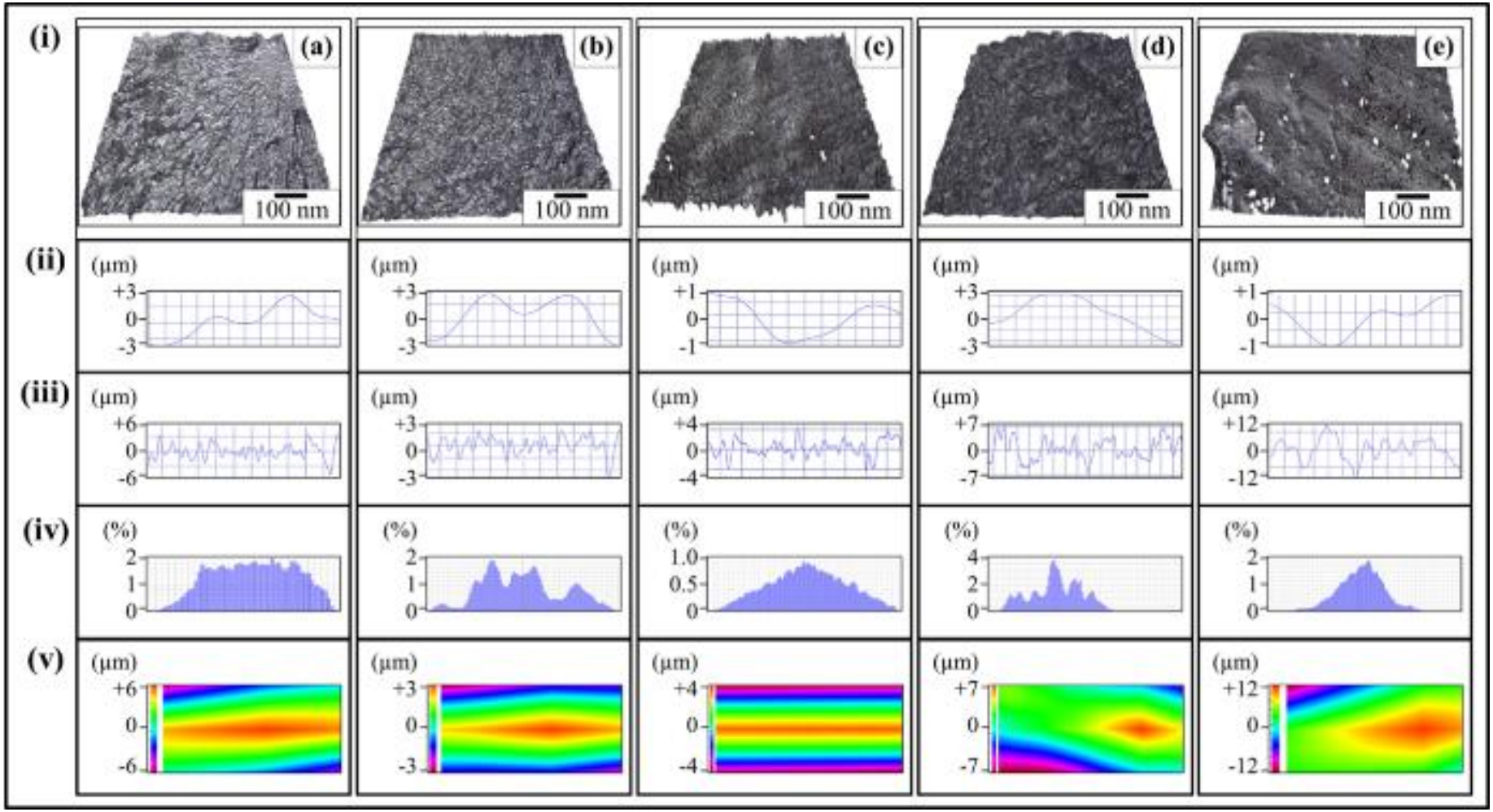

Figure 91: Surface roughness features of 0.5 wt% nanoclay-EP fractured tensile samples after treatment with abrasive papers for 1 min at 150 rpm: (a) as-cast, (b) treated with velvet cloth, (c) 1200P, (d) 320P, and (e) 60P. From top to bottom in all cases: (i) tensile images (ii) waviness, (iii) roughness, (iv) Gaussian distribution, and (v) surface profile.

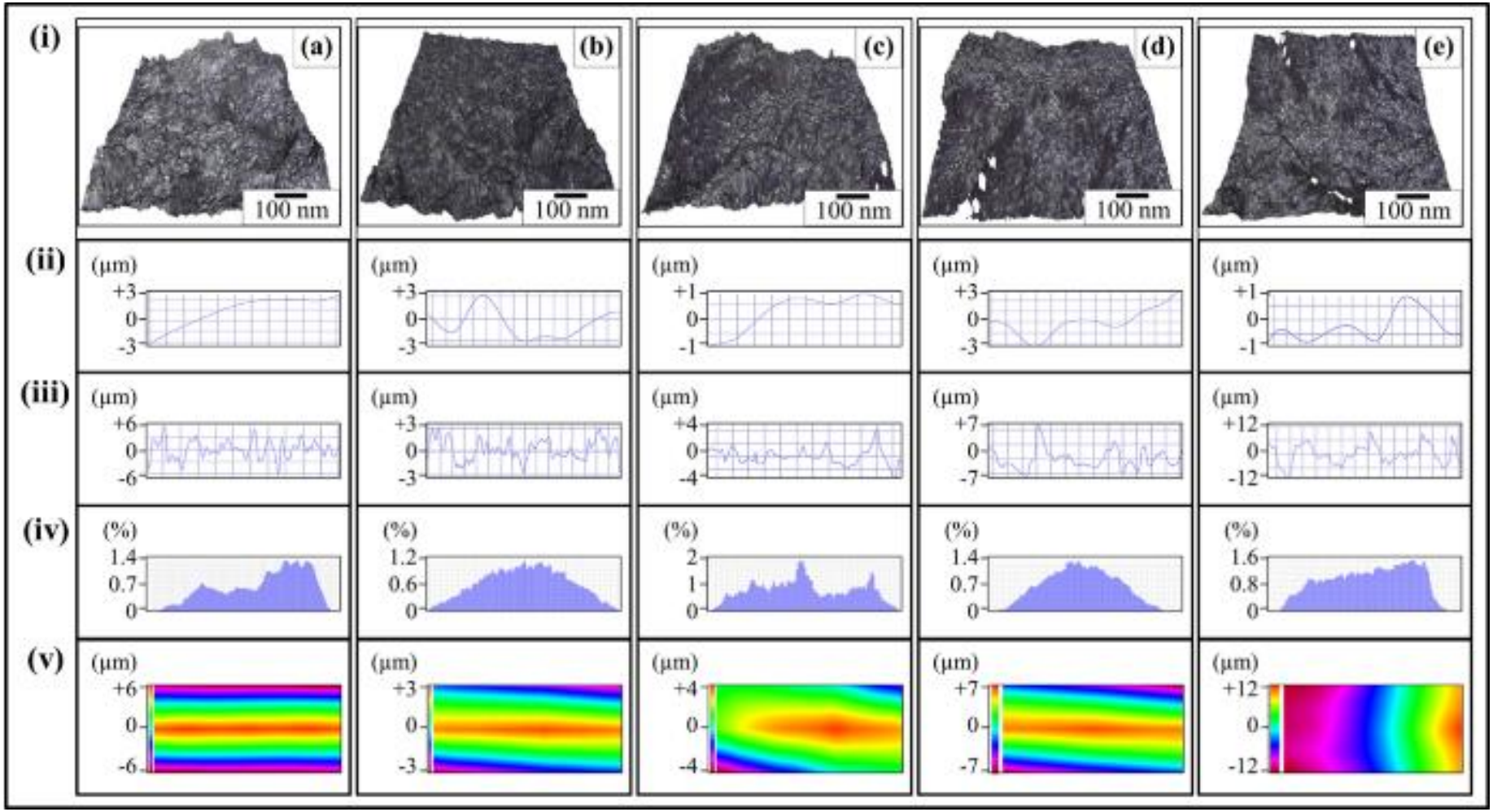

Figure 92: Surface roughness features of 0.25 wt% MLG-0.25 wt% nanoclay-EP fractured tensile samples after treatment with abrasive papers for 1 min at 150 rpm: (a) as-cast, (b) treated with velvet cloth, (c) 1200P, (d) 320P, and (e) 60P. From top to bottom in all cases: (i) tensile images (ii) waviness, (iii) roughness, (iv) Gaussian distribution, and (v) surface profile.

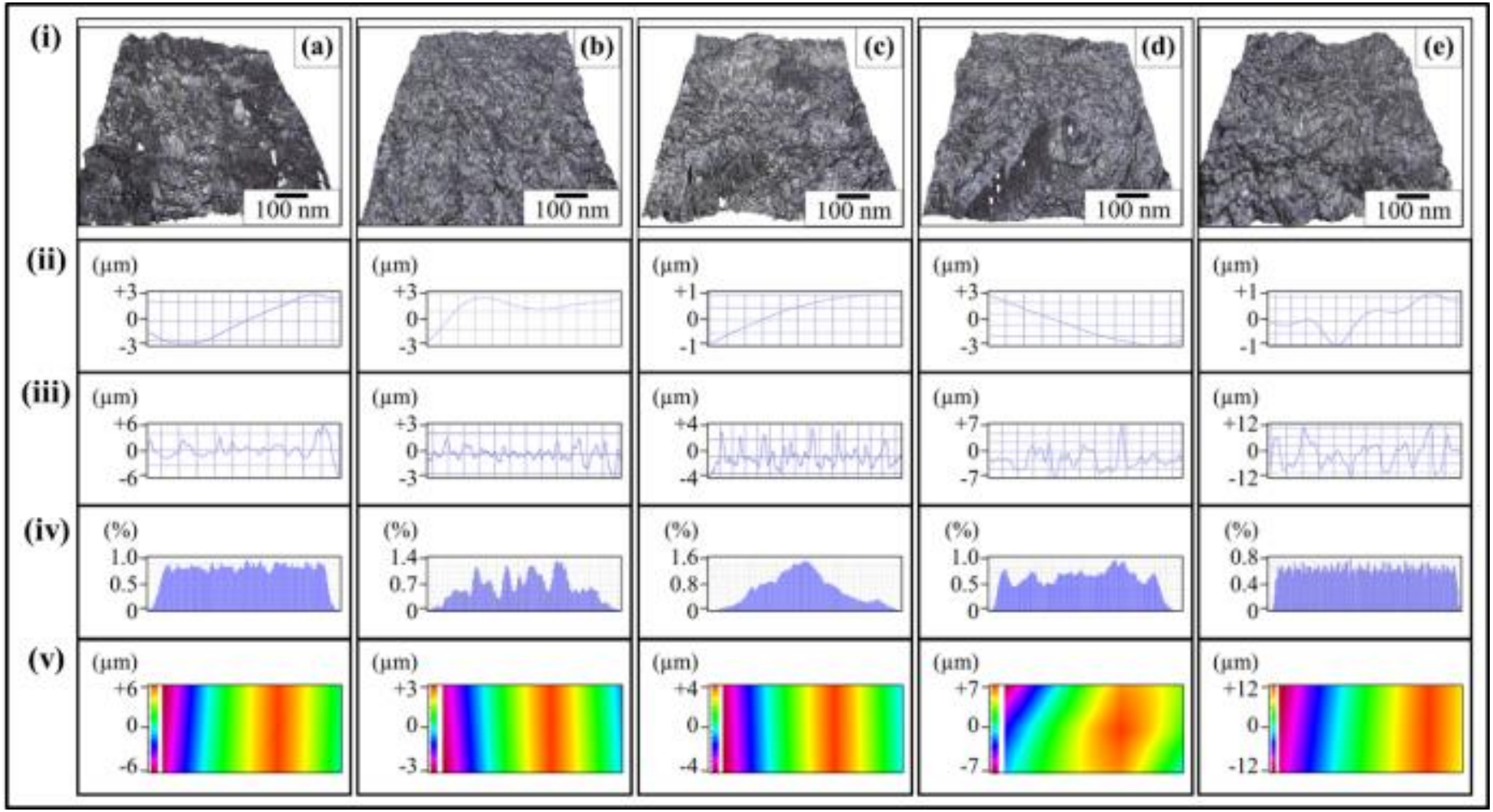

Figure 93: Surface roughness features of 1.0 wt% MLG-EP fractured tensile samples after treatment with abrasive papers for 1 min at 150 rpm: (a) as-cast, (b) treated with velvet cloth, (c) 1200P, (d) 320P, and (e) 60P. From top to bottom in all cases: (i) tensile images (ii) waviness, (iii) roughness, (iv) Gaussian distribution, and (v) surface profile.

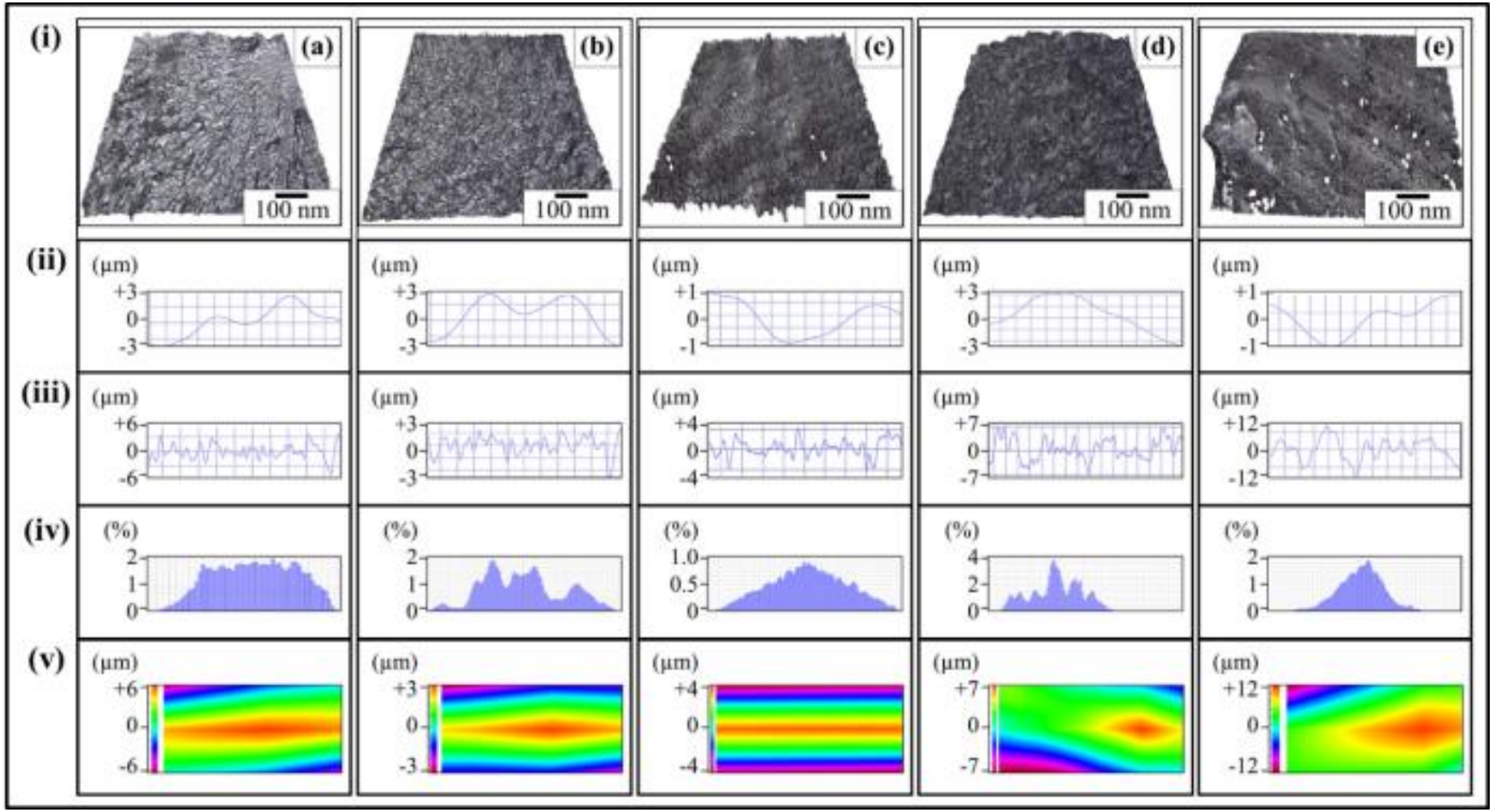

Figure 94: Surface roughness features of 1.0 wt% nanoclay-EP fractured tensile samples after treatment with abrasive papers for 1 min at 150 rpm: (a) as-cast, (b) treated with velvet cloth, (c) 1200P, (d) 320P, and (e) 60P. From top to bottom in all cases: (i) tensile images (ii) waviness, (iii) roughness, (iv) Gaussian distribution, and (v) surface profile.

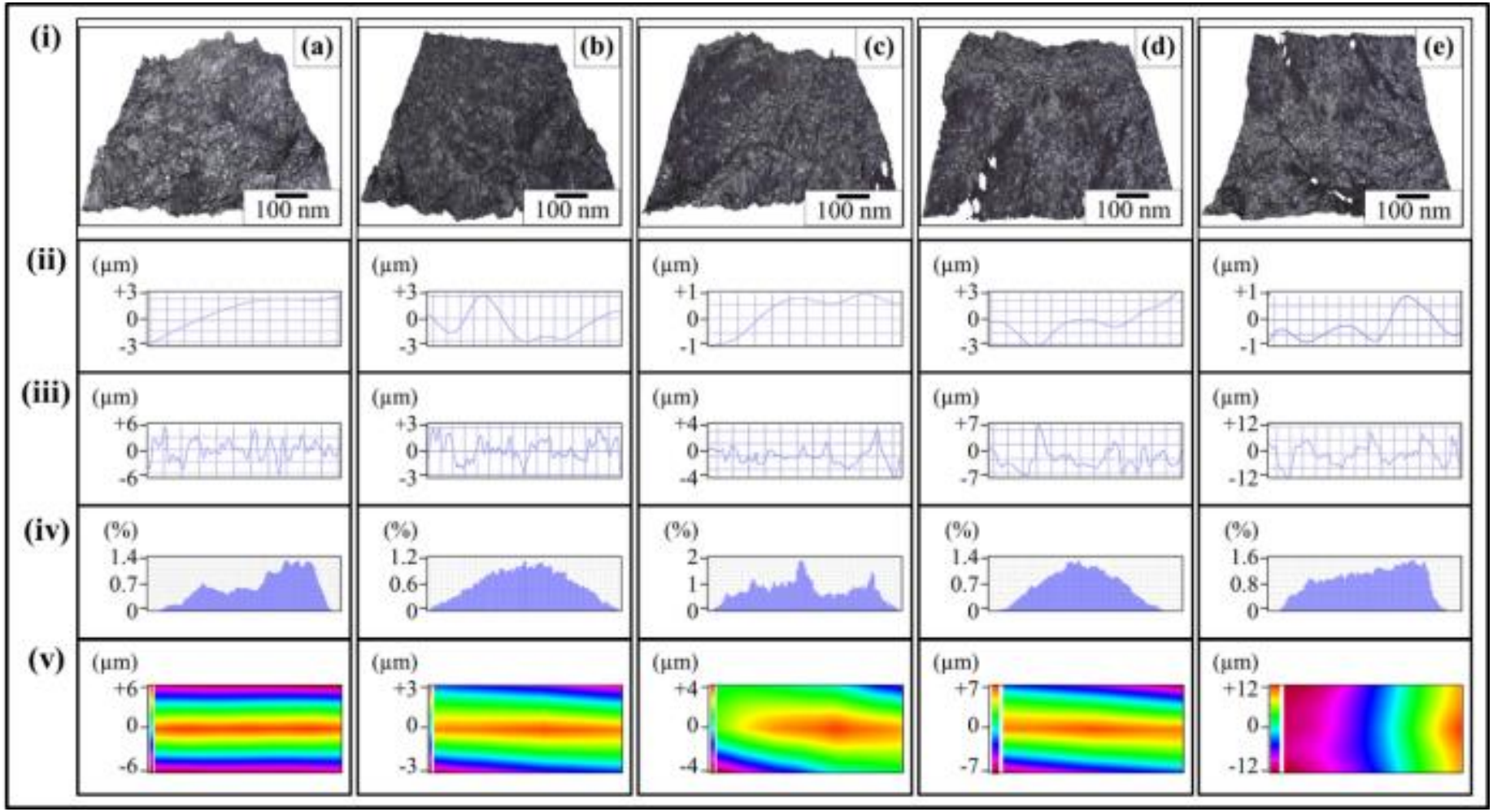

Figure 95: Surface roughness features of 0.5 wt% MLG-0.5 wt% nanoclay-EP fractured tensile samples after treatment with abrasive papers for 1 min at 150 rpm: (a) as-cast, (b) treated with velvet cloth, (c) 1200P, (d) 320P, and (e) 60P. From top to bottom in all cases: (i) tensile images (ii) waviness, (iii) roughness, (iv) Gaussian distribution, and (v) surface profile.

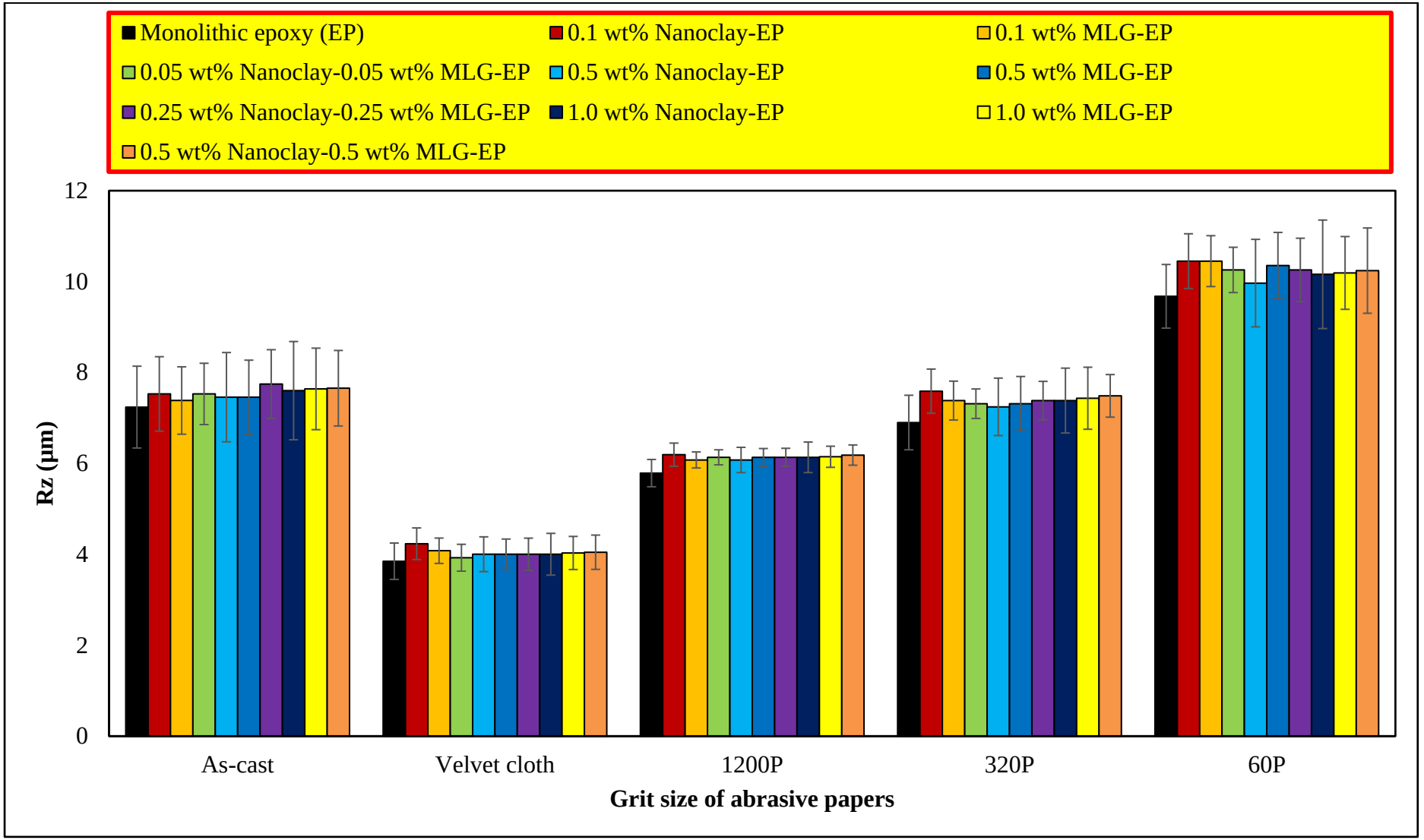

Figure 96: R_z values of fractured MLG-nanoclay-EP samples after treatment with abrasive papers for 1 min at 150 rpm.

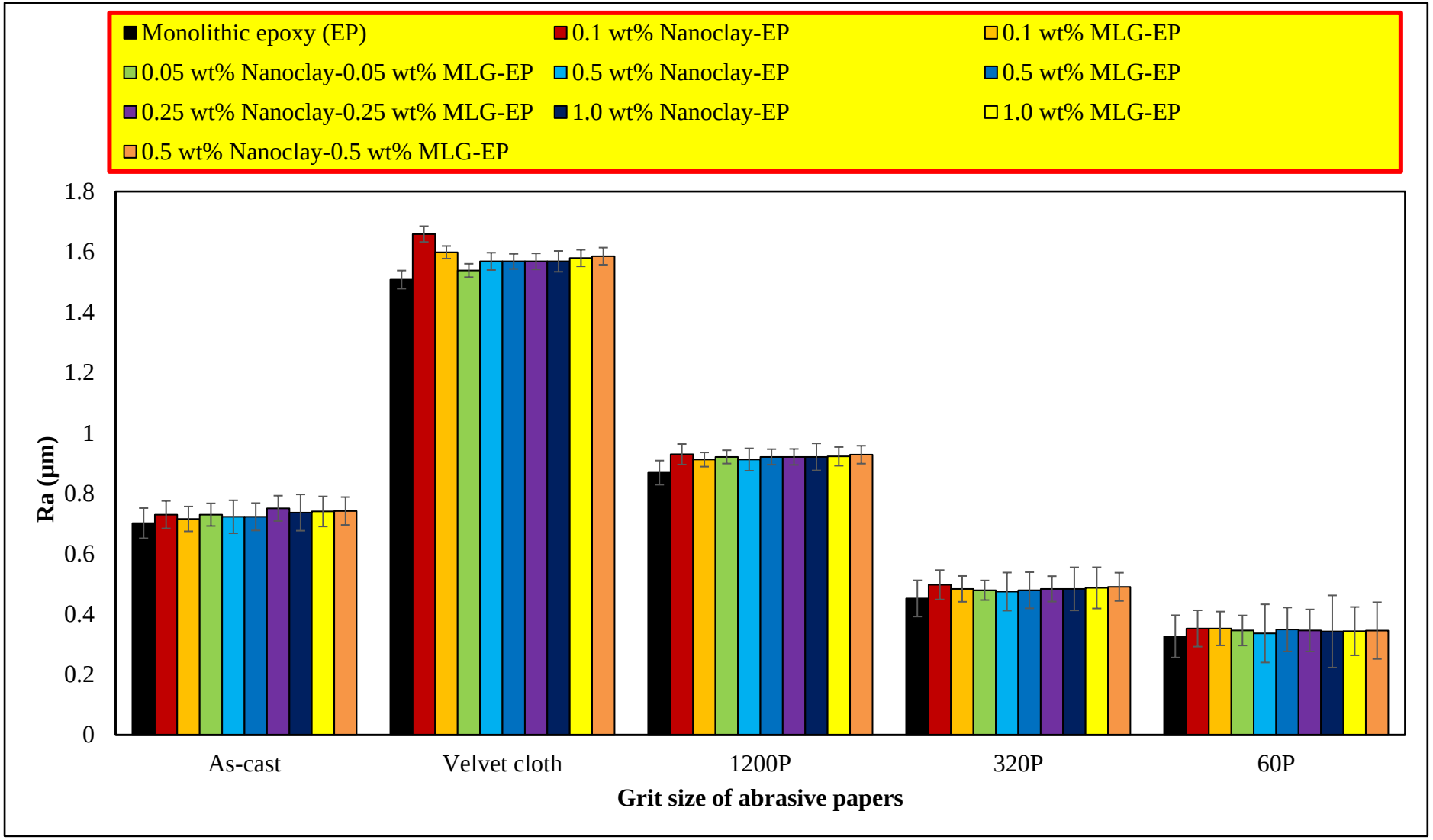

Figure 97: R_a values of fractured MLG-nanoclay-EP samples after treatment with abrasive papers for 1 min at 150 rpm.

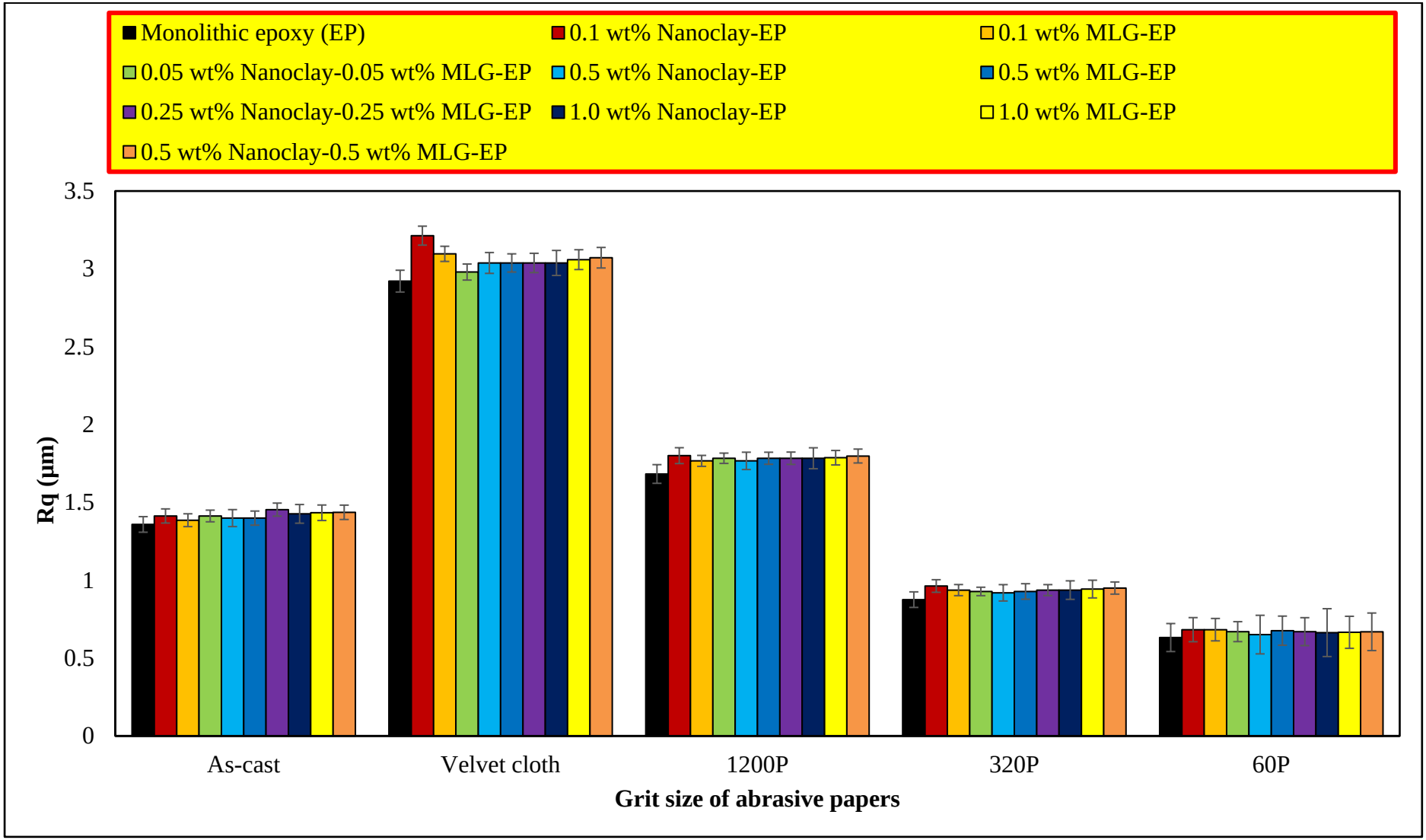

Figure 98: R_q values of fractured MLG-nanoclay-EP samples after treatment with abrasive papers for 1 min at 150 rpm.

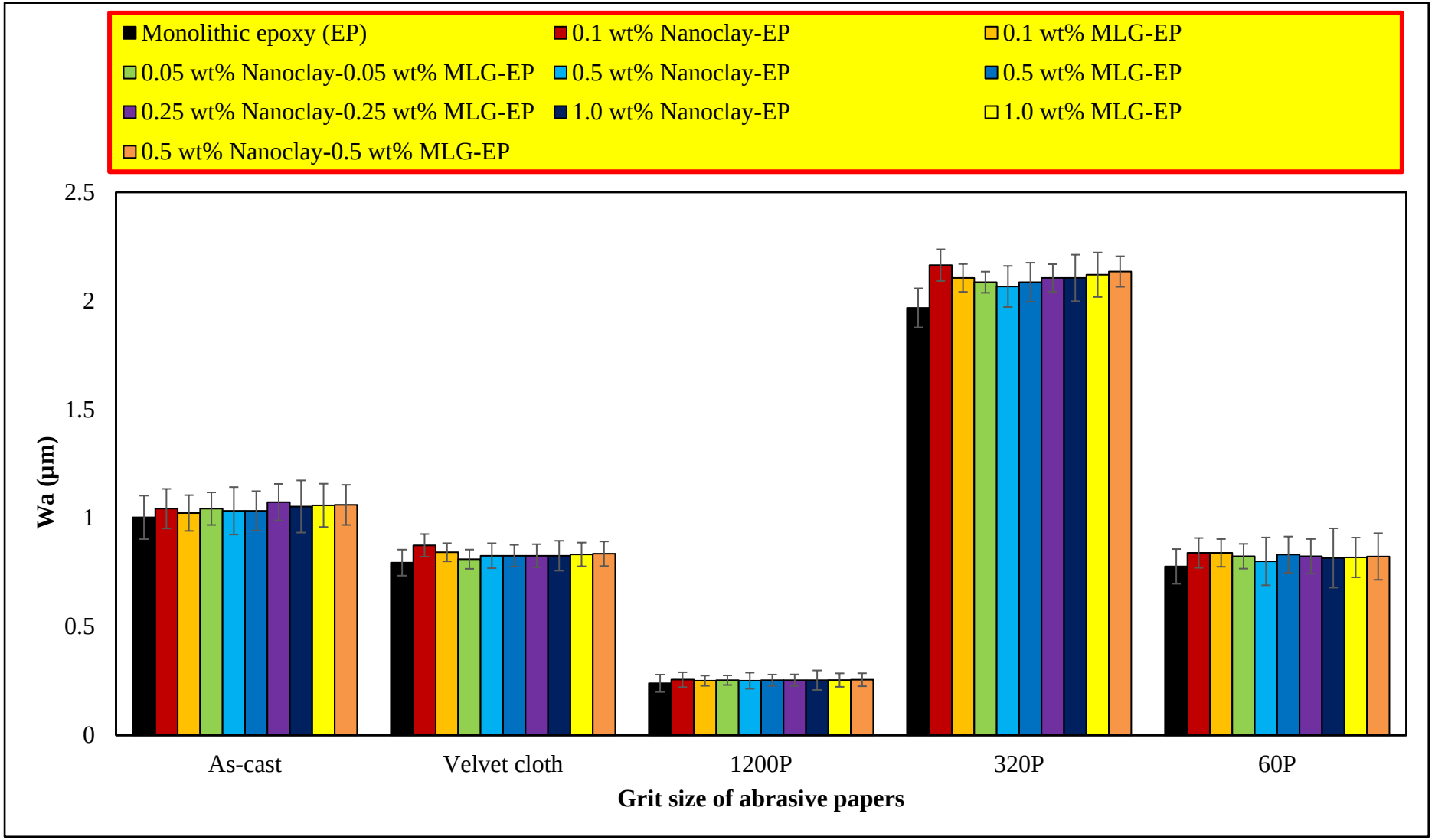

Figure 99: W_a values of fractured MLG-nanoclay-EP samples after treatment with abrasive papers for 1 min at 150 rpm.

crack is formed, it could not deflect much and rest of the fractured surface remained flat thereby decreasing the R_a value. Therefore, a high value of R_a (with low R_z value) can be an indicator of smoother samples surfaces, absence of agglomerates and uniform dispersion of nanofillers. On the other hand, a low value of R_a (with high R_z value) indicates the presence of deep surface notches, agglomerates, and non-uniform dispersion of nanofillers. A similar trend was observed in R_q values (Figure 98) as in R_a values. However, no specific trend was observed in surface waviness W_a (Figure 99) and may not be indicative of dispersion state of nanofillers and surface roughness features.

In the next chapter, conclusions of the work reported in the thesis are presented and based on the results reported, insight for the related future work is discussed.

Chapter-4

Conclusions and future work

24 Conclusions

In current work, the maximum increase in tensile and flexural properties, fracture toughness, and microhardness were observed at 0.3 wt% of MLG (MH). SEM images showed that MLG can obstruct the advancing cracks and significantly influence fracture mode. The monolithic epoxy and MLG-nanoclay-epoxy samples were produced and treated with abrasive papers and influence of surface roughness features was studied on mechanical properties, dynamic mechanical properties, and fracture mode. It was observed that as-cast samples had surface roughness which was reduced by treatment with velvet cloth and abrasive paper 1200P and increased by abrasive papers 320P and 60P. The maximum improvement in mechanical properties was observed when samples were treated with abrasive paper 1200P. It can also be concluded that the surface roughness beyond ±20 μm has detrimental effect on tensile strength and modulus of monolithic epoxy samples. Accordingly, the surface roughness below ±20 μm is benign for tensile properties of monolithic epoxy samples. It was further observed that tensile properties are more sensitive to topography than flexural properties. An efficient network of reinforcement particles can be achieved by using wide particle size distribution. When particle size distribution is narrow, the voids between the particles would not be filled and those filler-free or empty locations will be a preferred route for the cracks to surmount the reinforcement particles. On the other hand, when reinforcement has wide size distribution, the finer particles can occupy the empty spaces in between large

particles. It increases the filling ratio and makes an efficiently connected network of reinforcement. The wider morphology of reinforcement increases packing density, interfacial area, and mechanical interlocking with the polymer chains. The morphologically modified particles can significantly increase the coefficient of friction between reinforcement-reinforcement and reinforcement-matrix interfaces. A large amount of energy will be dissipated to work against friction that will increase the toughness of the samples prior to fracture. The surface roughness features of fractured patterns of polymer nanocomposites can be used to approximate the dispersion state, interfacial interactions, and presence of agglomerates, and overall influence of the incorporation of fillers on the mechanical properties of produced nanocomposites. A high value of R_a (with low R_z value) can be on indicator of smoother samples surfaces, absence of agglomerates and uniform dispersion of nanofillers. On the other hand, a low value of R_a (with high R_z value) indicates the presence of deep surface notches, agglomerates, and non-uniform dispersion of nanofillers. A similar trend was observed in R_q values as in R_a values. However, no specific trend was observed in surface waviness and may not be indicative of dispersion state of nanofillers and surface roughness features.

25 Future Work

In future, influence of morphology of functionalized fillers on damage tolerance and fracture toughness of epoxy based nanocomposites can be studied. The foundations for strapping up the treasure of physics, hidden within graphene structure, hinge on the ability to optimize the dispersibility of graphene in a solution. To tackle the dispersibility problems, surface modifications have been applied to tailor spatial distribution of MLG and CNT and their homogeneous dispersibility in host materials

[329]. The literature has proved the absence of consensus of MLG and CNT role in improving the properties of nanocomposites. Some studies have revealed improvements in properties via nano-fillers [169–171,330,331]. Others have observed either no improvements [174–176,332,333], or indeed reductions in properties [129–131,334,335]. The main reason for these differences in results was the functionalization of MLG and CNT that affected the dispersion and interfacial interactions of MLG and CNT in/with the polymer [336].

One of the key factors upon which the properties of polymer nanocomposites depend is the interfacial bond strength. The graphene surface is very smooth that results in weak interfacial bonding with the polymer [337]. In pristine form, MLG and CNT are inert towards polymers and interfacial bond primarily consists of Van der Waals forces. This weak bond cannot efficiently transfer load across filler-matrix interface. So, the surface properties of CNT have been modified by applying functional entities using two main methods: (1) Chemical or covalent functionalization, and (2) physical or non-covalent functionalization [338].

26 List of Publications

1. **Rasheed Atif**, Islam Shyha, Fawad Inam*. The Degradation of Mechanical Properties due to Stress Concentration Caused by Retained Acetone in Epoxy Nanocomposites. RSC Adv., 2016, 6, 34188. (Q1, IF: 3.289, Category: Chemistry-Multidisciplinary). http://pubs.rsc.org/en/content/articlelanding/2016/ra/c6ra00739b#!divAbstract.
2. **Rasheed Atif**, Jiacheng Wei, Islam Shyha, Fawad Inam*. Use of Morphological Features of Carbonaceous Materials for Improved Mechanical Properties of Epoxy Nanocomposites. RSC Adv., 2016, 6, 1351. (Q1, IF: 3.289, Category: Chemistry-Multidisciplinary). http://pubs.rsc.org/en/content/articlelanding/2015/ra/c5ra24039e#!divAbstract.
3. **Rasheed Atif**, Islam Shyha, Fawad Inam*. Mechanical, Thermal, and Electrical Properties of Graphene-Epoxy Nanocomposites – A Review. Polymers. (Q1, IF: 2.944, Category: Polymer Science). Polymers 2016, 8, 281; doi:10.3390/polym8080281. http://www.mdpi.com/2073-4360/8/8/281.
4. **Rasheed Atif**, Fawad Inam*. Reasons and Remedies for Agglomeration of Multi-Layer Graphene and Carbon Nanotubes in Polymers. Beilstein Journal of Nanotechnology (Q1, IF: 2.778, Category: Materials Science-Multidisciplinary). Beilstein J. Nanotechnol. 2016, 7, 1174–1196. http://www.beilstein-journals.org/bjnano/single/articleFullText.htm?publicId=2190-4286-7-109.
5. **Rasheed Atif**, Fawad Inam*. Influence of Macro-Topography on Damage Tolerance and Fracture Toughness of 0.1 wt% Multi-Layer Graphene/Nanoclay-Epoxy Nanocomposites. Polymers. Polymers 2016, 8(7), 239; doi:10.3390/polym8070239. (Q1, IF: 2.944, Category: Polymer Science). http://www.mdpi.com/2073-4360/8/7/239.
6. Mohd Shahneel Saharudin, **Rasheed Atif**, Islam Shyha, Fawad Inam. The degradation of mechanical properties in polymer nano-composites exposed to liquid media – a review. RSC Adv., 2016, 6, 1076. (Q1, IF: 3.289, Category: Chemistry-Multidisciplinary). http://pubs.rsc.org/en/content/articlelanding/2016/ra/c5ra22620a#!divAbstract.
7. Jiacheng Wei, **Rasheed Atif**, Thuc Vo, Fawad Inam*. Graphene Nanoplatelets in Epoxy System: Dispersion, Reaggregation, and Mechanical Properties of Nanocomposites. Journal of Nanomaterials 2015, 2015, 1-12. (Q2, IF: 1.758, Category: Materials Science-Multidisciplinary). http://www.hindawi.com/journals/jnm/2015/561742/.
8. **Rasheed Atif**, Islam Shyha, Fawad Inam*. Modeling and Experimentation of multi-layered nanostructured graphene-epoxy nanocomposites for enhanced thermal and mechanical properties. Journal of Compososite Materials 2016:1–12. (Q2, IF: 1.242, Category: Materials Science-Composites).

http://jcm.sagepub.com/content/early/2016/03/24/0021998316640060.abstract?rss=1.

9. Mohd Shahneel Saharudin, **Rasheed Atif**, Islam Shyha, Fawad Inam. The degradation of mechanical properties in halloysite nanoclay-polyester nanocomposites exposed to diluted methanol. Journal of Composite Materials. (Q2, IF: 1.153, Category: Materials Science-Composites). http://jcm.sagepub.com/content/early/2016/07/18/0021998316660178.abstract.
10. **Rasheed Atif**, Fawad Inam*. Fractography Analysis with Surface roughness features of 0.5 wt% Multi-Layer Graphene/Nanoclay Reinforced Epoxy Nanocomposites. AIMS Materials Science (Indexed in Thomson Reuters, Impact factor will start from 2017). AIMS Materials Science 3(3) : 1266-1280. http://www.aimspress.com/article/10.3934/matersci.2016.3.1266/abstract.html
11. **Rasheed Atif**, Fawad Inam*. Modeling and Simulation of Graphene Based Polymer Nanocomposites: Advances in the Last Decade. Graphene, 2016, 5, 96-142. (2-GJIF: 1.5). http://www.scirp.org/Journal/PaperInformation.aspx?PaperID=66126.
12. **Rasheed Atif**, Fawad Inam*. The dissimilarities between graphene and frame-like structures. Graphene, 2016, 5, 55-72. (2-GJIF: 1.5). http://www.scirp.org/journal/PaperInformation.aspx?PaperID=65466.
13. **Rasheed Atif**, Fawad Inam*. Influence of Macro-Topography on Damage Tolerance and Fracture Toughness of Monolithic Epoxy for Tribological Applications. World Journal of Engineering and Technology, 2016, 4, 335-360. (2-GJIF: 0.35). http://www.scirp.org/Journal/PaperInformation.aspx?PaperID=66980.
14. **Rasheed Atif**, Fawad Inam*. Influence of Macro-Topography on Damage Tolerance and Fracture Toughness of 0.5 wt% Multi-Layer Graphene/Nanoclay-Epoxy Nanocomposites. AIMS Materials Science (Indexed in Thomson Reuters, Impact factor will start from 2017). AIMS Materials Science 3(4) : 1294-1308. http://www.aimspress.com/article/10.3934/matersci.2016.4.1294.
15. **Rasheed Atif**, Fawad Inam*. Fractography Analysis with Surface roughness features of Multi-Layer Graphene Reinforced Epoxy Nanocomposites. Graphene, 2016, 5, 166-177. http://dx.doi.org/10.4236/graphene.2016.54014
16. **Rasheed Atif**, Fawad Inam*. Fractography Analysis with Surface roughness features of Monolithic Epoxy with Tailored Topography. World Journal of Engineering and Technology, 2016, 4, 517-52. http://dx.doi.org/10.4236/wjet.2016.44051.
17. **Rasheed Atif**, Fawad Inam*. Influence of Macro-Topography on Mechanical Properties of 1.0 wt% Multi-Layer Graphene/Nanoclay-Epoxy Nanocomposites. Journal of Composite Materials. (Q2, IF: 1.242, Category: Materials Science-Composites). http://journals.sagepub.com/doi/abs/10.1177/0021998316679016.

18. **Rasheed Atif**, Fawad Inam*. Fractography Analysis of 1.0 wt% Multi-Layer Graphene/Nanoclay Reinforced Epoxy Nanocomposites. Applied Composite Materials. (Q2, IF: 1.153, Category: Materials Science-Composites). http://journals.sagepub.com/doi/abs/10.1177/0021998316679017.
19. Mohd Shahneel Saharudin, **Rasheed Atif**, Fawad Inam*. Effect of Short-TermWater Exposure on the Mechanical Properties of Halloysite Nanotube-Multi Layer Graphene Reinforced Polyester Nanocomposites. Polymers 2017, 9, 27; doi:10.3390/polym9010027. http://www.mdpi.com/2073-4360/9/1/27.
20. Jiacheng Wei, **Rasheed Atif**, Mohd Shahneel Saharudin, Thuc Vo, Fawad Inam. Processing of Epoxy/Graphene Nanocomposites. 6th Chemical Nanoscience Symposium Newcastle 2016, Newcastle University, United Kingdom, March 17th, 2016.

27 Turnitin originality report:

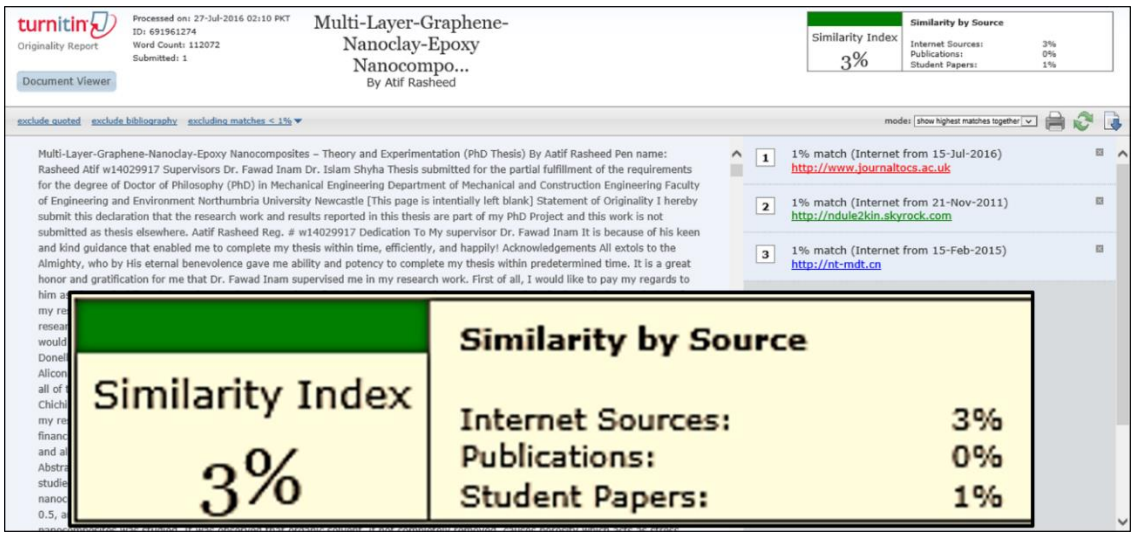

28 References:

[1] D.B. Miracle, S.L. Donaldson, eds., ASM Handbook Vol. 21, Composites, 2001.

[2] X.F. Yao, D. Zhou, H.Y. Yeh, Macro/microscopic fracture characterizations of SiO2/epoxy nanocomposites, Aerosp. Sci. Technol. 12 (2008) 223–230. doi:10.1016/j.ast.2007.03.005.

[3] B. Wetzel, P. Rosso, F. Haupert, K. Friedrich, Epoxy nanocomposites - fracture and toughening mechanisms, Eng. Fract. Mech. 73 (2006) 2375–2398. doi:10.1016/j.engfracmech.2006.05.018.

[4] W. Naous, X.Y. Yu, Q.X. Zhang, K. Naito, Y. Kagawa, Morphology, tensile properties, and fracture toughness of epoxy/Al2O3 nanocomposites, J. Polym. Sci. Part B-Polymer Phys. 44 (2006) 1466–1473. doi:10.1002/Polb.20800.

[5] B.C. Kim, S.W. Park, D.G. Lee, Fracture toughness of the nano-particle reinforced epoxy composite, Compos. Struct. 86 (2008) 69–77. doi:10.1177/0892705714556835.

[6] K. Wang, L. Chen, J. Wu, M.L. Toh, C. He, A.F. Yee, Epoxy nanocomposites with highly exfoliated clay: Mechanical properties and fracture mechanisms, Macromolecules. 38 (2005) 788–800. doi:10.1021/ma048465n.

[7] W. Liu, S. V. Hoa, M. Pugh, Fracture toughness and water uptake of high-performance epoxy/nanoclay nanocomposites, Compos. Sci. Technol. 65 (2005) 2364–2373. doi:10.1016/j.compscitech.2005.06.007.

[8] F.H. Gojny, M.H.G. Wichmann, U. Köpke, B. Fiedler, K. Schulte, Carbon nanotube-reinforced epoxy-composites: Enhanced stiffness and fracture toughness at low nanotube content, Compos. Sci. Technol. 64 (2004) 2363–2371. doi:10.1016/j.compscitech.2004.04.002.

[9] N. Yu, Z.H. Zhang, S.Y. He, Fracture toughness and fatigue life of MWCNT/epoxy composites, Mater. Sci. Eng. A. 494 (2008) 380–384. doi:10.1016/j.msea.2008.04.051.

[10] I. Srikanth, S. Kumar, A. Kumar, P. Ghosal, C. Subrahmanyam, Effect of amino functionalized MWCNT on the crosslink density, fracture toughness of epoxy and mechanical properties of carbon-epoxy composites, Compos. Part A Appl. Sci. Manuf. 43 (2012) 2083–2086. doi:10.1016/j.compositesa.2012.07.005.

[11] M.J. Mathews, S.R. Swanson, Characterization of the interlaminar fracture toughness of a laminated carbon/epoxy composite, Compos. Sci. Technol. 67 (2007) 1489–1498. doi:10.1016/j.compscitech.2006.07.035.

[12] M. Arai, Y. Noro, K. ichi Sugimoto, M. Endo, Mode I and mode II interlaminar fracture toughness of CFRP laminates toughened by carbon nanofiber interlayer, Compos. Sci. Technol. 68 (2008) 516–525. doi:10.1016/j.compscitech.2007.06.007.

[13] D.W.Y. Wong, L. Lin, P.T. McGrail, T. Peijs, P.J. Hogg, Improved fracture toughness of carbon fibre/epoxy composite laminates using dissolvable thermoplastic fibres, Compos. Part A Appl. Sci. Manuf. 41 (2010) 759–767. doi:10.1016/j.compositesa.2010.02.008.

[14] K.S. Novoselov, A.K. Geim, S.V. Morozov, D. Jiang, Y. Zhang, S.V. Dubonos, I. V. Grigorieva, a. a. Firsov, Electric Field Effect in Atomically Thin Carbon Films, Science. 306 (2004) 666–669. doi:10.1126/science.1102896.

[15] S. Stankovich, D.A. Dikin, G.H.B. Dommett, K.M. Kohlhaas, E.J. Zimney, E.A. Stach, R.D. Piner, S.T. Nguyen, R.S. Ruoff, Graphene-based composite materials., Nature. 442 (2006) 282–286. doi:10.1038/nature04969.

[16] Carlson R. L., Kardomateas G. A., Craig J. I., Mechanics of Failure Mechanisms in Structures, 1st ed., springer, 2012.

[17] P. Pokharel, Q.-T. Truong, D.S. Lee, Multi-step microwave reduction of graphite oxide and its use in the formation of electrically conductive graphene/epoxy composites, Compos. Part B Eng. 64 (2014) 187–193. doi:10.1016/j.compositesb.2014.04.013.

[18] M. Tian, L. Qu, X. Zhang, K. Zhang, S. Zhu, X. Guo, G. Han, X. Tang, Y. Sun, Enhanced mechanical and thermal properties of regenerated cellulose/graphene composite fibers., Carbohydr. Polym. 111 (2014) 456–62. doi:10.1016/j.carbpol.2014.05.016.

[19] Z. Xu, J. Zhang, M. Shan, Y. Li, B. Li, J. Niu, B. Zhou, X. Qian, Organosilane-functionalized graphene oxide for enhanced antifouling and mechanical properties of polyvinylidene fluoride ultrafiltration membranes, J. Memb. Sci. 458 (2014) 1–13. doi:10.1016/j.memsci.2014.01.050.

[20] R. Bkakri, A. Sayari, E. Shalaan, S. Wageh, A.A. Al-Ghamdi, A. Bouazizi, Effects of the graphene doping level on the optical and electrical properties of ITO/P3HT:Graphene/Au organic solar cells, Superlattices Microstruct. 76 (2014) 461–471.

doi:10.1016/j.spmi.2014.10.016.
[21] Y. Lian, F. He, H. Wang, F. Tong, A new aptamer/graphene interdigitated gold electrode piezoelectric sensor for rapid and specific detection of staphylococcus aureus, Biosens. Bioelectron. 65 (2014) 314–319. doi:10.1016/j.bios.2014.10.017.
[22] Z. Abdin, M.A. Alim, R. Saidur, M.R. Islam, W. Rashmi, S. Mekhilef, A. Wadi, Solar energy harvesting with the application of nanotechnology, Renew. Sustain. Energy Rev. 26 (2013) 837–852. doi:10.1016/j.rser.2013.06.023.
[23] W. Sun, R. Hu, H. Liu, M. Zeng, L. Yang, H. Wang, M. Zhu, Embedding nano-silicon in graphene nanosheets by plasma assisted milling for high capacity anode materials in lithium ion batteries, J. Power Sources. 268 (2014) 610–618. doi:10.1016/j.jpowsour.2014.06.039.
[24] A.A. Azeez, K.Y. Rhee, S.J. Park, D. Hui, Epoxy clay nanocomposites – processing, properties and applications: A review, Compos. Part B Eng. 45 (2013) 308–320. doi:10.1016/j.compositesb.2012.04.012.
[25] A. Aziz, H.N. Lim, S.H. Girei, M.H. Yaacob, M.A. Mahdi, N.M. Huang, A. Pandikumar, Silver/graphene nanocomposite-modified optical fiber sensor platform for ethanol detection in water medium, Sensors Actuators B Chem. 206 (2015) 119–125. doi:10.1016/j.snb.2014.09.035.
[26] N. Agnihotri, A.D. Chowdhury, A. De, Non-enzymatic electrochemical detection of cholesterol using β-cyclodextrin functionalized graphene., Biosens. Bioelectron. 63 (2015) 212–7. doi:10.1016/j.bios.2014.07.037.
[27] G. Nanocomposites, D. Galpaya, M. Wang, M. Liu, N. Motta, E. Waclawik, C. Yan, Recent Advances in Fabrication and Characterization of, 2012 (2012) 30–49.
[28] K.M.F. Shahil, A. a. Balandin, Thermal properties of graphene and multilayer graphene: Applications in thermal interface materials, Solid State Commun. 152 (2012) 1331–1340. doi:10.1016/j.ssc.2012.04.034.
[29] M.H. Al-Saleh, U. Sundararaj, Review of the mechanical properties of carbon nanofiber/polymer composites, Compos. Part A Appl. Sci. Manuf. 42 (2011) 2126–2142. doi:10.1016/j.compositesa.2011.08.005.
[30] R. Sanjinés, M.D. Abad, C. Vâju, R. Smajda, M. Mionić, a. Magrez, Electrical properties and applications of carbon based nanocomposite materials: An overview, Surf. Coatings Technol. 206 (2011) 727–733. doi:10.1016/j.surfcoat.2011.01.025.
[31] J.R. Potts, D.R. Dreyer, C.W. Bielawski, R.S. Ruoff, Graphene-based polymer nanocomposites, Polymer (Guildf). 52 (2011) 5–25. doi:10.1016/j.polymer.2010.11.042.
[32] F. Qin, C. Brosseau, A review and analysis of microwave absorption in polymer composites filled with carbonaceous particles, J. Appl. Phys. 111 (2012) 61301. doi:10.1063/1.3688435.
[33] S.-Y. Lee, S.-J. Park, Comprehensive review on synthesis and adsorption behaviors of graphene-based materials, Carbon Lett. 13 (2012) 73–87. doi:10.5714/CL.2012.13.2.073.
[34] V. Singh, D. Joung, L. Zhai, S. Das, S.I. Khondaker, S. Seal, Graphene based materials: Past, present and future, Prog. Mater. Sci. 56 (2011) 1178–1271. doi:10.1016/j.pmatsci.2011.03.003.
[35] H. Kim, A. a. Abdala, C.W. Macosko, Graphene/Polymer Nanocomposites, Macromolecules. 43 (2010) 6515–6530. doi:10.1021/ma100572e.
[36] V. Dhand, K.Y. Rhee, H.J. Kim, D.H. Jung, A Comprehensive Review of Graphene Nanocomposites : Research Status and Trends, J. Nanomater. 2013 (2015) 1–15.
[37] A. Santamaria, M.E. Muñoz, M. Fernández, M. Landa, Electrically conductive adhesives with a focus on adhesives that contain carbon nanotubes, J. Appl. Polym. Sci. 129 (2013) 1643–1652. doi:10.1002/app.39137.
[38] M.-Q. Yang, Y.-J. Xu, Selective photoredox using graphene-based composite photocatalysts., Phys. Chem. Chem. Phys. 15 (2013) 19102–18. doi:10.1039/c3cp53325e.
[39] G. Srinivas, Z.X. Guo, Graphene-based materials: Synthesis and gas sorption, storage and separation, Prog. Mater. Sci. (2014). doi:10.1016/j.pmatsci.2014.10.004.
[40] Z. Xu, L. Chen, B. Zhou, Y. Li, B. Li, J. Niu, M. Shan, Q. Guo, Z. Wang, X. Qian, Nano-structure and property transformations of carbon systems under γ-ray irradiation: a review, RSC Adv. 3 (2013) 10579. doi:10.1039/c3ra00154g.
[41] K. Hu, D.D. Kulkarni, I. Choi, V. V. Tsukruk, Graphene-polymer nanocomposites for structural and functional applications, Prog. Polym. Sci. 39 (2014) 1934–1972. doi:10.1016/j.progpolymsci.2014.03.001.
[42] R.J. Young, I. a. Kinloch, L. Gong, K.S. Novoselov, The mechanics of graphene nanocomposites: A review, Compos. Sci. Technol. 72 (2012) 1459–1476. doi:10.1016/j.compscitech.2012.05.005.
[43] I. Zaman, B. Manshoor, A. Khalid, S. Araby, From clay to graphene for polymer

nanocomposites—a survey, J. Polym. Res. 21 (2014) 429. doi:10.1007/s10965-014-0429-0.
[44] X. Sun, H. Sun, H. Li, H. Peng, Developing polymer composite materials: carbon nanotubes or graphene?, Adv. Mater. 25 (2013) 5153–76. doi:10.1002/adma.201301926.
[45] T. Kuilla, S. Bhadra, D. Yao, N.H. Kim, S. Bose, J.H. Lee, Recent advances in graphene based polymer composites, Prog. Polym. Sci. 35 (2010) 1350–1375. doi:10.1016/j.progpolymsci.2010.07.005.
[46] A. Rasheed, F.A. Khalid, Fabrication and properties of CNTs reinforced polymeric matrix nanocomposites for sports applications, IOP Conf. Ser. Mater. Sci. Eng. 60 (2014) 12009. doi:10.1088/1757-899X/60/1/012009.
[47] L. Yue, G. Pircheraghi, S.A. Monemian, I. Manas-Zloczower, Epoxy composites with carbon nanotubes and graphene nanoplatelets – Dispersion and synergy effects, Carbon N. Y. 78 (2014) 268–278. doi:10.1016/j.carbon.2014.07.003.
[48] P. Jean-Pierre, W. Roberto, Epoxy Polymers New Materials and Innovations, WILEY-VCH, 2010.
[49] M. Sanjay, Composites Manufacturing Materials, Product, and Process Engineering, CRC Press, 2002.
[50] V. Valery, M. Evgeny, Mechanics and Analysis of Composite Materials, Elsevier, 2001.
[51] C. Wongbong, L. Jo-Won, Graphene Synthesis and Applications, CRC Press, 2012.
[52] J.H. Warner, S. Fransizka, R. Mark, A. Bachmatiuk, Graphene: Fundamentals and Emergent Applications, Elsevier, 2013.
[53] K. Mikhail, K.M. Iosifovich, Graphene: Carbon in Two Dimensions, Cambridge University Press, 2012.
[54] E.L. Wolf, Graphene: A New Paradigm in Condensed Matter and Device Physics, OUP Oxford, 2013.
[55] M. Quintana, K. Spyrou, M. Grzelczak, W.R. Browne, P. Rudolf, M. Prato, Functionalization of Graphene, ACS Nano. 4 (2010) 3527–3533.
[56] X. Wang, J. Jin, M. Song, An investigation of the mechanism of graphene toughening epoxy, Carbon N. Y. 65 (2013) 324–333. doi:10.1016/j.carbon.2013.08.032.
[57] J. Jia, C.-M. Kan, X. Lin, X. Shen, J.-K. Kim, Effects of processing and material parameters on synthesis of monolayer ultralarge graphene oxide sheets, Carbon N. Y. 77 (2014) 244–254. doi:10.1016/j.carbon.2014.05.027.
[58] Y.-J. Wan, L.-C. Tang, L.-X. Gong, D. Yan, Y.-B. Li, L.-B. Wu, J.-X. Jiang, G.-Q. Lai, Grafting of epoxy chains onto graphene oxide for epoxy composites with improved mechanical and thermal properties, Carbon N. Y. 69 (2014) 467–480. doi:10.1016/j.carbon.2013.12.050.
[59] B.S. T.K., A.B. Nair, B.T. Abraham, P.M.S. Beegum, E.T. Thachil, Microwave exfoliated reduced graphene oxide epoxy nanocomposites for high performance applications, Polymer (Guildf). 55 (2014) 3614–3627. doi:10.1016/j.polymer.2014.05.032.
[60] Y. Zhang, Y. Wang, J. Yu, L. Chen, J. Zhu, Z. Hu, Tuning the interface of graphene platelets/epoxy composites by the covalent grafting of polybenzimidazole, Polymer (Guildf). 55 (2014) 4990–5000. doi:10.1016/j.polymer.2014.07.045.
[61] B. Ahmadi-Moghadam, M. Sharafimasooleh, S. Shadlou, F. Taheri, Effect of functionalization of graphene nanoplatelets on the mechanical response of graphene/ epoxy composites, Mater. Des. 66 (2014) 142–149. doi:10.1016/j.matdes.2014.10.047.
[62] J. Ma, Q. Meng, I. Zaman, S. Zhu, A. Michelmore, N. Kawashima, C.H. Wang, H.-C. Kuan, Development of polymer composites using modified, high-structural integrity graphene platelets, Compos. Sci. Technol. 91 (2014) 82–90. doi:10.1016/j.compscitech.2013.11.017.
[63] S. Chandrasekaran, N. Sato, F. Tölle, R. Mülhaupt, B. Fiedler, K. Schulte, Fracture toughness and failure mechanism of graphene based epoxy composites, Compos. Sci. Technol. 97 (2014) 90–99. doi:10.1016/j.compscitech.2014.03.014.
[64] Y.-J. Wan, L.-X. Gong, L.-C. Tang, L.-B. Wu, J.-X. Jiang, Mechanical properties of epoxy composites filled with silane-functionalized graphene oxide, Compos. Part A Appl. Sci. Manuf. 64 (2014) 79–89. doi:10.1016/j.compositesa.2014.04.023.
[65] I. Zaman, B. Manshoor, A. Khalid, Q. Meng, S. Araby, Interface modification of clay and graphene platelets reinforced epoxy nanocomposites: a comparative study, J. Mater. Sci. 49 (2014) 5856–5865. doi:10.1007/s10853-014-8296-y.
[66] T. Jiang, T. Kuila, N.H. Kim, J.H. Lee, Effects of surface-modified silica nanoparticles attached graphene oxide using isocyanate-terminated flexible polymer chains on the mechanical properties of epoxy composites, J. Mater. Chem. A. 2 (2014) 10557. doi:10.1039/c4ta00584h.
[67] M.M. Shokrieh, S.M. Ghoreishi, M. Esmkhani, Z. Zhao, Effects of graphene nanoplatelets and

graphene nanosheets on fracture toughness of epoxy nanocomposites, Fatigue Fract. Eng. Mater. Struct. 37 (2014) 1116–1123. doi:10.1111/ffe.12191.
[68] L.-C. Tang, Y.-J. Wan, D. Yan, Y.-B. Pei, L. Zhao, Y.-B. Li, L.-B. Wu, J.-X. Jiang, G.-Q. Lai, The effect of graphene dispersion on the mechanical properties of graphene/epoxy composites, Carbon N. Y. 60 (2013) 16–27. doi:10.1016/j.carbon.2013.03.050.
[69] S. Chandrasekaran, C. Seidel, K. Schulte, Preparation and characterization of graphite nano-platelet (GNP)/epoxy nano-composite: Mechanical, electrical and thermal properties, Eur. Polym. J. 49 (2013) 3878–3888. doi:10.1016/j.eurpolymj.2013.10.008.
[70] Z. Li, R. Wang, R.J. Young, L. Deng, F. Yang, L. Hao, W. Jiao, W. Liu, Control of the functionality of graphene oxide for its application in epoxy nanocomposites, Polymer (Guildf). 54 (2013) 6437–6446. doi:10.1016/j.polymer.2013.09.054.
[71] S. Shadlou, E. Alishahi, M.R. Ayatollahi, Fracture behavior of epoxy nanocomposites reinforced with different carbon nano-reinforcements, Compos. Struct. 95 (2013) 577–581. doi:10.1016/j.compstruct.2012.08.002.
[72] T. Jiang, T. Kuila, N.H. Kim, B.-C. Ku, J.H. Lee, Enhanced mechanical properties of silanized silica nanoparticle attached graphene oxide/epoxy composites, Compos. Sci. Technol. 79 (2013) 115–125. doi:10.1016/j.compscitech.2013.02.018.
[73] W. Liu, J. Kong, W.E. Toh, R. Zhou, G. Ding, S. Huang, Y. Dong, X. Lu, Toughening of epoxies by covalently anchoring triazole-functionalized stacked-cup carbon nanofibers, Compos. Sci. Technol. 85 (2013) 1–9. doi:10.1016/j.compscitech.2013.05.009.
[74] R. Wang, Z. Li, W. Liu, W. Jiao, L. Hao, F. Yang, Attapulgite–graphene oxide hybrids as thermal and mechanical reinforcements for epoxy composites, Compos. Sci. Technol. 87 (2013) 29–35. doi:10.1016/j.compscitech.2013.08.002.
[75] E. Alishahi, S. Shadlou, S. Doagou-R, M.R. Ayatollahi, Effects of Carbon Nanoreinforcements of Different Shapes on the Mechanical Properties of Epoxy-Based Nanocomposites, Macromol. Mater. Eng. 298 (2013) 670–678. doi:10.1002/mame.201200123.
[76] J. Ma, Q. Meng, A. Michelmore, N. Kawashima, Z. Izzuddin, C. Bengtsson, H.-C. Kuan, Covalently bonded interfaces for polymer/graphene composites, J. Mater. Chem. A. 1 (2013) 4255. doi:10.1039/c3ta01277h.
[77] H. Feng, X. Wang, D. Wu, Fabrication of Spirocyclic Phosphazene Epoxy-Based Nanocomposites with Graphene via Exfoliation of Graphite Platelets and Thermal Curing for Enhancement of Mechanical and Conductive Properties, Ind. Eng. Chem. Res. 52 (2013) 10160–10171. doi:10.1021/ie400483x.
[78] S. Chatterjee, F. Nafezarefi, N.H. Tai, L. Schlagenhauf, F. a. Nüesch, B.T.T. Chu, Size and synergy effects of nanofiller hybrids including graphene nanoplatelets and carbon nanotubes in mechanical properties of epoxy composites, Carbon N. Y. 50 (2012) 5380–5386. doi:10.1016/j.carbon.2012.07.021.
[79] S. Chatterjee, J.W. Wang, W.S. Kuo, N.H. Tai, C. Salzmann, W.L. Li, R. Hollertz, F. a. Nüesch, B.T.T. Chu, Mechanical reinforcement and thermal conductivity in expanded graphene nanoplatelets reinforced epoxy composites, Chem. Phys. Lett. 531 (2012) 6–10. doi:10.1016/j.cplett.2012.02.006.
[80] I. Zaman, T.T. Phan, H.-C. Kuan, Q. Meng, L.T. Bao La, L. Luong, O. Youssf, J. Ma, Epoxy/graphene platelets nanocomposites with two levels of interface strength, Polymer (Guildf). 52 (2011) 1603–1611. doi:10.1016/j.polymer.2011.02.003.
[81] S. Rana, R. Alagirusamy, M. Joshi, Development of carbon nanofibre incorporated three phase carbon/epoxy composites with enhanced mechanical, electrical and thermal properties, Compos. Part A Appl. Sci. Manuf. 42 (2011) 439–445. doi:10.1016/j.compositesa.2010.12.018.
[82] D.R. Bortz, C. Merino, I. Martin-Gullon, Carbon nanofibers enhance the fracture toughness and fatigue performance of a structural epoxy system, Compos. Sci. Technol. 71 (2011) 31–38. doi:10.1016/j.compscitech.2010.09.015.
[83] G. Zhang, J. Karger-Kocsis, J. Zou, Synergetic effect of carbon nanofibers and short carbon fibers on the mechanical and fracture properties of epoxy resin, Carbon N. Y. 48 (2010) 4289–4300. doi:10.1016/j.carbon.2010.07.040.
[84] M. Fang, Z. Zhang, J. Li, H. Zhang, H. Lu, Y. Yang, Constructing hierarchically structured interphases for strong and tough epoxy nanocomposites by amine-rich graphene surfaces, J. Mater. Chem. 20 (2010) 9635. doi:10.1039/c0jm01620a.
[85] S. Jana, W.-H. Zhong, Graphite particles with a “puffed” structure and enhancement in mechanical performance of their epoxy composites, Mater. Sci. Eng. A. 525 (2009) 138–146. doi:10.1016/j.msea.2009.06.052.
[86] M. a Rafiee, J. Rafiee, I. Srivastava, Z. Wang, H. Song, Z.-Z. Yu, N. Koratkar, Fracture and

fatigue in graphene nanocomposites., Small. 6 (2010) 179–83. doi:10.1002/smll.200901480.
[87] J. Loomis, B. Panchapakesan, Dimensional dependence of photomechanical response in carbon nanostructure composites: a case for carbon-based mixed-dimensional systems., Nanotechnology. 23 (2012) 2–21550115512. doi:10.1088/0957-4484/23/21/215501.
[88] ASM Handbook, Vol. 8. Mechanical Testing and Evaluation., 2000.
[89] A.A. Griffith, The Phenomena of Rupture and Flow in Solids, Philos. Trans. R. Soc. London. Ser. A, Contain. Pap. a Math. or Phys. Character. 221 (1921) 163–198. doi:10.2307/91192.
[90] W. Zhang, I. Srivastava, Y.F. Zhu, C.R. Picu, N. a. Koratkar, Heterogeneity in epoxy nanocomposites initiates crazing: Significant improvements in fatigue resistance and toughening, Small. 5 (2009) 1403–1407. doi:10.1002/smll.200801910.
[91] ASM Handbook Vol. 19, Fatigue and Fracture., (1996).
[92] H.Y. Sohn, C. Moreland, The effect of particle size distribution on packing density, Can. J. Chem. Eng. 46 (1968) 162–167. doi:10.1002/cjce.5450460305.
[93] Q. Chen, W. Liu, S. Guo, S. Zhu, Q. Li, X. Li, X. Wang, H. Liu, Synthesis of well-aligned millimeter-sized tetragon-shaped graphene domains by tuning the copper substrate orientation, Carbon N. Y. 93 (2015) 945–952. doi:10.1016/j.carbon.2015.05.108.
[94] X. Li, W. Cai, J. An, S. Kim, J. Nah, D. Yang, R. Piner, A. Velamakanni, I. Jung, E. Tutuc, S.K. Banerjee, L. Colombo, R.S. Ruoff, Large-area synthesis of high-quality and uniform graphene films on copper foils., Science. 324 (2009) 1312–1314. doi:10.1126/science.1171245.
[95] S. Bae, H. Kim, Y. Lee, X. Xu, J.-S. Park, Y. Zheng, J. Balakrishnan, T. Lei, H.R. Kim, Y. Il Song, Y.-J. Kim, K.S. Kim, B. Ozyilmaz, J.-H. Ahn, B.H. Hong, S. Iijima, Roll-to-roll production of 30-inch graphene films for transparent electrodes., Nat. Nanotechnol. 5 (2010) 574–578. doi:10.1038/nnano.2010.132.
[96] L. Gao, J.R. Guest, N.P. Guisinger, Epitaxial graphene on Cu(111), Nano Lett. 10 (2010) 3512–3516. doi:10.1021/nl1016706.
[97] Z.R. Robinson, P. Tyagi, T.R. Mowll, C. a. Ventrice, J.B. Hannon, Argon-assisted growth of epitaxial graphene on Cu(111), Phys. Rev. B - Condens. Matter Mater. Phys. 86 (2012). doi:10.1103/PhysRevB.86.235413.
[98] H. Ago, K. Kawahara, Y. Ogawa, S. Tanoue, M. a Bissett, M. Tsuji, H. Sakaguchi, R.J. Koch, F. Fromm, T. Seyller, K. Komatsu, K. Tsukagoshi, PS-13-15 Epitaxial Growth and Electronic Properties of Large Hexagonal Graphene Domains on Cu (111) Thin Film, 1 (2013) 438–439. doi:10.7567/APEX.6.075101.
[99] L. Zhao, K.T. Rim, H. Zhou, R. He, T.F. Heinz, a. Pinczuk, G.W. Flynn, a. N. Pasupathy, Influence of copper crystal surface on the CVD growth of large area monolayer graphene, Solid State Commun. 151 (2011) 509–513. doi:10.1016/j.ssc.2011.01.014.
[100] Y. Ogawa, B. Hu, C.M. Orofeo, M. Tsuji, K. Ikeda, S. Mizuno, H. Hibino, H. Ago, Domain Structure and Boundary in Single-Layer Graphene Grown on Cu (111) and Cu (100) Films, J. Phys. Chem. Lett. 3 (2012) 219–226. doi:10.1021/jz2015555.
[101] A.T. Murdock, A. Koos, T. Ben Britton, L. Houben, T. Batten, T. Zhang, A.J. Wilkinson, R.E. Dunin-Borkowski, C.E. Lekka, N. Grobert, Controlling the orientation, edge geometry, and thickness of chemical vapor deposition graphene, ACS Nano. 7 (2013) 1351–1359. doi:10.1021/nn3049297.
[102] Y. Hao, M.S. Bharathi, L. Wang, Y. Liu, H. Chen, S. Nie, X. Wang, H. Chou, C. Tan, B. Fallahazad, H. Ramanarayan, C.W. Magnuson, E. Tutuc, B.I. Yakobson, K.F. McCarty, Y. Zhang, P. Kim, J. Hone, L. Colombo, R.S. Ruoff, The role of surface oxygen in the growth of large single-crystal graphene on copper., Science. 342 (2013) 720–3. doi:10.1126/science.1243879.
[103] Y. a. Wu, A.W. Robertson, F. Schäffel, S.C. Speller, J.H. Warner, Aligned rectangular few-layer graphene domains on copper surfaces, Chem. Mater. 23 (2011) 4543–4547. doi:10.1021/cm201823s.
[104] G.-P. Dai, M.H. Wu, D.K. Taylor, K. Vinodgopal, Square-Shaped, Single-Crystal, Monolayer Graphene Domains by Low-Pressure Chemical Vapor Deposition, Mater. Res. Lett. 1 (2013) 67–76. doi:10.1080/21663831.2013.772078.
[105] H. Yan, Y. Tang, W. Long, Y. Li, Enhanced thermal conductivity in polymer composites with aligned graphene nanosheets, J. Mater. Sci. 49 (2014) 5256–5264. doi:10.1007/s10853-014-8198-z.
[106] Z. Xu, Y. Zhang, P. Li, C. Gao, Strong, Conductive, Lightweight, Neat Graphene Aerogel Fibers with Aligned Pores, ACS Nano. 6 (2012) 7103–7113. doi:10.1021/nn3021772.
[107] M. Terrones, O. Martín, M. González, J. Pozuelo, B. Serrano, J.C. Cabanelas, S.M. Vega-Díaz, J. Baselga, Interphases in Graphene Polymer-based Nanocomposites: Achievements and

Challenges, Adv. Mater. 23 (2011) 5302–5310. doi:10.1002/adma.201102036.
[108] T. Luo, J.R. Lloyd, Enhancement of Thermal Energy Transport Across Graphene/Graphite and Polymer Interfaces: A Molecular Dynamics Study, Adv. Funct. Mater. 22 (2012) 2495–2502. doi:10.1002/adfm.201103048.
[109] B. Bhushan, ed., Springer Handbook of Nanotechnology, 3rd ed., Springer, 2010. doi:10.1007/978-3-642-02525-9.
[110] K.T. Faber, A.G. Evans, Crack deflection processes—I. Theory, Acta Metall. 31 (1983) 565–576. doi:10.1016/0001-6160(83)90046-9.
[111] K.T. Faber, A.G. Evans, Crack deflection processes—II. Experiment, Acta Metall. 31 (1983) 577–584. doi:10.1016/0001-6160(83)90047-0.
[112] B.-B. Fan, H.-H. Guo, R. Zhang, Y. Jia, C.-Y. Shi, Structural Evolution during the Oxidation Process of Graphite, Chinese Phys. Lett. 31 (2014) 78102. doi:10.1088/0256-307X/31/7/078102.
[113] Z. Xu, K. Xue, Engineering graphene by oxidation: a first-principles study., Nanotechnology. 21 (2010) 45704. doi:10.1088/0957-4484/21/4/045704.
[114] W.-S. Kuo, N.-H. Tai, T.-W. Chang, Deformation and fracture in graphene nanosheets, Compos. Part A Appl. Sci. Manuf. 51 (2013) 56–61. doi:10.1016/j.compositesa.2013.03.020.
[115] M.J. Palmeri, K.W. Putz, L.C. Brinson, Sacrificial bonds in stacked-cup carbon nanofibers: biomimetic toughening mechanisms for composite systems., ACS Nano. 4 (2010) 4256–64. doi:10.1021/nn100661a.
[116] D. Lee, X. Zou, X. Zhu, J.W. Seo, J.M. Cole, F. Bondino, E. Magnano, S.K. Nair, H. Su, Ultrafast carrier phonon dynamics in NaOH-reacted graphite oxide film, Appl. Phys. Lett. 101 (2012) 21604. doi:10.1063/1.4736572.
[117] S.A. Shojaee, A. Zandiatashbar, N. Koratkar, D. a. Lucca, Raman spectroscopic imaging of graphene dispersion in polymer composites, Carbon N. Y. 62 (2013) 510–513. doi:10.1016/j.carbon.2013.05.068.
[118] a Tamburrano, F. Sarasini, G. De Bellis, a G. D'Aloia, M.S. Sarto, The piezoresistive effect in graphene-based polymeric composites., Nanotechnology. 24 (2013) 465702–465711. doi:10.1088/0957-4484/24/46/465702.
[119] H. Yang, F. Li, C. Shan, D. Han, Q. Zhang, L. Niu, A. Ivaska, Covalent functionalization of chemically converted graphene sheets via silane and its reinforcement, J. Mater. Chem. 19 (2009) 4632–4638. doi:10.1039/b901421g.
[120] G. Wang, X. Shen, B. Wang, J. Yao, J. Park, Synthesis and characterisation of hydrophilic and organophilic graphene nanosheets, Carbon N. Y. 47 (2009) 1359–1364. doi:10.1016/j.carbon.2009.01.027.
[121] S. Samanman, A. Numnuam, W. Limbut, P. Kanatharana, P. Thavarungkul, Highly-sensitive label-free electrochemical carcinoembryonic antigen immunosensor based on a novel Au nanoparticles–graphene–chitosan nanocomposite cryogel electrode, Anal. Chim. Acta. 853 (2015) 521–532. doi:10.1016/j.aca.2014.10.006.
[122] S.-Y. Lee, M.-H. Chong, M. Park, H.-Y. Kim, S.-J. Park, Effect of chemically reduced graphene oxide on epoxy nanocomposites for flexural behaviors, Carbon Lett. 15 (2014) 67–70. doi:10.5714/CL.2014.15.1.067.
[123] C.-C. Teng, C.-C.M. Ma, C.-H. Lu, S.-Y. Yang, S.-H. Lee, M.-C. Hsiao, M.-Y. Yen, K.-C. Chiou, T.-M. Lee, Thermal conductivity and structure of non-covalent functionalized graphene/epoxy composites, Carbon N. Y. 49 (2011) 5107–5116. doi:10.1016/j.carbon.2011.06.095.
[124] K. Chu, W. Li, H. Dong, F. Tang, Modeling the thermal conductivity of graphene nanoplatelets reinforced composites, EPL (Europhysics Lett. 100 (2012) 36001–36005. doi:10.1209/0295-5075/100/36001.
[125] S.-Y. Yang, W.-N. Lin, Y.-L. Huang, H.-W. Tien, J.-Y. Wang, C.-C.M. Ma, S.-M. Li, Y.-S. Wang, Synergetic effects of graphene platelets and carbon nanotubes on the mechanical and thermal properties of epoxy composites, Carbon N. Y. 49 (2011) 793–803. doi:10.1016/j.carbon.2010.10.014.
[126] N.-W. Pu, Y.-Y. Peng, P.-C. Wang, C.-Y. Chen, J.-N. Shi, Y.-M. Liu, M.-D. Ger, C.-L. Chang, Application of nitrogen-doped graphene nanosheets in electrically conductive adhesives, Carbon N. Y. 67 (2014) 449–456. doi:10.1016/j.carbon.2013.10.017.
[127] Q. Zhao, S. Hao, Toughening mechanism of epoxy resins with micro/nano particles, J Compos Mater. 41 (2007) 201–19. doi:10.1177/0021998306063361.
[128] Q. Zhao, S.. Hoa, P. Ouellette, Progressive failure of triaxial woven fabric (TWF) composites with open holes, Compos. Struct. 65 (2004) 419–431. doi:10.1016/j.compstruct.2003.12.004.

[129] Z.A. Ghaleb, M. Mariatti, Z.M. Ariff, Properties of graphene nanopowder and multi-walled carbon nanotube-filled epoxy thin-film nanocomposites for electronic applications: The effect of sonication time and filler loading, Compos. Part A Appl. Sci. Manuf. 58 (2014) 77–83. doi:10.1016/j.compositesa.2013.12.002.
[130] J. a. King, D.R. Klimek, I. Miskioglu, G.M. Odegard, Mechanical properties of graphene nanoplatelet/epoxy composites, J. Appl. Polym. Sci. 128 (2013) 4217–4223. doi:10.1002/app.38645.
[131] X. Wang, L. Song, W. Pornwannchai, Y. Hu, B. Kandola, The effect of graphene presence in flame retarded epoxy resin matrix on the mechanical and flammability properties of glass fiber-reinforced composites, Compos. Part A Appl. Sci. Manuf. 53 (2013) 88–96. doi:10.1016/j.compositesa.2013.05.017.
[132] W.P. Serena Saw, M. Mariatti, Properties of synthetic diamond and graphene nanoplatelet-filled epoxy thin film composites for electronic applications, J. Mater. Sci. Mater. Electron. 23 (2011) 817–824. doi:10.1007/s10854-011-0499-2.
[133] I. Zaman, H.-C. Kuan, Q. Meng, A. Michelmore, N. Kawashima, T. Pitt, L. Zhang, S. Gouda, L. Luong, J. Ma, A Facile Approach to Chemically Modified Graphene and its Polymer Nanocomposites, Adv. Funct. Mater. 22 (2012) 2735–2743. doi:10.1002/adfm.201103041.
[134] M.R. Loos, L.A.F. Coelho, S.H. Pezzin, S.C. Amico, The effect of acetone addition on the properties of epoxy, Polímeros. 18 (2008) 76–80. doi:10.1590/S0104-14282008000100015.
[135] K. Lau, M. Lu, H. Cheung, F. Sheng, H. Li, Thermal and mechanical properties of single-walled carbon nanotube bundle-reinforced epoxy nanocomposites: the role of solvent for nanotube dispersion, Compos. Sci. Technol. 65 (2005) 719–725. doi:10.1016/j.compscitech.2004.10.005.
[136] S. Hong, C. Wu, DSC and FTIR analysis of the curing behaviors of epoxy / DICY / solvent open systems, Thermochim. Acta. 316 (1998) 167–175. doi:10.1016/S0040-6031(98)00356-6.
[137] T. Morishita, Effects of the composition and molecular weight of maleimide polymers on the dispersibility of carbon nanotubes in chloroform, Carbon N. Y. 49 (2011) 5185–5195. doi:10.1016/j.carbon.2011.07.035.
[138] J. Yanmei, Dispersibility and chemical bonds between multi-walled carbon nanotubes and poly(ether ether ketone) in nanocomposite fibers, Mater. Chem. Phys. 135 (2012) 948–956. doi:10.1016/j.matchemphys.2012.05.083.
[139] G. Farzi, Effect of radical grafting of tetramethylpentadecane and polypropylene on carbon nanotubes' dispersibility in various solvents and polypropylene matrix, Polymer (Guildf). 50 (2009) 5901–5908. doi:10.1016/j.polymer.2009.10.020.
[140] S.-Z. Kang, A facile preparation of multiwalled carbon nanotubes modified with hydroxyl groups and their high dispersibility in ethanol, Colloids Surfaces A Physicochem. Eng. Asp. 384 (2011) 363–367. doi:10.1016/j.colsurfa.2011.04.036.
[141] B. Munkhbayar, Effect of grinding speed changes on dispersibility of the treated multi-walled carbon nanotubes in aqueous solution and its thermal characteristics, Chem. Eng. Process. 61 (2012) 36–41. doi:10.1016/j.cep.2012.06.013.
[142] M. Bastwros, G.-Y. Kim, C. Zhu, K. Zhang, S. Wang, X. Tang, X. Wang, Effect of ball milling on graphene reinforced Al6061 composite fabricated by semi-solid sintering, Compos. Part B Eng. 60 (2014) 111–118. doi:10.1016/j.compositesb.2013.12.043.
[143] H. Wu, B. Rook, L.T. Drzal, Dispersion optimization of exfoliated graphene nanoplatelet in polyetherimide nanocomposites: Extrusion, precoating, and solid state ball milling, Polym. Compos. 34 (2013) 426–432. doi:10.1002/pc.22425.
[144] M. Yu, D. Shao, F. Lu, X. Sun, H. Sun, T. Hu, G. Wang, S. Sawyer, H. Qiu, J. Lian, ZnO/graphene nanocomposite fabricated by high energy ball milling with greatly enhanced lithium storage capability, Electrochem. Commun. 34 (2013) 312–315. doi:10.1016/j.elecom.2013.07.013.
[145] X. Jiang, L.T. Drzal, Reduction in Percolation Threshold of Injection Molded High-Density Polyethylene / Exfoliated Graphene Nanoplatelets Composites by Solid State Ball Milling and Solid State Shear Pulverization, J. Appl. Polym. Sci. 124 (2011) 525–535. doi:10.1002/app.
[146] H. Wu, W. Zhao, G. Chen, One-Pot In Situ Ball Milling Preparation of Polymer / Graphene Nanocomposites, J. Appl. Polym. Sci. 125 (2012) 3899–3903. doi:10.1002/app.
[147] J. Xu, I.-Y. Jeon, J.-M. Seo, S. Dou, L. Dai, J.-B. Baek, Edge-Selectively Halogenated Graphene Nanoplatelets (XGnPs, X = Cl, Br, or I) Prepared by Ball-Milling and Used as Anode Materials for Lithium-Ion Batteries., Adv. Mater. 26 (2014) 7317–23. doi:10.1002/adma.201402987.
[148] W. Guo, G. Chen, Fabrication of graphene/epoxy resin composites with much enhanced

thermal conductivity via ball milling technique, J. Appl. Polym. Sci. 131 (2014) 40565–40569. doi:10.1002/app.40565.
[149] A.M. Rodriguez, P. Prieto, M. Prato, E. Va, Exfoliation of Graphite with Triazine Derivatives under Ball-Milling Conditions : Preparation of Few-Layer Graphene via Selective Noncovalent Interactions, ACS Nano. 8 (2014) 563–571. doi:10.1021/nn405148t.
[150] J. Xu, J. Shui, J. Wang, M. Wang, H. Liu, S.X. Dou, I. Jeon, Sulfur–graphene nanostructured cathodes via ball-milling for high-performance lithium–sulfur batteries, ACS Nano. 8 (2014) 10920–10930. doi:10.1021/nn5047585.
[151] G. Cravotto, P. Cintas, Sonication-assisted fabrication and post-synthetic modifications of graphene-like materials., Chemistry. 16 (2010) 5246–59. doi:10.1002/chem.200903259.
[152] M. Yi, Z. Shen, X. Zhang, S. Ma, Vessel diameter and liquid height dependent sonication-assisted production of few-layer graphene, J. Mater. Sci. 47 (2012) 8234–8244. doi:10.1007/s10853-012-6720-8.
[153] A. Ciesielski, P. Samorì, Graphene via sonication assisted liquid-phase exfoliation., Chem. Soc. Rev. 43 (2014) 381–98. doi:10.1039/c3cs60217f.
[154] S. Wang, L.A.L. Tang, Q. Bao, M. Lin, S. Deng, B.M. Goh, K.P. Loh, Room-temperature synthesis of soluble carbon nanotubes by the sonication of graphene oxide nanosheets., J. Am. Chem. Soc. 131 (2009) 16832–7. doi:10.1021/ja905968v.
[155] O. Akhavan, E. Ghaderi, A. Esfandiar, Wrapping bacteria by graphene nanosheets for isolation from environment, reactivation by sonication, and inactivation by near-infrared irradiation., J. Phys. Chem. B. 115 (2011) 6279–88. doi:10.1021/jp200686k.
[156] E.Y. Polyakova Stolyarova, K.T. Rim, D. Eom, K. Douglass, R.L. Opila, T.F. Heinz, A. V Teplyakov, G.W. Flynn, Scanning tunneling microscopy and X-ray photoelectron spectroscopy studies of graphene films prepared by sonication-assisted dispersion., ACS Nano. 5 (2011) 6102–8. doi:10.1021/nn1009352.
[157] P. Xu, J. Loomis, B. King, B. Panchapakesan, Synergy among binary (MWNT, SLG) nano-carbons in polymer nano-composites: a Raman study., Nanotechnology. 23 (2012) 315706. doi:10.1088/0957-4484/23/31/315706.
[158] Y.C. Cheng, T.P. Kaloni, Z.Y. Zhu, U. Schwingenschlögl, Oxidation of graphene in ozone under ultraviolet light, Appl. Phys. Lett. 101 (2012) 73110. doi:10.1063/1.4746261.
[159] E. Gracia-espino, G. Hu, A. Shchukarev, T. Wa, Understanding the Interface of Six-Shell Cuboctahedral and Icosahedral Palladium Clusters on Reduced Graphene Oxide : Experimental and Theoretical Study, J. Am. Chem. Soc. 136 (2014) 6626–6633. doi:10.1021/ja412259h.
[160] K. a. Velizhanin, N. Dandu, D. Solenov, Electromigration of bivalent functional groups on graphene, Phys. Rev. B. 89 (2014) 155414. doi:10.1103/PhysRevB.89.155414.
[161] L.R. Radovic, A. Suarez, F. Vallejos-Burgos, J.O. Sofo, Oxygen migration on the graphene surface. 2. Thermochemistry of basal-plane diffusion (hopping), Carbon N. Y. 49 (2011) 4226–4238. doi:10.1016/j.carbon.2011.05.037.
[162] L.R. Radovic, A.B. Silva-Tapia, F. Vallejos-Burgos, Oxygen migration on the graphene surface. 1. Origin of epoxide groups, Carbon N. Y. 49 (2011) 4218–4225. doi:10.1016/j.carbon.2011.05.059.
[163] C. Botas, P. Álvarez, C. Blanco, R. Santamaría, M. Granda, P. Ares, F. Rodríguez-Reinoso, R. Menéndez, The effect of the parent graphite on the structure of graphene oxide, Carbon N. Y. 50 (2012) 275–282. doi:10.1016/j.carbon.2011.08.045.
[164] Ž. Šljivančanin, A.S. Milošević, Z.S. Popović, F.R. Vukajlović, Binding of atomic oxygen on graphene from small epoxy clusters to a fully oxidized surface, Carbon N. Y. 54 (2013) 482–488. doi:10.1016/j.carbon.2012.12.008.
[165] M.S. Ahmed, H.S. Han, S. Jeon, One-step chemical reduction of graphene oxide with oligothiophene for improved electrocatalytic oxygen reduction reactions, Carbon N. Y. 61 (2013) 164–172. doi:10.1016/j.carbon.2013.04.080.
[166] F.-Y. Yuan, H.-B. Zhang, X. Li, H.-L. Ma, X.-Z. Li, Z.-Z. Yu, In situ chemical reduction and functionalization of graphene oxide for electrically conductive phenol formaldehyde composites, Carbon N. Y. 68 (2014) 653–661. doi:10.1016/j.carbon.2013.11.046.
[167] X. Jiang, J. Nisar, B. Pathak, J. Zhao, R. Ahuja, Graphene oxide as a chemically tunable 2-D material for visible-light photocatalyst applications, J. Catal. 299 (2013) 204–209. doi:10.1016/j.jcat.2012.12.022.
[168] J.S. Park, L. Yu, C.S. Lee, K. Shin, J.H. Han, Liquid-phase exfoliation of expanded graphites into graphene nanoplatelets using amphiphilic organic molecules., J. Colloid Interface Sci. 417 (2014) 379–84. doi:10.1016/j.jcis.2013.11.066.
[169] C.E. Corcione, F. Freuli, A. Maffezzoli, The aspect ratio of epoxy matrix nanocomposites

reinforced with graphene stacks, Polym. Eng. Sci. 53 (2013) 531–539. doi:10.1002/pen.23292.
[170] L. Ramos-Galicia, L.N. Mendez, A.L. Martínez-Hernández, a. Espindola-Gonzalez, I.R. Galindo-Esquivel, R. Fuentes-Ramirez, C. Velasco-Santos, Improved Performance of an Epoxy Matrix as a Result of Combining Graphene Oxide and Reduced Graphene, Int. J. Polym. Sci. 2013 (2013) 1–7. doi:10.1155/2013/493147.
[171] Z. Li, R.J. Young, R. Wang, F. Yang, L. Hao, W. Jiao, W. Liu, The role of functional groups on graphene oxide in epoxy nanocomposites, Polymer (Guildf). 54 (2013) 5821–5829. doi:10.1016/j.polymer.2013.08.026.
[172] W. Liu, K.L. Koh, J. Lu, L. Yang, S. Phua, J. Kong, Z. Chen, X. Lu, Simultaneous catalyzing and reinforcing effects of imidazole-functionalized graphene in anhydride-cured epoxies, J. Mater. Chem. 22 (2012) 18395. doi:10.1039/c2jm32708b.
[173] H. Yang, C. Shan, F. Li, Q. Zhang, D. Han, L. Niu, Convenient preparation of tunably loaded chemically converted graphene oxide/epoxy resin nanocomposites from graphene oxide sheets through two-phase extraction, J. Mater. Chem. 19 (2009) 8856. doi:10.1039/b915228h.
[174] D. Galpaya, M. Wang, G. George, N. Motta, E. Waclawik, C. Yan, Preparation of graphene oxide/epoxy nanocomposites with significantly improved mechanical properties, J. Appl. Phys. 116 (2014) 53518. doi:10.1063/1.4892089.
[175] W. Li, A. Dichiara, J. Bai, Carbon nanotube–graphene nanoplatelet hybrids as high-performance multifunctional reinforcements in epoxy composites, Compos. Sci. Technol. 74 (2013) 221–227. doi:10.1016/j.compscitech.2012.11.015.
[176] L. Cao, X. Liu, H. Na, Y. Wu, W. Zheng, J. Zhu, How a bio-based epoxy monomer enhanced the properties of diglycidyl ether of bisphenol A (DGEBA)/graphene composites, J. Mater. Chem. A. 1 (2013) 5081–5088. doi:10.1039/c3ta01700a.
[177] Y.-J. Wan, L.-C. Tang, D. Yan, L. Zhao, Y.-B. Li, L.-B. Wu, J.-X. Jiang, G.-Q. Lai, Improved dispersion and interface in the graphene/epoxy composites via a facile surfactant-assisted process, Compos. Sci. Technol. 82 (2013) 60–68. doi:10.1016/j.compscitech.2013.04.009.
[178] S.-Y. Yang, W.-N. Lin, Y.-L. Huang, H.-W. Tien, J.-Y. Wang, C.-C.M. Ma, S.-M. Li, Y.-S. Wang, Synergetic effects of graphene platelets and carbon nanotubes on the mechanical and thermal properties of epoxy composites, Carbon N. Y. 49 (2011) 793–803. doi:10.1016/j.carbon.2010.10.014.
[179] C.-H. Hsu, M.-H. Hsu, K.-C. Chang, M.-C. Lai, P.-J. Liu, T.-L. Chuang, J.-M. Yeh, W.-R. Liu, Physical study of room-temperature-cured epoxy/thermally reduced graphene oxides with various contents of oxygen-containing groups, Polym. Int. 63 (2014) 1765–1770. doi:10.1002/pi.4763.
[180] Y. Yang, W. Rigdon, X. Huang, X. Li, Enhancing graphene reinforcing potential in composites by hydrogen passivation induced dispersion., Sci. Rep. 3 (2013) 2086–2093. doi:10.1038/srep02086.
[181] M. Naebe, J. Wang, A. Amini, H. Khayyam, N. Hameed, L.H. Li, Y. Chen, B. Fox, Mechanical property and structure of covalent functionalised graphene/epoxy nanocomposites., Sci. Rep. 4 (2014) 4375–4382. doi:10.1038/srep04375.
[182] B. Qi, Z. Yuan, S. Lu, K. Liu, S. Li, L. Yang, J. Yu, Mechanical and thermal properties of epoxy composites containing graphene oxide and liquid crystalline epoxy, Fibers Polym. 15 (2014) 326–333. doi:10.1007/s12221-014-0326-5.
[183] S.-C. Shiu, J.-L. Tsai, Characterizing thermal and mechanical properties of graphene/epoxy nanocomposites, Compos. Part B Eng. 56 (2014) 691–697. doi:10.1016/j.compositesb.2013.09.007.
[184] G. Yu, P. Wu, Effect of chemically modified graphene oxide on the phase separation behaviour and properties of an epoxy/polyetherimide binary system, Polym. Chem. 5 (2014) 96–104. doi:10.1039/c3py00878a.
[185] T. Liu, Z. Zhao, W.W. Tjiu, J. Lv, C. Wei, Preparation and characterization of epoxy nanocomposites containing surface-modified graphene oxide, J. Appl. Polym. Sci. 131 (2014) 40236–40242. doi:10.1002/app.40236.
[186] F. Liu, K. Guo, Reinforcing epoxy resin through covalent integration of functionalized graphene nanosheets, Polym. Adv. Technol. 25 (2014) 418–423. doi:10.1002/pat.3256.
[187] L.-Z. Guan, Y.-J. Wan, L.-X. Gong, D. Yan, L.-C. Tang, L.-B. Wu, J.-X. Jiang, G.-Q. Lai, Toward effective and tunable interphases in graphene oxide/epoxy composites by grafting different chain lengths of polyetheramine onto graphene oxide, J. Mater. Chem. A. 2 (2014) 15058–15069. doi:10.1039/C4TA02429J.
[188] M. Martin-Gallego, M.M. Bernal, M. Hernandez, R. Verdejo, M. a. Lopez-Manchado, Comparison of filler percolation and mechanical properties in graphene and carbon nanotubes

filled epoxy nanocomposites, Eur. Polym. J. 49 (2013) 1347–1353. doi:10.1016/j.eurpolymj.2013.02.033.
[189] H. Ribeiro, W.M. Silva, M.-T.F. Rodrigues, J.C. Neves, R. Paniago, C. Fantini, H.D.R. Calado, L.M. Seara, G.G. Silva, Glass transition improvement in epoxy/graphene composites, J. Mater. Sci. 48 (2013) 7883–7892. doi:10.1007/s10853-013-7478-3.
[190] A.S. Wajid, H.S.T. Ahmed, S. Das, F. Irin, A.F. Jankowski, M.J. Green, High-Performance Pristine Graphene/Epoxy Composites With Enhanced Mechanical and Electrical Properties, Macromol. Mater. Eng. 298 (2013) 339–347. doi:10.1002/mame.201200043.
[191] X. Zhang, O. Alloul, Q. He, J. Zhu, M.J. Verde, Y. Li, S. Wei, Z. Guo, Strengthened magnetic epoxy nanocomposites with protruding nanoparticles on the graphene nanosheets, Polymer (Guildf). 54 (2013) 3594–3604. doi:10.1016/j.polymer.2013.04.062.
[192] X. Wang, W. Xing, X. Feng, B. Yu, L. Song, Y. Hu, Functionalization of graphene with grafted polyphosphamide for flame retardant epoxy composites: synthesis, flammability and mechanism, Polym. Chem. 5 (2014) 1145. doi:10.1039/c3py00963g.
[193] F. Ren, G. Zhu, P. Ren, Y. Wang, X. Cui, In situ polymerization of graphene oxide and cyanate ester–epoxy with enhanced mechanical and thermal properties, Appl. Surf. Sci. 316 (2014) 549–557. doi:10.1016/j.apsusc.2014.07.159.
[194] B. Qi, Enhanced thermal and mechanical properties of epoxy composites by mixing thermotropic liquid crystalline epoxy grafted graphene oxide, Express Polym. Lett. 8 (2014) 467–479. doi:10.3144/expresspolymlett.2014.51.
[195] S. Lu, S. Li, J. Yu, Z. Yuan, B. Qi, Epoxy nanocomposites filled with thermotropic liquid crystalline epoxy grafted graphene oxide, RSC Adv. 3 (2013) 8915. doi:10.1039/c3ra40404h.
[196] X.-J. Shen, Y. Liu, H.-M. Xiao, Q.-P. Feng, Z.-Z. Yu, S.-Y. Fu, The reinforcing effect of graphene nanosheets on the cryogenic mechanical properties of epoxy resins, Compos. Sci. Technol. 72 (2012) 1581–1587. doi:10.1016/j.compscitech.2012.06.021.
[197] C. Bao, Y. Guo, L. Song, Y. Kan, X. Qian, Y. Hu, In situ preparation of functionalized graphene oxide/epoxy nanocomposites with effective reinforcements, J. Mater. Chem. 21 (2011) 13290–13298. doi:10.1039/c1jm11434d.
[198] Q. Meng, J. Jin, R. Wang, H.-C. Kuan, J. Ma, N. Kawashima, A. Michelmore, S. Zhu, C.H. Wang, Processable 3-nm thick graphene platelets of high electrical conductivity and their epoxy composites., Nanotechnology. 25 (2014) 125707–125719. doi:10.1088/0957-4484/25/12/125707.
[199] A. Yu, P. Ramesh, M.E. Itkis, E. Bekyarova, R.C. Haddon, Graphite Nanoplatelet - Epoxy Composite Thermal Interface Materials, J. Phys. Chem. C. 111 (2007) 7565–7569. doi:10.1021/jp071761s.
[200] F. Yavari, H.R. Fard, K. Pashayi, M. a. Rafiee, A. Zamiri, Z. Yu, R. Ozisik, T. Borca-Tasciuc, N. Koratkar, Enhanced thermal conductivity in a nanostructured phase change composite due to low concentration graphene additives, J. Phys. Chem. C. 115 (2011) 8753–8758. doi:10.1021/jp200838s.
[201] S. Ganguli, A.K. Roy, D.P. Anderson, Improved thermal conductivity for chemically functionalized exfoliated graphite/epoxy composites, Carbon N. Y. 46 (2008) 806–817. doi:10.1016/j.carbon.2008.02.008.
[202] H. Fukushima, L.T. Drzal, B.P. Rook, M.J. Rich, Thermal conductivity of exfoliated graphite nanocomposites, J. Therm. Anal. Calorim. 85 (2006) 235–238. doi:10.1007/s10973-005-7344-x.
[203] S.H. Xie, Y.Y. Liu, J.Y. Li, Comparison of the effective conductivity between composites reinforced by graphene nanosheets and carbon nanotubes, Appl. Phys. Lett. 92 (2008) 1–3. doi:10.1063/1.2949074.
[204] W. Lin, R. Zhang, C.P. Wong, Modeling of Thermal Conductivity of Graphite Nanosheet Composites, J. Electron. Mater. 39 (2010) 268–272. doi:10.1007/s11664-009-1062-2.
[205] C.-W. Nan, R. Birringer, D.R. Clarke, H. Gleiter, Effective thermal conductivity of particulate composites with interfacial thermal resistance, J. Appl. Phys. 81 (1997) 6692–6699. doi:10.1063/1.365209.
[206] L. Hu, T. Desai, P. Keblinski, Thermal transport in graphene-based nanocomposite, J. Appl. Phys. 110 (2011) 1–6. doi:10.1063/1.3610386.
[207] Q. Li, Y. Guo, W. Li, S. Qiu, C. Zhu, X. Wei, M. Chen, C. Liu, S. Liao, Y. Gong, A.K. Mishra, L. Liu, Ultrahigh Thermal Conductivity of Assembled Aligned Multilayer Graphene/Epoxy Composite, Chem. Mater. 26 (2014) 4459–4465. doi:10.1021/cm501473t.
[208] Z. Fan, F. Gong, S.T. Nguyen, H.M. Duong, Advanced multifunctional graphene aerogel – Poly (methyl methacrylate) composites: Experiments and modeling, Carbon N. Y. 81 (2014)

396–404. doi:10.1016/j.carbon.2014.09.072.
[209] Z. Han, A. Fina, Thermal conductivity of carbon nanotubes and their polymer nanocomposites: A review, Prog. Polym. Sci. 36 (2011) 914–944. doi:10.1016/j.progpolymsci.2010.11.004.
[210] T. Franosch, F. Höfling, T. Bauer, E. Frey, Persistent memory for a Brownian walker in a random array of obstacles, Chem. Phys. 375 (2010) 540–547. doi:10.1016/j.chemphys.2010.04.023.
[211] H.M. Duong, D. V Papavassiliou, K.J. Mullen, S. Maruyama, Computational modeling of the thermal conductivity of single-walled carbon nanotube-polymer composites., Nanotechnology. 19 (2008) 065702–065710. doi:10.1088/0957-4484/19/6/065702.
[212] F. Gong, D. V. Papavassiliou, H.M. Duong, Off-Lattice Monte Carlo Simulation of Heat Transfer through Carbon Nanotube Multiphase Systems Taking into Account Thermal Boundary Resistances, Numer. Heat Transf. Part A Appl. 65 (2014) 1023–1043. doi:10.1080/10407782.2013.850972.
[213] F. Gong, Z. Hongyan, D. V Papavassiliou, K. Bui, C. Lim, H.M. Duong, Mesoscopic modeling of cancer photothermal therapy using single-walled carbon nanotubes and near infrared radiation: insights through an off-lattice Monte Carlo approach, Nanotechnology. 25 (2014) 205101–205112. doi:10.1088/0957-4484/25/20/205101.
[214] F. Gong, K. Bui, D. V. Papavassiliou, H.M. Duong, Thermal transport phenomena and limitations in heterogeneous polymer composites containing carbon nanotubes and inorganic nanoparticles, Carbon N. Y. 78 (2014) 305–316. doi:10.1016/j.carbon.2014.07.007.
[215] E.T. Swartz, R.O. Pohl, Thermal boundary resistance, Rev. Mod. Phys. 61 (1989) 605–668. doi:http://dx.doi.org/10.1103/RevModPhys.61.605.
[216] T. Ramanathan, S. Stankovich, D.A. Dikin, L. Hiu, H. Shen, S.T. Nguyen, L.C. Brinson, Graphitic Nanofillers in PMMA Nanocomposites—An Investigation of Particle Size and Dispersion and Their Influence on Nanocomposite Properties, J. Polym. Sci. Part B Polym. Phys. 45 (2007) 2097–2112. doi:10.1002/polb.21187.
[217] J.R. Potts, D.R. Dreyer, C.W. Bielawski, R.S. Ruoff, Graphene-based polymer nanocomposites, Polymer (Guildf). 52 (2011) 5–25. doi:10.1016/j.polymer.2010.11.042.
[218] G.H. Chen, D.J. Wu, W.G. Weng, W.L. Yan, Preparation of polymer/graphite conducting nanocomposite by intercalation polymerization, J. Appl. Polym. Sci. 82 (2001) 2506–2513. doi:10.1002/app.2101.
[219] H. Pang, T. Chen, G. Zhang, B. Zeng, Z.M. Li, An electrically conducting polymer/graphene composite with a very low percolation threshold, Mater. Lett. 64 (2010) 2226–2229. doi:10.1016/j.matlet.2010.07.001.
[220] G. Gonçalves, P. a. a. P. Marques, A. Barros-Timmons, I. Bdkin, M.K. Singh, N. Emami, J. Grácio, Graphene oxide modified with PMMA via ATRP as a reinforcement filler, J. Mater. Chem. 20 (2010) 9927–9934. doi:10.1039/c0jm01674h.
[221] X. Huang, X. Qi, F. Boey, H. Zhang, Graphene-based composites, Chem. Soc. Rev. 41 (2012) 666–686. doi:10.1039/c1cs15078b.
[222] Z. Fan, A. Marconnet, S.T. Nguyen, C.Y.H. Lim, H.M. Duong, Effects of heat treatment on the thermal properties of highly nanoporous graphene aerogels using the infrared microscopy technique, Int. J. Heat Mass Transf. 76 (2014) 122–127. doi:10.1016/j.ijheatmasstransfer.2014.04.023.
[223] T. Conduction, A.C. Nanotube, P. Nanocomposites, H.P. Density, Thermal Conduction in Aligned Carbon Nanotube À Polymer Nanocomposites with High Packing Density, ACS Nano. 5 (2011) 4818–4825. doi:10.1021/nn200847u.
[224] X. Fang, L.W. Fan, Q. Ding, X. Wang, X.L. Yao, J.F. Hou, Z.T. Yu, G.H. Cheng, Y.C. Hu, K.F. Cen, Increased thermal conductivity of eicosane-based composite phase change materials in the presence of graphene nanoplatelets, Energy and Fuels. 27 (2013) 4041–4047. doi:10.1021/ef400702a.
[225] K. Chu, W. Li, H. Dong, F. Tang, Modeling the thermal conductivity of graphene nanoplatelets reinforced composites, EPL (Europhysics Lett. 100 (2012) 36001–36005. doi:10.1209/0295-5075/100/36001.
[226] L. Gao, X. Zhou, Y. Ding, Effective thermal and electrical conductivity of carbon nanotube composites, Chem. Phys. Lett. 434 (2007) 297–300. doi:10.1016/j.cplett.2006.12.036.
[227] V.U. Unnikrishnan, D. Banerjee, J.N. Reddy, Atomistic-mesoscale interfacial resistance based thermal analysis of carbon nanotube systems, Int. J. Therm. Sci. 47 (2008) 1602–1609. doi:10.1016/j.ijthermalsci.2007.10.012.
[228] X.F. Zhou, L. Gao, Effective thermal conductivity in nanofluids of nonspherical particles with interfacial thermal resistance: Differential effective medium theory, J. Appl. Phys. 100 (2006)

24913. doi:10.1063/1.2216874.
[229] S. Ju, Z.Y. Li, Theory of thermal conductance in carbon nanotube composites, Phys. Lett. A. 353 (2006) 194–197. doi:10.1016/j.physleta.2005.11.086.
[230] A.K. Geim, Graphene : Status and Prospects, Science (80-.). 324 (2009) 1530–1535. doi:10.1126/science.1158877.
[231] A.K. Geim, K.S. Novoselov, The rise of graphene., Nat. Mater. 6 (2007) 183–191.
[232] W. Yan, W.-Y. He, Z.-D. Chu, M. Liu, L. Meng, R.-F. Dou, Y. Zhang, Z. Liu, J.-C. Nie, L. He, Strain and curvature induced evolution of electronic band structures in twisted graphene bilayer., Nat. Commun. 4 (2013) 1–7. doi:10.1038/ncomms3159.
[233] A.H.. Castro Neto, N.M.R.. Peres, K.S.. Novoselov, A.K.. Geim, F. Guinea, The electronic properties of graphene, Rev. Mod. Phys. 81 (2009) 109–162. doi:10.1103/RevModPhys.81.109.
[234] Y. Zhang, Y.-W. Tan, H.L. Stormer, P. Kim, Experimental observation of the quantum Hall effect and Berry's phase in graphene, Nature. 438 (2005) 201–204. doi:10.1038/nature04235.
[235] K.S. Novoselov, A.K. Geim, S. V. Morozov, D. Jiang, M.I. Katsnelson, I. V. Grigorieva, S. V. Dubonos, A.A. Firsov, Two-dimensional gas of massless Dirac fermions in graphene, Nature. 438 (2005) 197–200. doi:10.1038/nature04233.
[236] L. Zhao, M. Levendorf, S. Goncher, T. Schiros, L. Pálová, A. Zabet-Khosousi, K.T. Rim, C. Gutiérrez, D. Nordlund, C. Jaye, M. Hybertsen, D. Reichman, G.W. Flynn, J. Park, A.N. Pasupathy, Local atomic and electronic structure of boron chemical doping in monolayer graphene, Nano Lett. 13 (2013) 4659–4665. doi:10.1021/nl401781d.
[237] W. Han, R.K. Kawakami, M. Gmitra, J. Fabian, Graphene spintronics., Nat. Nanotechnol. 9 (2014) 794–807. doi:10.1038/nnano.2014.214.
[238] K.I. Bolotin, K.J. Sikes, Z. Jiang, M. Klima, G. Fudenberg, J. Hone, P. Kim, H.L. Stormer, Ultrahigh electron mobility in suspended graphene, Solid State Commun. 146 (2008) 351–355. doi:10.1016/j.ssc.2008.02.024.
[239] D. Stauffer, A. Aharony, Introduction to percolation theory., Second, Taylor & Francis, 1992.
[240] C. a. Martin, J.K.W. Sandler, M.S.P. Shaffer, M.K. Schwarz, W. Bauhofer, K. Schulte, a. H. Windle, Formation of percolating networks in multi-wall carbon-nanotube-epoxy composites, Compos. Sci. Technol. 64 (2004) 2309–2316. doi:10.1016/j.compscitech.2004.01.025.
[241] J.C. Grunlan, A.R. Mehrabi, M. V. Bannon, J.L. Bahr, Water-based single-walled-nanotube-filled polymer composite with an exceptionally low percolation threshold, Adv. Mater. 16 (2004) 150–153. doi:10.1002/adma.200305409.
[242] Y. Wang, J.W. Shan, G.J. Weng, Percolation threshold and electrical conductivity of graphene-based nanocomposites with filler agglomeration and interfacial tunneling, J. Appl. Phys. 118 (2015) 65101. doi:10.1063/1.4928293.
[243] R.L. McCullough, Generalized combining rules for predicting transport properties of composite materials, Compos. Sci. Technol. 22 (1985) 3–21. doi:10.1016/0266-3538(85)90087-9.
[244] J. Syurik, N. Alyabyeva, A. Alekseev, O. a. Ageev, AFM-based model of percolation in graphene-based polymer nanocomposites, Compos. Sci. Technol. 95 (2014) 38–43. doi:10.1016/j.compscitech.2014.02.006.
[245] R. Zallen, The physics of amorphous solids, (1983).
[246] N. Yousefi, M.M. Gudarzi, Q. Zheng, S.H. Aboutalebi, F. Sharif, J.-K. Kim, Self-alignment and high electrical conductivity of ultralarge graphene oxide–polyurethane nanocomposites, J. Mater. Chem. 22 (2012) 12709–12717. doi:10.1039/c2jm30590a.
[247] N. Yousefi, X. Sun, X. Lin, X. Shen, J. Jia, B. Zhang, B. Tang, M. Chan, J.-K. Kim, Highly aligned graphene/polymer nanocomposites with excellent dielectric properties for high-performance electromagnetic interference shielding., Adv. Mater. 26 (2014) 5480–7. doi:10.1002/adma.201305293.
[248] E. Kandare, A. a. Khatibi, S. Yoo, R. Wang, J. Ma, P. Olivier, N. Gleizes, C.H. Wang, Improving the through-thickness thermal and electrical conductivity of carbon fibre/epoxy laminates by exploiting synergy between graphene and silver nano-inclusions, Compos. Part A Appl. Sci. Manuf. 69 (2015) 72–82. doi:10.1016/j.compositesa.2014.10.024.
[249] B. Tang, G. Hu, H. Gao, L. Hai, Application of graphene as filler to improve thermal transport property of epoxy resin for thermal interface materials, Int. J. Heat Mass Transf. 85 (2015) 420–429. doi:10.1016/j.ijheatmasstransfer.2015.01.141.
[250] N. Burger, A. Laachachi, B. Mortazavi, M. Ferriol, M. Lutz, V. Toniazzo, D. Ruch, Alignments and network of graphite fillers to improve thermal conductivity of epoxy-based composites, Int. J. Heat Mass Transf. 89 (2015) 505–513.

doi:10.1016/j.ijheatmasstransfer.2015.05.065.
[251] C. Zeng, S. Lu, X. Xiao, J. Gao, L. Pan, Z. He, J. Yu, Enhanced thermal and mechanical properties of epoxy composites by mixing noncovalently functionalized graphene sheets, Polym. Bull. 72 (2014) 453–472. doi:10.1007/s00289-014-1280-5.
[252] F. Wang, L.T. Drzal, Y. Qin, Z. Huang, Mechanical properties and thermal conductivity of graphene nanoplatelet/epoxy composites, J. Mater. Sci. 50 (2014) 1082–1093. doi:10.1007/s10853-014-8665-6.
[253] T. Zhou, S. Nagao, T. Sugahara, H. Koga, M. Nogi, K. Suganuma, T.T. Nge, Y. Nishina, Facile identification of the critical content of multi-layer graphene oxide for epoxy composite with optimal thermal properties, RSC Adv. 5 (2015) 20376–20385. doi:10.1039/C4RA15881D.
[254] C. Zeng, S. Lu, L. Song, X. Xiao, J. Gao, L. Pan, Z. He, J. Yu, Enhanced thermal properties in a hybrid graphene–alumina filler for epoxy composites, RSC Adv. 5 (2015) 35773–35782. doi:10.1039/C5RA01967B.
[255] D. Tang, J. Su, Q. Yang, M. Kong, Z. Zhao, Y. Huang, X. Liao, Y. Liu, Preparation of alumina-coated graphite for thermally conductive and electrically insulating epoxy composites, RSC Adv. 5 (2015) 55170–55178. doi:10.1039/C5RA08010J.
[256] L. Pan, J. Ban, S. Lu, G. Chen, J. Yang, Q. Luo, L. Wu, J. Yu, Improving thermal and mechanical properties of epoxy composites by using functionalized graphene, RSC Adv. 5 (2015) 60596–60607. doi:10.1039/C5RA09410K.
[257] R. Wang, D. Zhuo, Z. Weng, L. Wu, X. Cheng, Y. Zhou, J. Wang, B. Xuan, A novel nanosilica/graphene oxide hybrid and its flame retarding epoxy resin with simultaneously improved mechanical, thermal conductivity, and dielectric properties, J. Mater. Chem. A. 3 (2015) 9826–9836. doi:10.1039/C5TA00722D.
[258] J.-W. Zha, T.-X. Zhu, Y.-H. Wu, S.-J. Wang, R.K.Y. Li, Z.-M. Dang, Tuning of thermal and dielectric properties for epoxy composites filled with electrospun alumina fibers and graphene nanoplatelets through hybridization, J. Mater. Chem. C. 3 (2015) 7195–7202. doi:10.1039/C5TC01552A.
[259] T. Zhou, Targeted kinetic strategy for improving the thermal conductivity of epoxy composite containing percolating multi-layer graphene oxide chains, Express Polym. Lett. 9 (2015) 608–623. doi:10.3144/expresspolymlett.2015.57.
[260] Y. Wang, J. Yu, W. Dai, Y. Song, D. Wang, L. Zeng, N. Jiang, Enhanced Thermal and Electrical Properties of Epoxy Composites Reinforced With Graphene Nanoplatelets, Polym. Compos. (2015) 556–565. doi:10.1002/pc.22972.
[261] X. Pu, H.-B. Zhang, X. Li, C. Gui, Z.-Z. Yu, Thermally conductive and electrically insulating epoxy nanocomposites with silica-coated graphene, RSC Adv. 4 (2014) 15297–15303. doi:10.1039/c4ra00518j.
[262] Y.-X. Fu, Z.-X. He, D.-C. Mo, S.-S. Lu, Thermal conductivity enhancement of epoxy adhesive using graphene sheets as additives, Int. J. Therm. Sci. 86 (2014) 276–283. doi:10.1016/j.ijthermalsci.2014.07.011.
[263] C. Esposito Corcione, A. Maffezzoli, Transport properties of graphite/epoxy composites: Thermal, permeability and dielectric characterization, Polym. Test. 32 (2013) 880–888. doi:10.1016/j.polymertesting.2013.03.023.
[264] C. Min, D. Yu, J. Cao, G. Wang, L. Feng, A graphite nanoplatelet/epoxy composite with high dielectric constant and high thermal conductivity, Carbon N. Y. 55 (2013) 116–125. doi:10.1016/j.carbon.2012.12.017.
[265] M.-C. Hsiao, C.-C.M. Ma, J.-C. Chiang, K.-K. Ho, T.-Y. Chou, X. Xie, C.-H. Tsai, L.-H. Chang, C.-K. Hsieh, Thermally conductive and electrically insulating epoxy nanocomposites with thermally reduced graphene oxide-silica hybrid nanosheets., Nanoscale. 5 (2013) 5863–71. doi:10.1039/c3nr01471a.
[266] T. Zhou, X. Wang, P. Cheng, T. Wang, D. Xiong, X. Wang, Improving the thermal conductivity of epoxy resin by the addition of a mixture of graphite nanoplatelets and silicon carbide microparticles, Express Polym. Lett. 7 (2013) 585–594. doi:10.3144/expresspolymlett.2013.56.
[267] M. a. Raza, a. V.K. Westwood, C. Stirling, Effect of processing technique on the transport and mechanical properties of graphite nanoplatelet/rubbery epoxy composites for thermal interface applications, Mater. Chem. Phys. 132 (2012) 63–73. doi:10.1016/j.matchemphys.2011.10.052.
[268] J. Kim, B. Yim, J. Kim, J. Kim, The effects of functionalized graphene nanosheets on the thermal and mechanical properties of epoxy composites for anisotropic conductive adhesives (ACAs), Microelectron. Reliab. 52 (2012) 595–602. doi:10.1016/j.microrel.2011.11.002.
[269] H. Im, J. Kim, Thermal conductivity of a graphene oxide–carbon nanotube hybrid/epoxy

composite, Carbon N. Y. 50 (2012) 5429–5440. doi:10.1016/j.carbon.2012.07.029.
[270] Y. Heo, H. Im, J. Kim, J. Kim, The influence of Al(OH)3-coated graphene oxide on improved thermal conductivity and maintained electrical resistivity of Al2O3/epoxy composites, J. Nanoparticle Res. 14 (2012) 1–10. doi:10.1007/s11051-012-1196-7.
[271] X. Huang, C. Zhi, P. Jiang, Toward Effective Synergetic Effects from Graphene Nanoplatelets and Carbon Nanotubes on Thermal Conductivity of Ultrahigh Volume Fraction Nanocarbon Epoxy Composites, J. Phys. Chem. C. 116 (2012) 23812−23820. doi:10.1021/jp308556r.
[272] M. Martin-gallego, R. Verdejo, M. Khayet, J. Maria, O. De Zarate, M. Essalhi, M.A. Lopez-manchado, Thermal conductivity of carbon nanotubes and graphene in epoxy nanofluids and nanocomposites, Nanoscale Res. Lett. 6 (2011) 1–7.
[273] T. D. Hoang, P. Joonkyu, H. Sang A, A. Muneer, S. Yongho, S. Koo, Electrical and Thermal Conductivities of Stycast 1266 Epoxy/Graphite Composites, J. Korean Phys. Soc. 59 (2011) 2760–2764. doi:10.3938/jkps.59.2760.
[274] A. Yu, P. Ramesh, X. Sun, E. Bekyarova, M.E. Itkis, R.C. Haddon, Enhanced thermal conductivity in a hybrid graphite nanoplatelet - Carbon nanotube filler for epoxy composites, Adv. Mater. 20 (2008) 4740–4744. doi:10.1002/adma.200800401.
[275] S. Wu, R.B. Ladani, J. Zhang, E. Bafekrpour, K. Ghorbani, A.P. Mouritz, A.J. Kinloch, C.H. Wang, Aligning multilayer graphene flakes with an external electric field to improve multifunctional properties of epoxy nanocomposites, Carbon N. Y. 94 (2015) 607–618. doi:10.1016/j.carbon.2015.07.026.
[276] X. Liu, X. Sun, Z. Wang, X. Shen, Y. Wu, J.-K. Kim, Planar Porous Graphene Woven Fabric/Epoxy Composites with Exceptional Electrical, Mechanical Properties, and Fracture Toughness, ACS Appl. Mater. Interfaces. 7 (2015) 21455–21464. doi:10.1021/acsami.5b06476.
[277] P. Ming, Y. Zhang, J. Bao, G. Liu, Z. Li, L. Jiang, Q. Cheng, Bioinspired highly electrically conductive graphene–epoxy layered composites, RSC Adv. 5 (2015) 22283–22288. doi:10.1039/C5RA00233H.
[278] G. Tang, Z.-G. Jiang, X. Li, H.-B. Zhang, S. Hong, Z.-Z. Yu, Electrically conductive rubbery epoxy/diamine-functionalized graphene nanocomposites with improved mechanical properties, Compos. Part B Eng. 67 (2014) 564–570. doi:10.1016/j.compositesb.2014.08.013.
[279] S. Dou, J. Qi, X. Guo, C. Yu, Preparation and adhesive performance of electrical conductive epoxy-acrylate resin containing silver-plated graphene, J. Adhes. Sci. Technol. 28 (2014) 1556–1567. doi:10.1080/01694243.2014.904766.
[280] G. Tang, Z.-G. Jiang, X. Li, H.-B. Zhang, Z.-Z. Yu, Simultaneous functionalization and reduction of graphene oxide with polyetheramine and its electrically conductive epoxy nanocomposites, Chinese J. Polym. Sci. 32 (2014) 975–985. doi:10.1007/s10118-014-1488-8.
[281] M. Monti, M. Rallini, D. Puglia, L. Peponi, L. Torre, J.M. Kenny, Morphology and electrical properties of graphene–epoxy nanocomposites obtained by different solvent assisted processing methods, Compos. Part A Appl. Sci. Manuf. 46 (2013) 166–172. doi:10.1016/j.compositesa.2012.11.005.
[282] H. Suherman, A.B. Sulong, J. Sahari, Effect of the compression molding parameters on the in-plane and through-plane conductivity of carbon nanotubes/graphite/epoxy nanocomposites as bipolar plate material for a polymer electrolyte membrane fuel cell, Ceram. Int. 39 (2013) 1277–1284. doi:10.1016/j.ceramint.2012.07.059.
[283] P. Mancinelli, T.F. Heid, D. Fabiani, A. Saccani, M. Toselli, M.F. Frechette, S. Savoie, E. David, Electrical conductivity of graphene-based epoxy nanodielectrics, 2013 Annu. Rep. Conf. Electr. Insul. Dielectr. Phenom. (2013) 772–775. doi:10.1109/CEIDP.2013.6748282.
[284] a. a. Al-Ghamdi, O. a. Al-Hartomy, F. Al-Solamy, A. a. Al-Ghamdi, F. El-Tantawy, Electromagnetic wave shielding and microwave absorbing properties of hybrid epoxy resin/foliated graphite nanocomposites, J. Appl. Polym. Sci. 127 (2013) 2227–2234. doi:10.1002/app.37904.
[285] J. Kim, H. Im, J. Kim, J. Kim, Thermal and electrical conductivity of Al(OH)3 covered graphene oxide nanosheet/epoxy composites, J. Mater. Sci. 47 (2011) 1418–1426. doi:10.1007/s10853-011-5922-9.
[286] Z. Fan, C. Zheng, T. Wei, Y. Zhang, G. Lu, Effect of Carbon Black on Electrical Property of Graphite Nanoplatelets/Epoxy Resin Composites, Polym. Eng. Sci. 49 (2009) 2041–2045. doi:10.1002/pen.
[287] N. Jović, D. Dudić, a. Montone, M.V. Antisari, M. Mitrić, V. Djoković, Temperature dependence of the electrical conductivity of epoxy/expanded graphite nanosheet composites, Scr. Mater. 58 (2008) 846–849. doi:10.1016/j.scriptamat.2007.12.041.

[288] J. Li, P.C. Ma, W.S. Chow, C.K. To, B.Z. Tang, J.-K. Kim, Correlations between Percolation Threshold, Dispersion State, and Aspect Ratio of Carbon Nanotubes, Adv. Funct. Mater. 17 (2007) 3207–3215. doi:10.1002/adfm.200700065.
[289] J. Sandler, M.S.. Shaffer, T. Prasse, W. Bauhofer, K. Schulte, a. . Windle, Development of a dispersion process for carbon nanotubes in an epoxy matrix and the resulting electrical properties, Polymer (Guildf). 40 (1999) 5967–5971. doi:10.1016/S0032-3861(99)00166-4.
[290] M.A. Berger, R.L. McCullough, Characterization and analysis of the electrical properties of a metal-filled polymer, Compos. Sci. Technol. 22 (1985) 81–106. doi:10.1016/0266-3538(85)90078-8.
[291] a. N. Rider, D.R. Arnott, The Influence of Adherend Topography on the Fracture Toughness of Aluminium-Epoxy Adhesive Joints in Humid Environments, J. Adhes. 75 (2001) 203–228. doi:10.1080/00218460108029601.
[292] M. Schuler, T.P. Kunzler, M. De Wild, C.M. Sprecher, D. Trentin, D.M. Brunette, M. Textor, S.G.P. Tosatti, Fabrication of TiO2-coated epoxy replicas with identical dual-type surface topographies used in cell culture assays, J. Biomed. Mater. Res. - Part A. 88 (2009) 12–22. doi:10.1002/jbm.a.31720.
[293] C.K. Lam, K.T. Lau, Tribological behavior of nanoclay/epoxy composites, Mater. Lett. 61 (2007) 3863–3866. doi:10.1016/j.matlet.2006.12.078.
[294] S. Yu, H. Hu, J. Ma, J. Yin, Tribological properties of epoxy/rubber nanocomposites, Tribol. Int. 41 (2008) 1205–1211. doi:10.1016/j.triboint.2008.03.001.
[295] S. Xia, Y. Liu, F. Pei, L. Zhang, Q. Gao, W. Zou, J. Peng, S. Cao, Identical steady tribological performance of graphene-oxide-strengthened polyurethane/epoxy interpenetrating polymer networks derived from graphene nanosheet, Polymer (Guildf). 64 (2015) 62–68. doi:10.1016/j.polymer.2015.03.036.
[296] R. Siegel, E. Hu, M. Roco, Editors, Nanostructure science and technology. A worldwide study. Prepared under the guidance of the IWGN, NSTC. WTEC, 1999.
[297] G. Pan, Q. Guo, J. Ding, W. Zhang, X. Wang, Tribological behaviors of graphite/epoxy two-phase composite coatings, Tribol. Int. 43 (2010) 1318–1325. doi:10.1016/j.triboint.2009.12.068.
[298] W. Brostow, M. Dutta, P. Rusek, Modified epoxy coatings on mild steel: Tribology and surface energy, Eur. Polym. J. 46 (2010) 2181–2189. doi:10.1016/j.eurpolymj.2010.08.006.
[299] W.H. Zhang, J.H. Hsieh, Tribological behavior of TiN and CrN coatings sliding against an epoxy molding compound, Surf. Coatings Technol. 130 (2000) 240–247. doi:10.1016/S0257-8972(00)00709-X.
[300] L. Chang, Z. Zhang, L. Ye, K. Friedrich, Tribological properties of epoxy nanocomposites. III. Characteristics of transfer films, Wear. 262 (2007) 699–706. doi:10.1016/j.wear.2006.08.002.
[301] J.M. Lackner, W. Waldhauser, C. Ganser, C. Teichert, M. Kot, L. Major, Mechanisms of topography formation of magnetron-sputtered chromium-based coatings on epoxy polymer composites, Surf. Coatings Technol. 241 (2014) 80–85. doi:10.1016/j.surfcoat.2013.07.040.
[302] C.M. Cotell, J.A. Sprague, F.A.J. Smidth, eds., ASM Handbook, Vol. 5. Surface Engineering, 1994.
[303] R. Atif, J. Wei, I. Shyha, F. Inam, Use of morphological features of carbonaceous materials for improved mechanical properties of epoxy nanocomposites, RSC Adv. 6 (2016) 1351–1359. doi:10.1039/C5RA24039E.
[304] J. Wei, R. Atif, T. Vo, F. Inam, Graphene Nanoplatelets in Epoxy System : Dispersion , Reaggregation , and Mechanical Properties of Nanocomposites, J. Nanomater. 2015 (2015) 1–12.
[305] M.S. Saharudin, R. Atif, I. Shyha, F. Inam, The degradation of mechanical properties in polymer nano-composites exposed to liquid media – a review, RSC Adv. 6 (2016) 1076–1089. doi:10.1039/C5RA22620A.
[306] S.L. Gao, E. Mäder, S.F. Zhandarov, Carbon fibers and composites with epoxy resins: Topography, fractography and interphases, Carbon N. Y. 42 (2004) 515–529. doi:10.1016/j.carbon.2003.12.085.
[307] J. Karger-Kocsis, H. Mahmood, A. Pegoretti, Recent advances in fiber/matrix interphase engineering for polymer composites, Prog. Mater. Sci. 73 (2015) 1–43. doi:10.1016/j.pmatsci.2015.02.003.
[308] S.I. Moon, J. Jang, Mechanical interlocking and wetting at the interface between argon plasma treated UHMPE fiber and vinylester resin, J. Mater. Sci. 34 (1999) 4219–4224. doi:10.1023/A:1004642500738.
[309] M. Nardin, I.M. Ward, Influence of surface treatment on adhesion of polyethylene fibres,

Mater. Sci. Technol. 3 (1987) 814–826. doi:10.1179/mst.1987.3.10.814.
[310] N.H. Ladizesky, I.M. Ward, The adhesion behaviour of high modulus polyethylene fibres following plasma and chemical treatment, J. Mater. Sci. 24 (1989) 3763–3773. doi:10.1007/BF02385768.
[311] D.W. Woods, I.M. Ward, Study of the oxygen treatment of high-modulus polyethylene fibres, Surf. Interface Anal. 20 (1993) 385–392. doi:10.1002/sia.740200510.
[312] B. Tissington, G. Pollard, I.M. Ward, A study of the influence of fibre/resin adhesion on the mechanical behaviour of ultra-high-modulus polyethylene fibre composites, J. Mater. Sci. 26 (1991) 82–92. doi:10.1007/BF00576036.
[313] R. Engelke, G. Engelmann, G. Gruetzner, M. Heinrich, M. Kubenz, H. Mischke, Complete 3D UV microfabrication technology on strongly sloping topography substrates using epoxy photoresist SU-8, Microelectron. Eng. 73–74 (2004) 456–462. doi:10.1016/j.mee.2004.03.017.
[314] D.S. Rickerby Matthews A, Advanced Surface Coatings: a Handbook of Surface Engineering, Chapman and Hall, Published in the USA, 1991.
[315] C. Jiang, J. Zhu, J. Han, W. Cao, The surface topography, structural and mechanical properties of Ge1−xCx films prepared by magnetron co-sputtering, J. Non. Cryst. Solids. 383 (2014) 126–130. doi:10.1016/j.jnoncrysol.2013.04.011.
[316] L. Guo, J. Ding, J. Yang, G. Cheng, Z. Ling, Effects of high hydrogen dilution ratio on surface topography and mechanical properties of hydrogenated nanocrystalline silicon thin films, Thin Solid Films. 519 (2011) 6039–6043. doi:10.1016/j.tsf.2011.04.117.
[317] R.K. Pitler, E.L. Langer, eds., ASM Handbook, Vol. 16. Machining., 1995. http://www.amazon.co.uk/ASM-Handbook-Machining-v-16/dp/0871700220.
[318] P.J. Blau, ed., ASM Handbook, Vol. 18. Friction, Lubrication, and Wear Technology., 2001. http://books.google.com.hk/books?id=eC-Zt1J4oCgC.
[319] Y.G. Yanovsky, E.A. Nikitina, Y.N. Karnet, S.M. Nikitin, Quantum mechanics study of the mechanism of deformation and fracture of graphene, Phys. Mesomech. 12 (2009) 254–262. doi:10.1016/j.physme.2009.12.007.
[320] Q. Lu, W. Gao, R. Huang, Atomistic simulation and continuum modeling of graphene nanoribbons under uniaxial tension, Model. Simul. Mater. Sci. Eng. 19 (2011) 54006. doi:10.1088/0965-0393/19/5/054006.
[321] T.C. Theodosiou, D. a. Saravanos, Numerical simulation of graphene fracture using molecular mechanics based nonlinear finite elements, Comput. Mater. Sci. 82 (2014) 56–65. doi:10.1016/j.commatsci.2013.09.032.
[322] Z. Ni, H. Bu, M. Zou, H. Yi, K. Bi, Y. Chen, Anisotropic mechanical properties of graphene sheets from molecular dynamics, Phys. B Condens. Matter. 405 (2010) 1301–1306. doi:10.1016/j.physb.2009.11.071.
[323] Y. Liu, Z. Xu, Multimodal and self-healable interfaces enable strong and tough graphene-derived materials, J. Mech. Phys. Solids. 70 (2014) 30–41. doi:10.1016/j.jmps.2014.05.006.
[324] F. Liu, P. Ming, J. Li, Ab initio calculation of ideal strength and phonon instability of graphene under tension, Phys. Rev. B - Condens. Matter Mater. Phys. 76 (2007) 1–7. doi:10.1103/PhysRevB.76.064120.
[325] B. Mortazavi, T. Rabczuk, Multiscale modeling of heat conduction in graphene laminates, Carbon N. Y. 85 (2015) 1–7. doi:10.1016/j.carbon.2014.12.046.
[326] R. Atif, I. Shyha, F. Inam, Modeling and experimentation of multi-layered nanostructured graphene-epoxy nanocomposites for enhanced thermal and mechanical properties, J. Compos. Mater. 0 (2016) 1–12. doi:10.1177/0021998316640060.
[327] A. Warrier, A. Godara, O. Rochez, L. Mezzo, F. Luizi, L. Gorbatikh, S. V Lomov, A.W. VanVuure, I. Verpoest, The effect of adding carbon nanotubes to glass/epoxy composites in the fibre sizing and/or the matrix, Compos. Part A Appl. Sci. Manuf. 41 (2010) 532–538. doi:10.1016/j.compositesa.2010.01.001.
[328] R. Atif, F. Inam, Modeling and Simulation of Graphene Based Polymer Nanocomposites : Advances in the Last Decade, Graphene. 5 (2016) 96–142. doi:http://dx.doi.org/10.4236/graphene.2016.52011.
[329] M. Abdalla, D. Dean, D. Adibempe, E. Nyairo, P. Robinson, G. Thompson, The effect of interfacial chemistry on molecular mobility and morphology of multiwalled carbon nanotubes epoxy nanocomposite, Polymer (Guildf). 48 (2007) 5662–5670. doi:10.1016/j.polymer.2007.06.073.
[330] K. Kalaitzidou, H. Fukushima, L.T. Drzal, Mechanical properties and morphological characterization of exfoliated graphite-polypropylene nanocomposites, Compos. Part A Appl. Sci. Manuf. 38 (2007) 1675–1682. doi:10.1016/j.compositesa.2007.02.003.

[331] J.J. Mack, L.M. Viculis, A. Ali, R. Luoh, G. Yang, H.T. Hahn, F.K. Ko, R.B. Kaner, Graphite nanoplatelet reinforcement of electrospun polyacrylonitrile nanofibers, Adv. Mater. 17 (2005) 77–80. doi:10.1002/adma.200400133.
[332] J. Cho, J.Y. Chen, I.M. Daniel, Mechanical enhancement of carbon fiber/epoxy composites by graphite nanoplatelet reinforcement, Scr. Mater. 56 (2007) 685–688. doi:10.1016/j.scriptamat.2006.12.038.
[333] A. Yasmin, I.M. Daniel, Mechanical and thermal properties of graphite platelet/epoxy composites, Polymer (Guildf). 45 (2004) 8211–8219. doi:10.1016/j.polymer.2004.09.054.
[334] S.-C. Wong, E. Sutherland, F. Uhl, Materials Processes of Graphite Nanostructured Composites Using Ball Milling, Mater. Manuf. Process. 21 (2006) 159–166. doi:10.1081/AMP-200068659.
[335] J. Li, J.K. Kim, M. Lung Sham, Conductive graphite nanoplatelet/epoxy nanocomposites: Effects of exfoliation and UV/ozone treatment of graphite, Scr. Mater. 53 (2005) 235–240. doi:10.1016/j.scriptamat.2005.03.034.
[336] D. Vennerberg, Z. Rueger, M.R. Kessler, Effect of silane structure on the properties of silanized multiwalled carbon nanotube-epoxy nanocomposites, Polymer (Guildf). 55 (2014) 1854–1865. doi:10.1016/j.polymer.2014.02.018.
[337] J.N. Coleman, U. Khan, W.J. Blau, Y.K. Gun'ko, Small but strong: A review of the mechanical properties of carbon nanotube–polymer composites, Carbon N. Y. 44 (2006) 1624–1652. doi:10.1016/j.carbon.2006.02.038.
[338] P.-C. Ma, N.A. Siddiqui, G. Marom, J.-K. Kim, Dispersion and functionalization of carbon nanotubes for polymer-based nanocomposites: A review, Compos. Part A Appl. Sci. Manuf. 41 (2010) 1345–1367. doi:10.1016/j.compositesa.2010.07.003.